THERMAL MANAGEMENT OF ELECTRIC VEHICLE BATTERY PACKS

BERNARD SAW LIP HUAT

NATIONAL UNIVERSITY OF SINGAPORE

2014

THERMAL MANAGEMENT OF ELECTRIC VEHICLE BATTERY PACKS

BERNARD SAW LIP HUAT
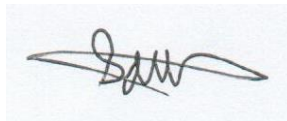### (M. Eng. Sc., UM)

A THESIS SUBMITTED

FOR THE DEGREE OF DOCTOR OF PHILOSOPHY
DEPARTMENT OF MECHANICAL ENGINEERING

NATIONAL UNIVERSITY OF SINGAPORE

2014

DECLARATION

I hereby declare that this thesis is my original work and it has been written by me in its entirety. I have duly acknowledged all the sources of information which has been used in the thesis.

This thesis has also not been submitted for any degree in any university previously.

BERNARD SAW LIP HUAT

15 AUGUST 2014

ACKNOWLEDGEMENTS

Accomplishing this dissertation is a major task, and I could not have accomplished it without the help of some people. Hence, it is my pleasure to acknowledge these people who have contributed their efforts directly or indirectly throughout my thesis.

First of all I would like to thanks National University of Singapore, Energy Market Agency and AUN/SEED Net-JICA for their financial contribution to my study.

Secondly, I would like to express my deepest gratitude and appreciation towards my dissertation supervisor. Professor Dr. Andrew Tay who has being supervising me through the semesters and providing me a lot of advice, support, patience and hours of constant dedication to my research. I have really enjoyed the scientific discussions that we had.

Many people from National University of Singapore should be acknowledged: researchers, technicians, administrative personnel for their support and valuable help throughout the research, especially Assoc. Prof Lee Poh Seng and Asst. Prof. Ernest Chua for lending the wind tunnel and Infra red camera. I am also indebted to all personnel from the Thermal Process laboratory, Material Research Laboratory and Control Laboratory for their assistance during the development of the project. Their kindness and thoughtful ways have made the progress of my dissertation much smoother.

Most important special gratitude to my beloved family for their prayer, love, support, understanding and encouragement during my PhD study.

<div align="right">Bernard Saw Lip Huat   August 2014</div>

TABLES OF CONTENTS

LIST OF PUBLICATIONS

1. Saw, L. H., Ye, Y., and Tay, A. A. O. (2013). Electrochemical-thermal analysis of 18650 Lithium Iron Phosphate cell. *Journal of Energy Conversion and Management*. **75**. 162-174.

2. Saw, L. H., and Tay, A. A. O. (2013). Thermal modeling and management of Li-ion batteries for electric vehicles. InterPACK 2013, Proc. ASME 2013 International Technical Conference and Exhibition on Packaging and Integration of Electronic and Phonic Microsystems. Burlingame, CA. USA.

3. Saw, L. H., Somasundaram K., Ye, Y., and Tay, A. A. O. (2014). Electro-thermal analysis of Lithium Iron Phosphate battery for electric vehicles. *Journal of Power Sources*. **249**. 231-238.

4. Saw, L. H., Ye, Y., and Tay, A. A. O. (2014). Electro-thermal analysis and integration issues of Lithium-ion battery for electric vehicles. *Applied Energy*. **131**. 97-107.

5. Saw, L. H., and Tay, A. A. O. (2014). A comparative study of the thermal performance of 18650 and 38120 cells for electric vehicles. *SGBM 2014, Singapore*.

6. Saw, L. H., Ye, Y., and Tay, A. A. O. (2014). Electro-thermal characterization of Lithium Iron Phosphate cell with equivalent circuit modeling. *Energy Conversion and Management*. **87**. 367-377.

7. Saw, L. H., Ye, Y., and Tay, A. A. O. (2014). Feasibility study of Boron Nitride coating on Lithium ion battery casing. *Journal of Applied Thermal Engineering*. **73**. 152-159.

8. Saw, L. H., Ye, Y., and Tay, A. A. O. (2014). Computational fluid dynamic and thermal analysis of Lithium-ion battery pack. *International Journal of Thermal Sciences*. (Under review).

9. Saw, L. H., Ye, Y., and Tay, A. A. O. (2014). Integration issues of Lithium-ion battery into battery pack for electric vehicles. *Journal of Cleaner Production*. (Under review).

SUMMARY

The electric vehicle (EV) is projected as one of the most sustainable solutions for future transportation. The Lithium-ion battery offers an attractive solution as an energy storage system for EVs due to its high theoretical energy density and great environmental friendliness compared to nickel cadmium and lead acid batteries. However, the main challenge for EVs nowadays is the performance and cycle life of the battery pack which is closely related to its thermal management. Temperature will affect the power of the battery pack, energy storage during regenerative braking and cell balancing. This will further influence the energy efficiency, drive-ability and cycle life of the battery. Large temperature variations in the module will lead to different charging/ discharging behavior and electrically unbalanced cells which curtail battery life. In this study, the temperature response and heat generated in different sizes and geometries of cells were investigated numerically and validated with experiments. The results shown that the cell temperature and heat generation are positively correlated with the charging/discharging rates and size of the cell. Next, the thermal management system of the battery packs using air and liquid cooling system were developed. Cooling fins were incorporated to increase the rate of cooling and reduce the variation of cell temperature across the pack. In air cooling, a novel design of cooling fins is proposed to resolve the high temperature at the downstream, which is a common problem for battery packs with a regular staggered arrangement of cells. Four independent design parameters- air mass flow rate, number of fins, fin thickness and fin material are used to investigate the performance of the air cooling fin. On the other hand, seven independent design parameters which

are flow direction, mass flow rate, length, width, longitudinal distance, transverse distance and number of zones for the cooling fin are used to investigate the performance of the liquid cold plate. Taguchi-Grey method is used to optimize the design parameters with respect to target responses such as specific performance, pressure drop and temperature uniformity. Then, parametric analysis of the cooling fin structure was conducted and regression analysis was used to correlate the average Nusselt number, average friction factor and variation of temperature with the Reynolds number and the physical dimension of the cooling fins. Lastly, integration issues of the cells into a battery pack are discussed from various points of view, such as types of cell, packaging, electric connection and control, thermal management, assembly, services and maintenance.

LISTS OF TABLES

xvi

LISTS OF FIGURES

LIST OF SYMBOLS

A	Exponential voltage, V
A_{mf}	Cross section flow area for cooling air per module, m^2
A_{ms}	Total module surface area exposed to cooling air, m^2
B	Exponential zone time constant, $(Ah)^{-1}$
BMS	Battery management system
BTMS	Battery Thermal Management System
C	Constant
C/I_t-rate	Discharge current in amperes during one hour discharge
$C_{P,air}$	Specific heat of air, $Jkg^{-1} K^{-1}$
$C_{p,eff}$	Specific heat capacity for the active battery material, $J kg^{-1} K^{-1}$
CFD	Computational Fluid Dynamics
DOD	Depth of discharge, %
DF	Degree of freedom
d_{ext}	Outer diameter of the tube, m
E_a	Activation energy, kJ
E_m	Thermodynamic voltage, V
E_0	Battery constant voltage, V
EV	Electric Vehicle
F	Faraday's constant, $C mol^{-1}$
FTP	Federal test Procedure
f	friction factor
H	Height, m
HEV	Hybrid Electric Vehicle

HWFET	Highway Fuel Economy Test
h	Convective heat transfer coefficient, W m^{-2} K^{-1}
h_{ext}	Convective heat transfer coefficient, Wm^{-2} K^{-1}
LFP	Lithium Iron Phosphate
j	Colburn J-factor
K	Polarization constant, V(Ah)$^{-1}$ or polarization resistance, Ω
k	Effective thermal conductivity of the active battery material, W m^{-1} K^{-1}
$k_{T,i}$	Thermal conductivity of the materials in each layer, W m^{-2} K^{-1}
k$_{air}$	Thermal conductivity of air, Wm^{-1}K^{-1}
$\dot{m}$	Mass flow rate of air, kgs^{-1}
Mq	Mean sum of squares
Mqe	Mean sum of squares due to error
MS	Mean sum of squares, dividing the Sq by v
NiMH	Nickel Metal Hydride
Nu	Nusselt number
NPM	Noise performance measure
OCV	Open circuit voltage, V
P	Power consumption, W
PVC	Polyvinyl Chloride
P-value	The probability of obtaining a test statistic at least as extreme as the one that was actually observed.
$\dot{Q}$	Amount of heat generated, W
R	Universal gas constant, J mol^{-1} K^{-1}
RC	Resistive and Capacitive

Re	Reynolds number
R-Sq	R-Square
R-Sq(adj)	Adjusted R Square
Re_∞	Reynolds number for incoming air at free stream
S	Standard error
SS	Sum of squares
SOC	State of charge, %
T	Absolute temperature, K
T_{ref}	Reference temperature, K
T_∞	Free stream temperature, K
TPM	Target performance measure
UDDS	Urban Dynamometer Driving Schedule
US06	Supplemental Federal Test Procedure (SFTP)
V	Volume of the cooling fin, m^3
V_h	Hysteresis voltage
W	Width, m
ξ	Porosity, %
ρ_{eff}	Effective density of the active battery material, kg m^{-3}
ε	Emissivity
σ	Stefan-Boltzmann constant, W m^{-2} K^{-4}
ρ_i	Density of the materials in each layer, kg m^{-3}
Δp	Pressure drop, Pa
μ_{air}	Dynamic viscosity of air, kgms^{-1}

CHAPTER 1

INTRODUCTION

1.1 General Introduction

The world relies heavily on fossil fuel to meet the daily power demand, ranging from electricity generation to transportation. In 2009, the logistics sector accounted for 61.7% of total world oil consumption and 23% of total world CO_2 emission respectively (International Energy Agency, 2011). Besides, burning fossil fuel deteriorates the air quality and leads to global warming. Harmful gas emissions such as carbon monoxide (CO), nitrogen oxides (NO_x), sulfur oxides (SO_x), carbon dioxide (CO_2), hydrocarbon (HC), particulate matter (PM) and non-methane hydrocarbons (NMHC) affect human health. The vehicle emission standards have been made extremely stringent to address the worldwide air quality issue. In the European Union Euro 6 was be implemented in 2014 to reduce the emission of CO from 2.72 g/km (Euro 1) to 1.0 g/km and HC + NO_x emission from 0.97 g/km (Euro 1) to 0 g/km.

Under the concern of environmental pollution, the automotive industry has been forced to shift its attention to clean energy. The internal combustion engine (ICE) technology is saturated and no alternative propulsion system can replace it. Hence, Electric Vehicles (EVs) and Fuel Cell Vehicles are projected as the most sustainable solutions for future transport (Bossche at al., 2006 and Omar et al., 2012). However, fuel cell technology is still immature, poor dynamic performance and long energy conversion times restrict their application in vehicles. Therefore, EVs have the potential to replace ICE vehicles until fuel cell technology becomes mature. Moreover, the US

government has targeted 1000,000 of EVs on the road by 2015 (US DOE, 2013).

The Li-ion battery was introduced by Sony in 1990 to replace unsafe and poor cycle life rechargeable metallic lithium battery (Nagaura, 1990 and Dhameja, 2002). Li-ion batteries have high energy density, light weight, low maintenance, relatively low toxic, fast charging capability, no memory effect, no periodic deliberate full discharge requirement and low self-discharge rate compare to Nickel Cadmium and Nickel Metal Hydride (NiMH) batteries. Hence, Li-ion batteries have been extensively investigated to replace NiMH and valve-regulated lead acid battery in EVs which have low energy density and depth of discharge (DOD%) (Zhang, 2007 and Liu, 2009). The potential candidates of Li-ion batteries for EVs are Lithium Cobalt Oxide (LiCO$_2$), Lithium Manganese Oxide (LiMn$_2$O$_4$), Lithium Iron Phosphate (LiFePO$_4$) and Lithium Nickel Manganese Cobalt Oxide (NMC) with different types of packaging such as spiral wound, elliptic and stacked plate make a good choice for the energy storage system (Ohzuk, 2007 and The Boston Consulting Group, 2013). As shown in Figure 1.1, Li-ion batteries have large specific energy density, specific power and lighter compare to other rechargeable batteries, making them an ideal choice for EVs (Liu, 2009). Therefore, it is projected that Li-ion batteries will be the choice for next generation EVs, plug in HEVs and HEVs.
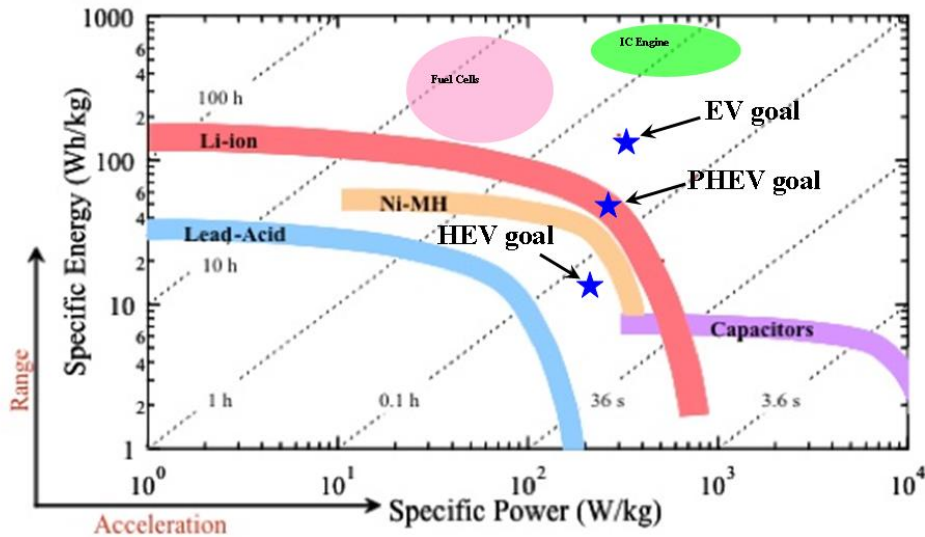
Figure 1.1 Ragone plot of energy storage devices for automotive applications.

In EVs, battery packs are formed by connecting the battery cells in series and in parallel and closely packed to provide the necessary power for the traction motor. Battery pack cycle life, capacity, fast charging, durability and the warranty are the parameters affecting the cost and reliability of the EVs and these depend on the thermal management system. Battery temperature and uniformity have a strong influence on the battery pack power, cell balancing and charge acceptance during regenerative braking. Large temperature variation will lead to electrically unbalanced cells and affect the electrochemistry process. The ideal operating temperature range is 25 ^{o}C to 40 ^{o}C for optimum performance of Li-ion batteries and calendar life, but the operating temperature of the vehicle could reach -30 ^{o}C to 70 ^{o}C (Pesaran, 2002). Under extreme conditions, thermal runaway of the cell may occur (Pesaran, 2001, Kuper et al., 2009 and Heckenberger, 2009). Pesaran et al. showed that the relative cycle life and capacity of the battery are inversely proportional to the temperature (Pesaran et al., 2009). Besides, the goal of 10 years life for EVs battery pack set by United State Advanced Battery Consortium (USABC) indicated a need for temperature control, even during

idling (Karditsas, 2012). This further emphasizes the need for a good understanding of the Li-ion battery thermal issues and thermal management of EV battery packs. Currently, the critical challenges increasing the market share of EVs are battery, cost, reliability, safety and charging duration. Besides, limited driving range, high cost, long charging time and vehicle safety are the most common consumers' negative perception on EVs. In particular, fast charging associated with the extensive heat generation and decreases in cycle life of batteries have spurred new interest in thermal management of battery systems. Hence, more research and development must be made to ensure that EVs offer similar capabilities and performance as conventional ICE vehicles. Otherwise, negative public perception can restrain technology growth.

1.2 Importance of the study

In order to design a realistic thermal management system for EV battery packs, it is important to characterize the thermal phenomena of the Li-ion cell for the required transient power response. However, the facility needed to carry out the testing incorporating a high power programmable battery tester, an environmental chamber and an accelerating rate calorimeter, is always expensive and requires several hundred hours of testing. The battery pack may not be comprehensively tested due to the limitations of the battery tester. Moreover, experimental testing does not enable innovative design and optimization of the thermal management system. For this, numerical modeling techniques such as electrochemical-thermal modeling and electro-thermal modeling must be used. Numerical modeling not only improves the understanding of the battery operating mechanism but also provides useful

internal information such as electrochemical reaction rates, heat generation, temperature distribution, concentration distribution which is difficult to obtain through experiments.

Battery temperature is the key factor which determines the performance and life of the battery pack. It influences the discharge power availability during startup and acceleration, storage capacity and energy recovery from regenerative braking. Subsequently, these would affect the fuel economy and operating range of EVs. The electrochemistry process inside the cell is greatly dependent on the temperature. Therefore, it is desirable to have a battery operated within a specific temperature range to ensure optimum performance and safety. In this study, various types of battery pack thermal management systems will be developed and tested such as air and liquid cooling systems to provide an effective solution for fast charging battery pack and prolong the cycle life of the cell and enhance the safety of the battery.

There are several issues associated with the integration of the Li-ion cells into the battery module and the battery pack such as electrical, battery power management system, thermal management, packaging, cost, assembly, recyclability, services and maintenance and safety. These issues are paramount to generate a comfortable and safe environment to bring out the best of each individual cell. Poor integration of cell into battery modules and packs may lead to safety concerns, poor performance, poor cycle life and higher cost of the EVs. Therefore, a converted EV using a Lithium Iron Phosphate battery pack will be used in a benchmarking study to provide a basic guideline for cell selection and integration of the cells for EV battery packs.

1.3 Research problem statement

Most of the EVs in the market are operated at a low charging rate. Therefore, the need for the battery thermal management system may not be obvious initially. Although some of the EV battery packs have a thermal management system installed, it is only suitable for low charging rate and less attention is paid on the temperature uniformity within the battery pack. The thermal management system design is less elaborate, and overheating of the batteries is commonly found. Ideally, Li-ion batteries should operate between 25 ^{o}C to 40 ^{o}C for optimum performance and life (Pesaran, 2002). The energy storage and cycle life of the cell can be reduced significantly when the cell is operated at a temperature above 40 ^{o}C or below 0 ^{o}C. High temperatures promote growth of the solid electrolyte interface layer and increase the internal resistance which would cause a reduction in the power delivery. Under extreme conditions, the separator will melt, cause an internal short circuit and lead to uncontrollable temperature rise (thermal runaway) in the cell. The energy and gases released from this reaction are dangerous and can cause an explosion or fire depending on the battery chemistry. On the other hand, the capacity will be reduced if the battery is operated at temperatures below 0 ^{o}C and lithium plating during charging will occur. While higher temperatures can be tolerated temporarily, if the temperature is above 60 ^{o}C for a prolonged period with the battery fully charged, there is a real possibility that the batteries may rupture, explode and catch fire due to thermal runaway. Besides, high density packing of batteries may prevent heat removal from cells at the center of the battery pack. Long term self-heating may cause the temperature of the cells to reach a self-sustaining thermal runaway condition.

In this situation, heat transfer from the faulty cell will also cause thermal runaway in the neighboring cells of the battery pack. Hence, the thermal runaway reaction will propagate to the entire battery pack (Mikolaiczak et al., 2011). Battery pack cycle life, capacity, high charging rate, durability and warranty are the main parameters affecting the cost and reliability of the EVs and these depend on the thermal management system. Battery temperature and uniformity have a strong influence on the availability of the charging and discharging power, cell balancing and charge acceptance during regenerative braking. A large variation of temperature in a battery pack can lead to different cells charging and discharging at different rates and lead to electrically unbalanced cells and reduce the performance of the battery pack. Variation of temperature within a battery cell should be kept between 5 $^{\circ}$C to 10 $^{\circ}$C while the variation of temperature across the battery pack should be kept within 3 $^{\circ}$C to 5 $^{\circ}$C. The cell at the highest temperature will set the limit on the power of the battery pack. A temperature difference of 5 $^{\circ}$C would lead to about 10% degradation of power capability, and an increment of 25% of thermal aging kinetics. The degradation could escalate to 50% for higher variations of temperature. Besides, the self-discharge rate would also be affected over a long period of time and would lead to a reduction in the effective operational state of charge (SOC) window (Kuper et al., 2009; Pesaran, 2001 and Heckenberger, 2009). Cyclic and thermal aging are two different types of aging associated with the Li-ion battery, thermal and cyclic aging define the calendar life of the battery. Thermal and cyclic aging decrease the capacity and increase the internal resistance of the cell. The rate depends on the cell temperature and SOC. A fully charged battery degrades faster than a partially

charged battery. An increase of the cell temperature by 10 ^{o}C to 15 ^{o}C reduces the cell life by 30 -50% (Kuper et al., 2009). This further emphasizes the need for a good understanding of the thermal issues of the Li-ion battery and a good thermal management system for a battery pack.

In the EV battery pack, Li-ion cells are connected in series and in parallel to deliver the required power for the traction motor and auxiliary systems. Different sizes of cell have been used to develop the EVs battery pack. For example, Tesla Roadster used more than 7000 pieces of 18650 cells (3100 mAh) for the Tesla Model S while Mitsubishi used 88 much larger prismatic cells (50 Ah) for their Mitsubishi i-MiEV. Using a larger number of small cells or a few large cells has its own advantages and disadvantages. The benefits of using small cells include cost efficiency, a lack of thermal aging tendency and improvements in safety. Conversely, the drawbacks include many interconnections, higher integration and assembly cost, lower weight and volume efficiency, lower reliability and complex wiring of the battery management system. On the other hand, utilizing larger cells has several advantages such as lower assembly cost, higher weight and volume efficiency, higher reliability, less complex interconnections and ease of troubleshooting. The disadvantages include higher cell production costs, low quality, thermal aging and capacity fading (Pesaran, 2009 and Andrea, 2010). Hence, there is a necessity to investigate the integration issues of the Li-ion battery into the battery pack.

1.4 Objectives of the study

The specific objectives of this research are:

1. To model the electro-chemistry, electrical and thermal behavior of the Lithium Iron Phosphate battery under different operating conditions.

2. To design and develop a novel and effective battery thermal management system for Li-ion battery pack operating at a high charging rate.

3. To investigate and optimize the cooling system of the battery pack.

4. To investigate the feasibility of replacing the polymer insulation on the battery casing with a Boron Nitride coating.

5. To investigate the integration issues of Li-ion cells into the battery pack.

1.5 Contribution of the study

The contribution of the present work is as follows:

1. A pseudo two dimensional electrochemical model coupled with a three-dimensional thermal model has been developed to analyze the coupled electrochemical-thermal behavior of the conventional 18650 Lithium Iron Phosphate battery during the charging and discharging processes. The effects of the outer can, heat shrink wrapping and influence of external contact resistance between the battery terminals and connectors, which have not been studied before, were investigated. The modeling results were validated with experimental data.

2. The modified Shepherd equation was coupled with a lumped thermal model to predict the electrical and thermal behavior of the 18650 and

38120 Lithium Iron Phosphate cells under constant current discharging, dynamic loading and different driving conditions such as Urban Dynamometer Driving Schedule, Highway Fuel Economy Driving Schedule and US06 Supplemental Federal Test Procedure. Experimental studies were conducted to validate the proposed model.

3. Third order Resistive Capacitive model with resistance and capacitance which varied with SOC and temperature was developed to track the electrical and thermal response of the cell under constant current and transient load conditions. Hysteresis effects were incorporated into the RC model of the LFP cell. The validated model was then used to predict the I-V and thermal characteristics of the battery pack under UDDS and US06 driving cycles.

4. A feasibility study of replacing the conventional polymer insulator of battery cells with a Boron Nitride coating was carried out to improve the heat dissipation from the battery. Coating parameters such as coating thickness and surface roughness were optimized using the Taguchi method.

5. Detailed three-dimensional numerical simulations were performed on the air-cooled battery pack with air flow parallel to the cylindrical cells. The heat transfer correlations deduced from the simulation results were used to predict the average temperature of the cells in the battery pack under 1, 3 and 5 I_t-rates of constant current charging. Experimental testing was carried out to validate the developed correlations.

6. Novel air cooling fins for 18650 cylindrical cells were developed. Detailed three-dimensional numerical simulations were performed to optimize the design of the cooling fins. Correlations of the Nusselt number, Colburn factor, friction factor and temperature uniformity were developed. Experimental studies were carried out to validate the correlations.

7. Novel liquid cooling fins were developed for battery packs employing prismatic and pouch cells. Detailed three-dimensional numerical simulations were performed to optimize the design of the liquid cold plate. Correlations of the Nusselt number, friction factor and temperature uniformity were derived from the simulation results. The numerical results are in very good agreement with the data obtained from experiments, suggesting that such an approach can be used for the systematic study of cooling fins.

8. The integration of LFP cells into the EV battery packs was investigated from various perspectives. This includes chemistry of Li-ion battery, packaging, electrical connections, battery management system, assembly, thermal management, service and maintenance, and testing.

1.6 Arrangement of the thesis contents

The report is subdivided into eleven chapters.

Chapter 1 gives a general view of the importance of the study, and gives a scenario of the problems to be investigated. Concepts and importance of the battery pack thermal management are also reviewed. Goals and objectives of the work are identified.

In chapter 2, a literature review of the various types of battery thermal management systems and Li-ion batteries are presented. Also, the open literature on electrochemical-thermal and electro-thermal modeling and experimental studies of various Li-ion battery packs are also discussed.

Chapter 3 describes the development of a new electrochemical-thermal modeling of a Li-ion battery. The details of the modeling parameters are reviewed in this chapter. Besides, the results of the numerical modeling and experimental work are elaborated.

Chapter 4 describes the development of a new battery model using a modified Shepherd equation. The details of the modeling parameters are reviewed in this chapter. The results of the numerical modeling and experimental work are presented and discussed.

Chapter 5 describes the development of a new equivalent circuit model of a Li-ion battery using a resistive capacitive (RC) model. The details of the modeling parameters are reviewed in this chapter. The results of the numerical modeling and experimental work are presented and discussed.

Chapter 6 describes a feasibility study of the effectiveness of the Boron Nitride coating on the battery casing surface in substituting the Polyvinyl Chloride heat shrink wrapping. The findings of the study and the optimization work of the experimental study are presented and discussed.

Chapter 7 presents the conceptual design, numerical simulation and experimental work for air cooling system with air flowing parallel to cylindrical cells. The performance of an air-cooled battery pack made up of cylindrical 38120 cells was investigated, where the cooling air flows in the spaces between the cylinders parallel to the axis of the cells. The findings of

the study and the critical analysis of the numerical simulation and experimental study are presented and discussed.

Chapter 8 presents the conceptual design, numerical simulation, optimization and experimental study of an air cooled system using fins. The findings of the study and the critical analysis of the numerical simulation, optimization using Taguchi-Grey method and parametric study of the cooling fins are discussed and compared with the experimental work on the cooling fins conducted in a wind tunnel.

Chapter 9 presents the conceptual design, numerical simulation, optimization and experimental study of liquid cooling systems. The findings of the study and the critical analysis of the numerical simulation and optimization study are discussed and compared with results of experiments carried out.

Chapter 10 presents the issues involved in the integration of Li-ion battery into an electric vehicle. The issues are discussed from various perspectives including assembly, electrical, battery management system, thermal management system, testing, etc.

In chapter 11, conclusions are drawn out based on the findings of the investigation. This chapter ends with the recommendations for future work.

CHAPTER 2

LITERATURE REVIEW

2.1 Introduction

This section highlights the various types of thermal management systems used in EV battery packs, electrochemical-thermal modeling and electro-thermal modeling of Li-ion batteries, cooling fins and related research done to date. In addition, the advantages and disadvantage of air and liquid cooling systems will be reviewed. Furthermore, various types of Li-ion batteries, their performance and safety specifications will be discussed.

2.2 Battery thermal management

Similar to conventional ICE vehicles, a battery pack in EVs or HEVs also needs a cooling system. Different types of cooling will influence the performance and cost of the battery pack thermal management system. The heat transfer medium could be air, liquid, phase change material (PCM), heat pipe or a combination of them. The selection of the cooling system depends on the constraints of the vehicle, installation costs and the external environment. In the extreme environment and working under heavy duty cycles, an active cooling system is preferred to offer more effective thermal management (Pesaran, 2001). The advantages and disadvantages of the different types of cooling systems will be discussed below:

2.2.1 Air cooling

Using air as a heat transfer medium is the simplest approach, but it is not as effective as heat transfer using a liquid. The heat generated from the battery is removed by using forced convection by directing or blowing ambient or cool air across the modules. The air cooling system can be further classified as

active or passive cooling and series or parallel air distribution.

2.2.1.1 Passive cooling

Passive cooling, the cooling air temperature must be kept within the range of 10 $^{\circ}$C – 35 $^{\circ}$C to ensure the Li-ion battery always operated at its optimum condition. In the early days, EVs and HEVs did not use heating or cooling units and depended on the blowing of ambient air to cool the batteries as shown in Figure 2.1. This is due to considerations of cost, mass and space, and the use of vehicles in mild climates (Pesaran, 2001).
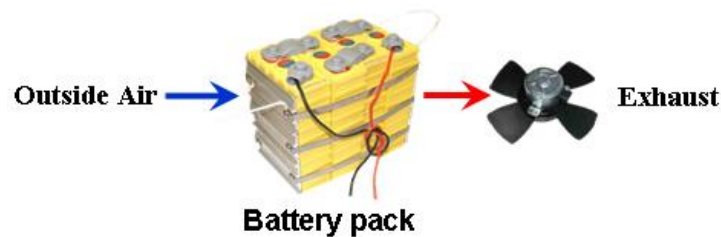
Figure 2.1 Passive cooling - outside air ventilation.

Besides, some automakers use cabin air to cool the battery pack. The advantage of this type of configuration is low complexity. The disadvantages include a limit of maximum flow rate of cooling air between 100 m^{3}h^{-1} and 250 m^{3}h^{-1} (depending on vehicle cabin air temperature), low cooling performance, noise, inhomogeneous temperature distribution within the battery pack, risk of fouling and potential safety concerns due to emission of toxic gases from the battery pack (Pesaran, 2001 and Heckenberger, 2009). Adequate sealing is needed to separate the cooling air circuit and venting plenum to ensure that the gases emitted during extremely abused conditions do not enter the passenger compartment. The schematic of cabin air ventilation and battery packs of Toyota Prius and Honda Insight are shown in Figure 2.2 and Figure 2.3 (Kelly and Rajagopalan, 2001), respectively.
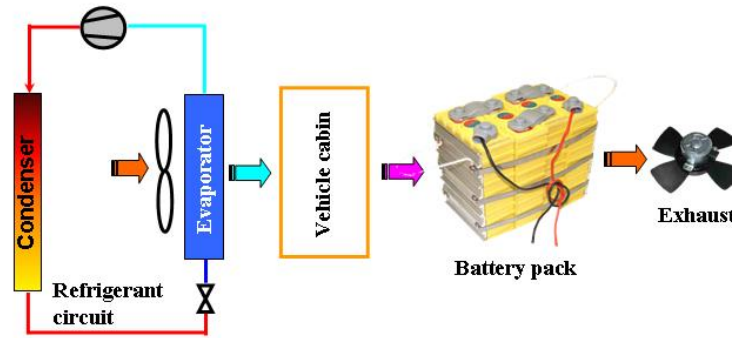
Figure 2.2 Passive cooling- Cabin air ventilation.
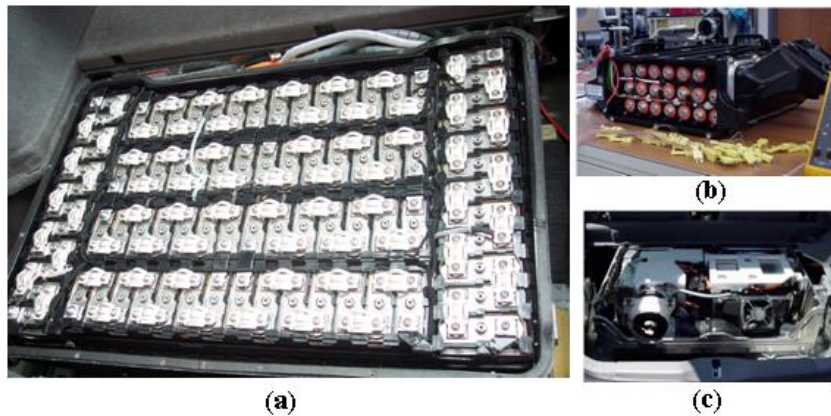
Figure 2.3 (a) GP NiMH battery pack for PHEV installed at the Toyota Prius. (b) Inner view of Honda Insight battery pack. (c) Outer view of Honda Insight battery pack.

2.2.1.2 Active cooling

In active cooling system, an auxiliary fan or air conditioner is used to supply cooling air directed through a channel to the battery pack to cool the heated battery. The advantages of this system are independence of the vehicle cabin air temperature and high cooling performance. The disadvantages are the extra packaging space required for the entire system, additional power consumption, inhomogeneous temperature distribution within the batteries and risk of fouling (Pesaran, 2001 and Heckenberger, 2009). The schematic of active air cooling and the battery pack of the Toyota Highlander hybrid are shown in Figure 2.4 and Figure 2.5 (source: http://www.hybridcars.com) respectively.
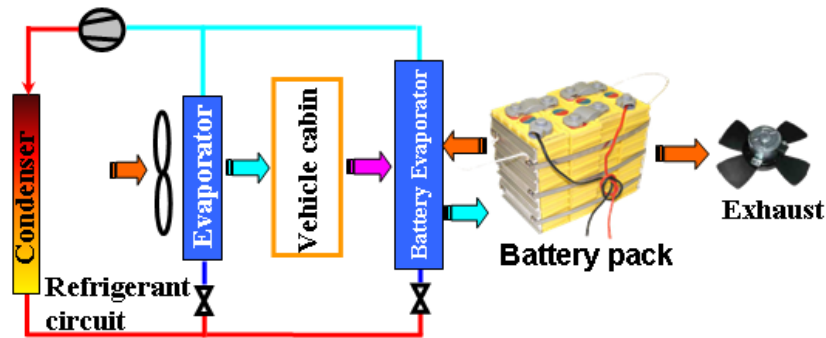
Figure 2.4 Independent air cooling.

Figure 2.5 Toyota Highlander hybrid battery pack.

2.2.1.3 Series versus parallel air distribution

For air thermal management systems, there are three methods for distributing air to the pack for cooling and heating, namely (Pesaran, 2001):

➢ Series cooling – Air enters from one end of the pack and leaves at the other end. The same amount of air is exposed to several battery modules.

➢ Parallel cooling – The total amount of air is split into equal portions, and each portion of air flows over a single module.

➢ Series-parallel cooling – series-parallel combinations can be configured and depend on the size and geometry of the battery modules.

Parallel cooling produces a more uniform temperature distribution among the battery cells (Pesaran et al., 1997, Pesaran et al., 1999 and Pesaran, 2002) as shown in Figure 2.6 for a lead acid battery pack.
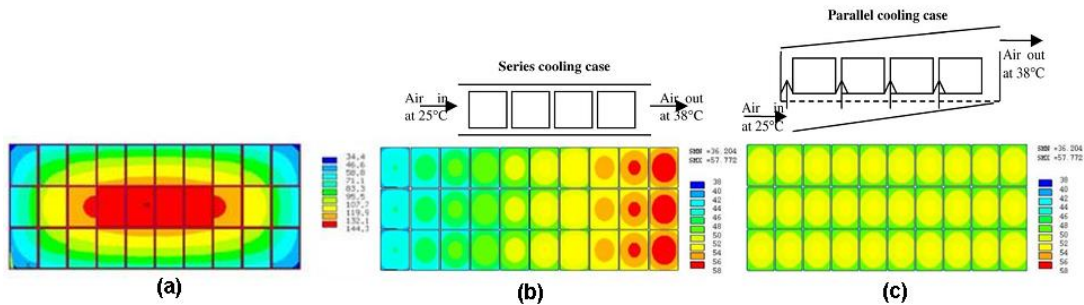
Figure 2.6 (a) Closed battery pack with no air flow. (b) Open battery pack with the series air flow, air direction from side to side. (c) Open battery pack with the parallel air flow, air flow direction from bottom to top.

2.2.2 Liquid cooling

Liquid cooling is more complex compared to air cooling. In the battery thermal management system utilizing liquid, the heat transfer between the battery and liquid is achieved by installing discrete tubing around the battery cells with a jacket around the battery cells, which places the heated liquid or cold plate to the battery cell surface or submerging the modules in a dielectric fluid. If the liquid thermal management system uses an indirect contact method, water or ethylene glycol or refrigerants can be used as the heat transfer medium. On the other hand, in direct contact methods, the liquid must be dielectric, such as silicone-based or mineral oils to avoid short circuiting. Similar to air cooling, liquid cooling can also be classified into passive cooling and active cooling systems.

The performance of direct contact liquid-cooled systems is higher than air cooling systems. This is because oil has thinner thermal boundary layer and higher fluid thermal conductivity compared to air. However, the high viscosity

of oil leads to higher pumping power and only low flow rates should be used. The heat transfer coefficient with oil is only 1.5 to 3 times higher than with air. Although, water or ethylene glycol used in indirect contact methods possesses lower viscosity and higher thermal conductivity as compared to oil, the total effective heat transfer coefficient is reduced due to the thermal contact resistance between the wall of jacket, plate or fins. (Pesaran, 2001). The cooling capability ($P_{dissipate}$) depends on the coolant temperature ($T_{coolant}$) near the cell (T_{cell}) and thermal resistance ($R_{thermal}$) between cell surfaces to coolant medium as shown in Equation 2-1 (Kuper et al., 2009). The average cell surface temperature will be reduced by the increasing coolant flow rate. In order to maintain the uniformity of cell temperature, the coolant temperature difference between inlet and outlet needs to be kept within 3 ^{o}C by providing adequate coolant flow rate.

$$P_{disspate} = \left(T_{cell} - T_{coolant}\right)/R_{thermal} \qquad (2\text{-}1)$$

2.2.2.1 Advantages and disadvantages of direct cooling

The advantages and disadvantages of direct cooling are highlighted below (Heckenberger, 2009 and Pesaran, 2001):

Advantages:

➢   The battery pack is more compact.

➢   The temperature distribution among the cells is more uniform.

➢   The cooling performance is higher.

Disadvantages:

➢   The battery cooling is only operated when power supply is available.

2.2.2.2 Advantages and disadvantages of indirect contact cooling

The advantages and disadvantages of indirect contact cooling are highlighted below (Heckenberger, 2009 and Pesaran, 2001):

Advantages:

➢ Higher annual average energy efficiency.

➢ Higher cooling performance compared to air cooling.

➢ Battery heating can be integrated.

➢ Ease of maintenance.

Disadvantages:

➢ The battery pack needs a larger space and increases the total weight.

➢ Higher cost due to needs of auxiliary components like chiller and heat sink.

➢ Higher inertia due to high thermal mass.

➢ Battery cooling is only operated when power supply is available.

Currently, the Mercedes S400 BlueHybrid uses a refrigerant-based direct cooling method for the Li-ion battery pack as shown in the top of the Figure 2.7. Cylindrical cells are immersed in the refrigerant to achieve optimum operating temperature and better temperature uniformity. The Chevrolet Volt uses indirect liquid-cooled battery modules as shown at the bottom of the Figure 2.7. Cold plates with N-channel shape are sandwiched between pouch cells to extract the heat generated from the cells (Source: http://www.zerohedge.com and http://www.phys.org).
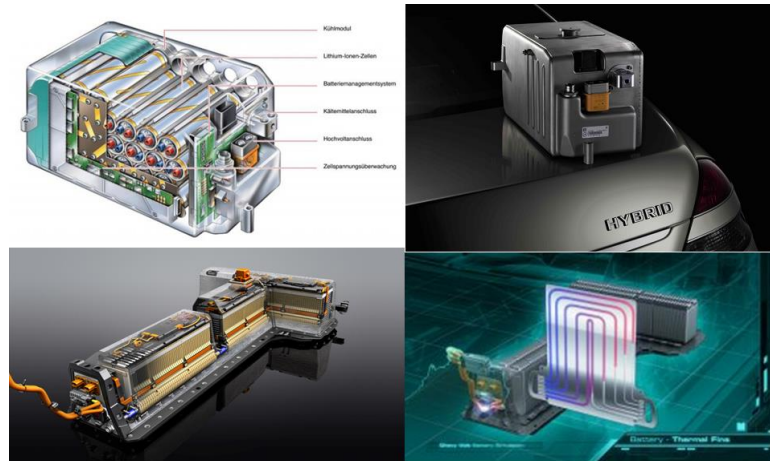
Figure 2.7 Top-Refrigerant-based direct cooling method.
Bottom- Indirect contact cooling using cold plates.

2.2.2.3 Refrigerated cooling

In refrigerated cooling system, the vehicle air conditioner heat exchanger is involved. This configuration allows reuse of the heat generated from the traction motor to provide the heating to the battery when the vehicles operate in extremely cold climate. For heating, the liquid exiting the air conditioner heat exchanger would pass through liquid-liquid heat exchanger would pass through a liquid/liquid heat exchanger (the other fluid is the vehicle engine/motor coolant), which heats the fluid before re-entering the battery pack. An auxiliary pump is needed to circulate the liquid and to cool the liquid by using external air. (Pesaran, 2001). The schematic diagram of the refrigerated cooling system is shown in Figure 2.8.
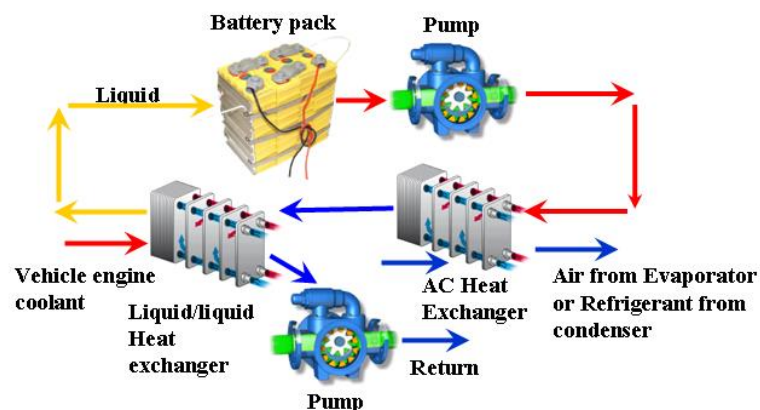
Figure 2.8 Refrigerated cooling and heating – liquid circulation.

2.2.3 Heat pipe

A heat pipe, which is also known as a passive heat pump, consists of a sealed container with inner surfaces having a capillary wicking material. The heat pipe operates by dissipating the heat through evaporating and condensing the cooling fluid in an endless cycle (Rao and Wang, 2011). Pulsating heat pipe (PHP) can also be used for the battery thermal management system. Swanepoel designed the thermal management for the Optima Spirocell (12 V, 65 Ah) lead acid battery using PHP technology (Swanepoel, 2001). The simulation and experimental results show that PHP should be constructed with d < 2.5 mm pipe and using ammonia as working fluid. The design of the PHP system is shown in Figure 2.9 (Swanepoel, 2001). The PHP was embedded into grooves of aluminum block with $L = 364$ mm, $W_e = 115$ mm, $W_a = 80$ mm and $W_c = 111$ mm. The evaporator length is $L_e = 1.953$ m and condenser length is 1.965 m. There 18 channels in the PHP. The grooves were filled with pure tin to ensure good thermal contact between the outer wall aluminum tube and aluminum blocks. Needle valve is used to control the flow of the fluid in the aluminum tube.
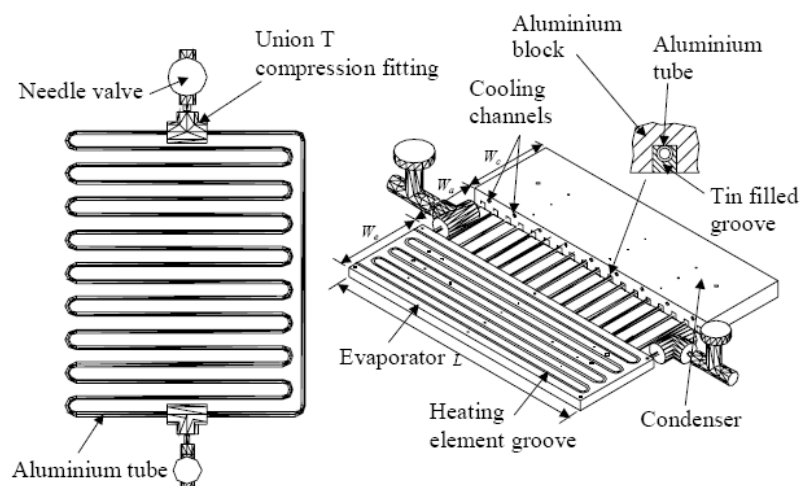
Figure 2.9 Aluminum closed loop PHP.

22

2.2.4 Phase change material

Phase Change Material (PCMs), also known as latent thermal storage materials, uses chemical bonds to store and release heat. The aggregate state of a PCM change from solid to liquid, when heat is absorbed (Demirbas, 2006 and Al-Hallaj et al., 2005). Paraffin wax is a PCM material that is commonly used. PCMs eliminate the need for auxiliary cooling systems such as pumps and fans, and improve power availability. PCMs with high latent heat of fusion are capable of absorbing large quantities of heat generated by the battery during discharging when integrated between the cells in a module. A PCM with high latent heat can prevent a sharp rise in battery temperature and ensure that the battery operates at its optimum temperature. The rate of heat removal can be enhanced by impregnating the PCM in a graphite matrix which possesses higher thermal conductivity (Demirbas, 2006 and Al-Hallaj et al., 2005). A PCM-enhanced battery pack offers advantages such as reduced peak temperatures, better temperature uniformity and reduced volume of the overall thermal management system. However, there are some disadvantages of PCM-enhanced battery packs such as heat accumulation at the PCM located at the center of the battery pack, additional weight and undesirable thermal inertia (Johnson et al., 2000; Hallaj and Selman, 2002; Sabbah et al., 2008; Kizilel et al., 2008; Alrashdan et al., 2010 and Rao et al., 2011).

A PCM is effective in suppressing the peak temperatures of the cell at high I_t-rate of charging and discharging. Moreover, the PCM is more effective in absorbing large amounts of heat released during thermal runaway of the cell as compared to air cooling. The highly conductive carbon matrix allows rapid heat transfer from the cell and maintains uniformity of cell temperature. The

assembly of a PCM-enhanced battery pack is shown in Figure 2.10 (Johnson et al., 2000). As shown in Figure 2.10 PCM Li-ion battery pack consisting of a block made of PCM material with holes in it to accommodate the cylindrical battery cells.
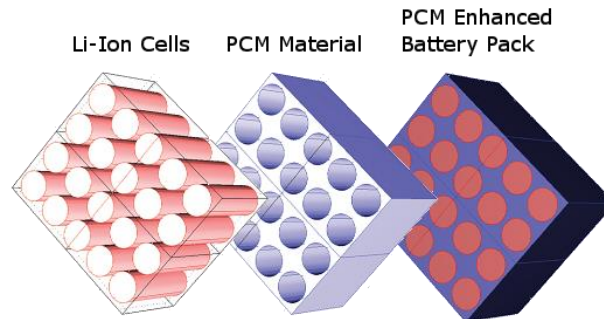
Figure 2.10 PCM Li-ion battery pack.

Kim et al. used a lumped capacitance model to benchmark the performance of a PCM thermal management system with forced air cooling (h = 15 $Wm^{-2}K^{-1}$) and natural convection cooling (h = 6 $Wm^{-2}K^{-1}$) for a Li-ion battery pack under 40 A single discharge for 9 minutes (Kim et al., 2008). The thermal performance of the battery pack is shown in Figure 2.11. The large thermal mass of the PCM results in a low battery pack peak temperature. Nevertheless, a large thermal mass and a smaller heat transfer at the surface give rise to a slower cooling rate for the PCM. At a high temperature of 40 ^{o}C, the PCM reaches its melting point and prevents further rise in temperature by converting the heat generated from the battery into latent heat as the wax in the matrix melts. Therefore, the PCM module has the lowest temperature rise and slowest cool-down as the stored heat is slowly rejected to the environment (Kim et al., 2008). Currently, the use of PCM in commercial EVs/ HEVs/ PHEVs is still being developed.

at **25**°C ambient → no phase change   at **40**°C ambient → phase change
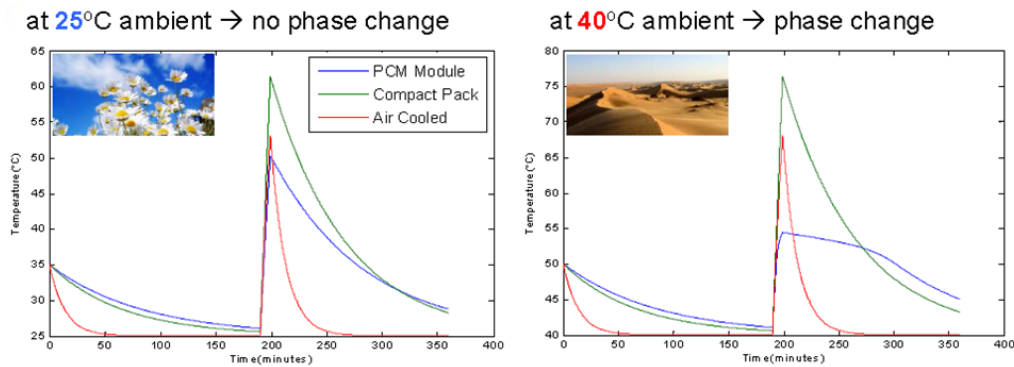
Figure 2.11 Thermal performance of battery pack at different ambient conditions.

2.3 Related research on battery thermal management system

Zolot et al. investigated the performance of the Toyota Prius NiMH battery pack at various temperatures (0 ^{o}C, 25 ^{o}C and 40 ^{o}C) using US06 driving cycle (Zolot et al., 2002). The thermal management system of the battery pack performs well for the test carry out at 25 ^{o}C. The maximum temperature of the battery pack is 43.0 ^{o}C and the variation of temperature across the battery pack is about 5 ^{o}C. At 40 ^{o}C, the thermal management system of the battery pack is able to maintain the temperature of the cell under 52 ^{o}C and the variation of the cells temperature is below 5 ^{o}C. However, the thermal management systems performed poorly at 0 ^{o}C and large temperature gradient (> 11 ^{o}C) is developed across the battery pack.

Pesaran and Keyser used thermal imaging camera to evaluate the thermal behavior and temperature distribution in the module and analyze any abnormal thermal behavior occurred as shown in Figure 2.12 (Pesaran and Keyser, 2001) which shows some typical hot spots in the thermal images of an Optima valve regulated lead acid HEV module. (a) Face at end of charge. (b) Side at end of charge. (c) Face at end of 2C discharge. (d) Side at end of 2C discharge. (e) Thermal images of three Saft HEV Li-ion cells after eight US06 test. (f) Thermal images of a Evercel Nickel Zinc cell at the end of C/1 discharge.
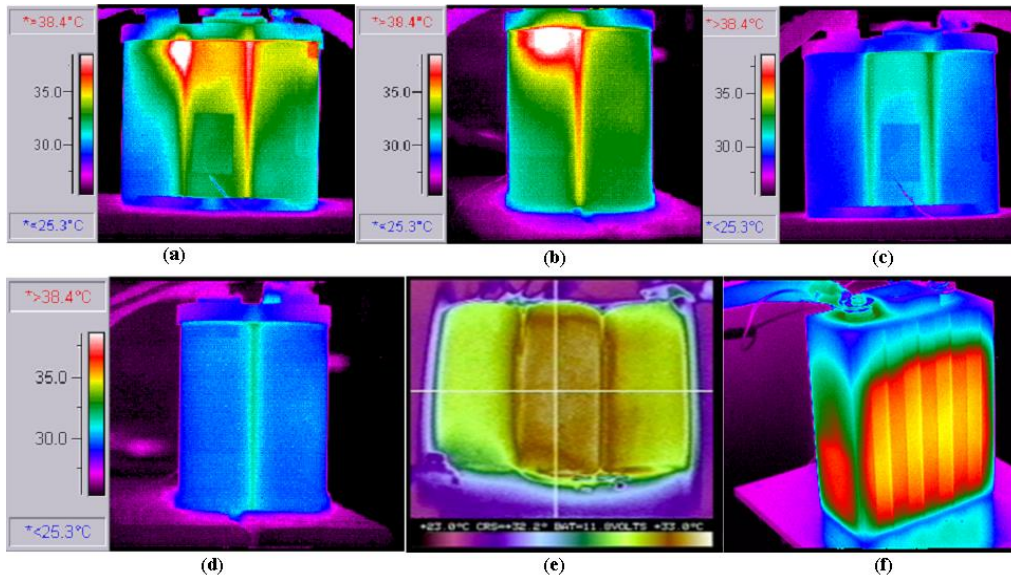
Figure 2.12 Thermal images of various types of battery.

Ghosh et al. designed a battery pack cooling system for Ford Fusion Hybrid and Mercury Milan Hybrid (Ghosh et al., 2009 and Ghosh et al., 2010). CFD simulation was used to evaluate the performance of the cooling system. The configuration of battery pack comprised of 4 D-size NiMH cells arranged in series and 8 D-size NiMH cells arranged in parallel. The fan scroll and diffuser design and CFD analysis results of the battery module are shown in Figure 2.13. As shown in top of the Figure 2.13, cooling air is discharged from the battery pack through the tapered diffuser and dumped out of the vehicle. A wrap angle design of the cell holder as shown at the bottom right of Figure 2.13 is used to resolve excessive cooling on the cell p1-n1 which faces the inlet of the cooling air. The varied wrap angles will raise the temperature of cell p1-n1 and p2-n2 while maintain the cells at downstream (p3-n3 and p4-n4) slightly cooler. A small temperature gradient of 1.2 $^{\circ}$C within the battery cell is achieved by using a wrap angle of 15 degree for cell p1-n1 and p2-n2 and 0 degree for cell p3-n3 and p4-n4. However, this type of design will incur additional pressure drop in the battery pack.
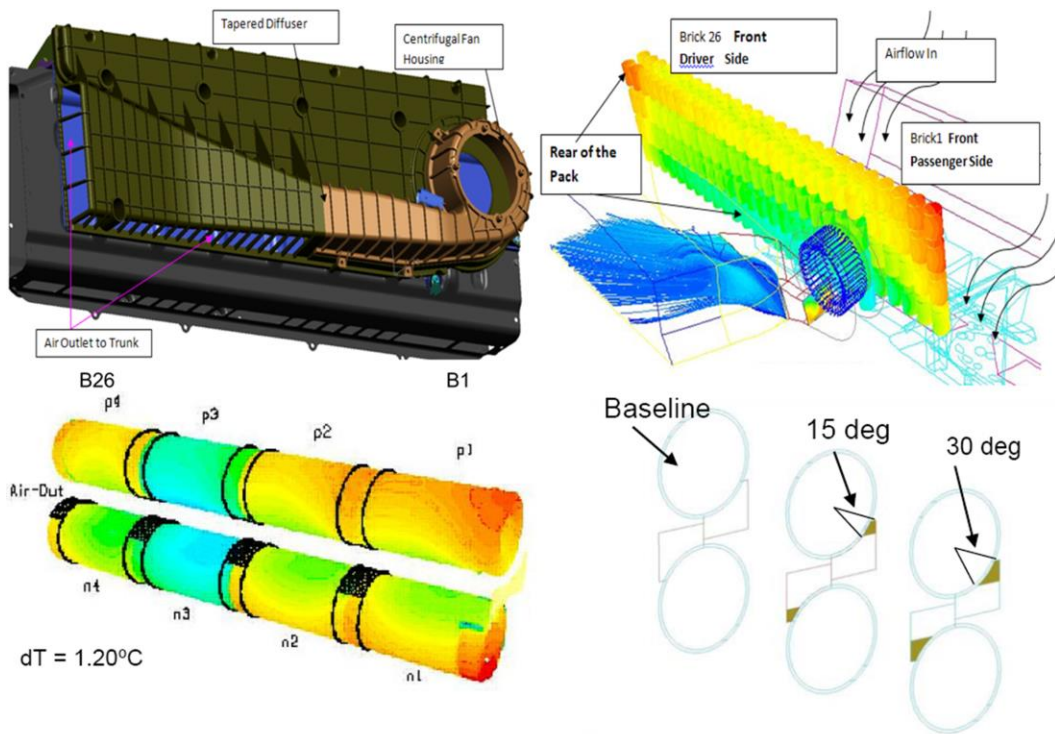
Figure 2.13 Diffuser design and CFD analysis results of the battery module.

Pesaran et al. used finite element analysis method to investigate the different electrical and thermal behavior of prismatic Panasonic NiMH cells and modules manufacture in year 2001 and 2004 (Pesaran, 2005). The results are verified using IR thermography. Hot spots were found near interconnect of the cell manufactured in 2001 as shown in Figure 2.14(a). The contact resistance between two adjacent cells was reduced by introducing additional welding on cell manufactured in 2004 as shown in Figure 2.14(b). The model did not capture the transient behavior of the internal resistance of the battery caused by electrochemical changes during charging/discharging.
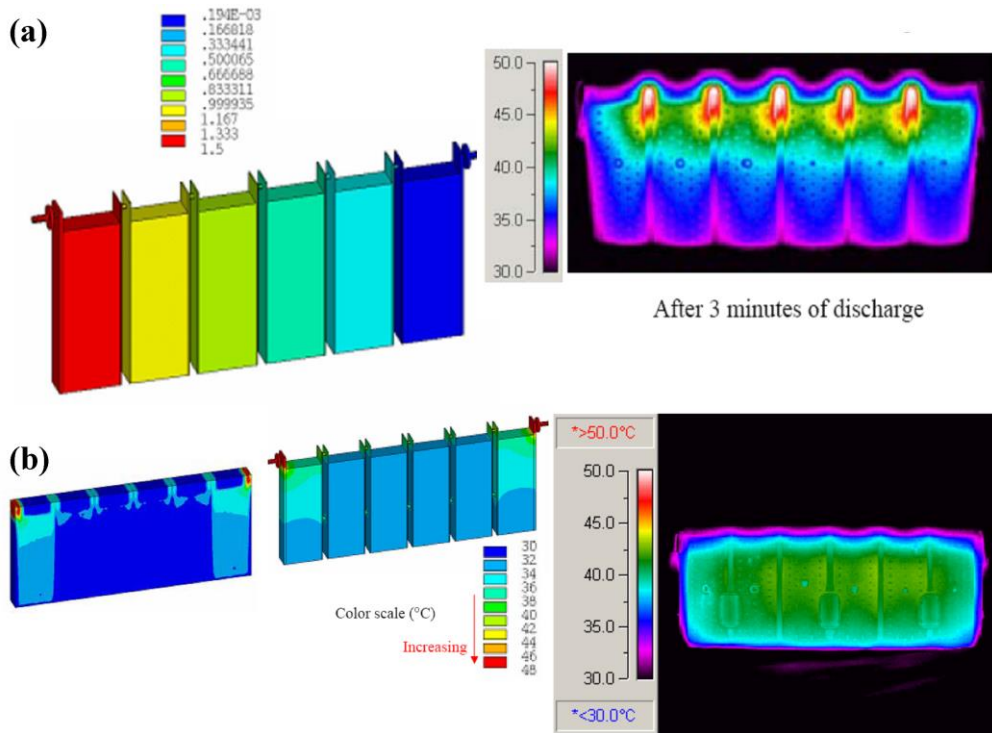
Figure 2.14 (a) Voltage, current and temperature of the cell. (a). With effect of contact resistance.(b) Improving the contact resistance at the terminals.

The feasibility of reciprocating air flow to improve temperature uniformity and reduce the maximum temperature of Li-ion battery ($LiMn_2O_4/C$) was investigated by Mahmud and Park (Mahmud and Park, 2011). The numerical study revealed that when the reciprocating period is short, the temperature distribution is more uniform and maximum cell temperature is reduced. As compared to uni-directional flow, reciprocating period of 120s is effective to reduce the cells temperature difference of the battery system by 4 ^{o}C and maximum temperature by 1.5 ^{o}C. Although reciprocating air flow is effective in reducing the temperature of the cells at the both ends, but the cell at the center is always higher. However, reciprocating air flow will introduce a sudden change of air flow path and large momentum of air flow will be produced. The schematic of reciprocating cooling and CFD results are shown in Figure 2.15.
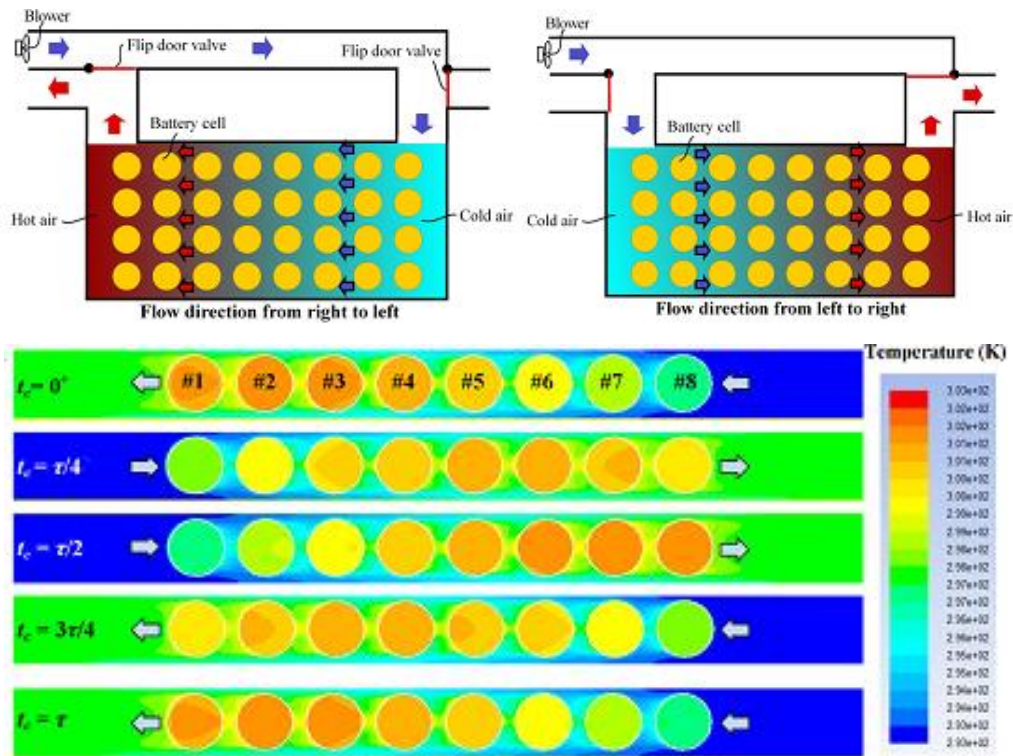
Figure 2.15 Battery pack with reciprocating air cooling.

Alaoui and Salameh developed a thermal management system for Solectria electric vehicle based on Peltier-effect heat pumps (Alaoui and Salameh, 2005). The basic thermal unit setup and thermal management block diagram are illustrated in Figure 2.16(a). Cooling air for the battery pack is supplied by the axial fan and forced through the heat sinks to create greater turbulence and achieve higher heat transfer rates. The heat transfer performance is improved by factor of three to four by installing a fan. On the other hand, a blower is used to supply cooled or heated air into the battery pack. As shown in top right of the Figure 2.16, the thermal management system consists of three thermoelectric units, thermoelectric controller to control the temperature and hose system to distribute the cooling air. The performance of the thermal management system in heating and cooling modes is shown in Figure 2.16(b). Temperature A is the temperature in the frontal battery compartment while B is at the rear battery compartment. 1.5 Ah

capacity of the battery was needed to warm up the EV batteries from 17 $^{\circ}$C to 29 $^{\circ}$C. On the other hand, 2.6 Ah capacity of the battery was needed to cool EV battery pack from 17 $^{\circ}$C to 9 $^{\circ}$C.
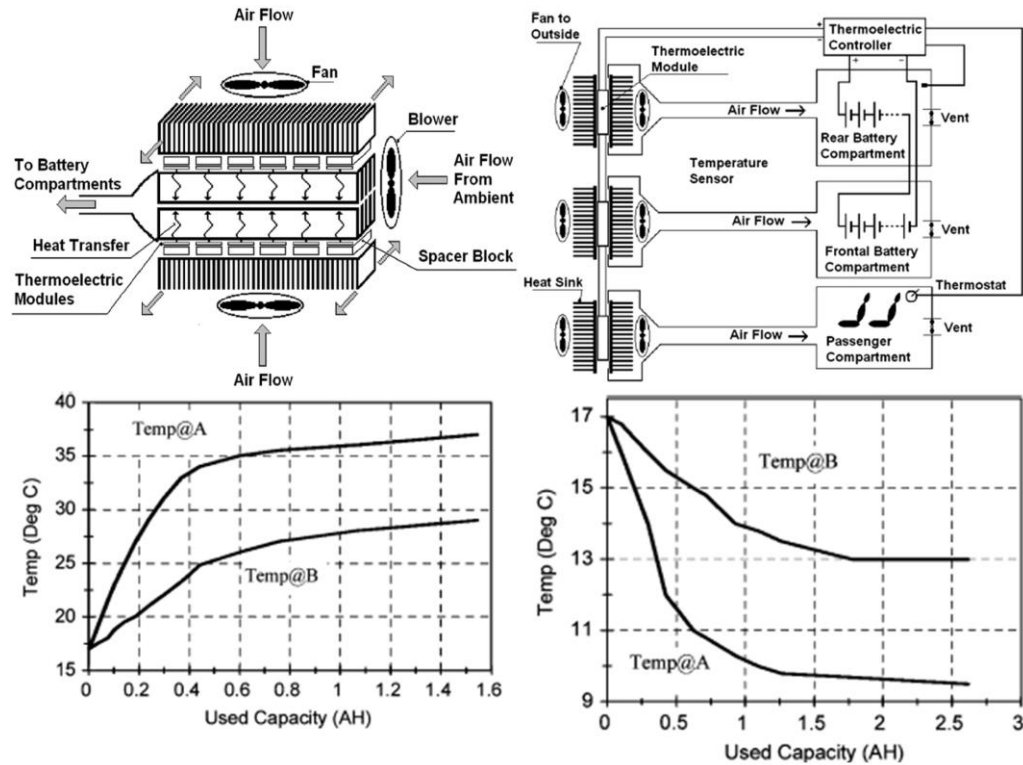
Figure 2.16 (a) Peltier thermal unit setup. (b) Thermal performance in heating and cooling.

2.4 Lithium ion battery

2.4.1 Battery chemistry

A Li-ion battery comprises of four essential components which are anode, cathode, electrolyte and separator. A separator which is usually made of Polyvinylidene difluoride (PVDF) material, is a micro-porous membrane used to isolate anode and cathode to prevent short-circuit. The electrolyte is a mixture of organic solvents and an electrolyte at a certain concentration to provide an interface for the ionic movement associating with the redox reactions on two electrodes to electrolyte interfaces (Nagaura, 1992 and Dhameja 2002). There are several types of Lithium electrolytes salt used in Li-

ion batteries such as Litihum Hexafluorophosphate (LiPF$_6$), Lithium Tetrafluroborate (LiBF$_4$), Lithium Triflate (LiSO$_3$CF$_3$) and Lithium tris (trifluoromethanesulfonyl) methide (LiC(SO$_2$CF$_3$)$_3$) (Wenige et al., 1997). The organic solvent used in the electrolyte can be Ethyl Carbonate (EC), Propylene Carbonate (PC), Diethyl Carbonate (DEC) or Dimethyl Carbonate (DMC). 1M LiPF$_6$/EC:DEC is the most commonly used electrolyte and has the highest electrical conductivity as compared to other electrolytes (Wenige et al., 1997 and Fagas et al., 2014). The electric conductivity of the electrolyte and physical properties of the organic solvent are given in Figure 2.17 (Wenige et al., 1997 and Fagas et al., 2014). The typical chemical reactions at the anode and cathode during the charging and discharging processes are represented by Equation 2-2 to Equation 2-4. During charging, the Lithium ions intercalate into solid particles of the negative electrode and de-intercalate from solid particles of the positive electrode. During discharging, the reaction occurs in the reverse direction. Heat is generated within the cell during charging and discharging. The advantages of the Li-ion batteries as compared to other rechargeable batteries are shown in Table 2.1 (Zhang 2007 and Battery University, 2001).

(a)	2.22		4.25		5.12		6.56	[mS/cm]
(b)	LiSO$_3$CF$_3$		LiBF$_4$		LiC(SO$_2$CF$_3$)$_3$		LiPF$_6$	

Solvent	Dipole Moment	Dielectric Constant	Melting Point	Boiling Point	Density	Molar Volume
	(μ/D)	K or (ε)	(^{o} C)	(^{o} C)	(g/cm^3)	(dm^{-3}/mol)
Ethyl carbonate (EC)	4.9	89.78	37	248	1.32	62
Propylene carbonate (PC)	4.94	66.14	-49	242	1.2	84
Diethyl carbonate (DEC)	0.94	2.82	-43	126	0.97	122
Dimethyl carbonate (DMC)	0.88	3.12	3	90	1.06	84
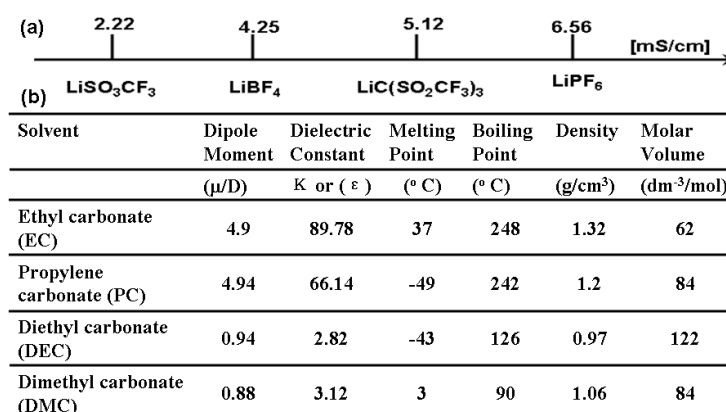
Figure 2.17 (a) Comparison of various electrolytes for lithium-ion batteries based on electrical conductivity. (b) Physical properties of organic solvents at 25 ^{o}C.

Table 2.1 Comparison of the performances of various types rechargeable
batteries.

Parameters	Lead acid	NiCd	NiMH	Li-ion
Normal Voltage, V	2.0	1.2	1.2	3.6
Specific Energy, Wh kg^{-1}	30-50	45-80	60-120	100
Specific Energy, Wh L^{-1}	60	150	200	230
Specific Power, W kg^{-1}	130	200	250	330
Energy Efficiency, %	65	80	85	95
Cycle life, times	200-300	500-1000	300-500	1000
Environment Hazard	Medium	Low	Medium	High
Safety	Medium	High	High	Low
Cost	Low	Low	Medium	High
Self-discharge, %/month	5%	25-30%	30-35%	<10%
Memory effect	No	Yes	Yes	No

Positive electrode

$$LiXXO_2 \underset{discharge}{\overset{charge}{\rightleftarrows}} Li_{1-x}XXO_2 + Li^+ + xe^- \qquad (2\text{-}2)$$

Negative electrode

$$C + xLi^+ + xe^- \underset{discharge}{\overset{charge}{\rightleftarrows}} Li_xC \qquad (2\text{-}3)$$

Overall reaction

$$LiXXO_2 + C \underset{discharge}{\overset{charge}{\rightleftarrows}} Li_xC + Li_{1-x}XXO_2 \qquad (2\text{-}4)$$
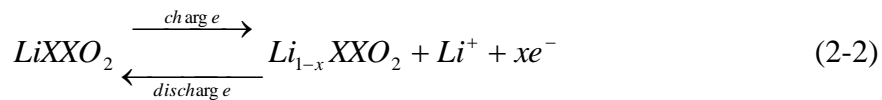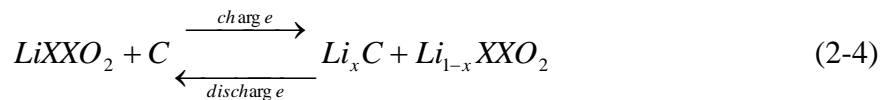
Li-ion batteries are named according to its cathode materials. There is a variety of Li-ion batteries available in the market with different specific energy and voltage for diverse applications. Common anode materials used in the Li-ion battery is graphite, hard carbon, meso-carbon microbeads (MCMB), graphene, Lithium Titanate Oxide ($Li_4Ti_5O_{12}$), Lithium Silicide ($Li_{4.4}Si$) and Lithium Germanium ($Li_{4.4}Ge$) (Schalkwijk and Scrosati, 2002). Materials for the cathode in Li-ion batteries are selected according to the anode material. Common cathode materials are Lithium Cobalt Oxide ($LiCoO_2$), Lithium Manganese Oxide ($LiMnO_4$), Lithium Iron Phosphate ($LiFePO_4$), Lithium Vanadium Phosphate ($LiVPO_4$), Lithium Nickel Manganese Cobalt (NMC)

and Lithium Nickel Cobalt Aluminum Oxide (NCA) (Fagas et al., 2014 and Schalkwijk and Scrosati, 2002). The chemical, electrical and physical characteristics of the Li-ion battery available in the market are summarized in Table 2.2 (Battery University, 2011, Ohzuk and Brodd, 2007 and Bandhauer et al., 2011).

Table 2.2 Characteristic of the commonly used Lithium-ion batteries.

Specifications	$LiCoO_2$ (LCO)	$LiMn_2O_4$ (LMO)	$LiFePO_4$ (LFP)	$LiNiMnCoO_2$ (NMC,NCM,CMN, CNM,MNC, MCN)
Voltage, V	3.60	3.80	3.30	3.60/3.70
Charge limit, V	4.20	4.20	3.60	4.20
Cycle life	500-1000	500-1000	1000-2000	1000-2000
Specific energy, Wh/kg	150-190	100 -135	90-120	140-180
Specific power	1C	10C, 40 C pulse	35 C continuous	10 C
Safety	Average. Requires protection circuit and cell balancing. Requirements for small formats with 1 or 2 cells can be relaxed.		Very safe, needs cell balancing and voltage protection.	Safer than Li-Cobalt. Needs cell balancing and voltage protection.
Thermal runaway	150 $^{\circ}$C	250 $^{\circ}$C	270 $^{\circ}$C	210 $^{\circ}$C
In use since	1994	1996	1999	2003
Researchers, manufacturers	Sony, Sanyo, GS Yuasa, LG Chem, Samsung, Hitachi, Toshiba	Samsung, Sanyo, GS Yuasa, LG Chem, Toshiba, Moli Energy, NEC, Hitachi	GS Yuasa, BYD, JCI/Saft, Lishen, A123, Valence	Sony, Sanyo, LG Chem, GS Yuasa, Hitachi, Samsung

2.4.2 Packaging

Various types of packaging are available for Li-ion battery such as a cylindrical cell with spirally wound active material (14500, 14650, 18650, 26650, 38120, 38140, 40152, 42120, 63219 and 76306), prismatic cells with the elliptically wound active material (053048, 063048, 073048, 083448, 123582, 103450, and 1865140) and pouch cell with a stacked plate of active material (Battery and energy technologies, 2014). Aluminum and stainless steel are usually used for cylindrical or prismatic cell can (Schalkwijk and Scrosati, 2002). While the pouch cell is using soft packaging, which is usually metalized plastic (Schalkwijk and Scrosati, 2002). The capacity of the cell positively correlates with the area of the active material in the spirally and elliptically wound cells and with the number of stacked plates in the pouch cell. The cylindrical cells are named according to their diameter and height. This also applies to the prismatic cell, where the name is according to the

length, width and height of the cell. For example, in the Lithium Iron Phosphate cell, the diameter and height for the 18650 cell is 18 mm and 65 mm, respectively and the nominal capacity of the cell is about 1.2-1.5 Ah. On the other hand, for large diameter of the cylindrical cell such as 76306, the capacity of the cell could reach 100 Ah (Headway, 2014). The cylindrical and prismatic cell also contains safety protection components such as positive temperature coefficient (PTC), pressure activated disconnect and gas release vent. PTC is used to limit the current in overheating conditions such as overcharge and short circuit (Zhang, 2007). The rupture vent is utilized to release the pressure buildup in the cell under thermal or mechanical abuse conditions. These safety features may temporarily or permanently disable the operation of the cell when internal temperature or pressure is dramatically increased in a short time (Zhang, 2007). As shown in Figure 2.18, cylindrical cells contain spirally-wounded electrodes, while prismatic cells are formed by winding the electrodes around a flat mandrel to create an elliptic spiral. On the other hand, pouch cells are formed by stacking the electrode plates together and housed in an aluminum soft pouch. The comparison of various cell format parameters is shown in Table 2.3 (Andrea, 2010).

Table 2.3 Comparison of cell formats.

Parameter	Small cylindrical	Large cylindrical	Prismatic	Pouch
Shape	Encased in a metal cylinder, usually 65-mm long	Encased in a metal or hard plastic cylinder	Encased in semi-hard plastic or metal case	Contained in a soft bag
Connections	Welded nickel or copper strips or plates	Treaded stud for nut or threaded hole for bolt	Thread hole for bolt	Tabs that are clamped, welded, or soldered
Retention against expansion when fully charged	Inherent from cylindrical shape	Inherent from cylindrical shape	Requires retaining plates at ends of battery	Requires retaining plates at ends of battery
Appropriateness for small projects	Poor: high design effort, requires welding, labor intensive	Good: some design effort	Excellent: little design effort	Very poor: design effort too high
Appropriateness for production runs	Good: welded connections are reliable	Good	Excellent	Good: high performance
Field replacement	Not possible	Possible but not easy	Easy	In general not possible
Delamination	Not possible	Not possible	Possible	Highly possible
Compressive force holding	Excellent	Excellent	Poor	Extremely poor
Thermal management	Not favorable	Not favorable	Favorable	Favorable
Heat dissipation	Poor	Poor	Fair	Good
Local stress	No	No	No	Yes
Safety	Good, integrated with PTC	Good, integrated with PTC	Good, integrated with PTC	Poor, no safety feature included
Ease of assembly	Poor	Poor	Excellent	Poor

34
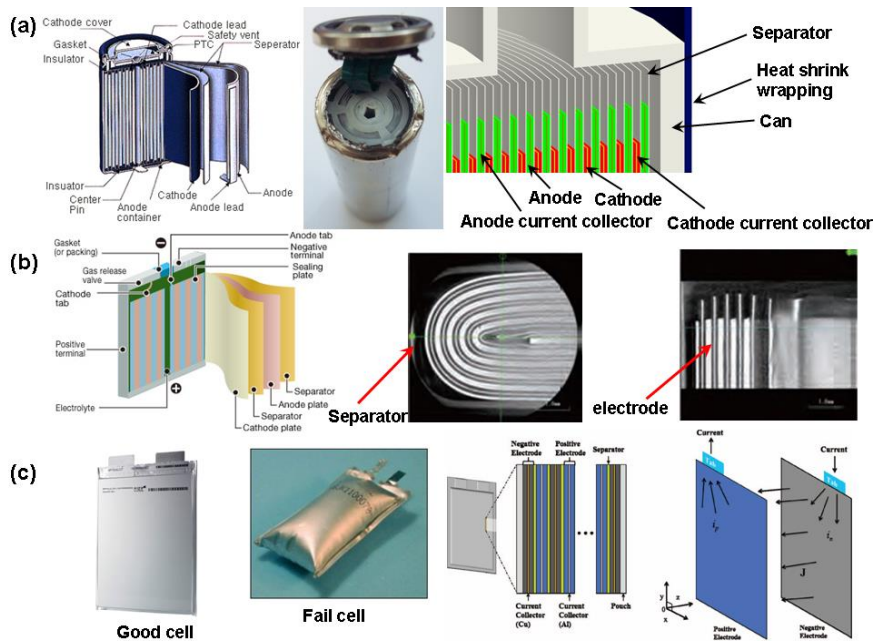
Figure 2.18 Schematic various types of Li-ion batteries.

2.4.3 Electric connection

Several cells are connected in series to build up the required voltage, and in parallel connection of the cells to build up the capacity required for EVs. The typical voltage of a battery module is less than 50V, and the voltage above 50 V is classified as hazardous by the National Electric Code of USA (Schalkwijk and Scrosati, 2002). Electrical connection of the battery pack or battery module is realized by connecting the bus bar that is made of copper, nickel plated steel or nickel strip to individual cells. Spot welding or screws are commonly used to establish the connection between the cells. Spot welding is mostly used for small format cylindrical cells and pouch cells. This type of connection creates the lowest contact resistance but does not encourage changing of faulty cells.

2.4.4 Battery management system

EV battery pack comprised cell modules, module interconnects, battery pack management system (BPMS) and battery thermal management system. The battery module consists of a cell, cell housing, bus bar, sensors, electronic

controls and ducting for thermal management system (Schalkwijk and Scrosati, 2002). The sensors are connected to a microcontroller module called battery management system (BMS). With the battery pack that comprised multiple cell modules, BMS will be linked to the master module or battery pack management system via standard communication protocol such as Controller Area Network (CAN) bus (Schalkwijk and Scrosati, 2002). BMS protect the cell against abuse such as over-voltage and under-voltage, over current during charging or discharging, over-temperature, under-temperature and cell balancing (Battery Technology, 2014). The BMS can be further divided into analog and digital systems. Analog BMS only has voltage protection, current protection and a switch to turn off the battery. On the other hand, a digital BMS also possess the basic functions of the analog BMS but include more advanced functions such as SOC estimation, state of health (SOH) estimation, coolant flow rate control, regenerative braking control, charger control, etc. A conceptual view of the battery pack is shown in Figure 2.19 (Schalkwijk and Scrosati, 2002).
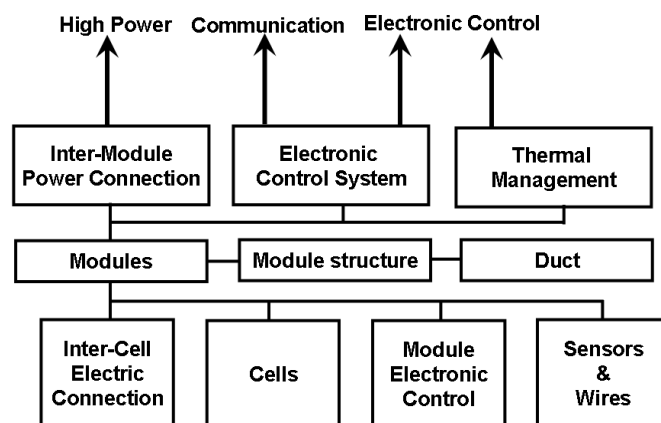
Figure 2.19 Concept scheme for Lithium-ion battery pack.

2.4.5 Service and maintenance

Replacing a new unit of a battery pack is a common practice for HEVs. However, for a high voltage battery pack used in EVs, full replacement of the battery pack is prohibited (Battery University, 2011). The usual practice for servicing an EV battery pack is to replace the battery module that contained a faulty cell in an aging battery pack. Due to aging of the battery, the old battery capacity is always lower than a new battery. If the replacement cell is not properly selected, it will cause an electrical imbalance in the battery module especially for the cells connected in series. Hence, the Li-ion battery must have a good cycle-life of 1000 at 80% of DOD and a calendar life of 10 years as highlighted in USABC is long term goal of EVs as shown in Table 2.4 (Brodd, 2013 and Karditsas, 2012).

Table 2.4 Long term technical goals for EV batteries.

Parameter (Units) of fully burdened system	Minimum Goals for Long Term Commercialization	Long Term Goal
Power Density, W/L	460	600
Specific power-Discharge, 80% DOD/30 sec, W/kg	300	400
Specific Power-Regen, 20% DOD/10 sec, W/kg	150	200
Energy Density-C/3 Discharge, Wh/L	230	300
Specific Energy – C/3 Discharge rate, Wh/kg	150	200
Specific Power/Specific Energy ratio	2:1	2:1
Total Pack Size, kWh	40	40
Life, Years	10	10
Cycle Life-80% DOD, Cycles	1000	1000
Power & Capacity Degradation, % of rated spec	20	20
Selling Price-25,000 units @ 40kWh, $/kWh	< 150	100
Operating Environment, ^{o}C	-40 to + 50 20% Performance Loss (10% Desired)	-40 to + 85
Normal Recharge time	6 hours (4 hours Desired)	3 to 6 hours
High Rate Charge	20-70% SOC in < 30 minutes @ 150 W/kg (< 20 min @270 W/kg Desired)	40 -80% SOC in 15 minutes
Continuous discharge in 1 hour-No-failure, % of rated energy capacity	75	75

2.4.6 Testing

Lithium ion batteries have excellent energy density and terminal voltage featuring a high level of safety. This is caused by the lithium inside the cell is always in the ionic state under normal operating range, rather than in a metallic or alloy state (Lithium ion rechargeable batteries, 2014). However, in order for the Li-ion battery to be used in the vehicles, the cell, module and

battery pack need to be tested and pass the standard provided such as ISO 12405-1/2, IEC 62660-1/2 and JIS C 8711 (Omar et al., 2012; ISO 12405-1/2, 2014; IEC 62660-1/2, 2014 and JIS C 8711, 2013). Those standards described the specific test procedures to evaluate the suitability of the cell used in HEVs and EVs which covered various aspects such as power capability, life cycle test, reliability, abuse test and safety test of the cell.

2.5 Numerical modeling of Lithium ion battery

2.5.1 Electrochemical-thermal model

Li-ion battery models have been developed for numerical simulations to predict the charging or discharging, thermal behavior and design optimization. The electrochemical model captures the spatiotemporal dynamics of Li-ion concentration, potential of an electrode in each phase and the intercalation reactions are governed by Butler-Volmer kinetics (Moura, 2011).

Fuller et al. and Doyle et al. modeled the galvanostatic charge and discharge of the dual lithium ion insertion cell under isothermal conditions (Doyle et al., 1993 and Fuller et al., 1994). The concentrated solution theory was used to describe the transport of Li in the electrolyte. A superposition approach was used to simulate the intercalations and deintercalations of Li in the active electrode material.

Fuller et al. also found that, increasing the concentration in the depth of the porous electrode will lead to an increase of the ohmic drop of the cell system. Thin electrodes will attain large power density, but low maximum energy density (Fuller et al., 1994). During the high discharge rate, a sudden drop in the cell potential was found and is due to concentration polarization. At high current densities, the electrolyte concentration is driven to zero, closer

to the separator and preventing 100% utilization of the electrode. The problem can be solved by increasing the electrolyte concentration to improve the performance of the cell at high rates of discharge

The voltage drop in the Li-ion battery results from three major irreversibly processes which are activation losses, ohmic losses and mass transport or concentration losses (Larminie and Dicks, 2003).

Doyle and Newman used numerical simulation to model and predict the performance of the $Li_xC_6 | Li_yMn_2O_4$ system at 25 ^{o}C and compared with the experimental data for cells having different electrode thicknesses and electrolyte compositions (Doyle and Newman, 1996). From the simulation, it was found that the system is dominated by an ohmic drop in the plasticized electrolyte phase. The authors used film resistance on the electrode particles or contact resistances between the cell layers to describe the additional resistance found in an experimental cell. A large specific energy of about 100 Whkg^{-1} was obtained with less porous and thicker electrodes. However, additional resistance exists in the experimental cell and is not predicted by numerical simulations. In order to predict the discharge behavior of the cell more accurately, the mathematical model has to be improved.

Cai and White extended the pseudo 2D electrochemical model of $Li_xC_6 |$ $Li_yMn_2O_4$ in COMSOL to study the thermal effects (Cai and White, 2011). Three types of heat sources are considered in the models, namely reaction heat, reversible heat generation and ohmic heat generation. The study focused on galvanostatic discharge process at different rates under different cooling conditions. As can be seen in Figure 2.20(a), under adiabatic condition, the temperature of the cell surface may reach 380 K. On the other hand, under

natural convection with h = 10 Wm^{-2} K^{-1}, surface temperature of the cell is almost constant at 300 K. The surface temperature of the cell for 1C, 2C and 3C rate of discharge is about 305 K, 313 K and 325 K respectively as shown in Figure 2.20(b). However, the study is only focusing on 1D simulations and assumed the cell temperature is uniformly distributed and may not accurately predict the actual discharge behavior of a Li-ion battery.
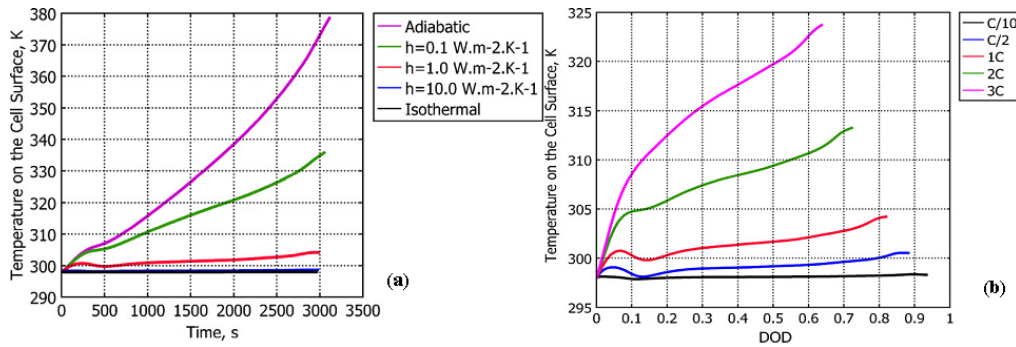
Figure 2.20 Simulation results for the temperature on the cell surface.

Heat generation characteristics of a cylindrical Lithium Manganese Oxide battery system has been studied through a coupled electrochemical-thermal model with full consideration of electrolyte transport properties as functions of temperature and Li-ion concentration (Zhang, 2011). Three different types of heat sources were considered which are ohmic heat, active polarization heat and reaction heat. Convective heat transfer, radiation heat transfer and the effect of battery geometry were employed in the thermal boundary condition. It was found that, ohmic heat contributed about 54% in the total heat generated while 30% is contributed by electrochemical reaction and the rest is contributed by polarization heat. The skin temperature at 1.7 I_t agreed well with the measurement data which was 312.43 K. Li-ion concentration and its gradients, separator thickness and electrode thickness were the crucial factors affecting the heat generation of the battery.

Sato used thermodynamic analysis of battery reactions to categorize the specific heat generation of the Lithium Cobalt Oxide battery (Sato, 2001). The heat generation of Li-ion battery depends on the charging and discharging action. The reaction heat is endothermic during charging and exothermic doing discharging. Three different types of heat sources are involved which are reaction heat, polarization heat and joule heat.

Jeon and Baek investigated the thermal behavior of the cylindrical li-ion battery ($LiCoO_2$) during the discharge cycle using ABAQUS finite element analysis solver (Jeon and Baek, 2011). Set of energy equations including joule heating and entropy change were assigned to the cell to carry out a transient simulation. Entropy and joule heating dominated at a low and high discharge rate, respectively. The maximum temperature is located at the center of the cell. The temperature difference between the cell surface and the center is negligible. However, the effect of the current tab which has a significant effect on the temperature of large prismatic cells and Li-polymer battery is not considered in the current study (Williford et al., 2009 and Kim et al., 2009).

A multi-dimensional thermal and electrochemical coupled model is developed based on micro-macroscopic modeling approach to predict the temperature distribution inside the cell and overall temperature evolution of the large size Li-ion battery for EVs and HEVs applications (Gu and Wang, 2000). The system of Li-ion battery investigated was (Li_xC_6 | $Li_yMn_2O_4$). In their modeling, lumped thermal model was used assuming the Biot number was equal to zero under adiabatic conditions. Heat generation predicted by using a coupled model was lower compared to a decoupled model. Conversely, a coupled model showed a gradually decreased total heat generation rate until

the final abrupt rise at the end of discharging and this was caused by a sharp increase of surface over-potential for the electrode reaction. A fully coupled thermal and electrochemical model was necessary to predict the thermal and electrical behavior of the cell. Besides, the simulated cell shows large temperature gradients along the height direction and non-uniformity of electrode reaction rate and electrolyte concentration were found. However, this study was only based on two dimensional model numerical studies and does not compare with any experimental work.

Srinivasan and Wang also conducted a similar numerical simulation study to investigate heat generation on $Li_xC_6|Li_yMn_2O_4$ battery system based on local heat generation (Srinivasan and Wang, 2003). The reversible heat was found to be an important parameter to determine the final temperature of the cell and this parameter was not considered by previous authors. The experimental voltage was used to estimate the heat generation under isothermal environment. The heat generation of the cell was predicted by applying the expression developed by Bernardi et al. (Bernardi et al., 1985). The results show that, the reaction distribution in the porous electrodes was not uniform and introduce about 15% in predicting the heat generation. Moreover, heat generation prediction using calorimetric data is less reliable and will result in a significant deviation of about 40%.

Fang et al, also used an electrochemical–thermal coupled model to predict the performance of Li-ion cell (Li_xC_6 | $Li_yMn_2O_4$) at a higher C rate (1 C, 2C, 5C and 10C) and by neglecting reversible heat (Fang et al., 2010). The simulation and experimental work were carried out for a room temperature of 25 ^{o}C. The simulation and experimental results for voltage and temperature are

agreed well for 2C, 5C and 10 C rates of constant current charging and discharging as shown in Figure 2.21. However, the temperature of the cell during pulse test current profile is not given and validated with experimental results. Besides, the effect of Solid Electrolyte Interface (SEI) layer is not modeled and investigated.
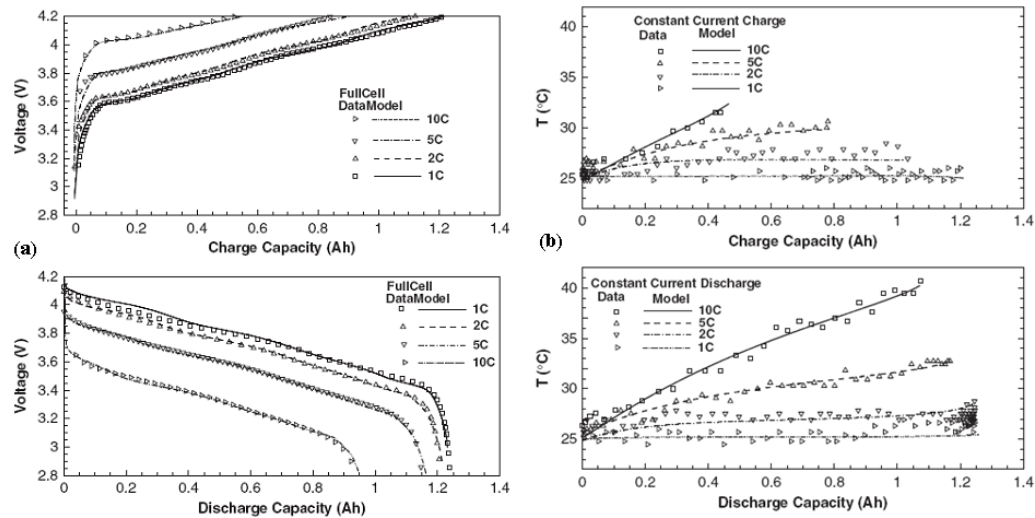
Figure 2.21 Experimental and simulated data of the cell voltage and temperature.

Chen et al. developed a detailed three dimensional thermal model to examine the thermal behavior of a lithium battery ($Li_xC_6 | Li_yCoO_2$) (Chen et al., 2005). Local convection and radiation were considered simultaneously in the numerical study to enhance the accuracy. The simulation results from the detailed model showed an asymmetric temperature distribution inside the battery. This is due to different rate of cooling on each surface. The maximum temperature was located at the center of the battery. The contact layer between the electrode and separator reduces the rate of cooling and provides the extra heat capacity to suppress the temperature rise. Strong forced convection was effective in reducing the maximum temperature inside the battery, but increases the non-uniformity of the temperature distribution inside the cell.

Smith and Wang used a 1D electrochemical and a lumped thermal model to explore limiting regions of pulse power operating of 72 cells, 6 Ah and 276 V nominal Li-ion battery pack ($Li_xC_6 \mid Li_yMn_2O_4$) (Smith and Wang, 2006). Solid phase Li transport was the main parameter which determined the high rate performance of the cell. 320 W of heat generated from the battery pack was found in a US06 cycle at 25 ^{o}C. At lower ambient temperature, more heat is generated. On the other hand, the heat generated during the less aggressive FUDS and HWFET cycles is less. Ohmic heating was dominant for pulse operation type of HEVs and the equivalent circuit model was sufficient to predict the generation rate for various driving cycles and control strategies. The study also concluded that forced air convection (h= 10.1 $Wm^{-2}K^{-1}$) is enough to maintain the battery temperature below the 52 ^{o}C PNGV operating limit for the worst case US 06 cycle.

Wu et al. investigated the temperature distribution in a Li-ion battery (12 Ah, 40 mm diameter and 110 mm height) (Wu et al., 2002). From the study, the heat generated from the battery at high discharge rate was difficult to remove through natural convection. The temperature of the battery might reach 65 ^{o}C with a discharge rate of 10 A. However, this problem could be solved using forced convection with metal fins and heat pipe. The overall temperature of the cell was reduced, but the temperature distribution became non-uniform. The temperature difference between the center and the surface cell was about 20 ^{o}C.

Fleckenstein et al. investigated current density and SOC inhomogeneities caused by the temperature difference through equivalent circuit simulation and experiment (Fleckenstein et al., 2011).Reversible heat and ohmic heat were

considered as the primary heat sources. The SOC drift of the cell was caused by the temperature dependence of the open circuit potential and the temperature-dependent ratio of charge-to-discharge pulse impedance. Electrical inhomogeneities were found in the simulation and experiment when three cells were connected in parallel. The SOC difference between those cells was about 5.3%, and is due to OCV-hysteresis which is significant in the $LiFePO_4$/C system. Therefore, the cells connected in parallel must have a sufficient resting period to allow for self balancing to ensure homogeneity in the SOC distribution and reduce the possibility of cell aging.

2.5.2 Empirical and equivalent circuit model

Accurate battery models are needed for the development of control strategies and the evaluation of the performance of EV battery packs during driving tests which required significant amounts of time and cost. Therefore, a good battery model is needed to predict the battery performance in terms of charge (SOC), battery voltage, current, temperature, heat generation and dynamic behavior over the driving cycles. Although electrochemical models can predict the aging and thermal behavior of the Li-ion battery, coupled time variant spatial partial differential equations make them complex and impossible to implement into a real time control system (Menard et al., 2010). Hence, relatively simple empirical and electrical circuit models involving a combination of voltage sources, resistors and capacitors which are linked to the state of charge of the battery by simple mathematical expressions. These simple mathematical expressions allow for rapid calculation times and are useful for predicting battery behavior in a real time system simulation or control algorithm. Besides, their parameters do not refer to the physical data of

the battery (Menard et al., 2010; Chen and Rincon-Mora, 2006; Kroeze and Krein 2008 and Urbain et al., 2008). Three different models have been used, namely the internal resistance battery model (Rint), the resistance-capacitance model (RC) and the Partnership-for-a-New-Generation-of-Vehicle model (PNGV). The thermal model used to predict the temperature of the battery pack is the lumped capacity model (Kuper et al., 2009).

The internal resistance model (R_{int}) consists of a voltage source (U_{oc}) and resistor (R_o). The parameters vary with SOC, temperature, direction of current flow (I_L) and state of health. The battery is modeled as an equivalent circuit with no rate-dependent resistances. The limitations of the R_{int} model include the model's voltage response that is too sensitive to load changes, and an internal resistance that remains constant with the current magnitude and temperature as well as SOC (Pesaran, 2001; Heckenberger, 2009; Kuper et al., 2009 and He et al., 2011).

The resistance-capacitance battery model (RC) is another battery model developed by Saft for their high power Li-ion cell (Johnson, 2002). The electrical model consists of two capacitors (C_b and C_c) and three resistors (R_t, R_e and R_c). C_b represents the capability of Li-ion battery to store charge chemically. C_c represents the surface effects of the cell (the immediate amount of current a battery can deliver based on time constants associated with the diffusion of materials and chemical reactions). Resistors R_t, R_e, R_c are terminal resistor, end resistor and capacitor resistor, respectively. U_b and U_c are the voltage across C_b and C_c, respectively (Johnson et al., 2000 and He et al., 2011).

The PNGV battery model was developed by the National Renewal Energies Laboratory (NREL) to overcome the limitations of the R_{int} and RC models by including temperature and SOC parameter variations, voltage limits, an SOC estimator and a thermal model. U_d and U_{PN} are the voltages across $1/U'_{oc}$ and C_{PN}, respectively. I_{PN} represents the current flow out from C_{PN}. The internal resistance model, the RC model and the PNGV model are shown in Figure 2.22.
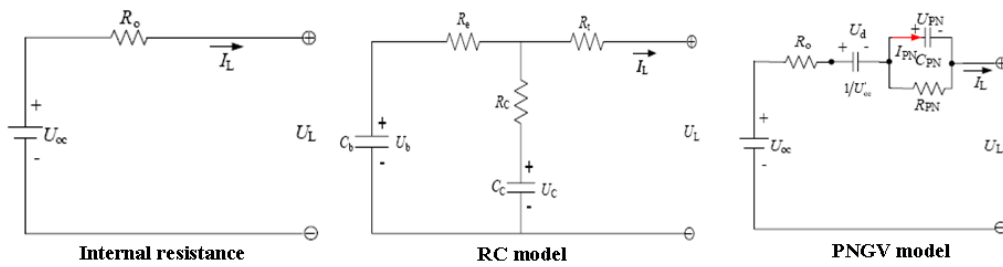
Figure 2.22 Battery models for Li-ion battery.

The equivalent circuit model used Thevenin equivalents, impedances or run time based models to represent the characteristics of the cell (Kroeze and Krein, 2008). In the Thevenin models, the open circuit voltage is assumed constant and a network of resistors and capacitors is used to track the response of the cell to the transient loads (Jung and Kang, 2014, Hu, et al., 2012; Kroeze and Krein, 2008; Chen and Rincon-Mora, 2006 and Tsang et al., 2010). The accuracy of the predictions depends on the number of parallel resistive-capacitive networks. There are numerous resistive-capacitive (RC) networks available in the literature such as first order RC (Awarke et al., 2012; Tsang et al., 2010 and Chiang et al., 2011), second order RC (Jung and Kang, 2014; Benger et al., 2008 and Dubarry and Liaw, 2007) and third order RC (Kroeze and Krein, 2008 and Andre et al., 2011) models. Hysteresis behaviors are often added to the model to improve the prediction. Among these models, most of them are developed based on isothermal conditions and the parameters

are constant over a wide range of temperature, limiting their use in on-board battery management systems (Hu et al., 2009; Hu et al., 2012 and Rahmoun et al., 2013). On the other hand, an impedance-based model employed an AC-equivalent impedance model in the frequency domain through impedance spectroscopy. A complex equivalent network (Z_{ac}) is utilized to fit the impedance spectra (Chen and Rincon-Mora, 2006). This type of model cannot predict the response of the cell and is only working for a fixed SOC and temperature setting (Buller et al., 2005). The runtime based electrical model used discrete or continuous time implementations in the SPICE simulator to determine the variable in the complex electric circuit network. There are several disadvantages associated with the runtime based electrical model when predicting the current varying load conditions (Chen and Rincon-Mora, 2006). Among these models, Thevenin model with its reasonable accuracy in predicting the SOC and I-V characteristics and temperature is more suitable to be implemented into the vehicle power control system and battery testing.

Tremblay and Dessaint developed a battery dynamic model using Matlab Simulink to predict the electrical behavior of four different types of battery which is lead acid, Li-ion, NiCd and NiMH (Tremblay and Dessaint, 2009 and Tremblay, 2007). The model's parameters (fully charged voltage, exponential voltage and nominal voltage) were extracted from the discharge curve of the battery at low C-rate. The simulation results of the cell voltage showed good agreement with the experimental dynamic charge and discharge of the cell and the error is within 5%. Besides, the battery model is included in the SimPower Systems simulation software to predict the electrical response of a fuel cell

electric vehicle (Tremblay and Dessaint, 2009 and Tremblay, 2007). However, the thermal response of the cell are not investigated and validated.

Chen and Evans used Shepherd equation (Shepherd, 1965) coupled with Bernardi et al. (Bernardi et al., 1985) heat generation equation to predict the electrical and thermal response of the Lithium polymer electrolyte battery under galvanostatic discharge (Chen and Evans, 1994). The simplified Federal Urban Driving Schedule was used to estimate the heat generation, internal temperature and external temperature variations of the cell with and without regenerative braking. Under natural convection, the external cell temperature could reach to 373 K without regenerative braking. However, the study was purely simulation and did not validate with any experimental data.

Ceraolo et al. developed a high fidelity electrical model with thermal dependence to investigate the electrical and thermal behavior of the LiNiCoMnO$_2$ cell (Ceraolo et al., 2011). The first order RC model parameters were extracted from the voltage response of the 10% SOC of pulse discharge current at 5 ^{o}C, 20 ^{o}C and 40 ^{o}C. The simulation results were validated with an independent driving cycle and the error between simulated data and experimental measurement was about 2%. However, no validation was done on the thermal response of the cell.

A layered technique to break up the parameter estimation problem into small tasks was applied to estimate the third order RC parameter for a lithium Iron Phosphate cell (Huria et al., 2012). The simulated results were then validated with the experimental results with a mean residual error of 0.7 mV.

Huria et al. proposed an SOC evaluation algorithm for the Lithium Iron Phosphate cell that exhibited a hysteresis phenomenon (Huria et al., 2014).

Flat open circuit voltage and state of charge (OCV-SOC) relation of Lithium Iron phosphate battery will cause difficulties in determining the SOC from OCV measurements. The hysteresis will cause inaccurate of SOC prediction during the charging or discharging operation using RC models. Extended Kalman filter was used to treat the error in the OCV-SOC relationship of the model, while the errors in the experimental measurement are treated with Enhanced Kalman Filter. Besides, the author also proposed that, yearly calibration of the battery used in the vehicle with the model is needed to increase the prediction of the SOC.

2.5.3 Experimental studies

Roth and Doughty investigated the thermal abuse performance of two advanced chemistry material for Li-ion battery and compared with Sony 18650 cells (Roth and Doughty, 2004). The materials are MCM graphite-based anode and $LiNi_{0.85}CoO_2$ cathode material, and MAG10 anode graphite and $LiNi_{0.80}Co_{0.15}Al_{0.05}O_2$ cathode material. Accelerating rate calorimeter and differential scanning calorimeter were used to determine the thermal runaway response of these cells as a function of state of charge and aging. The thermal abuse performance of the cell is dependent on the state of charge and the morphology of the anode material.

Forgez et al. developed a lumped parameter thermal model of a cylindrical $LiFePO_4$/graphite Li-ion battery (26650) for the micro controller in BMS (Forgez et al., 2010). Heat transfer coefficient and heat capacity of the cell are determined from the surface and internal temperature of the battery under room temperature. A temperature difference of about 10 ^{o}C was observed between the center and surface of the battery. The error of the

temperature model and actual reading is less than 1.5 $^{\circ}$C. The lumped model and the experimental results for a 26650 cell are shown in Figure 2.23.
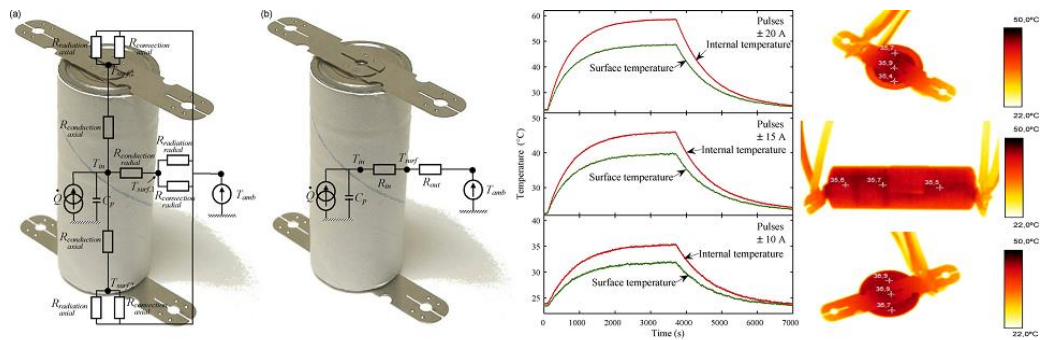
Figure 2.23 Lumped model and experimental results for 26650 cell.

Onda et al. and Ohshima et al. characterized the thermal behavior of 18650 Li-ion cells (Sony, LiCoO$_2$) under adiabatic conditions (Onda et. al, 2006 and Ohshima et al., 2006). The cell surface temperature rise during charging is lower than during discharging. The highest cell surface temperature during discharging is about 100 $^{\circ}$C at 3C, while the cell surface temperature was about 33 $^{\circ}$C during charging at 1.5 C rate. At 3C of discharging, the temperature difference between cell center and surface is about 1.9 $^{\circ}$C. The lumped capacitance model was also used to calculate the amount of heat generated. In their model only reaction heat and ohmic heat were considered.

Hallaj et al. investigated the performance and thermal behavior of commercial Li-ion batteries using electrochemical-calorimetric methods (Hallaj et al., 2000). The manufacturers of the Li-ion cells were Sony (coke|LiCoO$_2$), Panasonic (graphite|LiCoO$_2$) and AT&T (graphitized carbon fiber|LiCoO$_2$). The measurement of the rate of cooling for the cells was endothermic during charging and exothermic during discharging as shown in Figure 2.24. The endothermic effect due to entropy of reaction was more dominant at the beginning of charging. At the end of charging, ohmic and

51

polarization impedance increased significantly and surpasses the entropy effect. However, the Panasonic cell exhibited endothermic reaction during discharging at E = 4.0V, this was probably due to phase change in the $LiCoO_2$ material or structural transformation in the graphite anode material. Similar results were obtained by Takano et al. when investigating the entropy change in the Li-CoO$_2$ cell during charging and discharging (Takano et al., 2002). Cell impedance is dependent on the state of charge of the battery and is higher at the end of discharge due to polarization concentration.
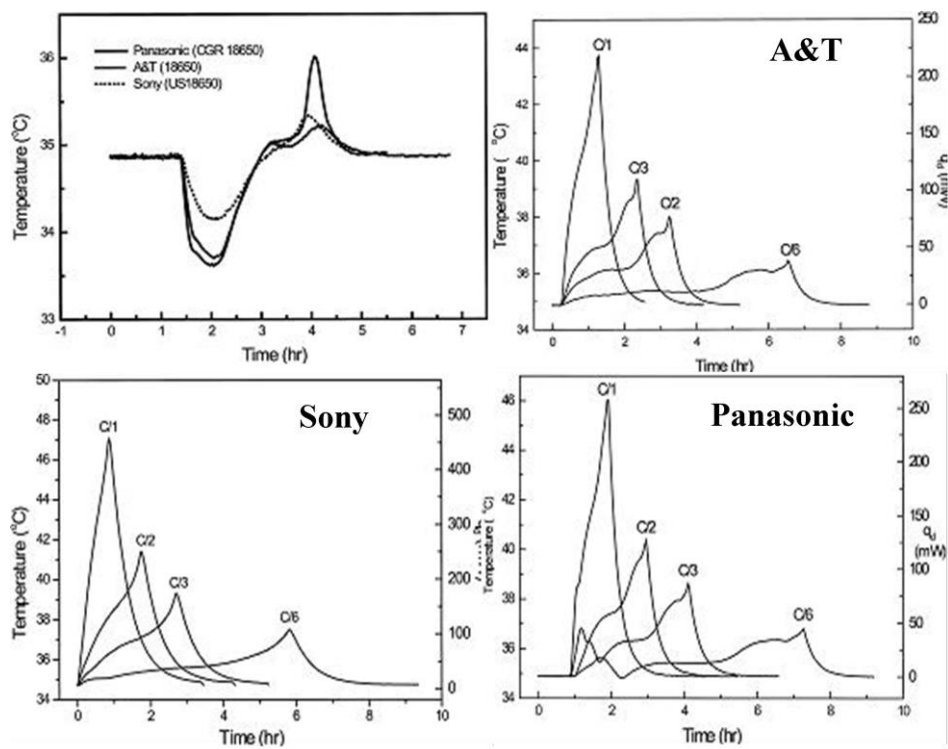
Figure 2.24 Test results of $LiCoO_2$ battery by various manufacturers.

Hysteresis of open circuit voltage of a battery is a commonly found in Nickel-Metal Hydride (NiMH) and Li-ion cell (Thele et al., 2008; Barker et al., 1996; Roscher et al., 2011 and Tang et al., 2011). In Li-ion battery, the hysteresis effect on Lithium Iron Phosphate is more significant than cobalt, nickel or manganese based battery (Barker et al., 1996; Roscher et al., 2011 and Tang et al., 2011). In cobalt, nickel and manganese based Li-ion battery,

due to the high gradient in the specific relation between SOC and OCV, the impact of hysteresis on the cell's OCV is negligible. On the other hand, the OCV of the Lithium Iron Phosphate cell shows a plateau voltage over a wide range of SOC. The relationship between OCV and SOC during charging and discharging is path dependent and leads to distortion in OCV to SOC static mapping (Roscher et al., 2011). The hysteresis will cause unreliable OCV reconstruction in the battery management system uses a model-based state estimation approach. However, the hysteresis phenomenon can be reduced by increasing the relaxation duration before the OCV of the cell is taken.

Apart from studies on a single cell, energy management studies have been conducted on battery packs as well. Minimization of the energy loss in the cell assemblies to allow maximization of the energy harvesting in the battery pack is crucial in energy management. High electrical contact resistance will cause difficulties in cell balancing, large variation of the cell temperature, reduce the storage capability of the cell and lead to localized heating, and in the extreme case, to cell explosion. A recent study established that the electrical contact resistance due to imperfect surface features between the connectors and cell terminal will cost about 20% loss in the total energy flow in and out of the battery (Taheri et al., 2011).

2.6 Heat transfer from extended surfaces

Fins that extend from the wall of the object into the surrounding fluid are useful in increasing the heat rate. The thermal conductivity of the fin material has a strong influence on the temperature distribution along the fin. Fin materials should have a high thermal conductivity to reduce temperature variations from the fin base to the tip. These extended surfaces come with a

variety of forms and configurations as shown in Figure 2.25 (Kays and London, 1964, Thermopedia, 2012 and Lienhard, 2008).
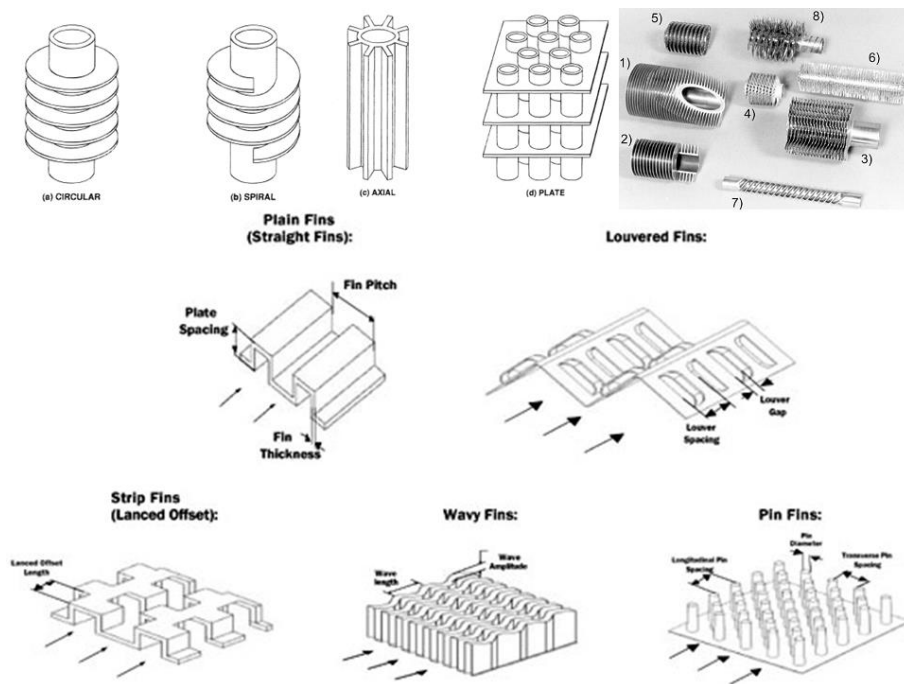
Figure 2.25 Various type of fin used to enhance the heat transfer.

Comparison of heat transfer pressure for different types of fins over the whole range of Reynolds number is shown in Figure 2.26. The efficiency of straight fins is better than other type of fin over the whole range of typical Reynolds numbers. At Reynolds number of 4000 the heat transfer per unit of pressure drop for a straight fin is three times better than that for a pin fin. On the other hand, from the size point of view (heat transfer per unit height), pin fins are the best choice, while straight fins are the most inefficient. Weight is always an important factor in the design of heat exchangers for transportation. For this criterion, the louvered fin is the most efficient as compared to other types of fins over a wide range of Reynolds numbers. Pin fins which can be incorporated directly into the casting of the heat exchanger are the least expensive. On the hand, louvered fins which require additional machining operations have higher setup costs as compared to straight fins and pin fins

(Hall and Marthinuss, 2004). A comparison of pressure drop, size, weight and cost for different types of fins is tabulated in Table 2.5. If all the parameters are weighted equally, louvered fin are the best design for a compact heat exchanger. Although pin fins have advantages in term of cost and size, they score poorly on pressure drop and weight. Lastly, straight fins will be an alternative choice for avionics heat exchangers if the pressure drop is the limiting factor.
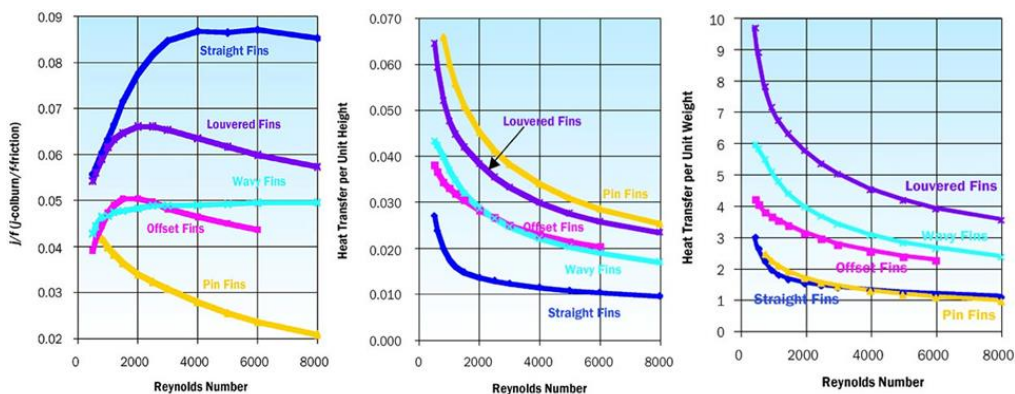
Figure 2.26 Comparison of the different type of fins performance.

Table 2.5 Comparison of all parameters (Hall and Marthinuss, 2004)

Fin configuration	ΔP	Size	Weight	Cost	Average
Straight	1	5	4	2	3
Offset	4	3	3	4	3.5
Pin	5	1	5	1	3
Wavy	3	4	2	3	3
Louver	2	2	1	5	2.5

The operating characteristics of the cold plate used in the battery pack are determined by the geometry of the channel, route, width and length (Jarrett and Kim, 2011 and Jarrett and Kim, 2014). A serpentine-channel cooling plate was proposed for the liquid cooling system battery pack. Numerical optimization was carried out to investigate the channel width and position to achieve the smallest pressure drop, average temperature and temperature uniformity. In order to avoid a local optimization of the cold plate design,

Latin hypercube sampling was used to select the cold plate design as shown in Figure 2.27. The cold plate needs to have a narrow inlet channel and widening toward the outlet to balance the effect of velocity, heat transfer area and fluid-solid temperature gradient to achieve the highest temperature uniformity. However, the study was focused on low flow rate of the coolant and did not validate with any experimental results.
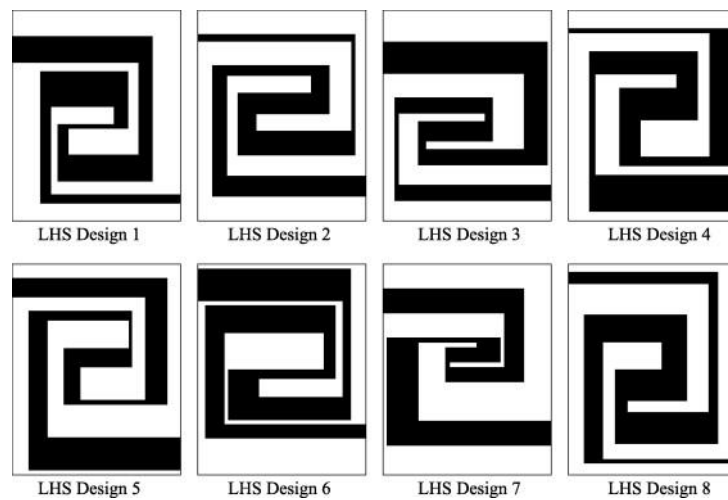
Figure 2.27 Different configuration of cold plate design.

Jin et al. introduce an oblique fin design for the liquid cold plate used in the EVs battery pack (Jin et al., 2014). The main objective to introduce an oblique cut on the conventional straight channel is to improve the heat transfer and temperature uniformity along the axial direction by breaking the developed thermal boundary layer. Experimental results show that the heat transfer coefficient of oblique mini-channel is higher than conventional straight fin at low flow rate. However, the pressure drop of the oblique fin is higher than straight fin at low pressure. Besides, there is not a significant difference between the performance of oblique fin and straight fin channels at high flow rates.

Huisseune et al. developed the heat transfer and friction correlation of a single row of helically finned tubes through experimental investigated

(Huisseune et al., 2010). The transverse tube pitch of the helical finned tube was varied parametrically. The Nusselt number and friction factor were correlated using minimum area Reynolds number and described in Equation 2-5 and 2-6, respectively. The correlations show a similar trend as existing correlation from the open literature.

$$Nu = 0.495\, Re_c^{0.509} \left(\frac{X_t}{d_{ext}} \right)^{-0.209} \tag{2-5}$$

$$f = 2.271\, Re_c^{-0.325} \left(\frac{X_t}{d_{ext}} \right)^{-1.849} \tag{2-6}$$

Chapman and Lee carried out a comparative thermal test of the straight fin, cross-cut rectangular pin fin and elliptic pin heat sink using a wind tunnel and numerical simulation (Chapman and Lee, 1994). The elliptical pin was effective in reducing the vortex effect to achieve minimum pressure loss and enhance the thermal performance of the heat sink. The, straight fin with enhanced lateral conduction along the fins and the lowest flow bypass characteristic was found to be effective in dissipating the concentrated heat source.

Leon et al. investigated the geometrical effect of the cooling fins in staggered arrangement (Leon et al., 2004). Three different types of fin geometries (in-line rectangular, staggered rectangular and rounded staggered shape) were investigated. It was found that the rounded staggered shape could provide the cooling effect similar to conventional straight fin at low flow rate but reduce the power consumption by 60%.

Kim et al. investigated the heat transfer and pressure drop characteristics of the conventional zigzag channel and NACA 0020 airfoil shape fin of the

printed circuit heat exchanger model (Kim et al., 2008). The simulation results show that airfoil shape fin possesses similar total heat transfer rate per unit volume of the conventional zigzag channel. Owing to the streamlined shape of the airfoil fin, the pressure drop is reduced to one-twentieth of the conventional zigzag channel.

Sparrow and Samie measured the heat transfer and pressure drop of the one and two-row array finned-tubes using wind tunnel (Sparrow and Samie, 1985). The Nusselt number and pressure drop coefficient for one-row arrays were highly affected by the transverse pitch. On the other hand, the Nusselt number for the first row of the two-row array was not affected by the longitudinal pitch when they were in-line. The Nusselt number of the finned-tube in a staggered array was higher than that for an in-line array. The pressure drop across the finned-tube in an in-line array was half that of the one-row value and affected by the longitudinal pitch.

Sahin et al. used the Taguchi method to optimize the fin arrangement of the heat exchanger (Sahin et al., 2005). The effect of the heat exchanger parameters such as fin height, fluid velocity, streamwise distance between slices, spanwise distance between slices, fin width, spanwise distance between the fins, angle of attack and streamwise distance between fins were investigated using a L_{18} ($2^1 3^7$) orthogonal array. The optimized parameters of the heat exchanger were fin width of 15 mm, angle of attack of 15 ^{o}C, fin height of 100 mm, spanwise distance between fins of 20 mm, stream-wise distance between fins of 10 mm, spanwise distance between slices of 20 mm, stream-wise distances between slices of 20 mm at a flow velocity of 4 ms^{-1} under heating power of 1185 W.

58

Wiberg and Lior developed a heat transfer correlation for a cylinder in axial turbulent flow (Wiberg and Lior). The flow conditions in front of the cylinder were modified by placing a turbulence generating grid and circular disk of 1/3 diameter and 2/3 diameter. A layer of thermo-chromic liquid crystal was coated on the electrically strip foil on the cylinder surface were used to study the heat transfer. The experimental results show that the average Nusselt number over the cylinder was increased by 25% when the turbulence intensity was increased to 6.7% from 0.1%. The non-uniformity of the Nusselt number along the axial direction was also reduced by inserting a flow modification in front of the cylinder.

Saini and Webb investigated the heat transfer performance of a straight fin heat sink used for computer cooling using a Fortran computer code (Saini and Webb, 2003). Two different types of heat sinks were used in the study. The heat sink dimensions used for the duct flow case studied was 65 x 60 mm x 44 mm, and for the impinging flow case, 80 x 60 mm x 29 mm. It was mentioned that increasing the fin height would decrease the convection resistance. The effect of fin height on convection resistance for impinging flow is lower than for duct flow. For a nominal base area and fan speed, impinging flow has 28% lower convection resistance than duct flow. Increasing the fan speed up to 25% would reduce the heat sink convection resistance by 15% and increase the heat rejection capability of the heat sink-fan combination by 11 %. Maximum heat rejection through 25% increase of the fan speed on (80 mm x 60 mm) is about 83.2 W. In addition, increasing the total base area by 33% with a 25% increase in fan speed will result in a 29% decrease in the convection resistance for duct flow case. In the duct flow, straight fins perform

better than pin fins. On the other hand, pin fins perform better in impinging flow.

2.7 Summary

Several researchers have developed the mathematical models to predict the electrochemical process occurring within the Li-ion battery, charging and discharging behavior and various thermal models have been established to account for the heat generated in the battery. However, most of the studies were focused on the $LiCoO_2$ or $LiMn_2O_4$ system using electrochemical-thermal models. The thermal models employed in these studies range from lumped models which treated the layer structure of the cells as a homogeneous material with effective thermal properties, assumed a uniform cell temperature distribution, and used heat generation data obtained from experiments, to detailed models that couple the electrochemical model with the thermal model using heat generation and temperature-dependent physical properties. Most of these thermal models did not consider the outer can and the heat shrink wrapping present in commercially available batteries and the influence of contact resistance between the battery terminals and the external connectors. Besides, very few modeling works have been carried out to investigate the behavior of Lithium Iron Phosphate cells. Aside from heat generation inside the battery, the effects of the electrical contact resistance of the contact interface of the cell terminals and the bus bar have been ignored. The contact resistance effect can decrease the temperature uniformity within the cell dramatically and further induce a performance decline due to unbalanced charging and discharging. Hence, this is a significant factor which should be taken into account in the cell modeling and thermal management system

design. The EV thermal management systems that have been developed to date are only suitable for low C rate charging of up to C/5-C/8. Therefore, design and development of a compact, light-weight, easily-maintained, reliable and more effective and efficient thermal management system is necessary for a high charging rate EVs or HEVs battery pack to prolong the life time, optimize the performance and reduce the thermal ageing of the battery. Therefore, it is necessary to investigate the electrical and thermal response of the $LiFePO_4$ battery under steady state and transient conditions. Then, the maximum heat generation condition will be used to develop a high-efficiency, intelligent thermal management system to fulfill the requirements of a fast-charging and high-power-density battery. Lastly, the integration issues of different formats of cells in the EVs battery pack will be reviewed to develop a high performance and cost effective battery pack.

CHAPTER 3

ELECTROCHEMICAL-THERMAL MODELING

3.1 Introduction

In this chapter, the electrochemical-thermal modeling of the Lithium Iron Phosphate (LFP) cell will be discussed. Although several researchers have developed mathematical models to predict the electrochemical and thermal behavior of the Li-ion battery, most of the studies were focused on the $LiCoO_2$ or $LiMn_2O_4$ systems and the simulations of the battery were based on one dimensional models. The effect of metal casing, heat shrink wrapping and influence of external contact resistance between the battery terminals and external connectors have not been modeled. Very few modeling works have been carried out to investigate the electrochemical and thermal behavior of the LFP cell. The aim of this work is twofold: first, to investigate the electrochemical and thermal behavior of a commercially available 18650 LFP battery using mathematical modeling and experiments, and second to apply the developed model to study the effect of contact resistance between the cell terminals and external connectors. A pseudo two-dimensional electrochemical model is coupled with a lumped three-dimensional thermal model to predict the electrochemical and thermal behavior of a spirally wound LFP battery. The model predictions are compared with experimental data. The models are useful to provide a fundamental understanding of the internal transport processes in a Li-ion cells and theoretical reference for a fast-charging battery cooling system design.

3.2 Mathematical modeling

3.2.1 Pseudo two-dimensional electrochemical model

The Li-ion cell used in this study is known as LFP battery and consists of current collector, electrodes, separator and electrolyte. A schematic diagram of the 18650 LFP cell electrochemical model is shown in Figure 3.1.
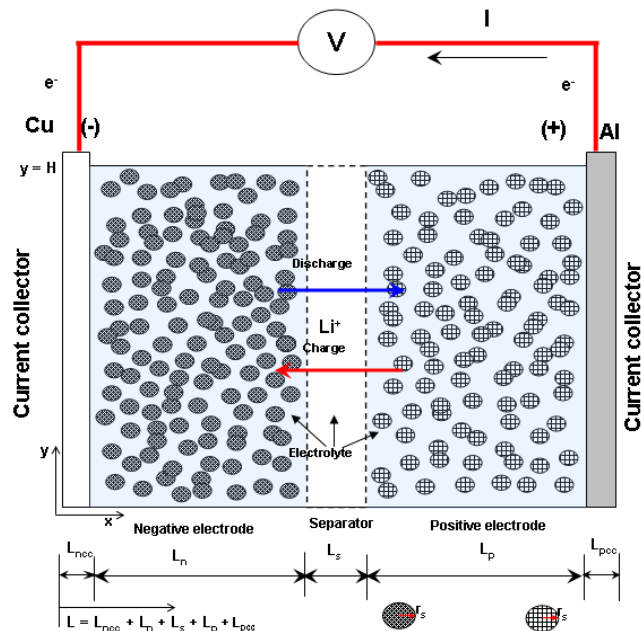
Figure 3.1 Schematic of LFP cell electrochemical model.

The cell was dissected to obtain the physical dimension of the current collector, electrodes, separator, casing thickness, gasket, etc as shown in Figure 3.2.

Figure 3.2 (a) 18650 cell. (b) After stripping off the heat shrink wrapping. (c) Positive terminal. (d) Negative terminal. (e). Unwinding the current collectors. (f). Tab and coated electrode.

The thickness of the current collectors, electrodes, separator, outer can and heat shrink wrap were measured using a LEICA DM 2500 M optical microscope. The height and length of the electrodes were measured with the stainless steel ruler. The dimensions and parameters used in the model are tabulated in Table 3.1 and Table 3.2. During the charging process, the lithium ions intercalate into the solid particles of the negative electrode and de-intercalate from the solid particles of the positive electrode. The electrons released during the process will flow through the external circuit to the negative electrode. This traveling direction will be reversed during the discharging process. Heat is generated within the cell and dissipated in all directions. The electrochemical reactions of Li-ion cell at the anode and cathode during charging and discharging action are represented by Equations 3-1 and 3-2 as below:

Positive electrode
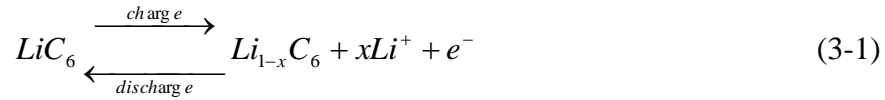
$$LiC_6 \xrightarrow[\text{\textit{disch}arg\,e}]{\text{\textit{ch}arg\,e}} Li_{1-x}C_6 + xLi^+ + e^-$$ (3-1)

Negative electrode

$$xLi + xe^- + Li_{1-x}FePO_4 \xrightarrow[\text{\textit{disch}arg\,e}]{\text{\textit{ch}arg\,e}} LiFePO_4$$ (3-2)
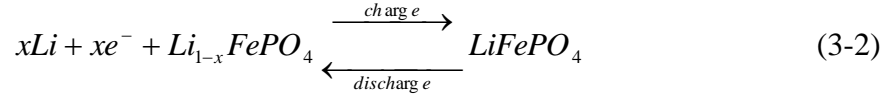
Heat is generated within the cell and dissipated in all directions. The basic assumptions used to model the Li-ion battery are as follows (Gu and Wang, 2000):

1. Gas generated during the reaction is neglected and no side reaction occurred.

2. A concentrated binary electrolyte is assumed (Fuller et al., 1994).

3. The Butler −Volmer equation is used to describe the charge transfer kinetics.

4. Diffusion and migration are involved in the transport of ionic species in the electrolyte.

5. The active material in positive and negative electrodes comprised of spherical particles with uniform size to form a constant porosity.

6. The transportation of Li inside the electrodes is by diffusion and guided by a constant diffusion coefficient.

7. Interfacial chemical equilibrium exists in the solid active material phases. This is due to the large mass diffusivity of electrolyte and electronic conductivities or small particle size of the active material.

The model will be used to solve for five dependent variables:

➢ ϕ_s Electric potential

➢ ϕ_l Electrolyte potential

- ➢ $\Delta\phi_{s,film}$ Potential losses at the Solid Electrolyte Interface (SEI).

- ➢ c_s Concentration of Lithium in the electrode particles.

- ➢ c_l Electrolyte salt concentration

- ➢ T Temperature of the battery

Table 3.1 Thermal and electrical cell specifications of the LFP cell.

Parameter	Value	Parameter	Value
Nominal voltage, V	3.2	Cu current collector thickness, μm	20
Nominal capacity, Ah	1.3	Al current collector thickness, μm	10
Cell weight, g	30	Separator thickness, μm	10
Can thickness, mm	0.3	Positive electrode height, cm	5.65
Heat shrink wrap material	PVC	Negative electrode height, cm	5.8
Heat shrink wrap thickness, μm	15	Positive electrode length, cm	7.6
Mandrel diameter, mm	4.0	Negative electrode length, cm	8.3
Positive electrode mass, g	14.88	Negative electrode mass, g	11.83
Positive electrode thermal conductivity, $Wm^{-1}K^{-1}$	0.20	Positive electrode thickness (2sided), μm	130
Negative electrode thermal conductivity, $Wm^{-1}K^{-1}$ (Chen et al., 2006)	1.04	Negative electrode thickness (2sided), μm	90
Positive current collector thermal conductivity, $Wm^{-1}K^{-1}$ (Chen et al., 2006)	170	Heat capacity positive electrode, $Jkg^{-1}K^{-1}$ (Srinivasan, 2010)	750
Negative current collector thermal conductivity, $Wm^{-1}K^{-1}$ (Chen et al., 2006)	398	Heat capacity negative electrode, $Jkg^{-1}K^{-1}$ (Chen et al., 2006)	1437
Positive current collector density, kgm^{-3} (Chen et al., 2006)	2770	Heat capacity positive current collector, $Jkg^{-1}K^{-1}$ (Chen et al., 2006)	875
Negative current collector density, kgm^{-3} (Chen et al., 2006)	8933	Heat capacity negative current collector, $Jkg^{-1}K^{-1}$ (Chen et al., 2006)	385
Positive electrode density, kgm^{-3} (Wang et al., 2007)	3600	Separator heat capacity, $Jkg^{-1}K^{-1}$ (Chen et al., 2006)	1978
Negative electrode density, kgm^{-3} (Chen et al., 2006)	1347	Separator density, kgm^{-3} (Chen et al., 2006)	1009
Separator thermal conductivity, $Wm^{-1}K^{-1}$ (Chen et al., 2006)	0.3344	Electrolyte thermal conductivity, $Wm^{-1}K^{-1}$ (Chen et al., 2006)	0.6
Electrolyte density, kgm^{-3} (Chen et al., 2006)	1130	Electrolyte heat capacity, $Jkg^{-1}K^{-1}$ (Chen et al., 2006)	2055

Table 3.2 Model input parameters for simulation of 1.3 Ah cell.

Parameter	Negative electrode	Separator	Positive electrode
Particle radius, r (m) (Gu and Wang, 2000 and Smith and Wang, 2006)	12.5×10^{-6}	N/A	1.0×10^{-6}
Filler volume fraction, ε_f (Gu and Wang, 2000)	0.172	0.276	0.259
Electrolyte phase volume fraction, ε_l (Gu and Wang, 2000)	0.357	0.724	0.444
Maximum Li concentration in solid, $c_{s,max}$ (mol m^{-3}) (Srinivasan and Wang, 2003)	26390	N/A	22800
Electric conductivity, σ (S m^{-1}) (Fang et al., 2010 and Thorat, 2009)	100	N/A	0.04
Initial electrolyte concentration, $c_{s,0}$ (mol m^{-3}) (Gu and Wang, 2000)	2000	2000	2000
Charge transfer coefficient, α_a, α_c (Smith and Wang, 2006)	0.5, 0.5	N/A	0.5, 0.5
SEI film resistance, R_{SEI} (Ω m^2)	0	N/A	0
Electrolyte mean molar activity coefficient, f (Smith and Wang, 2006)	1.0	1.0	1.0
Li diffusion coefficient in solid, D (m^2 s^{-1}) (Gu and Wang, 2000 and Wang, 2007)	3.9×10^{-14}	N/A	8×10^{-14}
Li diffusion coefficient in electrolyte, D (m^2 s^{-1}) (Thorat et al., 2011)	3×10^{-10}	3×10^{-10}	3×10^{-10}
Bruggeman tortuosity exponent (Fang et al., 2010)	1.5	1.5	1.5
Charge-transfer coefficients, α_a, α_c (Srinivasan and Wang 2003)	0.5	N/A	0.5
$1I_t$ discharge/charging current density, I (Am^{-2})	0	N/A	10
Electrical double layer capacitance, C_{dl} (F m^{-2}) (Thorat et al., 2011)	0.2	N/A	0.08
Transport number of Li-ion, t_+ (Doyle and Newman, 1996)	0.22		
Reference temperature, T_{ref} (K)	298.15		
Stefan-Boltzmann constant, σ (W m^{-2} K^4)	5.67×10^{-8}		
Emissivity of heat shrink wrapping, ε (Mikron, 2012)	0.95		
Emissivity of battery casing (Mikron, 2012)	0.19		
Connector contact resistance, R_{cc} (Ω) (Fu et al., 2012)	0.01		
Faraday's constant, F (C mol^{-1})	96487		
Universal gas constant, R (J mol^{-1} K^{-1})	8.3145		
Heat Transfer coefficient, Wm^{-2}K^{-1} (estimated)	5		

The porous electrode theory is used to model the electrode which consists of active materials and electrolyte. The solid active material and electrolyte are treated as superimposed with their own volume fractions ε_s and ε_l respectively.

Electrolyte diffusion coefficient $\left(D_{l,eff} = \varepsilon_l^{3/2} D_l\right)$, electric conductivity $\left(\sigma_{l,eff} = \varepsilon_l^{3/2} \sigma_l\right)$ and electrical conductivity in the electrode $\sigma_{s,eff} = \left(1 - \varepsilon_l - \varepsilon_f\right)^{3/2} \sigma_s$ are corrected with the Bruggeman factor to account for the porosity and the tortuosity effects (Smith et al., 2007 and Cai and White, 2011). The current density (i_s) and charge balance are based on Ohm's law in the electrode and are defined in Equation 3-3 and Equation 3-4, respectively (Smith et al., 2007 and Cai and White, 2011).

$$i_s = \sigma_{s,eff} \nabla \phi_s \tag{3-3}$$

$$\nabla \cdot i_s = j \tag{3-4}$$

The transfer current (j) resulted from Li insertion and removal is given by Equation 3-5 (Gu and Wang, 2000).

$$j = \begin{cases} a_{s,a} i_{loc,a} & \text{in the negative electrode} \\ 0 & \text{in the separator} \\ a_{s,c} i_{loc,c} & \text{in the positive electrode} \end{cases} \tag{3-5}$$

Reaction rates for intercalation and de-intercalation reaction of Li as in Equations 3-1 and 3-2 are assumed to follow the Butler-Volmer rule as shown in Equation 3-6 (Smith et al., 2007 and Doyle and Newman, 1996).

$$i_{loc} = i_0 \left\{ \exp\left[\frac{\alpha_a F}{RT}(\eta) \right] - \exp\left[-\frac{\alpha_c F}{RT}(\eta) \right] \right\} \tag{3-6}$$

The exchange current density (i_o) depends on the lithium concentrations in the electrolyte and solid active materials as in Equation 3-7 (Doyle and Newman, 1996). k_c and k_a are determined by the initial species concentration and exchange current density.

$$i_0 = F(k_c)^{\alpha_a} (k_a)^{\alpha_c} (c_{s,\max} - c_s)^{\alpha_a} (c_s)^{\alpha_c} \left(\frac{c_l}{c_{l,ref}} \right)^{\alpha_a} \tag{3-7}$$

A resistive film, which is also known as Solid Electrolyte Interface (SEI) is formed on the solid particles. The SEI causes an additional loss on the electrodes. To model the SEI, an extra solution variable for the potential variation over the film is incorporated. The governing equation is Equation 3-8 (Gu and Wang, 2000).

$$\Delta\phi_{s,SEI} = i_{loc}R_{SEI} \tag{3-8}$$

Due to the lack of clear physical justification of R_{SEI}, a zero value of R_{SEI} is used in the present work. The activation over-potential for all electrode reactions in the electrode then received an extra potential contribution and is defined as in Equation 3-9 (Gu and Wang, 2000).

$$\eta = \phi_s - \Delta\phi_{s,SEI} - \phi_l - E_{eq} \tag{3-9}$$

The equilibrium potential is a function of State of Charge (SOC) and temperature. It can be approximated by Taylor's first expansion as shown in Equation 3-10 (Cai and White, 2011).

$$E_{eq} = E_{0,ref} + \left(T - T_{ref}\right)\frac{\partial E_{eq}}{\partial T} \tag{3-10}$$

In the current study, the open circuit voltage for LFP (Thorat et al., 2011) and graphite (Safari and Delacourt, 2011) electrodes at 25 $^{\circ}$C are represented by Equation 3-11 and Equation 3-12 respectively.

$E_{eq,c}$ = 2.567462 + 57.69[1 - tanh(100z + 2.9163927)] + 0.442953 tan^{-1}(-65.41928z +64.89741) + 0.097237 tan^{-1} (-160.9058z + 154.590) (3-11)

$E_{eq,a}$ = 0.6379 + 0.5416 exp(-305.5309z) + 0.044 tanh[-(z − 0.1958)/0.1088] − 0.1978 tanh[(z-1.0571)/0.0854] - 0.6875 tanh[(z + 0.0117)/0.0529] − 0.0175tanh[(z − 0.5692)/0.0875] (3-12)

The dE_{eq}/dT of carbon (Kumaresan et al., 2008) and LiFePO$_4$ (Viswanathan et al., 2010) electrodes in function equilibrium potential vs SOC correlations are shown in Figure 3.3.
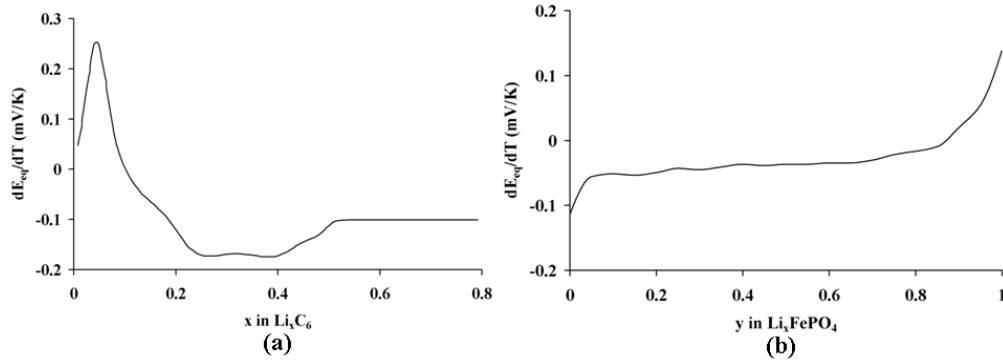
Figure 3.3 Entropic heat as a function of SOC for (a) Carbon and (b) LiFePO$_4$.

Conservation of charge during the electrolyte phase is also governed by Ohm's law as shown below (Doyle and Newman, 1996).

$$\nabla \cdot \left(\sigma_{l,eff} \nabla \phi_l + \frac{2\sigma_{l,eff} RT}{F} \left(1 + \frac{\partial \ln f}{\partial \ln c_l} \right)(t_+ - 1)\nabla \ln c_l \right) = -j \qquad (3\text{-}13)$$

The concentrated solution theory is used to model the transport process in the electrolyte phase. The electrolyte is treated as a binary with single organic solvent (Smith et al., 2007 and Doyle and Newman 1996). The conservation of Li-ion in the electrolyte can be defined as below (Gu and Wang, 2000).

$$\frac{\partial(\varepsilon_l c_l)}{\partial t} = \nabla \cdot \left(D_{l,eff} \nabla c_l \right) + \frac{1 - t_+}{F} j \qquad (3\text{-}14)$$

The concentration dependent function is used to model the electrical conductivity of the electrolyte consisting of LiPF$_6$ in 1:1 mixture of Ethylene Carbonate (EC) and Diethylene Carbonate (DEC). The resulting electrolyte conductivity used in the model is defined in Equation 3-15 (Thorat, 2009).

$$\sigma_l = \sigma_{ref} \left(\frac{1.262(c/c_{ref})}{1 + 0.2(c/c_{ref})^2 + 0.08(c/c_{ref})^4} + 0.014 \right) \qquad (3\text{-}15)$$

$$\sigma_{ref} = 7.8\,mScm^{-1}, \quad c_{ref} = 1\,mol\,dm^{-3}$$

The electrode is assumed to consist of spherical particles with the reaction occurring on the particle surface and the Lithium diffuses to and from the surface of the particles. The mass balance of Li-ion in the particles is governed by Fick's second law given in Equation 3-16 (Doyle and Newman, 1996).

$$\frac{\partial c_s}{\partial t} = \nabla \cdot \left(D_s \nabla c_s \right) \qquad (3\text{-}16)$$

The specific surface area of an electrode composed of particles with spherical morphology is defined in Equation 3-17 (Gu and Wang, 2000). In this model, the particle size is assumed to be uniformly distributed.

$$a_s = \frac{3}{r_s} \left(1 - \varepsilon_l - \varepsilon_f \right) \qquad (3\text{-}17)$$

The electrochemical double layer capacitance is a dynamic phenomenon associated with the activation phenomenon which is related to the electric charge population. During the charging/discharging process, electrons will accumulate on the electrode side while Li-ion will accumulate on the electrolyte side. A Helmholtz layer which is equivalent to an electric capacitor will be created and two different conductive areas are in contact (Menard et al., 2010). The effect of the double layer capacitance is also considered and modeled using Equation 3-18 (Schalkwijk and Scrosati, 2002).

$$i_{dl} = \left(\frac{\partial \phi_s}{\partial t} - \frac{\partial \phi_l}{\partial t} \right) a_s C_{dl} \qquad (3\text{-}18)$$

The electrolyte is assumed to be confined within the cell and there is no reaction on the surfaces of the anode and the cathode current collector. The boundary conditions for the electrolyte are defined as shown below (Gu and Wang, 2000):

$$-D_{l,eff} \left. \frac{\partial c_l}{\partial x} \right|_{x=L_{ncc}} = -D_{l,eff} \left. \frac{\partial c_l}{\partial x} \right|_{x=L_{ncc}+L_n+L_s+L_p} = 0 \qquad (3\text{-}19)$$

$$-\sigma_{l,eff} \left. \frac{\partial \phi_l}{\partial x} \right|_{x=L_{ncc}} = -\sigma_{l,eff} \left. \frac{\partial \phi_l}{\partial x} \right|_{x=L_{ncc}+L_n+L_s+L_p} = 0 \qquad (3\text{-}20)$$

In the separator, the entire current is carried by the lithium ions and therefore there is continuity of charge and species flux in the liquid phase across the electrode/separator interface. The charge flux will be equal to the total current density.

Insulating conditions apply to the solid phase current at the electrode/separator interface. This boundary condition is given below in Equation 3-21 (Gu and Wang, 2000).

$$-\sigma_{s,eff} \left. \frac{\partial \phi_s}{\partial x} \right|_{x=L_{ncc}+L_n} = -\sigma_{s,eff} \left. \frac{\partial \phi_s}{\partial x} \right|_{x=L_{ncc}+L_n+L_s} = 0 \qquad (3\text{-}21)$$

The charge flux at the current collector is equal to the current density applied to the cell. This boundary condition is given in Equation 3-22 (Gu and Wang, 2000).

$$-\sigma_{s,eff} \left. \frac{\partial \phi_s}{\partial x} \right|_{x=L_{ncc}+L_n+L_s+L_p+L_{pcc}} = \frac{I}{A} \qquad (3\text{-}22)$$

The solid phase potential is set to be zero in the negative current collector boundary or in other words, the negative current collector is grounded (Gu and Wang, 2000), i.e.

$$\phi_s \big|_{x=0} = 0 \qquad (3\text{-}23)$$

At the center of the spherical particle of the active material there is no flux (Gu and Wang, 2000),

$$\left. \frac{\partial c_s}{\partial r} \right|_{r=0} = 0 \qquad -D_s \left. \frac{\partial c_s}{\partial r} \right|_{r=r_s} = \frac{j}{a_s F} \qquad (3\text{-}24)$$

3.2.2 Thermal model

A schematic diagram of the 18650 LFP cell thermal model is shown in Figure 3.4.
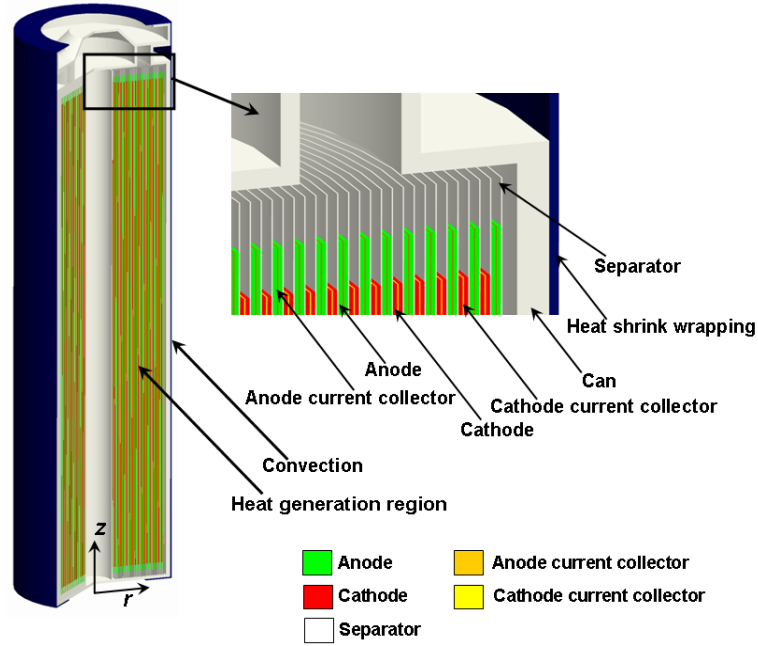
Figure 3.4 Schematic of 18650 LFP cell thermal model.

The resistance to conduction within the solid is much less than the resistance to convection outside the battery surface. Therefore, it can be assumed that the temperature profile in the cell is fairly uniform (Rao and Newman, 1997). The chemistry of the cell is not affected significantly by small variations of temperature. Therefore, the electrochemical model is coupled with a lumped thermal model to determine the temperature distribution of the entire cell. The general thermal energy equation used to model the heat conduction for the cell (Fang et al., 2010).

$$\rho_{eff} C_{p,eff} \frac{dT}{dt} = \nabla \cdot k_T \nabla T + Q_r + Q_j + Q_{rev} + Q_c \qquad (3\text{-}25)$$

The boundary conditions of the Li-ion battery are determined by Newton's cooling law and thermal radiation (Cai and White, 2011):

73

$$-k_{T,eff} \left.\frac{\partial T}{\partial x}\right|_{x=L} = h(T - T_\infty) + E\sigma_{sb}\left(T^4 - T_\infty^4\right) \tag{3-26}$$

The total reaction heat generation rate is defined as (Cai and White, 2011):

$$Q_r = i_{loc} a_s \left(\phi_s - \phi_l - E_{eq}\right) \tag{3-27}$$

The total ohmic heat generation rate is defined as (Cai and White, 2011):

$$Q_j = \sigma_{s,eff} \nabla\phi_s \cdot \nabla\phi_s + \left(\sigma_{l,eff} \nabla\phi_l \cdot \nabla\phi_l + \frac{2\sigma_{l,eff} RT}{F}(t_+ - 1)\left(1 + \frac{\partial \ln f}{\partial \ln c_l}\right)\nabla \ln c_l \cdot \nabla\phi_l\right) \tag{3-28}$$

The total reversible heat generation rate is defined as (Cai and White, 2011):

$$Q_{rev} = i_{loc} a_s T\left(\frac{\partial E_{eq}}{\partial T}\right) \tag{3-29}$$

The heat generation rate due to the effect of connector contact resistance (R_{cc}) is neglected in the first part of this study and is given by (Fang et al., 2010):

$$Q_c = \left(I^2 \frac{R_{cc}}{A_{cc}}\right)/Vol \tag{3-30}$$

The battery consists of several layers of electrodes and separator wound spirally into a cylinder. Therefore, the thermal conductivity in the battery model is considered to be anisotropic. The thermal conductivity is higher in the axial direction compared to the radial direction for the current geometry of 18650 LFP cell (Chen et al., 2006). Hence, the thermal conductivity in the radial and axial directions (Chen et al., 2006):

$$k_{T,r} = \frac{\sum L_i}{\sum \dfrac{L_i}{k_{T,i}}}, \quad k_{T,ang} = \frac{\sum L_i k_{T,i}}{\sum L_i} \tag{3-31}$$

The thermal conductivity of the active material in the cell in the x, y and z directions are given by (Chen et al., 2006):

$$k_{T,x} = \frac{|y|}{r} \frac{\sum L_i k_{T,i}}{\sum L_i} + \frac{|x|}{r} \frac{\sum L_i}{\sum L_i / k_{T,i}}, k_{T,y} = \frac{|x|}{r} \frac{\sum L_i k_{T,i}}{\sum L_i} + \frac{|y|}{r} \frac{\sum L_i}{\sum L_i / k_{T,i}},$$

$$k_{T,z} = \frac{\sum L_i k_{T,i}}{\sum L_i} \tag{3-32}$$

The total density of the active material in the cell is given by (Chen et al., 2006):

$$\rho = \frac{\sum L_i \rho_i}{\sum L_i} \tag{3-33}$$

The total heat capacity of the active material in the cell is given by (Chen et al., 2006):

$$C_p = \frac{\sum L_i C_{p,i}}{\sum L_i} \tag{3-34}$$

3.3 Numerical and experimental procedure

The electrochemical and thermal model equations are solved simultaneously using commercial finite-element solver-COMSOL Multiphysics 4.3. The center of the cell is assumed to be fully filled with electrolyte. Five unknowns (ϕ_s, ϕ_l, c_s, c_l, T) are solved using direct solver GMRES subroutine in conjunction with Gauss-Seidal and Multigrid preconditioners with a relative convergence tolerance of 10^{-4}. A grid independent test was carried out to refine the grid size until the simulation results are not affected by further refinement of the mesh and the relative error of the results is kept within 5%. The battery domain was discretized into 6922 elements. The outputs of the model are temperature, species and concentration distribution, heat generation and cell potential. Natural convection and

radiation are assumed for the cooling of the cell.

Commercial 1.3Ah 18650 cells with graphite anode coated on the copper current collector, Lithium Iron Phosphate (LiFePO$_4$) cathode coated on the aluminum current collector, electrolyte (LIPF$_6$) in EC:DEC 1:1 and Polyvinylidene Fluoride (PVDF) separator was used in the experiments. The charging and discharging of the battery was conducted using a battery cycler (Maccor Instrument 4000). The simulation model was validated using constant current charge and discharge experiments ranging from 1I_t (1.3 A) to 5I_t (6.5 A). The I_t-rate as per the standard IEC61434 is defined as (Omar et al., 2012)

$$I_t = \frac{C}{1\,hour} \tag{3-35}$$

where I_t represents the discharge current in amperes during one hour discharge and C is the measured capacity of a battery pack or cell. The cut off voltage for constant current discharging was 2.3 V whereas for constant current charging it was 4.2V and kept constant until the current dropped to 0.1 A. The surface temperature of the battery was measured using twelve thermocouples (T-types) attached to different locations on the cells. Three thermocouples were attached in the axial direction and on the four sides of the battery surface as shown in Figure 3.5.
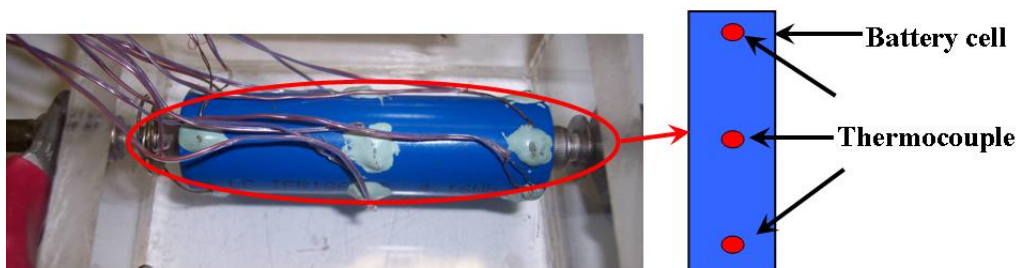
Figure 3.5 (a). Experimental setup for temperature measurement.
(b). Location of thermocouples attached to the surface of the cell.

The measurement of battery surface temperatures during charging and discharging at different I_t-rates were done at room temperature of 25 ^{o}C under natural convection. All the tests were repeated three times and the average value was taken. The temperature readings were recorded using the HP 34970A data acquisition system. The effective thermal conductivity of the 20 mm compact LiFePO$_4$ pellet was characterized using C-Therm TCI Thermal Conductivity Analyzer and calculated using Koh and Fortini model (equation 3-36) because the thermal conductivity of the LiFePO$_4$ powder cannot be accessed (Koh and Fortini, 1973).

$$\frac{k_{T,eff}}{k_0} = \frac{1-\xi}{1+11\xi^2}$$

(3-36)

3.4 Results and discussion

3.4.1 Evolution of cell potential

(a)
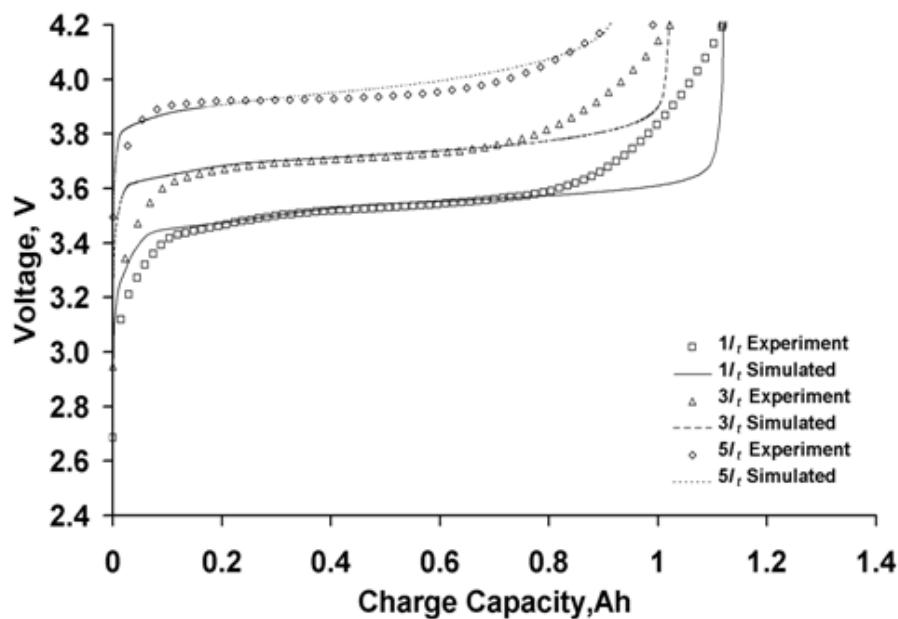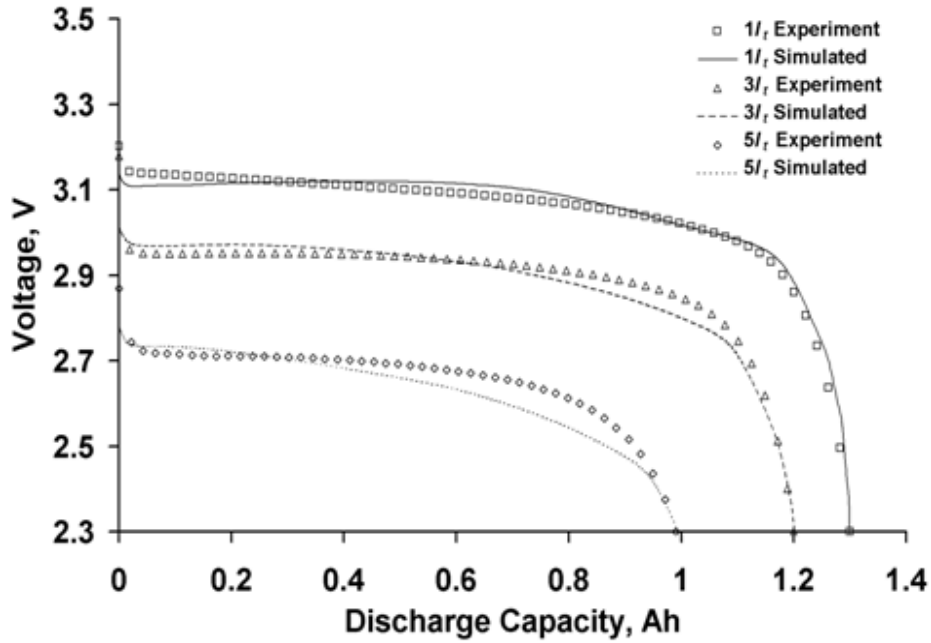
Figure 3.6 Experimental and simulated cell potential for (a) Charging.
(b) Discharging.

Figure 3.6 shows the capacity of the cell obtained by experiment and numerical simulation at different rates of charging and discharging at constant current. Only the constant current results are shown. The simulation results agree well with the experimental data with just some deviation towards the end of the process. The averaged relative error for the simulated and measured voltage at $1I_t$, $3I_t$ and $5I_t$ charging is 2.1%, 1.7% and 1.4%, respectively. The averaged relative error of the simulated and measured voltage at $1I_t$, $3I_t$ and $5I_t$ discharging is 1.0%, 1.7% and 2.1%, respectively. The deviation observed between the experimental and simulated results of voltage is probably due to the presence of the Solid Electrolyte Interface (SEI) layer inside the battery and the effect of particle size. The effect of SEI is not modeled and an average particle size is used in this work. In an actual cell, the particle size has a normal distribution. The voltage drop during discharging of the cell is mainly due to the increase in the internal resistance at the end of the discharging

78

process (Omar et al., 2012). Solution resistance, contact resistance of the electrode to the current collector, matrix resistance, kinetic resistance and diffusion resistance are components of the internal resistance of the cell (Srinivasan and Newman, 2004). The steep increase at the end of discharging indicated that the positive electrode was fully filled with Li during discharging and the steep increase at the end of charging indicated that the negative electrode was fully filled with Li. At high I_t-rates, the experimental cell voltage diverged significantly from the simulated open circuit voltage. This was probably due to the difference in the reaction rate, reduction of ohmic resistance and the change of species mass diffusivity with temperature (Srinivasan and Wang, 2003). At $5I_t$ of constant current charging, the maximum capacity of the cell was reduced by 20% compared to $1I_t$ (1.12 Ah). On the other hand, the maximum capacity that can be drawn from the cell at $5I_t$ of constant current discharging was about 24% less than the capacity at $1I_t$ (1.3 Ah). The reduction of cell capacity at high I_t-rates can be quantified by the Peukert equation (Omar et al., 2012):

$$C_{bp} = T_{dis} \cdot I_{dis}^{k} \tag{3-37}$$

Equation 3-37 shows that, the higher the discharge current, the smaller the capacity available in the cell. For charging the cell to full capacity, two modes of operation are involved, namely constant current and constant voltage.

3.4.2 Evolution of cell temperature
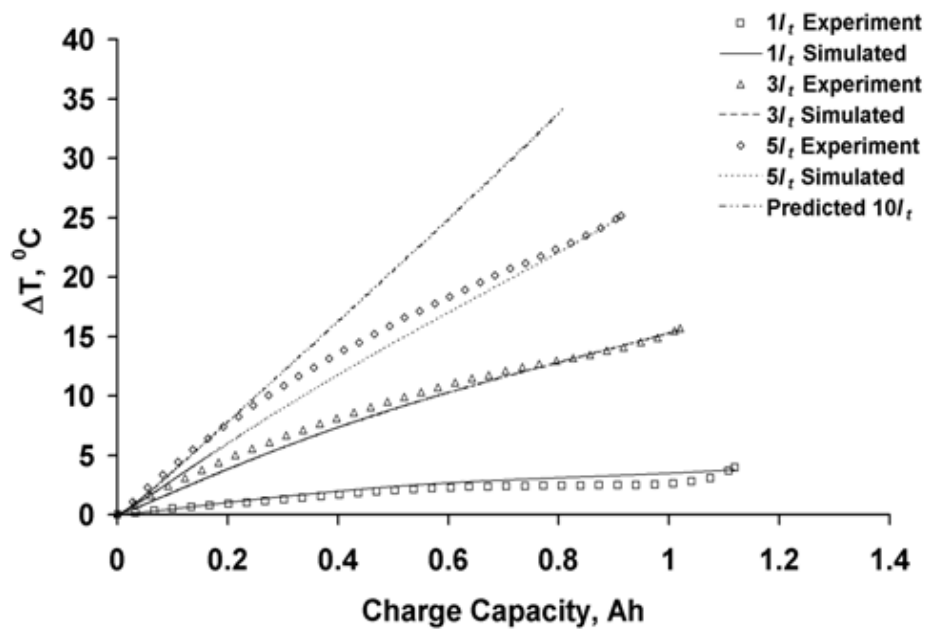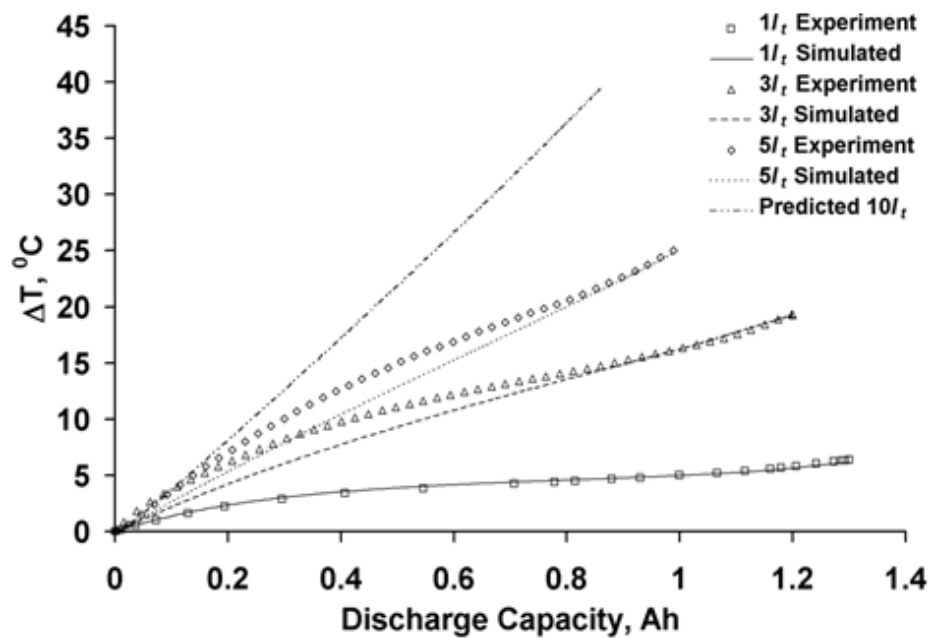
Figure 3.7 Experimental and simulated cell temperature (a) Charging.
(b) Discharging.

Figure 3.7 shows the average measured and simulated temperature rise on

the cell surface at different I_t-rates of charging and discharging. Apparently,

the average temperature of the cell was increased stepwise with the state of

charge and sharply toward the end of the charging or discharging process. This was probably caused by large polarization during the end of the charging and discharging process. There was good agreement between the simulated and measured cell surface temperature. As expected, the temperature has a positive correlation with the charging/discharge current. The final temperature changes during charging at $1I_t$, $3I_t$ and $5I_t$ were 3.9 ^{o}C, 15.6 ^{o}C and 25.2 ^{o}C, respectively. The averaged relative error for the simulated and measured temperature at $1I_t$, $3I_t$ and $5I_t$ charging was 20.4%, 10.4% and 12.8%, respectively. The final temperature changes during discharging at $1I_t$, $3I_t$ and $5I_t$ were 6.1 ^{o}C, 24.8 ^{o}C and 25.1 ^{o}C, respectively. The averaged relative error of the simulated and measured temperature at $1I_t$, $3I_t$ and $5I_t$ discharging is 6.2%, 15.7% and 13.3%, respectively. At low I_t-rates of charging or discharging, the heat generated can be dissipated effectively by natural convection and good thermal equilibrium was achieved. Therefore, only a small variation of the temperature was observed. As compared to low I_t-rates, a large amount of heat was generated at $5I_t$ and the cell did not have sufficient time to dissipate the heat. Hence, the temperature of the cell kept increasing, resulting in reduced ohmic, kinetic and mass transfer losses in the cell and increment in the mass transfer of solid and liquid phases. The average measured surface temperature of the cell deviated significantly from the simulated results during high I_t-rates. This was probably caused by the thermal resistance between the plastic shrink wrap with the battery casing which was not considered in this study. Forced convection cooling can be used to suppress the high temperature during high I_t-rates of charging/discharging.

3.4.3 Heat generation of the cell
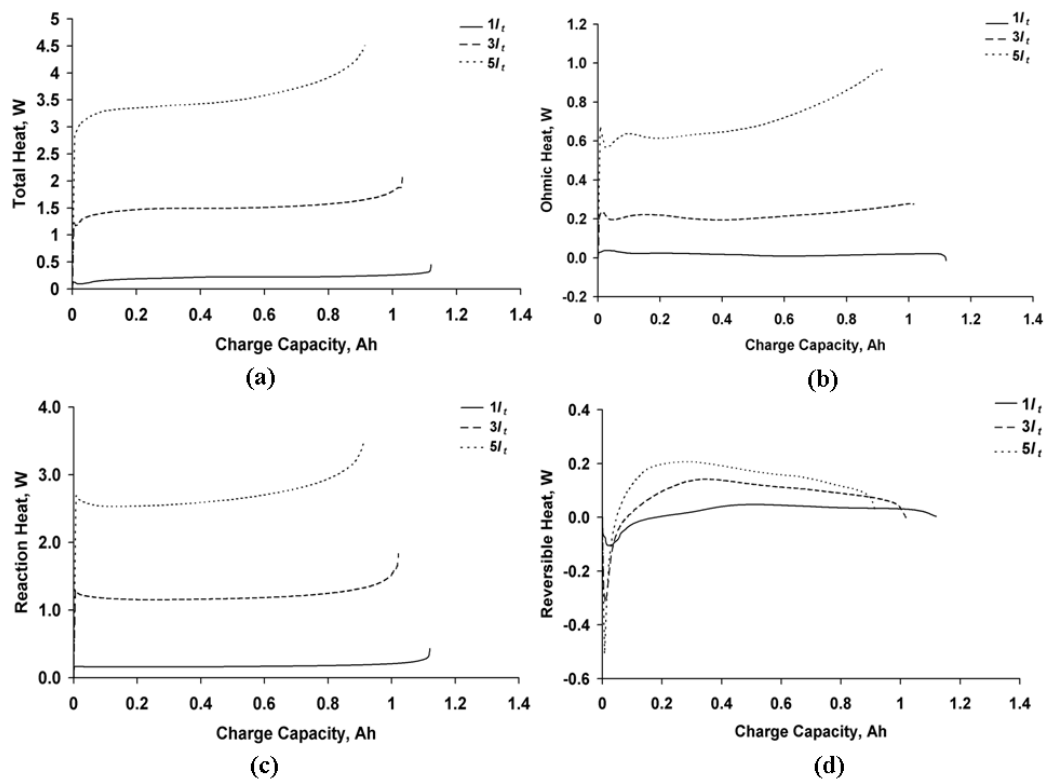
Figure 3.8 Heat generation for different I_t-rates of charging. (a) Total heat.
(b) Ohmic heat. (c) Reaction heat. (d) Reversible heat.
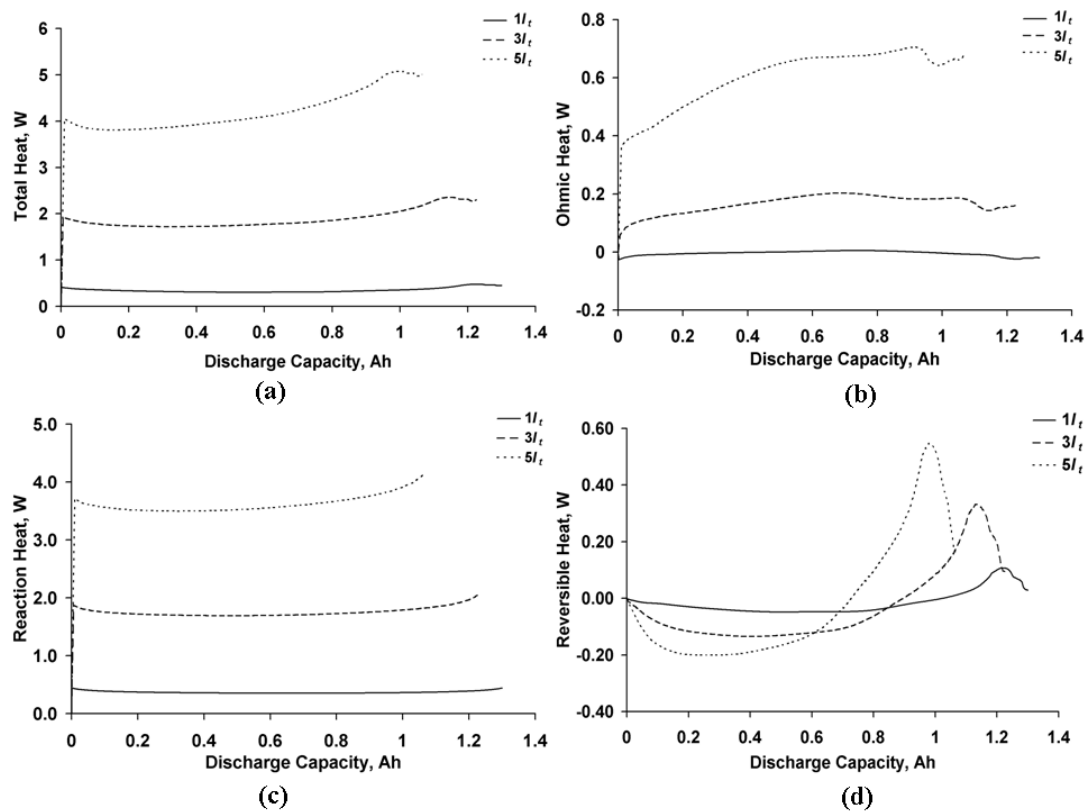
Figure 3.9 Heat generation for different I_t-rates of discharging. (a) Total
heat. (b) Ohmic heat. (c) Reaction heat. (d) Reversible heat.

Figure 3.8 and Figure 3.9 show the types of heat generation associated with the charging and discharging process. The total heat generation in the cell comprises ohmic heat, reaction heat and reversible heat. As the I_t-rate increased, the total heat generation accelerated. This led to a rapid increase of the cell temperature as shown in Figure 3.8(a) and Figure 3.9(a). The primary heat generated in the cell was reaction heat. The effect of ohmic and reversible heats became more significant at high I_t-rates. The higher electric conductivity of the graphite and LFP phase resulted in lower ohmic heat generation in the matrix phase as shown in Figure 3.8(b) and Figure 3.9(b). The reduction of the ohmic heat at the end of discharging shows that ohmic heat generated from the electrolyte phase as in Eq. 3-28 is the dominant process. Due to the large potential present during the end of the discharging process, diffusion of Li-ions in the electrolyte solution reduces the ionic current in the electrolyte phase (Smith, 2006). Figure 3.8(c) and Figure 3.9(c) show that reaction heat was the main source of heat generation during charging and discharging of the cell. Reversible heat is associated with the entropy change in the electrochemical reactions. The reversible heat was endothermic at the beginning of charging and rapidly became exothermic as the process proceeded and gradually reduced as the charging approached the end as shown in Figure 3.8(d). During discharging, the reversible heat was gradually changed from endothermic to exothermic and with a rapid increase and sharp decrease towards the end of the process as shown in Figure 3.9(d). The temperature of the cell grew slower at the initial stage and increased rapidly at the end of discharging which corresponded to the rapid increase of the reversible heat. Therefore, reversible heat was an important parameter for cell

modeling. During charging, reaction heat contributed about 80%, ohmic heat contributed about 15% and reversible heat, which was the minor source contributed about 5% of the total heat generated. On the other hand, reaction heat contributed about 85%, followed by ohmic heat, which was about 10% and reversible heat only contributed about 5% of the total heat generated during discharging.
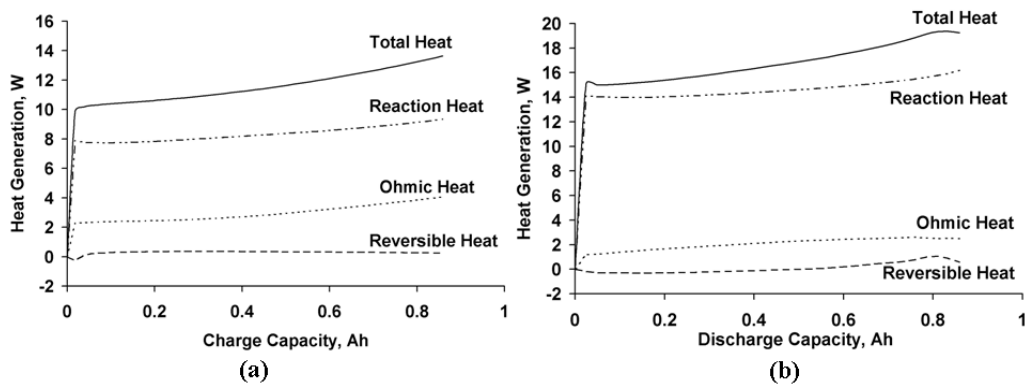
Figure 3.10 Heat generation for $10I_t$. (a) Charging and (b) Discharging.

$10I_t$ of charging was simulated to assess the feasibility of LFP cell for fast charging application. The potential of the cell rose to the cutoff voltage of 4.2 V. The final temperature of the cell surface could reach 59 ^{o}C as shown in Figure 3.7(a) while the heat generated during the process is illustrated in Figure 3.10(a). The total heat generated rose nearly 200% compared to $5I_t$ (Figure 3.8(a) and Figure 3.9(a)). The average heat generated during $10I_t$ discharging was about 40% more than that for the same rate of charging as shown in Figure 3.10(b) with about 40 ^{o}C increases in the average cell temperature. However, the optimum operating temperature for Li-ion battery is between 0 ^{o}C and 40 ^{o}C and the battery life cycle, capacity, durability, warranty and safety are highly dependent on the operating temperature. Therefore, the pulse charging technique with short relaxation periods and short discharge pulses during charging can be used to substitute conventional direct

current charging of the battery to avoid overheating the battery during charging. Besides, an active thermal management system must be carefully designed for the electric vehicle battery pack using a fast charging approach to ensure that the cells operate safely, prolong the life span and prevent thermal runaway of the cells.

3.4.4 Concentration distribution in the cell

The concentration profiles at the negative electrode, separator and positive electrode for different I_t-rates of charging and discharging are shown in Figure 3.11.

(a)
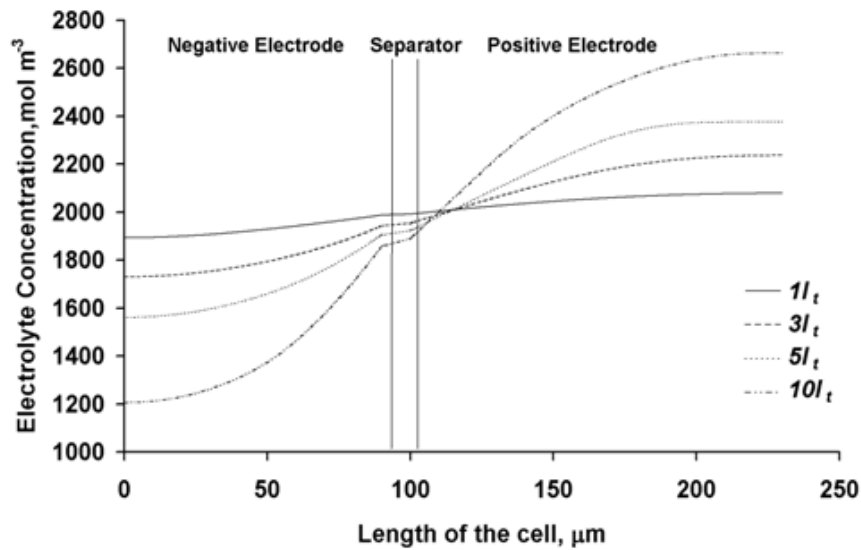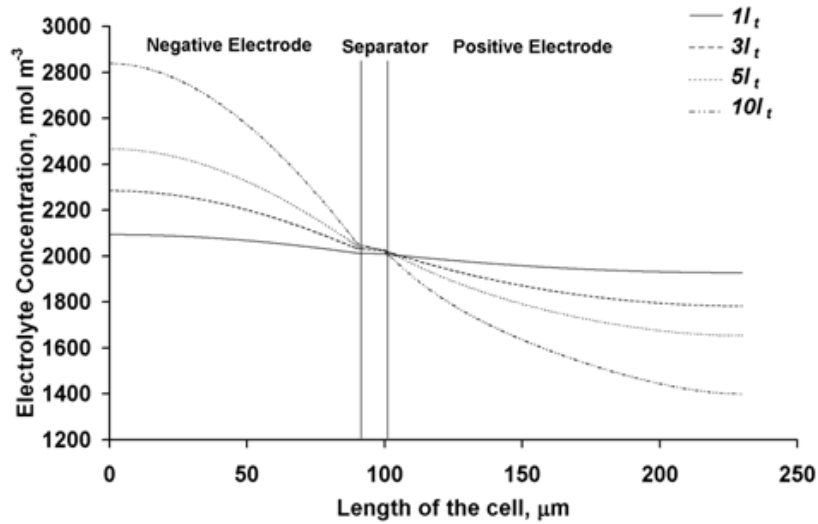
Figure 3.11 Concentration profiles of the electrolyte. (a) Charging.
(b) Discharging.

The performance of the cell was limited by the diffusion of lithium in the electrolyte and the active solid material phase. During the charging process, the lithium ion concentration in the negative electrode was lower than that in the positive electrode due to intercalation reaction. The lithium ion distribution was reversed during the discharging process and mainly determined by the de-intercalation of lithium ion in the negative electrode. The lithium ion concentration gradient increases with the I_t-rates. The lithium ion concentration profile at $1I_t$ was almost flat, which indicates a better diffusion of the lithium ion in the electrolyte at low I_t-rates. Besides, the Li-ion concentration gradient was the main factor which determined the ohmic heat generation in the electrolyte and the ohmic heat generation has a positive correlation with the gradient of the lithium ion concentration.

3.4.5 Effect of electrical contact resistance

The effect of electrical contact resistance between connectors and cell terminals was also investigated. The contact resistance was taken as 10 mΩ based on a worst case scenario (Fu et al., 2012). These external energy

losses have always been overlooked in the energy management of the battery pack. The electrical power loss due to electrical contact resistance is given by $P = I^2(R_{cc}/A_{cc})$. This electrical power loss is in the form of heat generated at the connector-cell terminal interface. Figure 3.12 shows the effect of the electrical contact resistance on the cell potential and temperature evolutions during $5I_t$ charging and discharging.

(a)

(b)
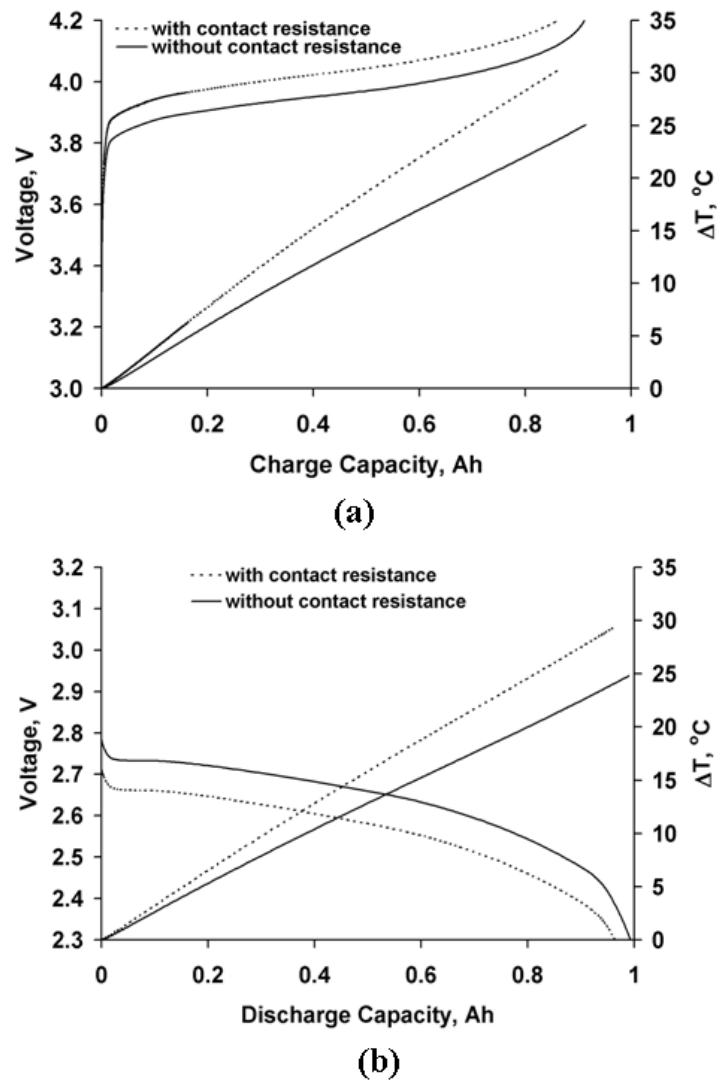
Figure 3.12 Effect of contact resistant on cell voltage and average temperature evolutions during $5I_t$ (a) Charging. (b) Discharging.

The power loss is about 0.42 W at each terminal of the cell. Compared to the charging process without contact resistance, the average temperature rise of the cell during charging with contact resistance was increased from

25.2 °C to 30.4 °C. The capacity of the cell was reduced by 5.4 % to overcome the power loss caused by the electrical contact resistance. During the discharging process, the electrical contact resistance reduced the maximum capacity of the cell at constant current discharging by 3%. The average temperature rise of the cell during the end of discharge was increased from 24.8 °C to 29.4 °C. The effect of the contact resistance on the heat generated during charging and discharging at $5I_t$ is shown in Figure 3.13.
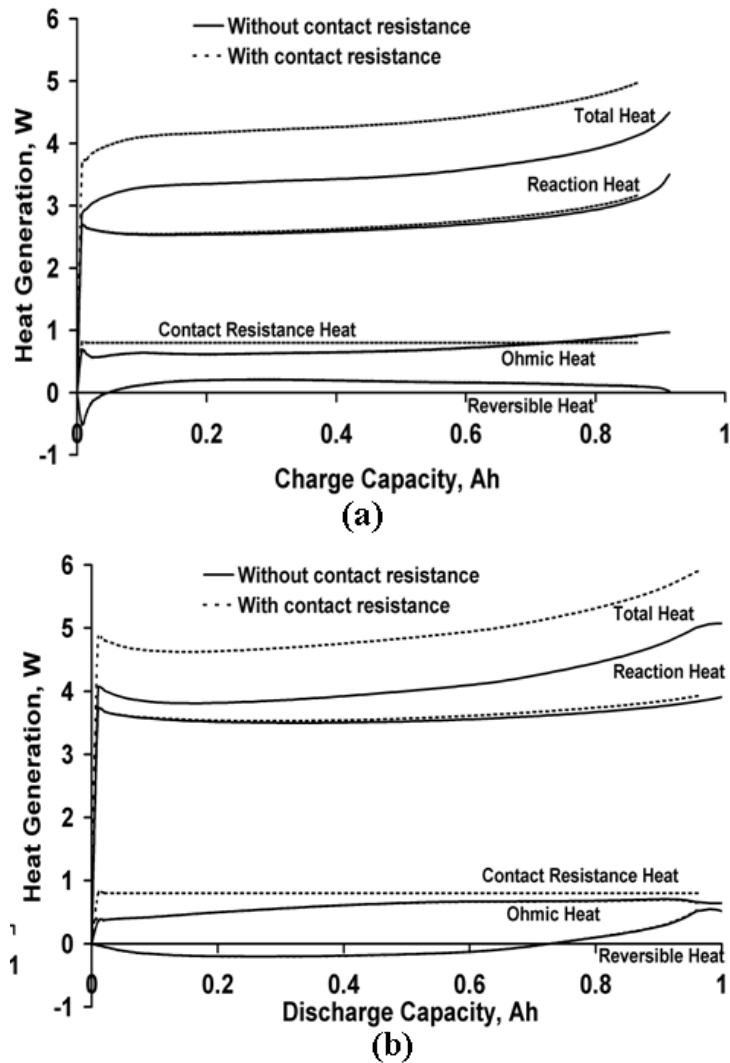
Figure 3.13 Heat generated for $5I_t$ with and without effect of contact resistance. (a) Charging. (b) Discharging.

As shown in Figure 3.13, total heat transfer during $5I_t$ charging and discharging for the cell with poor contact resistance is higher than the cell without contact resistance. The average rise in total heat generated in the cell during $5I_t$ charging or discharging with poor contact resistance is about 20% and mainly contributed by contact resistance heat. The effect of electric contact resistance is localized and concentrated at the terminals and further deteriorate the temperature uniformity of the cell. Figure 3.14 shows the contour plot of the cell temperature distribution at the end of charging and discharging.
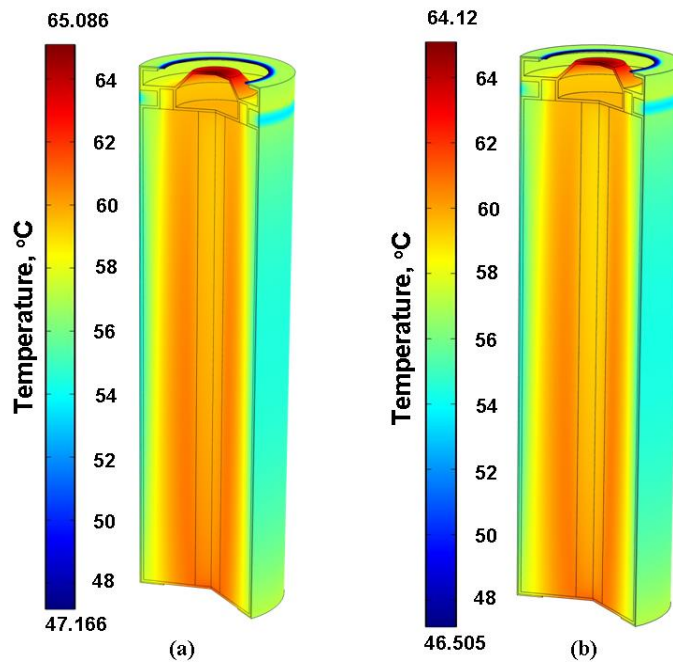
Figure 3.14 Contour of temperature distribution in the cell during $5I_t$ of (a) Charging. (b) Discharging.

There are hot spots at the top and bottom end of the cell. A large temperature gradient is found across the cell in the radial direction. The temperature distribution in the axial direction was uniform due to large thermal conductivity in this direction. So the main temperature variation is in the radial direction. The temperature difference across the radial direction was about 10 ^{o}C during the end of the charging or discharging.

The cell temperature is at the higher limit of the allowable temperature within the cell. The contact resistance effect decreased the temperature uniformity within the cell dramatically and further induced a performance decline due to unbalanced charging and discharging. Hence, this is a significant factor which should be accounted in the cell connector design and battery assembly. Therefore, rigid contact between the connectors and terminals is needed to reduce the power losses and improve the temperature uniformity.

3.5 Summary

An electrochemical-thermal model was developed to investigate the electrochemical and thermal behavior of the cell during charging and discharging. Good agreement between the simulation results and experiment was achieved. The heat generated in the cell was contributed by reaction heat, ohmic heat and reversible heat. Numerical simulation results showed that reaction heat was the major heat source during the charging and discharging process. The heat generation rate of the cell was positively correlated with the I_t-rates. In addition, imperfect contact between the terminals of the cell will cause development of large temperature gradients within the cell, affecting the cell capacity. The difference between maximum and minimum temperatures at the end of the charging/discharging process was about 10 ^{o}C, which was on the high side of the allowable temperature variation of Li-ion batteries. Therefore, a proper cooling system design and assembly of the battery and connectors is needed for EVs and HEVs with fast charging.

CHAPTER 4

EMPIRICAL MODELING

4.1 Introduction

Before the battery pack is installed into the EV, the battery pack needed to be evaluated under various driving cycle test. Experimental testing of the battery pack always required expensive facility such as high power programmable battery cycler and huge environment chamber to accommodate the battery pack. Although electrochemical models can predict the aging and thermal behavior of the Li-ion battery, the solution of the resulting coupled time-variant spatial partial differential equations takes too much time to solve. Hence, it is not practical to use detailed CFD simulations to investigate the performance of the battery pack on the driving cycle tests. Although there are some battery modeling works found in the open literature, most of the studies are focused on electrical behavior of the battery and do not make comparisons with experimental work. So there is a need to develop relatively simple mathematical models to predict the LFP cell temperatures. In view of the challenges in experimental testing and detailed modeling, the objective of this work is twofold. First, a modified Shepherd equation coupled with a lumped thermal model has been used to predict the cell voltage, heat generation, temperature rise of the cell during constant-current discharging and Simplified Federal Urban Driving Schedule (SFUDS) cycle for an 18650 and 38120 LFP cells and is validated with experiments; and second, to apply the validated single cell model to investigate the thermal response of the battery pack of a converted EV under Urban Dynamometer Driving Schedule (UDDS), Highway Fuel Economy Driving Schedule (HWFET) and US06 Supplemental

Federal Test Procedure (SFTP) driving cycles. The results are discussed in terms of the total heat generated during these driving cycles and the evolution of the battery pack temperature for a forced convection cooling system.

4.2 Mathematical model

4.2.1 Battery model

A battery model is needed to define its voltage in terms of current and state of charge (SOC). In this study, the modified Shepherd model is employed to represent the voltage dynamics of the LFP cell (Tremblay, 2007 and Tremblay 2009). A typical discharge curve of the Li-ion battery is shown in Figure 4.1 (Tremblay 2007 and Tremblay 2009).
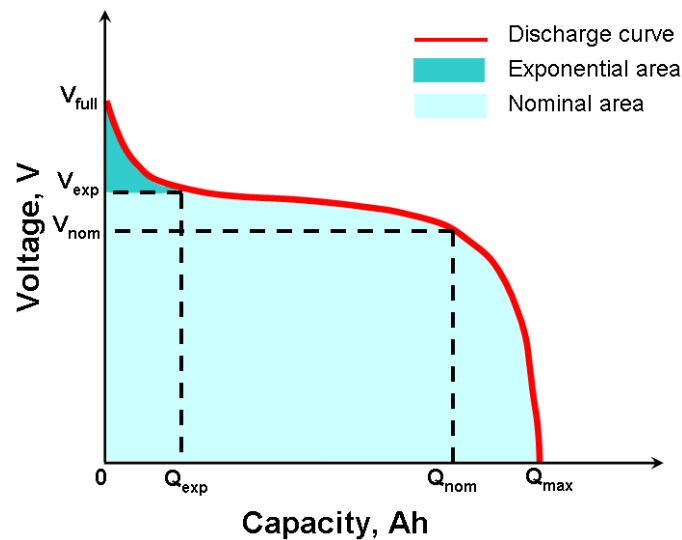
Figure 4.1 Typical discharge characteristic of Li-ion battery.

The discharge curve of the Li-ion battery can be divided into three sections. The first section represents the exponential potential drop of the cell during initial discharge. The second section represents the amount of charge that can be extracted from the cell before reaching the nominal voltage of the cell. The last section represents the total discharge of the cell, when the voltage of the cell drops rapidly to the cut off voltage. The modified Shepherd equation for charging and discharging is given by Equation 4-1 and Equation

4-2, respectively (Shepherd 1965, Tremblay 2007 and Tremblay 2009). It is assumed that the internal resistance of the cell is constant throughout the charging and discharging cycle and doesn't change with the I_t-rates. The temperature effect on the battery model behavior is neglected and the model parameters for discharging and charging are identical.

Charging (i*<0)

$$V_{batt} = E_0 - R \cdot i - K \frac{Q}{it - 0.1 \cdot Q} \cdot i^* - K \left(\frac{Q}{Q - it} \right) it + Aexp(-B \cdot it) \qquad (4\text{-}1)$$

Discharging (i*>0)

$$V_{batt} = E_0 - R \cdot i - K \frac{Q}{Q - it} \cdot i^* - K \left(\frac{Q}{Q - it} \right) it + Aexp(-B \cdot it) \qquad (4\text{-}2)$$

The voltage of the cell at a fully charged state is given by (Tremblay 2007 and Tremblay 2009).

$$V_{full} = E_0 - R \cdot i + A \qquad (4\text{-}3)$$

The voltage at the exponential section is given by (Tremblay 2007 and Tremblay 2009).

$$V_{exp} = E_0 - K \frac{Q}{Q - Q_{exp}} \cdot (Q_{exp} + i) - R \cdot i + Aexp\left(\frac{-3}{Q_{exp}} \cdot Q_{exp} \right) \qquad (4\text{-}4)$$

The voltage of the cell at the nominal zone is given by (Tremblay 2007 and Tremblay 2009).

$$V_{nom} = E_0 - K \frac{Q}{Q - Q_{nom}} \cdot (Q_{nom} + i) - R \cdot i + Aexp\left(\frac{-3}{Q_{exp}} \cdot Q_{nom} \right) \qquad (4\text{-}5)$$

4.2.2 Thermal model

It is assumed that Biot number for the battery is less than 0.1 and the resistance to conduction within the battery is much less than the resistance to convection outside the battery. Therefore, the temperature inside the cell can

be assumed to be fairly uniform (Rao and Newman, 1997). Besides, it is also assumed that the physical properties of the cell are uniform and are not affected significantly by temperature. The battery model is coupled with a lumped thermal model to determine the heat generation and the average surface temperature of the cell. A general energy balance equation used to model the battery system is defined in Equation 4-6 where an effectively "black" surrounding was assumed (Chen and Evans, 1994).

$$\rho C_p \frac{dT_{surf}}{dt} = Q_{gen} - hA_s \left(T_{surf} - T_\infty \right) - E\sigma_{sb} \left(T_{surf}^4 - T_\infty^4 \right) \tag{4-6}$$

The heat generation in the Li-ion battery consists of ohmic heat, irreversible heat and reversible heat (Fang et al., 2010). Reaction heat or irreversible heat generation is due to the transfer of electrons to or from the electrode during the electrochemical reaction. Reversible heat generation is due to the entropy changes at cathode and anode. Ohmic heat generation is due to the ohmic resistance of the solid active materials and electrolyte. The entropy change in the electrodes is related to the change of their equilibrium potential with temperature (*dU/dT)* and this varies with SOC. Here, this relation is adopted from the work of Forgez et al. (Forgez et al., 2010). Heat generation due to contact resistance is also added to the overall heat generation within the cell given by (Thomas and Newman, 2003).

$$Q_{gen} = i \left(E_0 - V_{batt} + T \frac{dU}{dT} \right) + i^2 R_c \tag{4-7}$$

4.2.3 Battery pack thermal model

Different types of cooling systems will influence the performance and cost of the battery pack thermal management system. The heat transfer medium could be air, liquid, heat pipes and phase change material (PCM), or a

combination of them. The architecture of the cooling strategy includes series flow, parallel flow and a combination of series and parallel flow. The selection of the cooling system depends on the constraints of the vehicle, installation costs and the external environment. In the extreme environment and working under heavy duty cycles, an active cooling system is preferred to offer more effective thermal management. In this study, parallel air flow strategy is adopted to investigate the thermal response of the battery pack with a certain number of modules. Each module will have the same inlet air temperature that will result in a more uniform pack temperature (Pesaran, 2002) and hence it is sufficient to study a single module in the entire pack. A schematic diagram of the battery pack and the air flow is shown in Figure 4.2 (Pesaran, 2002). The heat transfer coefficient for natural convection and forced convection is given in Equation 4-8 (Pesaran 2002 and Incropera et al., 2007).
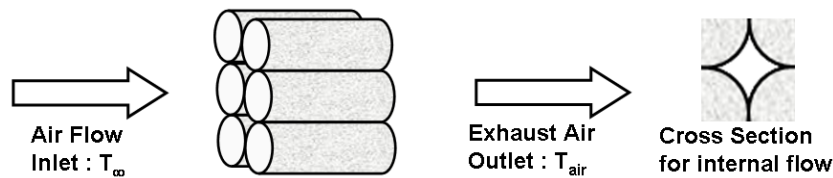
Figure 4.2 Schematic of active air cooling system of an EV battery pack.

$$h = \begin{cases} h_{forced} = 30\left(\dfrac{\dot{m}/\rho_{air}A_{mf}}{5}\right)^{0.8} & T_{module} > 35\ ^{o}C \\ h_{natural} = 4 & T_{module} \le 35\ ^{o}C \end{cases} \qquad (4\text{-}8)$$

4.3 Numerical and experimental procedure

Commercial 1.3Ah 18650 cells and 8.0 Ah 38120 cells with graphite anode coated on the copper current collector, LFP cathode coated on the aluminum current collector, filled with an electrolyte of $LiPF_6$ in EC:DEC 1:1 and Polyvinylidene Fluoride (PVDF) separator were used in experiments. The cell used in this study is shown in Figure 4.3.

Figure 4.3 18650 LFP cell (left). 38120 LFP cell (right).

The charging and discharging of the battery was conducted using a battery cycler (Maccor Instrument 4000). According to the procedure due to Tremblay et al. (Tremblay 2007 and Tremblay 2009), the cell is discharged at 0.2 I_t and the parameters E_0, K, A and B are extracted from the discharge curve. The cut off voltage for constant current discharging was 2.3 V. Charging was done in two modes: constant current charging until 4.2 V followed by constant voltage charging until the current dropped to 0.1 A. Before discharging, the cell is charged at 0.1 I_t followed by one hour of rest. Slow rate of charging is necessary to ensure that the chemical process within the cell occurs at the similar rate to the transfer of electric energy. Internal resistance (R) of the battery is measured using an impedance analyzer (Solartron analytical 1400). The values of the extracted parameters and other dimensions for 18650 cell and 38120 cell used in the simulation are provided in Table 4.1 respectively.

Table 4.1 LFP cells parameters.

Parameters	Cell	
	18650	38120
Nominal Voltage, V	3.2	3.2
Nominal Capacity, mAh	1300	8000
Cathode material	LiFePO$_4$	LiFePO$_4$
Anode material	Graphite	Graphite
Terminal connector	Spring loaded	Screw
Diameter, m	0.018	0.038
Length, m	0.065	0.0146
Weight, kg	0.030	0.355
Specific heat, Jkg^{-1}K^{-1}	900	998
E$_0$, V	3.21	3.27
R, Ω	0.03	0.0034
K, Ω or V(Ah)$^{-1}$	0.0119	0.00216
A, V	0.2711	0.0854
B, (Ah)$^{-1}$	152.130	23.097
Reference temperature, T_{ref} (K)	298.15	298.15
Emissivity of heat shrink wrapping, ε (Mikron, 2012)	0.95	0.95
Stefan-Boltzmann constant, σ (W m^{-2} K^4)	5.67 x 10^{-8}	5.67 x 10^{-8}
Heat Transfer coefficient for constant current discharging, Wm^{-2}K^{-1} (estimated)	8	8

The surface temperature of the battery was measured using twelve thermocouples (T-type) attached to different locations on the cells. Three thermocouples were attached in the axial direction and four sides of the battery surface as shown in Figure 4.4.
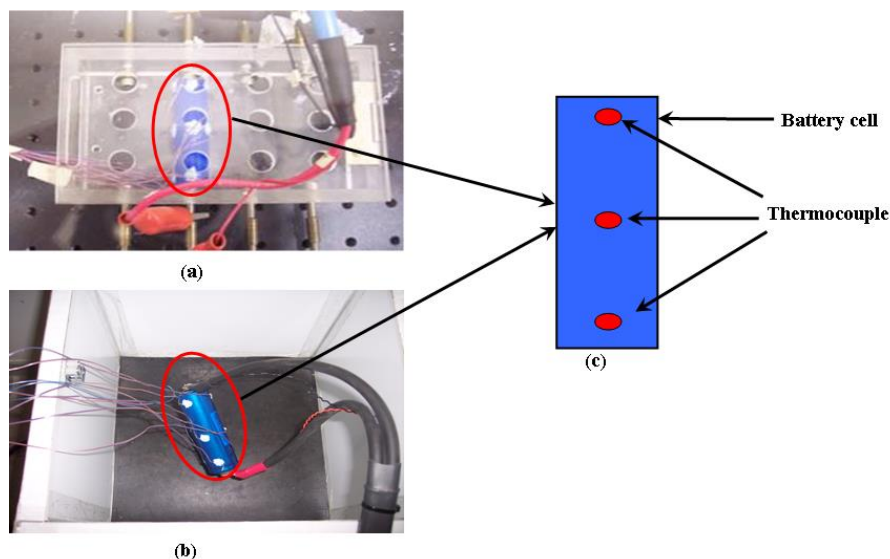
Figure 4.4 Location of thermocouples attachment to the battery surface.
a) 18650 cell. b) 38120 cell.

Measurement of battery surface temperature during charging and discharging at different I_t-rates was done at a room temperature of 25 ^{o}C under natural convection. All the tests were repeated three times and the average value was taken. Temperature readings were recorded using the HP 34970A data acquisition system. The specific heat capacity of the cell was measured using adiabatic accelerating rate calorimeter (THT ARC). The measurement of the specific heat capacity of the cells is discussed in section 4.4. Vehicle specific parameters used for driving cycle simulations are tabulated in Table 4.2.

Table 4.2 Vehicle and cooling system specific parameters.

Parameters	Value
Vehicle mass, kg	1828
Frontal area, m^2	3.238
Coefficient of drag, Cd	0.35
Electric motor	75 kW, 200 Nm max
Battery pack	19.2 kWh
Number of 18650 cell per module	180
Number of 38120 cell per module	28
Number of modules	28
A_{mf} per module, m^2	0.00417
A_{sm} per module, m^2	0.662
Mass flow rate of cooling air for battery pack, cfm	140, 280, 700
Surrounding temperature, ^{o}C	30

The battery and thermal model equations are solved simultaneously using Matlab-Simulink 2011b. Parameters extracted are entered into the battery model in Simulink to investigate the electrical and thermal response of the cell during constant current discharging and SFUDS. Outputs of the simulation model are voltage, current, heat generation and surface temperature of the cell. Heat is dissipated from the cell by natural convection and radiation. The model was validated using constant current discharging experiments ranging from 1 I_t (1.3 A) to 3 I_t (3.9 A) and SFUDS dynamic power profile. Under SFUDS test, the cell is subjected to continuous charging and discharging until

its SOC reaches 10%. This validated model was then used to study the thermal response of the battery pack for a converted Hyundai Trajet EV under UDDS, HWFET and US06 driving cycles that are illustrated in Figure 4.5.
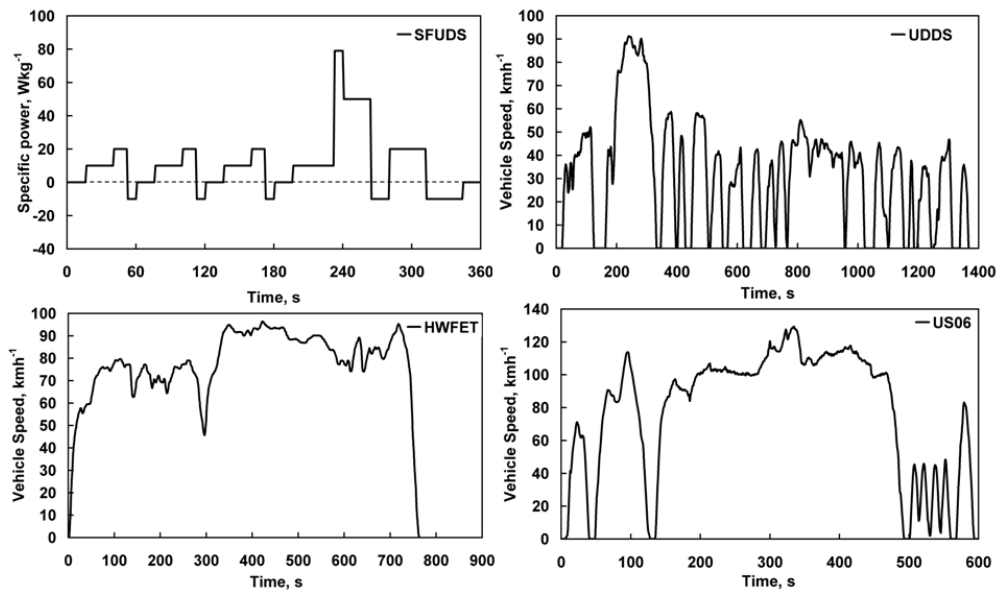
Figure 4.5 Testing cycle for single cell and EV battery pack.

4.4 Specific heat measurement

The heat capacity measurement of the LFP cells is carried out using a THT Accelerating Rate Calorimeter (ARC). For the cylindrical cell, three cells are used to carry out the specific heat measurement.

4.4.1 Specific heat capacity of 18650 cell

The initial and end temperatures are 23 ^{o}C and 65 ^{o}C, respectively. Specified and achieved temperature rates are 0.2 Kmin^{-1} and 0.24 Kmin^{-1}. The results of the specific heat measurement of 18650 cells are shown in Table 4.3 and Equation 4-9.

$$C_P = -0.0000489T^2 + 0.00493512T + 0.806244 \qquad (4\text{-}9)$$

Table 4.3 Specific heat capacity at different temperature.

Temperature, ^{o}C	Specific heat capacity, Jg^{-1}K^{-1}
26	0.901
45	0.929
62	0.922

4.4.2 Specific heat capacity of 38120 cell

The initial temperature and end temperature are 24 $^{\circ}$C and 65 $^{\circ}$C respectively. Specified and achieved temperature rates are 0.2 K min^{-1} and 0.16 Kmin^{-1}. The results of the specific heat measurement of 38120 cells are shown in Table 4.4 and Equation 4-10.

$$C_p = 0.00003351T^2 - 0.0016737T + 1.01811 \qquad (4\text{-}10)$$

Table 4.4 Specific heat capacity at different temperature.

Temperature, $^{\circ}$C	Specific heat capacity, Jg^{-1}K^{-1}
30	0.998
48	1.015
65	1.051

As shown in Table 4.3, the C_p of the 18650 cell is only increased by 2.3% when temperature increased from 26 $^{\circ}$C to 62 $^{\circ}$C. On the other hand, the C_p for the 38120 cell increased by 5.31% when temperature rose from 30 $^{\circ}$C to 65 $^{\circ}$C as shown in Table 4.4. Since the variation of the C_p is less than 10% regardless the cell size, the C_p for LFP cells can be treated as constant.

4.5 Results and discussion

4.5.1 Validation of the cell potential for 18650 cell

Discharge characteristics of the cell predicted by the battery model and experimental data are provided in Figure 4.6(a). The averaged relative error of the simulated and measured voltage is about 0.9%. This is followed by comparing the predicted results of the model with the experimental discharge curves at 1, 2, and 3 I_t-rates as shown in Figure 4.6(b).
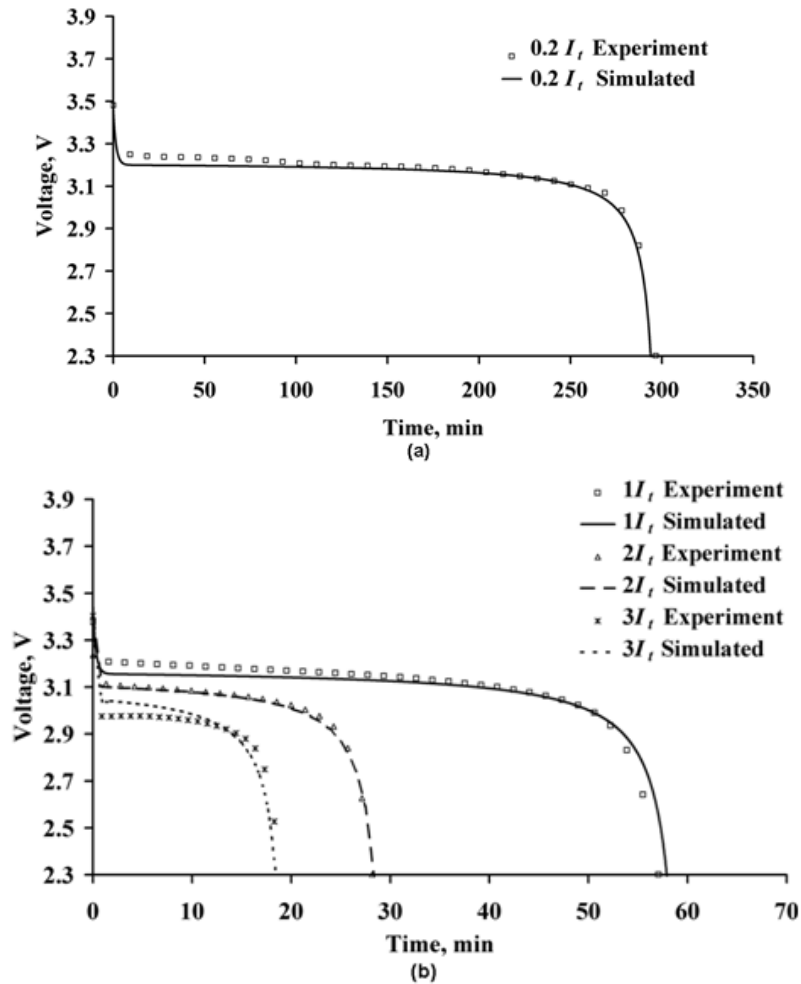
Figure 4.6 (a) Model calibration: Cell voltage during discharge at 0.2 I_t to extract the model parameters. (b) Validation of battery model: Cell voltage during discharge at 1, 2, and 3 I_t-rates.

The model predictions match well with the experiments with an averaged relative error of 1.2%, 0.8% and 2.1%, respectively for the various discharge rates. At 3 I_t of constant current discharging, the maximum capacity of the cell was reduced by 8% less than the capacity at 0.2 I_t (1.3 Ah). The reduction in the cell capacity at high I_t-rates is given by Peukert equation (equation 3-37). The discharge capacity of the cell reduces as the discharge current increases.

4.5.2 Validation of the cell potential for 38120 cell

The experimental and simulated transient voltages of the 38120 battery model using 0.2 I_t of discharge curve are shown in Figure 4.7(a) while the prediction error is given in Figure 4.7(b).
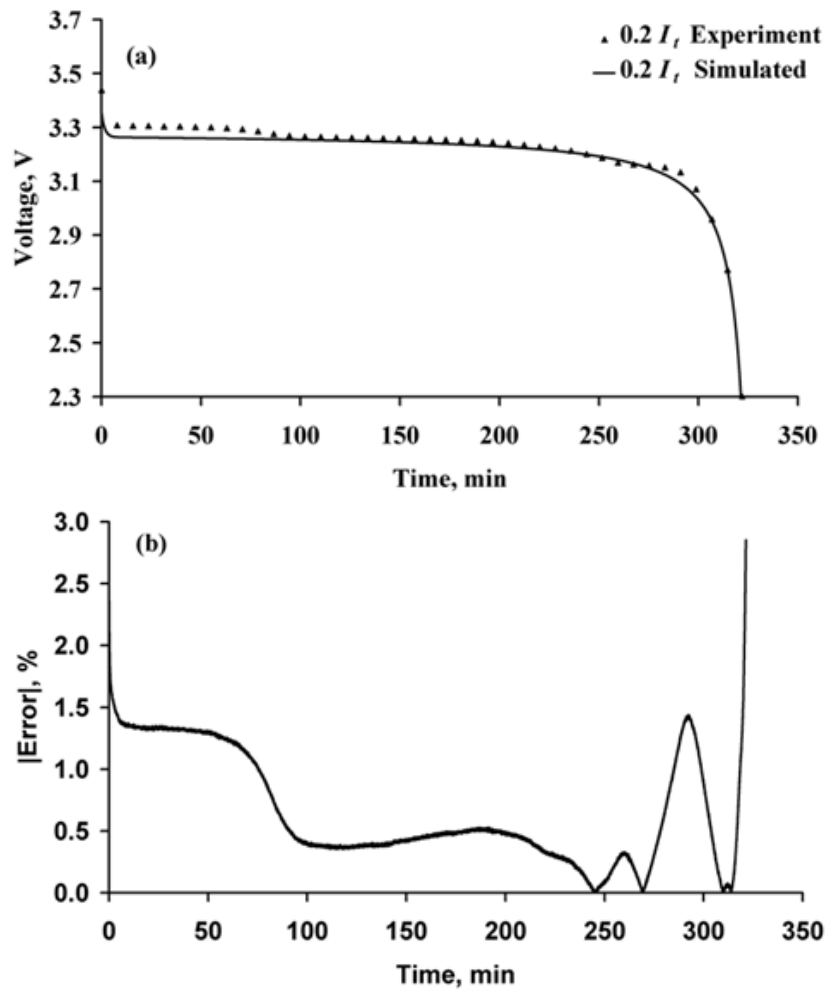
Figure 4.7 (a). 38120 cell voltage during discharge at 0.2 I_t to extract the model parameters.(b). Error of voltage prediction.

The highest error of the simulation results as compared to experimental data is about -0.06 V (1.82%) during initial discharge, while at the end of discharge it is less than 3%. In Figure 4.8 the measured and simulated transient voltage for the 38120 cell during 1, 2 and 3 I_t-rates of discharge is shown.
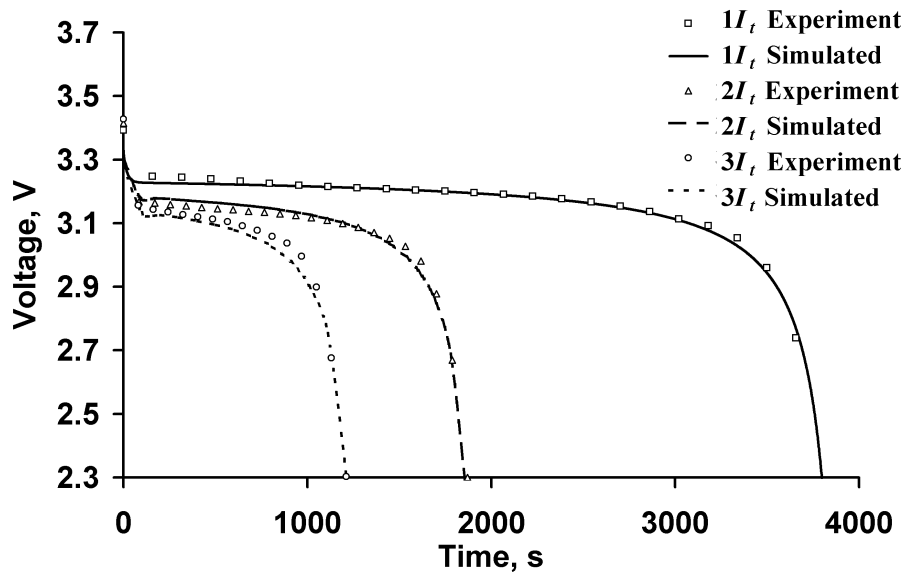
Figure 4.8 Comparison of simulated and experimental data at 1, 2 and 3 I_t-rates.

Comparisons of simulated and measured voltage show that the battery model provides a good estimation of the electrical behavior of the cell at various I_t-rates. Averaged relative error for 1, 2, 3 I_t-rates are 0.3%, 0.5% and 0.9% respectively. Discharging at high I_t-rates could cause a rise in cell temperature. In addition, the internal resistance of the cell is dependent on temperature, thus the error of prediction at 3 I_t is slightly larger as compared to 1 and 2 I_t-rates. Although the cell nominal rating is 8 Ah, the final capacity resulting from 1 I_t of discharge could reach 8.6 Ah. The final capacity at the end of 3 I_t of discharge is about 8.4 Ah which is about 3.5% less than the capacity at 0.2 I_t (8.7 Ah). On the other hand, at 3 I_t discharge of the 18650 cell suffered more capacity loss of about 8% compared to its capacity at 0.2 I_t (Kim et al., 2012).

4.5.3 Evolution of the 18650 cell temperature and heat generation

The average measured and simulated temperature rise of the cell surface at different I_t-rates of discharging is shown in Figure 4.9.

103
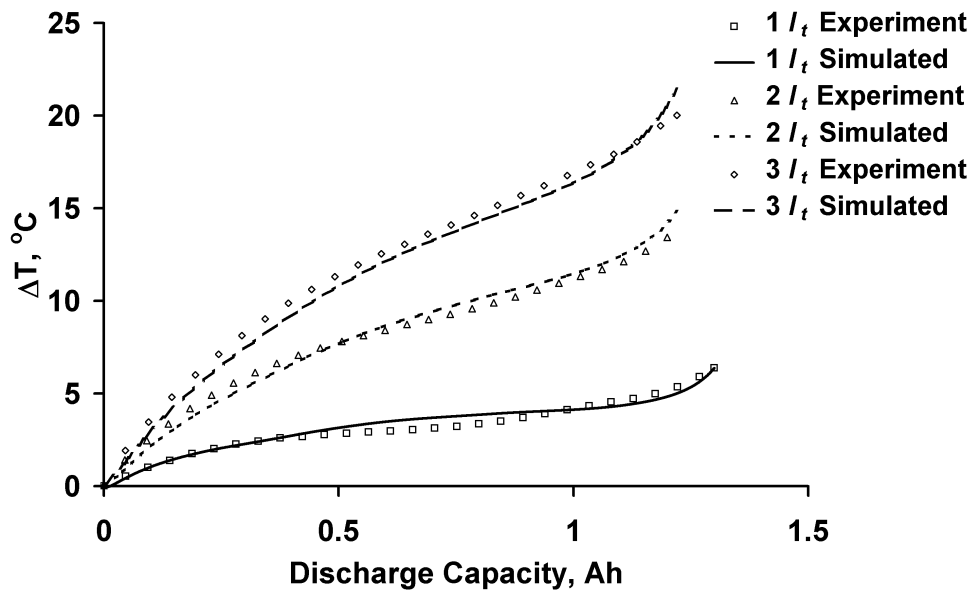
Figure 4.9 Temperature rise of the battery during discharge at various I_t-rates.

The temperature of the cell has a positive relationship with the I_t-rates. The sharp rise of the temperature towards the end of discharge is probably due to the polarization effect of the cell. The simulated results agree well with the experimental results. The averaged relative error between the simulation results and the experiments at 1, 2, and 3 I_t-rates of discharging are 8.33%, 7.66% and 7.12%, respectively. The measured average temperature rise of the cell at the end of discharging at 1, 2, and 3 I_t-rates is 6.4 ^{o}C, 13.9 ^{o}C and 20.0 ^{o}C respectively. At low I_t-rates of discharging, heat generated from the cell can be effectively dissipated by natural convection and only a temperature rise of less than 10 ^{o}C is observed. On the other hand, a large amount of heat is generated at 3 I_t and natural convection is not sufficient to dissipate it and keep the battery within the recommended operating temperature range. The total heat generation predicted by modeling at different I_t-rates during discharging is shown in Figure 4.10. A large amount of heat is generated towards the end of the discharge. The maximum amount of heat generated for 1, 2, and 3 I_t-rates, is 0.59 W, 1.47 W and 3.14 W per cell, respectively.
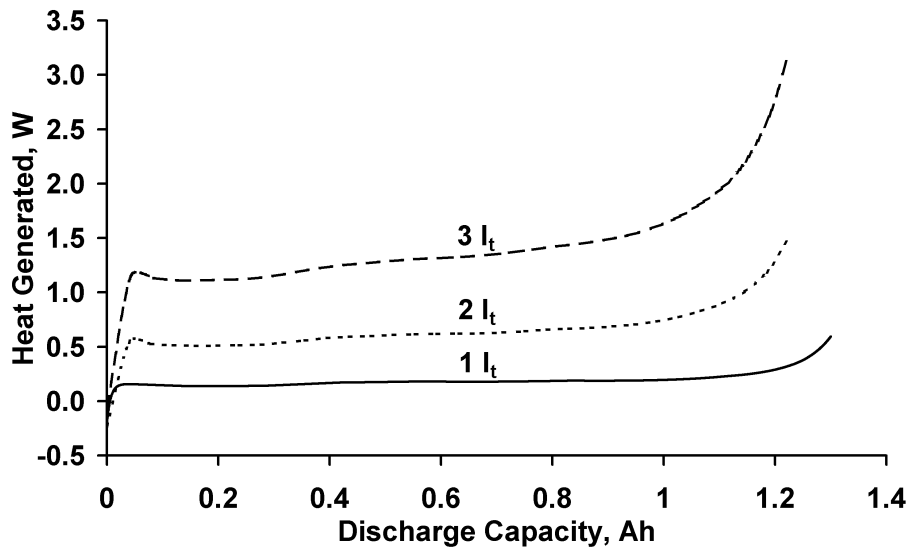
Figure 4.10 Heat generation for different I_t-rates of discharging predicted by the model.

4.5.4 Evolution of the 38120 cell temperature and heat generation

Simulated and measured average skin temperature of the 38120 cell at different I_t-rates of discharging under natural convection (5 $Wm^{-2}K^{-1}$) is shown in Figure 4.11.
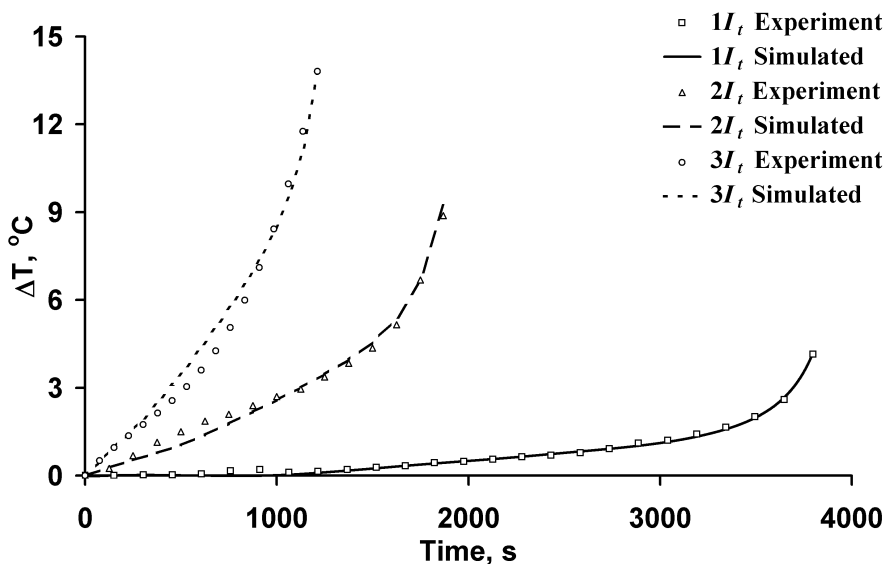
Figure 4.11 Temperature rise of the battery during discharge at 1, 2 and 3 I_t-rates.

The results show that at high I_t-rates of discharging, temperature rise of the cell is significant. The skin temperature of the cell could rise to 13.8^{o}C at 3 I_t-rate and the cell exhausted its energy in 20 min. Natural convection is no

105

longer sufficient to keep the cell temperature within safe operating limits. Therefore, a battery thermal management system is required in this situation. The averaged difference between the experimental and simulated temperature rises for 1, 2 and 3 I_t-rates of discharging are 9.8%, 9.2% and 9.8%, respectively. At 3 I_t of discharge, the skin temperature of the 38120 cell is about 6°C less than that for the 18650 cell at a similar rate of discharge. Heat exchange surface area per unit jelly roll volume of the cell is a critical factor in the rate of cooling from the cell to the environment (Chen et al., 2006). The heat transfer area per unit volume of the 18650 and 38120 cells are 222.22 m^{-1} and 105 m^{-1}, respectively. As the ratio of surface area to volume decreases, the heat transfer ability of the cell was reduced and the internal temperature of the cell is increased (Kim et al., 2007). Although the skin temperature of the 38120 cell is lower than that of the 18650 cell, the temperature inside the cell is higher. Even though, the smaller cell has a higher skin temperature at a similar I_t-rate of charging and discharging, this is still lower than the big cell. Sometimes, this will give false information to the user that a large cell performs better than a smaller cell in the thermal aspect.

Estimated total heat generation rate in the 38120 battery is depicted in Figure 4.12.
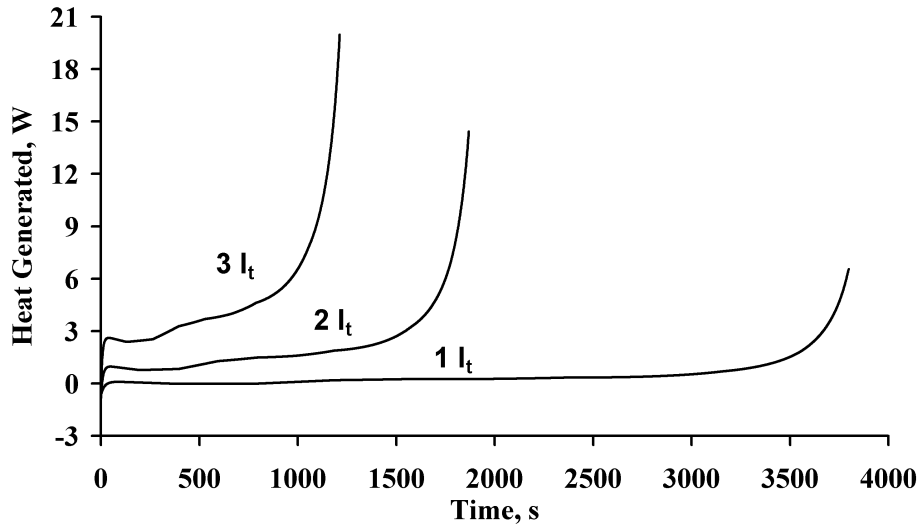
Figure 4.12 Heat generated of 38120 cell during discharge at 1, 2 and 3 I_t-rates.

6.5 W, 14 W and 20 W of heat per cell were generated towards the end of 1-3 I_t-rate of discharge, respectively. Heat generated from the battery is also positively correlated to the size and capacity of the cell. Heat generated from the 18650 cell is only 9% of that for the 38120 cell at 1 I_t of discharge, while the heat generated at 3 I_t is about 15% of 38120 cell in a similar I_t-rate of discharge.

4.5.5 Internal temperature of the 18650 and 38120 cells

Temperature distribution of 38120 and 18650 cells under different cooling conditions at the end of 3 I_t of discharge is provided in Figure 4.13.

107
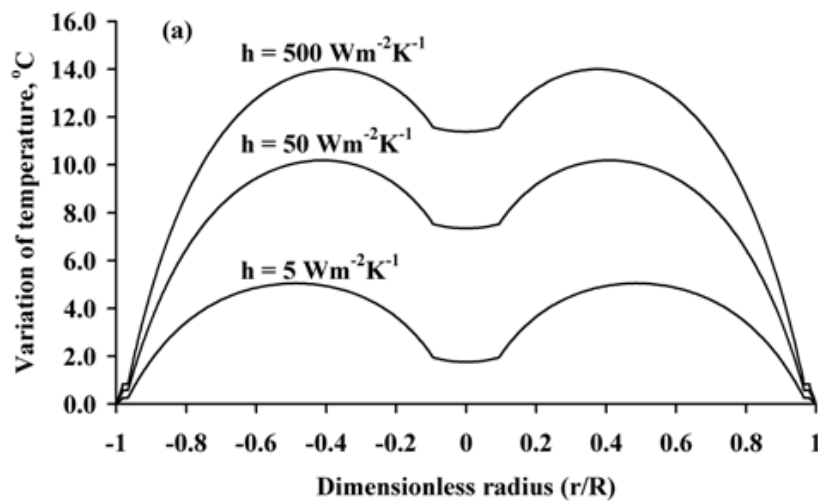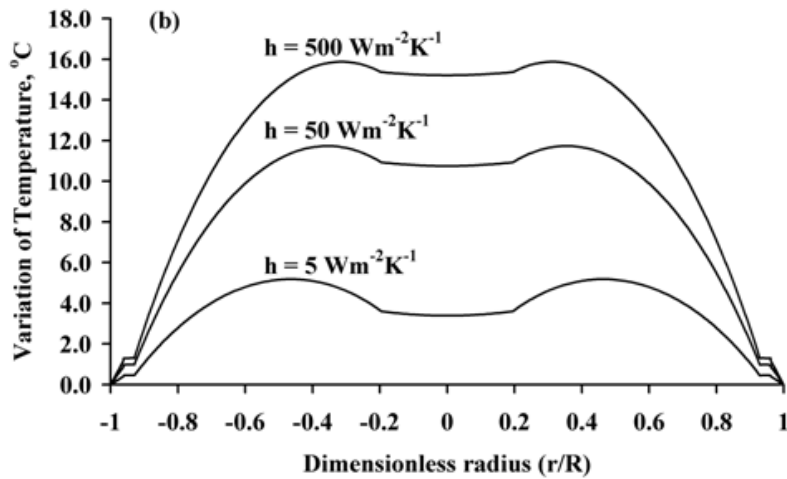
Figure 4.13 Predicted variation of internal temperature of the cell. (a) 38120 cell. (b) 18650 cell at 3 I_t-rates.

Due to the anisotropic nature of layered active material inside the battery, the temperature distribution in the axial direction of the cell is fairly uniform (Chen et al., 2006) and a temperature gradient is expected only in the radial direction of the cell. Heat shrink film which is used for insulation of the metal casing will prevent the heat generated in the cell from being effectively dissipated to the environment. Therefore, a temperature jump was found between the insulator and metal casing of the cell as shown in the initial and end section as in Figure 4.13. The maximum temperature region of the cell is located in the active material region near the hollow core. The hollow core situated at the center of the cell is a product of the cell manufacturing process. During cell sealing process, an electrolyte will be injected into the active material and the hollow core will be filled with the electrolyte as well. An attempt to measure the internal temperature of the cell at the hollow core region may not produce any useful information on the maximum temperature of the cell (Forgez et al., 2010 and Chen et al., 2006). As shown in Figure 4.13, the temperature in the hollow core region is lower than the active material near the hollow core region. 5 ^{o}C of temperature difference was developed in the

38120 cell during 3 I_t of constant current discharge under natural convection as shown in Figure 4.13 (a). The maximum internal temperature of the cell may reach 44 ^{o}C for 3 I_t of constant current discharge. On the other hand, the temperature difference in the 18650 cell is also 5 ^{o}C under natural convection (5 Wm^{-2}K^{-1}) and the maximum temperature in the active material region is about 50 ^{o}C. The temperature difference in the cell will increase when strong forced convection is used to cool. The heat transfer coefficient is increased to 500 Wm^{-2}K^{-1}, the temperature gradient for the 38120 and 18650 cells rise to 14 ^{o}C and 16 ^{o}C, respectively as shown in Figure 4.13. Opposite to excellent thermal conductivity of the metal casing, the active material region is a poor thermal conductor. Although the current collectors of the cell are made of copper and aluminum, but porous electrodes and separators are poor conductors. The main function of a separator is to insulate the anode and the cathode layers while providing an effective transport medium for Li-ion. Poor thermal properties of the separator will prevent the heat from being effectively dissipated to the outer environment and it further proves that heat flux inside the large cell is not always outward (Chen et al., 2006). Therefore, the safety of the battery cannot be simply determined by measuring the skin temperature of the cell. Using strong forced convection to cool the cell is not encouraged as this will introduce undesirable temperature gradient in the cell and accelerate the thermal aging.

In the open literature, there are various types of degradation models used to investigate the cycle life of the battery (Wang et al., 2011, Han et al., 2014 and Omar et al., 2014). In the current study, the thermal aging model proposed

by J. Wang et al is adopted and the thermal aging of the LiFePO$_4$ cell can be represented by the Arrhenius equation (Wang et al., 2011):

$$Q_{loss} = 30330\,exp\left(\frac{-31500}{8.314 \cdot T}\right)A_h^{0.552} \qquad (4\text{-}9)$$

The capacity loss of the cell at 30 ^{o}C, 40 ^{o}C, 50 ^{o}C and 60 ^{o}C for a total of 1000Ah throughput is 5.12%, 7.65%, 11.12% and 15.81%, respectively. This further indicates that 10 ^{o}C of temperature difference will lead to additional 3% to 5% reduction in the cycle life of the cell. Compared to strong convection cooling of the battery outer surface, improving the thermal properties of the separator and internal structure of the cell or filling the hollow core with heat absorbing medium is more effective in improving the rate of cell cooling.

4.5.6 Dynamic behavior of the 18650 cell under SFUDS

In the SFUDS testing cycle, the battery is operated under a repeated 360s cycle of charging and discharging at certain specific power as shown in Figure 4.5. Variation of the current and voltage during the first cycle of the SFUDS profile is shown in Figures 4.14(a) and Figure 4.14(b) respectively.

(a)

Figure 4.14 (a) Current, (b) Voltage during the first 360 s cycle of the SFUDS profile.

Maximum current for discharging is about 0.97 A corresponding to a specific power of 79 Wkg^{-1}. The averaged relative error in the experimental data and simulated results of current is 0.56%. The over potential of the cell during the first cycle is high ($\approx$ 3.3 V) and the energy being discharged from the cell is about 1%. The averaged relative error between the experimental and simulated values of over potential is found to be 0.18%.

The thermal response of the battery is studied for more numbers of repeated cycles until it reaches the cut-off voltage and the predicted average heat generation data is shown in Figure 4.15.
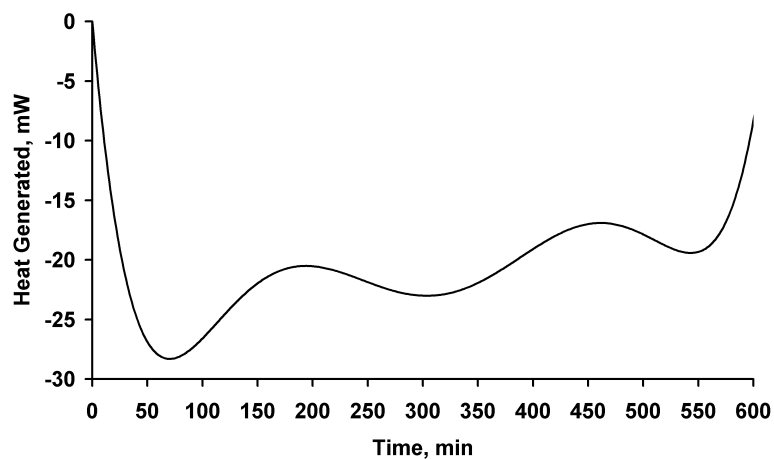
Figure 4.15 Average heat generation of the cell during 600 min of the SFUDS cycle predicted by the model.

111

The average heat generation rate of the cell during 600 min of the SFUDS cycle is relatively small as compared to the constant current discharging and can be neglected. The average heat generated from the first cycle of SFUDS is about -0.46 mJ. Endothermic heat generation is observed during the initial 75 min of the cycle and heat generation rate is gradually reduced as the dynamic charging and discharging process proceeds. Towards the end of the SFUDS cycle, heat generated from the cell contributes to the increase of the overall cell temperature.

The comparison of experimental data and model predictions for the voltage and temperature profile of the cell for 600 min of the SFUDS cycle is shown in Figures 4.16(a) and 4.16(b) respectively.

(a)
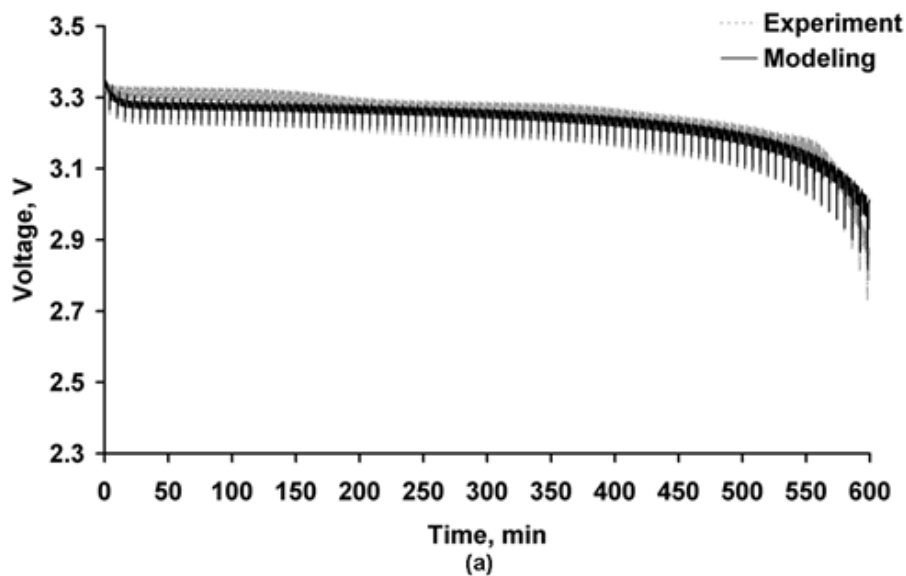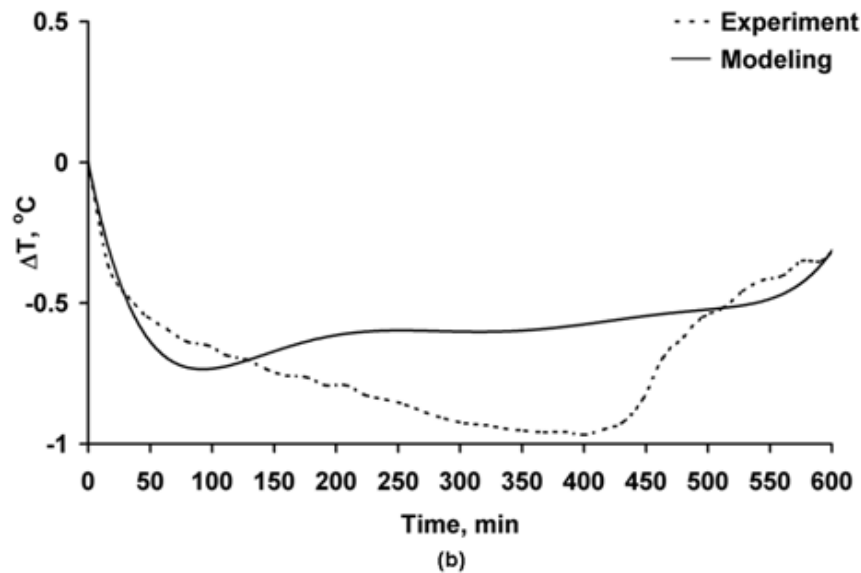
Figure 4.16 Comparison of measured and simulated SFUDS profile of a Li-ion cell. (a) Voltage, (b) Temperature.

In general, the voltage of the cell decreases with the number of cycles and oscillates in phase. As shown in Figure 4.16(a), there is only a small difference between the measured and simulated cell voltages. A substantial amount of heat is generated towards the end of the SFUDS cycle. Therefore, the temperature of the cell slowly increases at the end of the cycle as shown in Figure 4.16(b). The heat generated in the cell can be effectively dissipated by natural convection and the cell is kept within safe operating limits. The deviation between the experimental and simulation results is probably due to the inaccuracy of the thermocouple and the battery thermal model. The accuracy of the simulation results can be improved further by including the reversible heat term in the battery model. This validated model can now be extended to a battery pack and employed to study the thermal response of it under various driving cycles as discussed in the next section.

4.5.7 Dynamic behavior of the 38120 cell under SFUDS

Validation of battery model dynamic behavior required comparison with an independent set of series charging and discharging test. SFUDS, featuring

113

360s of repeating charging and discharging at certain specific power was used for this study. The voltage and current response plots of the simulated results and the experimental measurements on the 38120 cell in the first 360s are depicted in Figure 4.17.
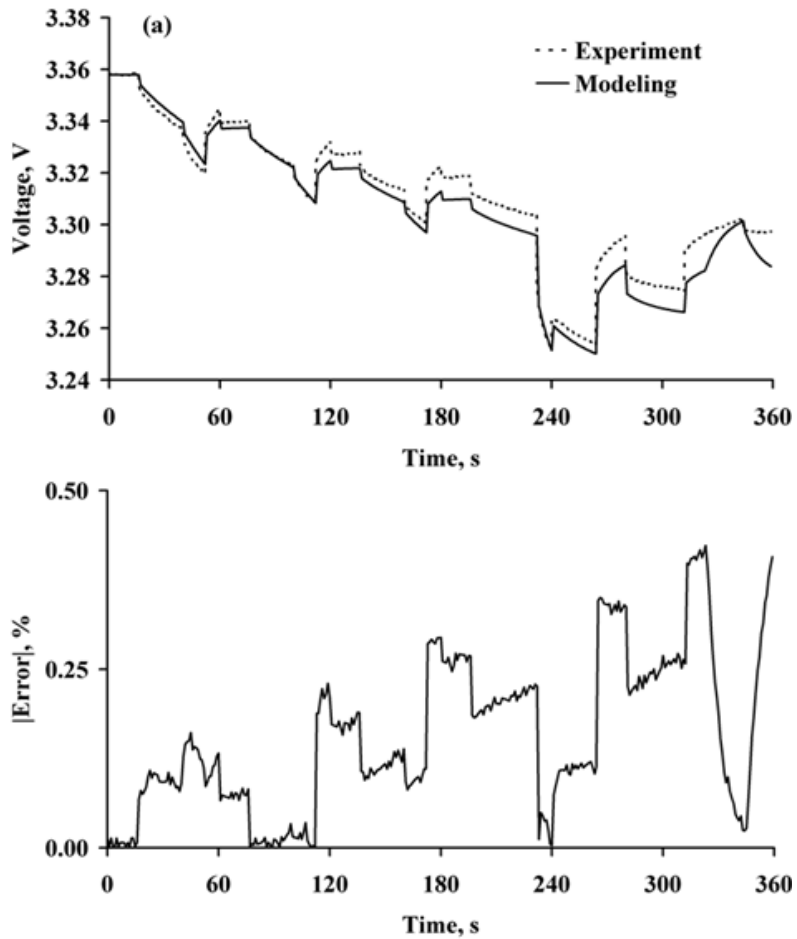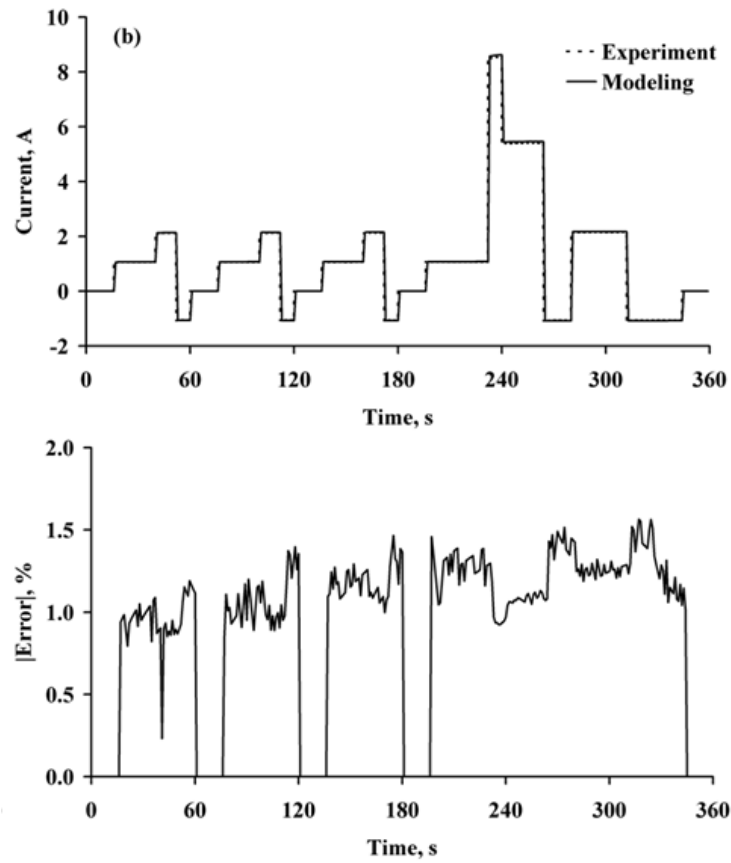
Figure 4.17 Validation of battery model using SFUDS (a) Voltage , (b) current.

The error graph shows that the discrepancy between the model and experiment for the voltage is below 0.5% and below 2% for the current. Figure 4.18 shows both experimental and simulated voltage and temperature profiles for the 38120 cell for 450 min of the SFUDS cycle.
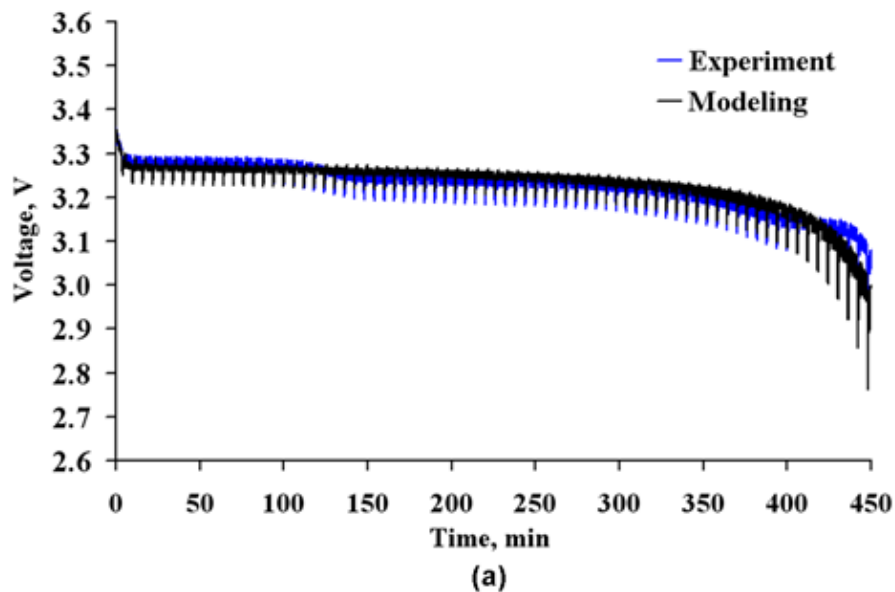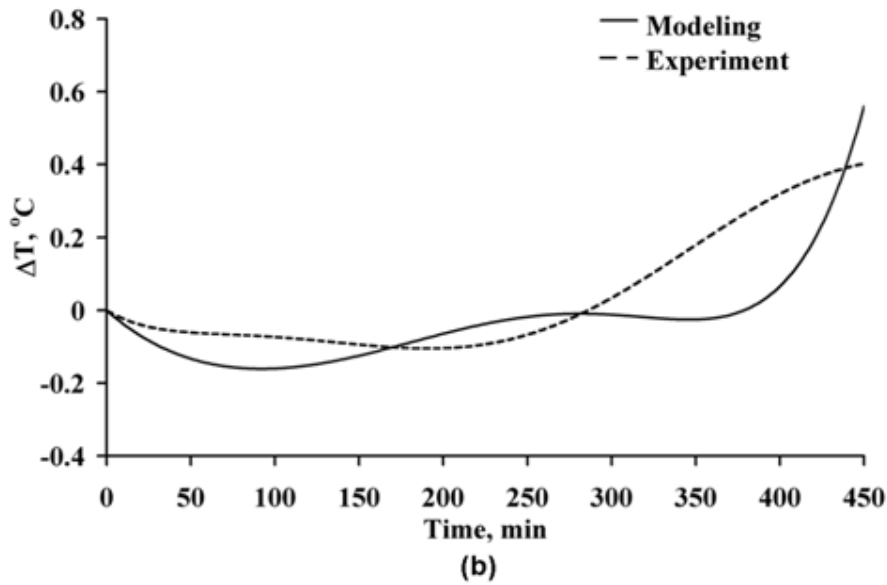
Figure 4.18 Comparison of experiment and modeling results for 450 min of SFUDS profile. (a) Voltage, (b) Temperature.

The voltage drops to the lowest point during 79 W kg^{-1} specific power discharge within each sub-cycle of 360s. The voltage of the cell decreases with the number of sub-cycles and oscillates in phase with the power pulses. The voltage of the cell gradually decreases as the SOC of the cell ceases to cut off voltage to maintain the power requirement of the cycles. Good agreement is observed between the simulated and experimental results. The total heat generated for 450 min of a SFUDS test on the 38120 cell is about 106 J which can be effectively dissipated by natural convection and the overall change of the cell skin temperature is within 1 ^{o}C. Endothermic heat generation is observed during the initial 280 min of the test. Then, the heat generation rate gradually increased and became exothermic as the charging and discharging process continued, contributing to the rise of the overall cell temperature. The deviation of experimental and simulation results is probably due to accuracy of the thermocouple and also battery thermal model. The accuracy of the simulation results can be improved further by including the reversible heat term in the battery model. Therefore, the battery model is crucial to provide an

insight of battery state during testing in an economic and nondestructive way without over-charging or over-discharging of the cell.

4.5.8 Thermal responses of the 18650 cell battery pack

The thermal response of the battery pack designed for the converted EV under different driving cycles is provided in Figures 4.19 to Figure 4.21.
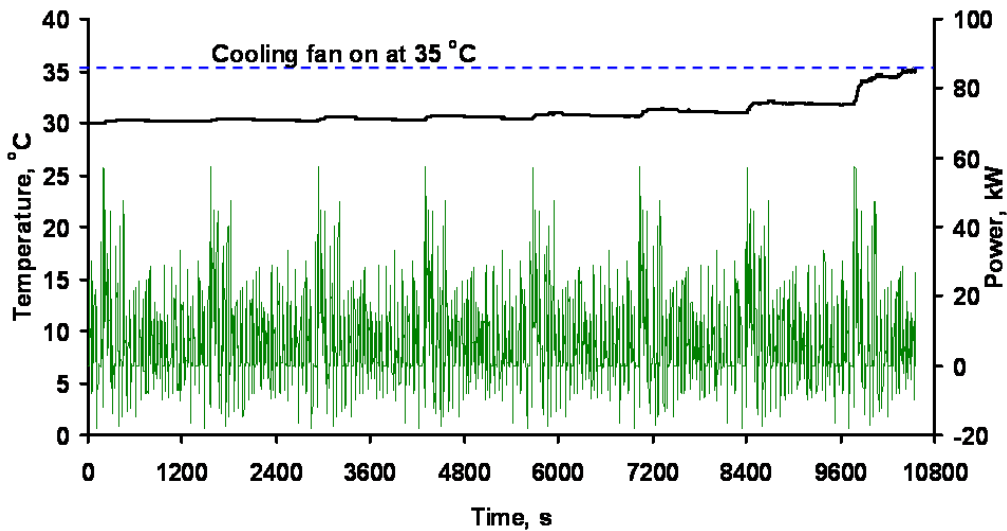
Figure 4.19 Thermal response of battery pack to UDDS cycle at 30 °C.
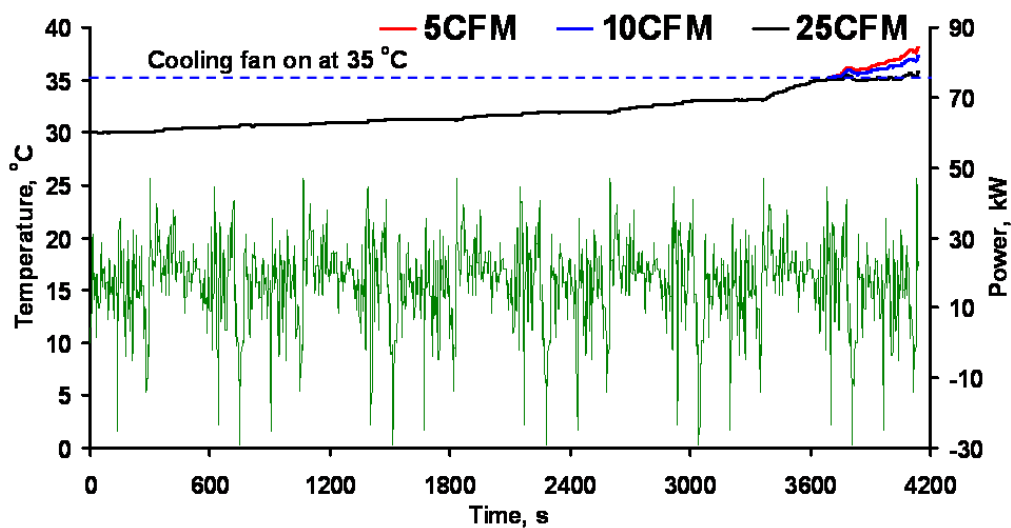
Figure 4.20 Thermal response of battery pack to HWFET cycle at 30 °C.
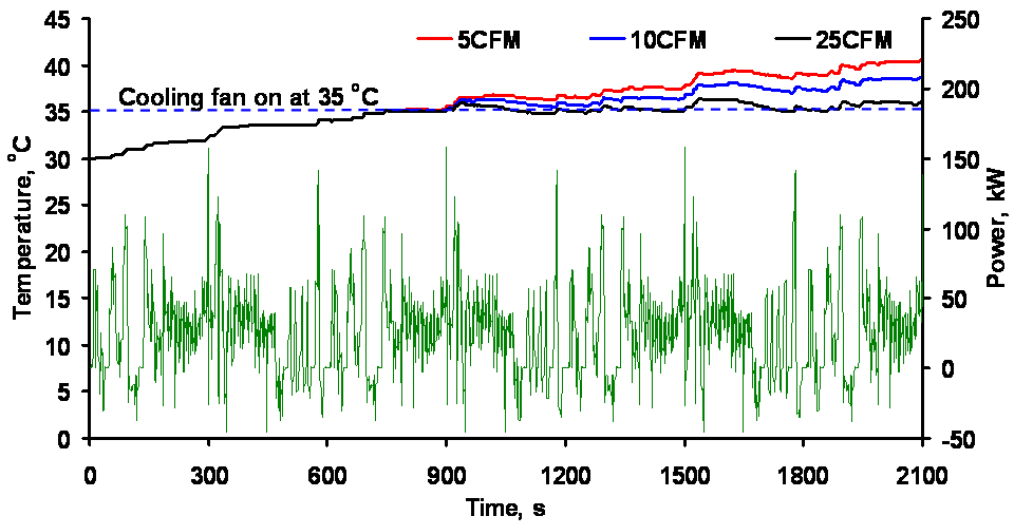
Figure 4.21 Thermal response of battery pack to US06 cycle at 30 ^{o}C.

A thermostat feature is also included in the Simulink model with a set temperature of 35 ^{o}C i.e., air flow from the blower will start only when the temperature of the battery pack rises above this set value. Beyond, 35 ^{o}C, a blower will be activated to deliver 5, 10 or 25 CFM of cooling air per module (140, 280 or 700 CFM for a battery pack). The battery pack delivers power for 176 min (7.7 cycles), 69 min (5.4 cycles) and 35 min (3.5 cycles) of UDDS, HWFET and US06 driving cycles, respectively before reaching the cut off voltage of 64.4 V. The temperature of the battery pack increased constantly during the cycle and reaches the maximum at the end of the cycle. The heat generated through the UDDS and HWFET cycles are small and hence can be effectively dissipated by natural convection. Battery module temperature at the end of the UDDS and HWFET cycle is about 35 ^{o}C as shown in Figure 4.19 and Figure 4.20. As shown in Figure 4.21, US06 cycle has a more aggressive driving profile as compared to the UDDS and HWFET cycles. Hence, more energy is charged and discharged to and from the battery pack and consequently more heat is generated. The battery pack is predicted to generate 4.93 MJ of energy on a US06 cycle at 30 ^{o}C. As expected, the temperature rise

118

of the battery pack in the US06 cycle is faster than the UDDS and HWFET cycles. The blower is turned on at 744 s when the average temperature of the battery pack reaches 35 $^\circ$C. The average temperature of the battery module at the end of discharge with 5 CFM of cooling air is about 41 $^\circ$C and the maximum temperature rise at the end of the cycle is about 11 $^\circ$C. In order to cool the battery pack further, 25 CFM of cooling air is blown to dissipate the heat generated and the average temperature of the battery module is brought to 36.5 $^\circ$C. The blower is operating for about 22.65 min of the total duration of the testing. The higher the flow rate of the cooling air, the slower the temperature rise of the battery module but parasitic loss and power consumption will be higher for higher flow rates. Table 4.5 provides the total energy used for propulsion as well as the energy recovered through regenerative braking (charging) for the various cycles.

Table 4.5 Energy distribution per cell in the 18650 battery pack.

Driving cycle	Discharging, MJ	Charging, MJ	Heat generation, MJ
UDDS	81.91	9.09	3.026
HWFET	73.06	2.17	3.237
US06	58.99	5.71	4.937

UDDS is an intensive start and stop driving cycle, therefore the total energy used and recovered is highest. The amount of energy recovered through the HWFET cycle represents the highway driving condition and is the lowest among the three driving cycles.

The selection of battery cells to build a battery pack is an essential task to optimize performance, prolong the life cycle with affordable cost. Smaller cells are favorable for thermal management and cost effective but a high number of electrical connections may result in higher chances of failure and energy loss especially due to contact resistance. Although larger cells

(prismatic and pouch cell) offer lower weight to-volume ratio, cost is higher, quality of the cells is not guaranteed and difficult in terms of thermal management. Therefore, a careful consideration is required to select the type of cell to build a battery pack for a certain application.

4.5.9 Thermal responses of the 38120 cell battery pack

Since the US06 is the most aggressive driving cycle as compared to UDDS and HWFET, it was chosen to investigate the thermal response of the battery pack. Thermal response of the 38120 cell battery pack under the US06 driving cycle is shown in Figure 4.22.
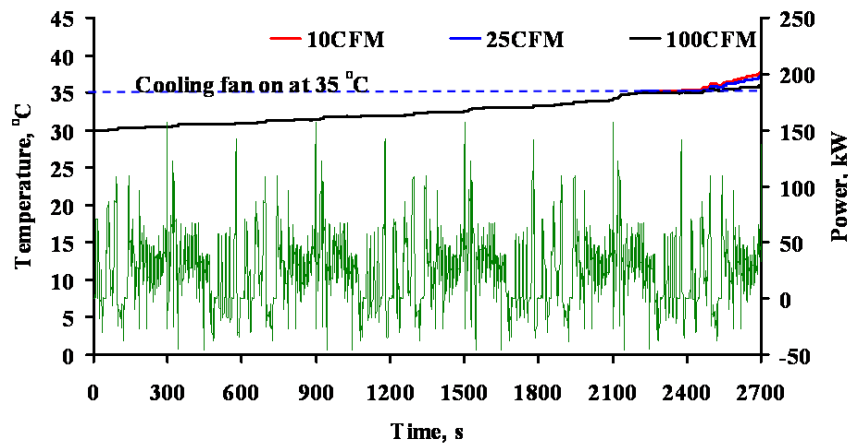
Figure 4.22 Thermal response of 38120 battery pack under US06 driving cycle.

The battery pack is subjected to 600s of the repeated US06 cycle until the voltage of the battery pack reached 64 V. The 38120 cell battery pack is able to complete 4.5 cycles of US06 and deliver power for 45.1 min. The temperature of cells increases continuously in the cycling process and reaches the maximum at the end of the cycle. At the end of the cycle, the average temperature of the battery in the module is 38.1 ^{o}C, 37.6 ^{o}C and 36 ^{o}C for 10 CFM, 25 CFM and 100 CFM of air flow per module respectively. The total flow rate of air is 280, 700 or 2800 CFM for the 38120 cell battery pack which consists of 28 modules. As compared to 18650 cell battery pack, the 38120

cell battery pack has higher energy used, higher energy gained from regenerative braking and higher capacity. The heat generated from the 38120 cell module is not as intense as the 18650 cell module. As shown in Table 4.5 and Table 4.6, heat generated from the 38120 cell battery pack is about 33% less than that for the 18650 cell battery pack.

Table 4.6 Energy distribution per cell for 38120 battery pack.

Driving cycle	Discharging, MJ	Charging, MJ	Heat generation, MJ
UDDS	84.99	9.49	2.037
HWFET	75.75	2.17	1.746
US06	75.73	7.40	3.319

This is caused by the additional heat generated from the contact resistance of the spring loaded terminal connector for the 18650 cells. On the contrary, screw connector is used for the 38120 cells to connect the cell and the contact resistance is very low (~ 0.6 miliohm). Only 0.45 kJ of heat is generated by the contact resistance throughout the cycle for the 38120 cell battery pack. On the other hand, the effect of contact resistance of the 18650 cell pack contributed 0.764 MJ of heat generated.

For the initial 2200s, natural convection is sufficient to dissipate the heat generated from the 38120 cell battery pack in the US06 cycle. The blower came in after 2200s (3.6 cycles) to supply cooled air to chill the cells and attempt to bring down the cell skin temperature to below 35 $^{\circ}$C. Conversely, skin temperature of the 18650 cell reached 35 $^{\circ}$C as soon as 1.2 cycles (744 s) of the US06 cycle were completed. The cross sectional flow area for cooling air per 38120 cell module is 0.00868 m^2 and is about twice the flow area of the 18650 cell module. Hence, mass flow rate of cooling air for the 38120 cell module needs to be doubled to achieve a similar cooling condition as for the 18650 cell module. Although the blower is only operated for 8.3 min, large

mass flow of air (2800 CFM per pack) is needed to suppress the temperature rise of the cell. In this case, a huge blower is needed and this will increase the cost and power consumption of the pack thus reducing the driving range of the EV.

The maximum temperature difference within the cell under strong forced convection, 25 CFM for the 18650 cell module and 100 CFM for the 38120 cell module was investigated. As shown in Figure 4.23, the maximum temperature difference of the 38120 cell could reach 6 ^{o}C, although there is only 4 ^{o}C of temperature difference developed in the 18650 cells at the end of the US06 cycle. As shown in Table 4.1 and Figure 4.13, 18650 and 38120 cells with different heat transfer areas per unit volume have led to a different trend of temperature evolution during the US06 driving cycle. 18650 cell reach 35 ^{o}C at about 900 min while for 38120 cell The internal temperature of the 18650 cell and the 38120 cell could reach 38 ^{o}C and 39 ^{o}C respectively. Hence, a cell with a larger diameter will have a larger temperature difference as compared to a small cell.
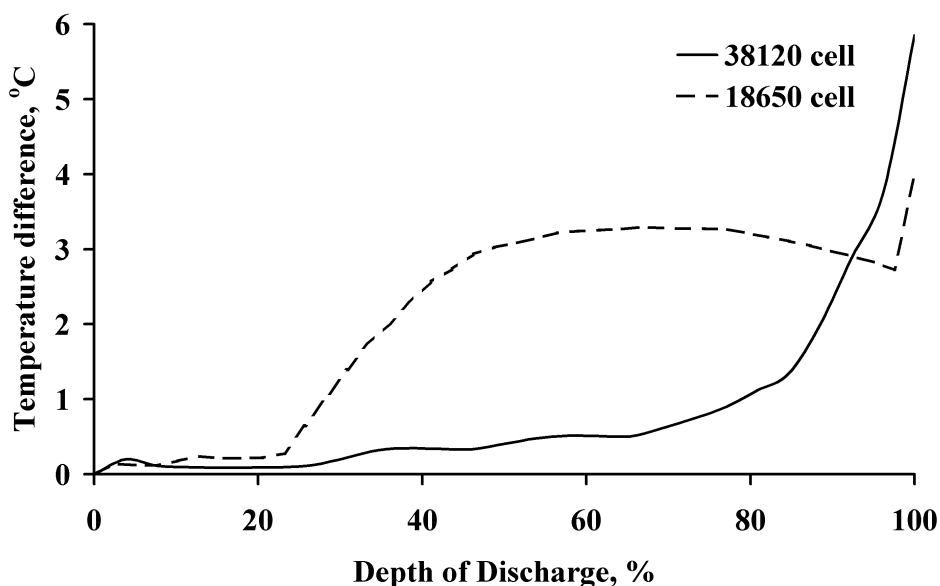
Figure 4.23 Gradient of 18650 and 38120 cell internal temperature for US06 driving cycle under maximum cooling capacity.

The effect of using liquid cooling on the 38120 cell battery pack was also investigated. For the closed pack architecture of the 38120 cell module, laminar flow of ethylene glycol is sufficient to maintain the temperature rise of the cell surface below 5 ^{o}C as illustrated in Figure 4.24.
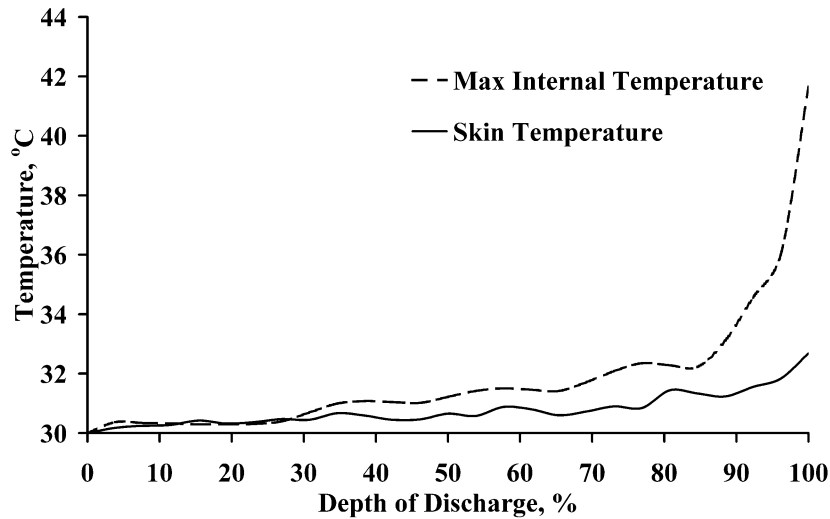
Figure 4.24 Cell skin temperature and maximum internal temperature of 38120 cell under laminar flow of ethylene glycol.

Although the skin temperature of the 38120 cell is successfully maintained at 33 ^{o}C, large temperature gradients develop inside the cell. The internal temperature of the cell could reach 42 ^{o}C which brings adverse effects to the cell cycle life and accelerates the thermal aging of the cell.

On the other hand, immersion cooling using 3M Novec 7000 engineering fluid or Fluorinert electronic liquid could be a solution for thermal management of large Li-ion cell. The cells are immersed in the liquid and take advantage of the large latent heat of vaporization of the liquid to achieve cooling.

4.6 Summary

A detailed battery model is developed to investigate the performance and thermal response of two different sizes of the cylindrical cell. The model which is based on the modified Shepherd model by extracting the data

obtained from the 0.2 I_t-rate of constant current discharge curve is able to predict dynamic behavior of the cell with good accuracy. Detailed information about the battery operating parameters such as SOC, I-V characteristics, skin temperature and internal temperature of the cell can be obtained. The simulation results showed good agreement with experimental data under various operating conditions. Heat generated in the cell is positively correlated with the I_t-rates and diameter of the cell. Heat exchange surface area per unit volume of the cell is a critical factor that determines the rate of cooling from the cell to the external environment.

As the ratio of surface area to volume is reduced, the heat loss from the cell decreases and the internal temperature rises. The maximum temperature region inside the cell is located in the circular region of active material near the hollow core. Due to the large thermal resistance and insulation effect of the separator, the temperature difference of the cell in the radial direction is significant and it increases with the diameter of the cell. This contributes to the slow rise of large cell skin temperature. Smaller sizes have better temperature distribution in the cell. Therefore, measuring skin temperature of the cell is not sufficient as a safety reference for cell operation.

Strong forced convection cooling should be avoided as it will increase the cell internal temperature gradient and accelerate the rate of thermal aging. The validated battery model was used to investigate the evolution of the battery pack temperature of a converted EV with different cooling air flow rate under the UDDS, HWFET and US06 driving cycles. The heat generated from the battery module is highest for the aggressive US06 driving cycle and lowest for the UDDS driving cycle. In a less aggressive driving condition for UDDS and

HWFET, natural convection is sufficient to maintain the cell temperature below 35 ^{o}C. On the other hand, the US06 cycle requires forced convection cooling. Hence, a well designed thermal management system is needed for the EV battery pack especially under aggressive driving conditions to ensure safe and reliable operation of the battery pack.

CHAPTER 5

EQUIVALENT CIRCUIT MODELING

5.1 Introduction

Although empirical models such as those developed in Chapter 4 can give good predictions on the battery electrical and thermal behavior, they were developed based on isothermal condition and the parameters are assumed to be constant over a wide range of temperature which limits their use in on-board battery management systems. Hence, an equivalent circuit model with cell parameters which vary with temperature and SOC is introduced to predict the I-V and thermal characteristics of a 10 Ah LFP pouch cell under constant-current discharge and pulse charge-discharge cycles. Hysteresis of the open circuit voltage (OCV) of a battery is commonly found in NiMH and Li-ion cells. The hysteresis effect on LFP cell is more significant as compared to Cobalt, Nickel or Manganese-based batteries. The relationship between OCV and SOC during charging and discharging is path dependent and leads to distortion in the OCV to SOC static mapping. The hysteresis effect will cause unreliable OCV reconstruction in the battery management system. Therefore, hysteresis effects need to be incorporated into the battery model to improve its accuracy and make it suitable to accurately predict voltage and thermal behavior of the LFP cell. The simulation results are validated with experimental data. The equivalent circuit model is then extended to the whole battery pack to investigate the thermal response of the converted EV battery pack under Urban Dynamometer Driving Schedule (UDDS) and US06 Supplemental Federal Test Procedure (SFTP) test cycles. Through simulations,

the electrical and thermal behavior of the cell can be predicted and applied to the EV power control system and battery thermal management system design.

5.2 Mathematical model

5.2.1 Equivalent circuit model

The equivalent circuit model is commonly used to define the electrical and thermal performance of the specific battery in terms of current and SOC. In this study, the third order RC model is used to express the electrical behavior of the Lithium Iron Phosphate cell. Parasitic losses are not modeled in the current study due to high coulombic efficiency and relatively low self-discharge as compared to other types of battery (Huria et al., 2012 and Ceraolo et al., 2011). The proposed equivalent circuit model includes the temperature effect as an independent variable in lookup tables to overcome the limitation of the models in the current literature. 5 ^{o}C, 25 ^{o}C and 40 ^{o}C are used as dependent parameters for the resistor, capacitor and open circuit potential. Figure 5.1 shows a schematic diagram of the model with one serial resistance and three RC branches.
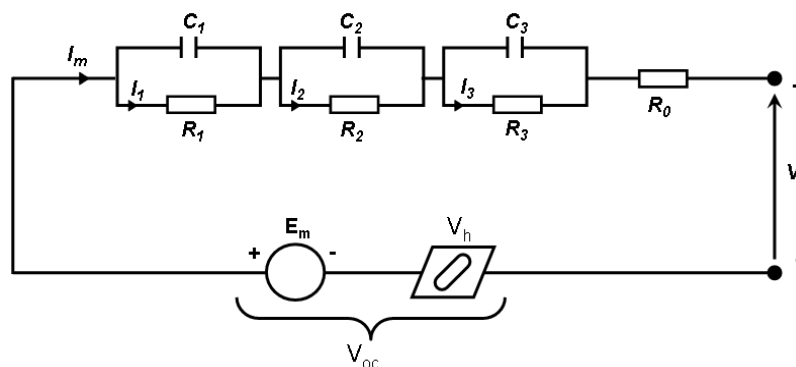
Figure 5.1 The equivalent circuit model used for this study.

OCV of the RC model can be computed by using Equation 5-1 while SOC of the cell is given by Equation 5-2. In total, there are eight parameters in the function of operating conditions used for the study as in Equations 5-1 to 5-3

(Kroeze and Krein, 2008 and Huria et al., 2014). The parameters of the battery model are represented by lookup tables. Hysteresis effects are taken into consideration in the model.

$$V_{batt} = V_{oc}(SOC,T) - I_m R_0(SOC,T) + I_m R_t(\tau_1, \tau_2, \tau_3) \qquad (5\text{-}1)$$

$$SOC(t) = SOC(0) + \frac{1}{C_Q} \int_0^t I_m(t) \cdot dt \qquad (5\text{-}2)$$

$$
\begin{aligned}
R_t = &\, R_1(SOC,T) e^{-\frac{1}{R_1(SOC,T)C_1(SOC,T)}t} + R_2(SOC,T) e^{-\frac{1}{R_2(SOC,T)C_2(SOC,T)}t} \\
&+ R_3(SOC,T) e^{-\frac{1}{R_3(SOC,T)C_3(SOC,T)}t}
\end{aligned}
\qquad (5\text{-}3)
$$

The number of RC branches in the equivalent circuit is an important factor determining the accuracy of the prediction and complexity of the model. In this study, the number of RC branches used in the modeling was determined using the transient response of the cell voltage during the relaxation phase when the pulse current was removed. The experimental data are fitted with exponential equations to determine the number of RC branches and the results are shown in Figure 5.2.
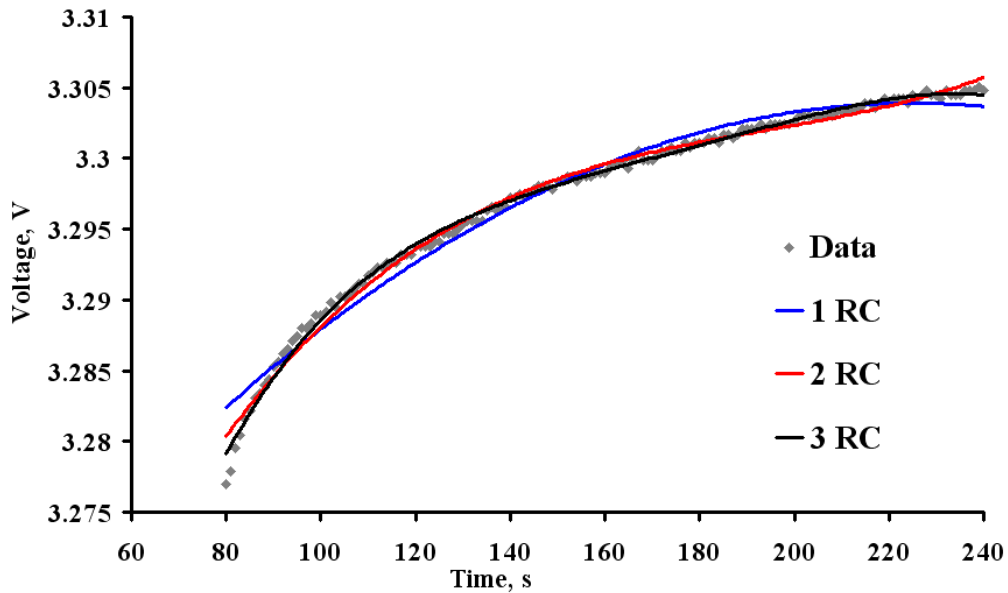
Figure 5.2 Curve fit to determine the number of RC branches used in this study.

The R-squared value for one RC branch, two RC branches and three RC branches are 0.878, 0.957 and 0.9919, respectively. From the fitting results, it is shown that one RC branch and two RC branches did not produce a satisfactory match to the experimental data. Although one RC branch and two RC branches are simple, it could not reproduce the experimental results with sufficient accuracy. Thus, three RC branches with the highest R-squared value were selected for this study as a compromise between accuracy and complexity.

5.2.2 Thermal model

Temperature plays an important role in determining the SOC, model parameters and capacity of the cell. Resistance to external convection from the battery surface is higher than conduction within the battery (Rao and Newman, 1997). Heat generated by the cell is dissipated through convection and radiation. A general energy balance equation (equation 4-7) proposed by Bernardi et al. was used to model the total heat generated in the cell. Joule heat and reversible heat are the two main heat sources in the cell. The reversible heat term is computed using the relation of dU/dT with the SOC proposed by Forgez. et al. (Forgez et al., 2010).

The general energy balance of the battery thermal model is given by Equation 5-4 and the boundary condition on the outer surface of the cell is defined by Equation 5-5. The density, emissivity and thermal conductivity of the pouch cell are given in Table 5.1.

$$\rho C_p \frac{dT}{dt} = \lambda \frac{\partial^2 T}{\partial x^2} + Q_{gen} \tag{5-4}$$

$$-\lambda \frac{\partial T}{\partial x}\bigg|_{x=L} = h(T - T_\infty) + E\sigma_{sb}\left(T^4 - T_\infty^4\right) \tag{5-5}$$

Table 5.1 Parameters of the pouch cell.

Parameter	Value	Parameter	Value
Nominal voltage, V	3.0	Cell thickness, m	0.0106
Nominal capacity, Ah	10.0	Cell width, m	0.07335
Weight, kg	0.261	Cell height, m	0.1634
Cathode material	LiFePO$_4$	Anode material	Graphite
Specific heat capacity, Jkg^{-1}K^{-1}	1200	Aluminum casing thickness, m	113x10^{-6}
Heat Transfer coefficient, Wm^{-2}K^{-1} (estimated)	10	Reference temperature, T_{ref}, K	298.15
Density, kgm^{-3}	2054.39	Emissivity (estimated)	0.090
Thermal conductivity in y and z direction, Wm^{-1}K^{-1} (Ye at al., 2014)	18.4	Thermal conductivity in the x direction, Wm^{-1}K^{-1}	0.34

5.2.3 Thermal model for EV battery pack

Modeling of the EV battery pack is based on the Hyundai Trajet and the battery pack is designed using pouch cells to provide a similar power capacity as in the 18650 cell and 38120 cell battery packs shown in Table 4.2. The battery pack comprised twenty eight modules and each module is constructed using twenty four pouch cells. Since the modules in the battery pack are identical, it is sufficient to study the thermal response of a single module. The thermal response of the battery pack is investigated using the UDDS and US06 driving cycles shown in Figure 4.5.

5.3 Numerical and experimental procedure

Commercial 10 Ah pouch cells with graphite anode coated on the copper current collector and Lithium Iron Phosphate cathode coated on the aluminum current collector were used in the experiments. The details of the cell are shown in Table 5.1. The cells were tested at three different temperatures of 5 ^{o}C, 25 ^{o}C and 40 ^{o}C in an environmental chamber (Weiss, WKL 34) to extract the parameters needed. The charging and discharging of the cell were conducted using a battery cycler (Maccor Instrument 4000). Pulse discharge characterization tests in 10% decrements of SOC at 1 I_t-rate were carried out

on 10 Ah cells at three different temperatures. One hour rest was imposed between pulse discharges to ensure that the OCV of the cell is stable to obtain a reliable estimation of the model parameters. The temperature of the cell was measured using fourteen thermocouples (T-type) attached to different locations of the cell. A heat flux sensor (Captec) is appended to the center of the cell to measure the heat dissipated from the cell. The measurement of the battery surface temperature discharge at different I_t-rates was done at a room temperature of 25 ^{o}C under natural convection. The temperature readings were recorded using a HP 34970A data acquisition system. The specific heat capacity and heat generated in the cell is measured using an adiabatic accelerating rate calorimeter (THT ARC). A pulse discharging-charging test at 5 I_t-rate is used as a verification test for the battery model. The bulk cross-plane thermal conductivity of the pouch cell was measured using TPS 2500 S (TechMax Technical Co. Ltd).

The equivalent circuit model parameters for each temperature were calculated using a parameter estimation function in the Matlab-Simulink 2011b. In the resulting model, it was assumed that the pouch cell impedance does not change with the magnitude of discharge current (Huria et al., 2012). Lookup tables which provide flexibility were chosen for parameterization of the RC model. The pulse discharge technique will provide enough information of the open circuit voltage and RC network for the numerical optimizer to isolate the parameters in the RC network into the lookup table. The pulse discharge profile was iteratively simulated and compared with the experimental results to extract the battery parameters using the command line parameter estimation capability of the Design Optimization function in the

Simulink. The nonlinear least-squares algorithm was used to compute the error gradient across each of the 56 parameters (8 tables*7 breakpoints) to minimize the sum of squared error. This will produce a set of one-dimensional lookup tables versus SOC for the eight parameters at each temperature (5 ^{o}C, 25 ^{o}C and 40 ^{o}C). The results of the estimated voltage and experimental data at 5 ^{o}C, 25 ^{o}C and 40 ^{o}C are shown in Figure 5.3.

132
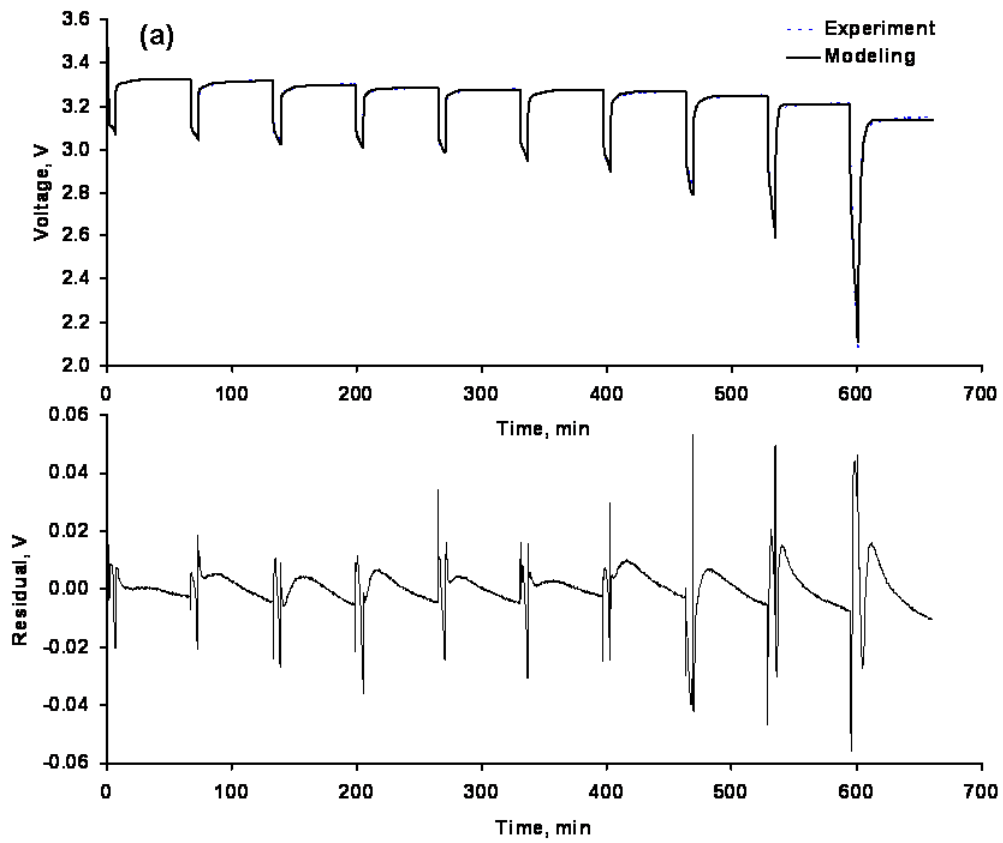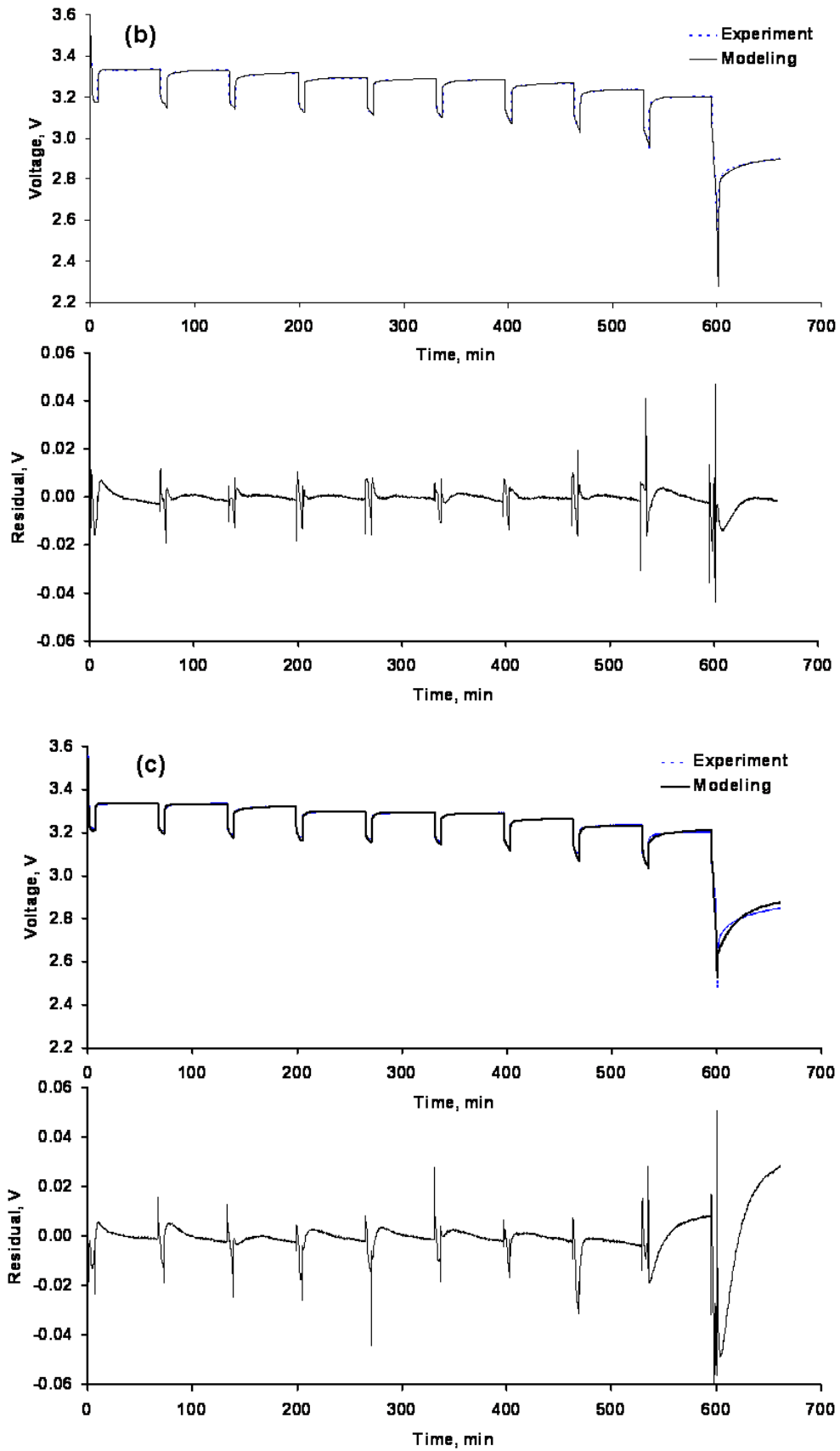
Figure 5.3 Experimental and simulated discharge curves and corresponding to the voltage residual for the pouch cell at the end of estimation process for different temperature. (a) 5 ^{o}C, (b) 25 ^{o}C and (c) 40 ^{o}C.

The battery model is able to reproduce the reduction of battery OCV during pulse discharge. The results of the model parameters are shown in Figure 5.4.
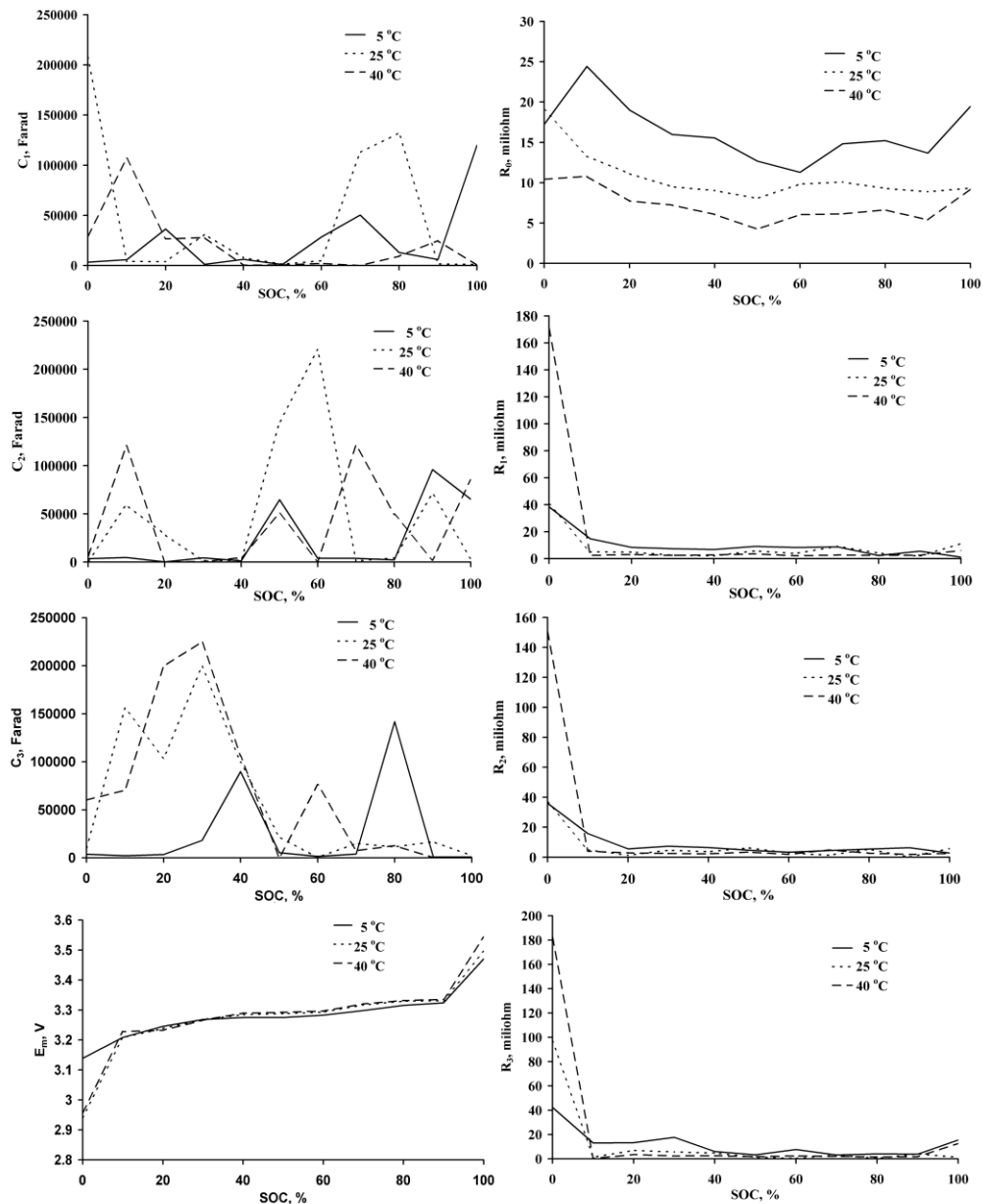
Figure 5.4 Model parameters obtained through estimation for the present study.

The parameters of the model circuit elements are described using lookup tables with seven different points of SOC spaced slightly bias toward initial and end of discharge. The parameter values in the two dimensional table are linearly interpolated during simulation to determine the electrical

characteristics of the cell. The model is then coupled with the thermal model to estimate the heat generated and surface temperature of the cell under natural convection.

Besides, an independent set of experiments is needed to validate the battery model. The battery model was validated using constant current discharge and pulse discharge and charge. Finally, the validated model was utilized to investigate the thermal response of the battery pack for a converted Hyundai Trajet EV using UDDS and US06 test cycles under natural convection cooling.

In order to investigate the development of the pouch cell internal temperature under 5 I_t-rate of constant current discharge, the thermal model of the pouch cell as shown in Figure 5.5 is used.
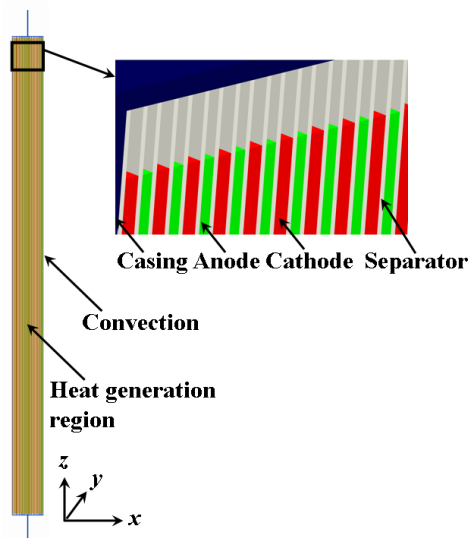
Figure 5.5 Schematic of lithium iron phosphate pouch cell thermal model.

The pouch cell consists of several layers of electrodes and separator stacking together. In this study, the active material region is assumed to be a single domain with uniform heat generated. The thermal conductivity of the active material region is considered anisotropic. The thermal conductivity in the x direction is 0.34 $Wm^{-1}K^{-1}$, y and z direction are 18.4 $Wm^{-1}K^{-1}$. The heat

transfer coefficient of 10 Wm^{-2}K^{-1} (natural convection) and 100 Wm^{-2}K^{-1} (forced air convection) were used for the current study. The thermal model together with the appropriate boundary conditions was solved with commercial finite element solver, COSMOL Multiphysics 4.3b. The effects of external current tabs were neglected in this study. Tetrahedral element was used to mesh the pouch cell geometry and direct solver GMRES was chosen with a relative convergence tolerance of 10^{-6} for the modeling. The number of elements used in this study is 1381320. All computations were carried out on a computer with a 3.40 GHz Quad core processor and 32 GB Random Access Memory (RAM). In addition, the grid independent test was carried out to refine the grid size until the simulation results are not affected by further refinement of the mesh.

5.4 Results and discussion

5.4.1 Validation of the cell potential

Parameter estimation results of the pouch cell at 5 ^{o}C, 25 ^{o}C and 40 ^{o}C are presented in Figure 5.3. A comparison of the estimated results and experimental data shows that the battery model gives a good estimate of the electrical behavior of the cell. The residuals of voltage error are in millivolts and shown in the lower part of the figure. As shown in Figure 5.3, the battery model is able to capture the change of OCV during the discharge process. Towards the end of the discharge process with SOC 10% (last pulse) the residual of the OCV is slightly higher. The maximum residual is about -55 mV, 45 mV and -58 mV for 5 ^{o}C, 25 ^{o}C and 40 ^{o}C, respectively. Although the residual of the voltage during pulse discharge is higher at the end of discharge, it would not affect the prediction. In EV applications, the Li-ion battery is

136

normally discharged till 90% of SOC and the cell is not fully-discharged in order to protect the cell. In the battery model, the two dimensional parameters in Figure 5.4 are interpolated over the temperatures to simulate the charging and discharge process of the cell.

As a common practice, the important model parameter, OCV is measured after a relaxation period following a short and gradual charging or discharging period (Roscher et al., 2011). In this study, the relaxation duration was varied from 1 min, 30 min to 1 hour to investigate the effect of relaxation time on the accuracy of OCV measurement. From the results shown in Figure 5.6(a), there is a large gap between the result for 1 min and 30 min of relaxation, showing that 1 min of relaxation duration is insufficient for accurate OCV measurement. On the other hand, OCV measurement at 30 min is close to OCV reading at 1 hour, suggesting that 30 min of relaxation duration is adequate for accurate OCV measurement. Therefore, 1 hour relaxation duration was taken in our tests to ensure the accuracy of the measured OCV.
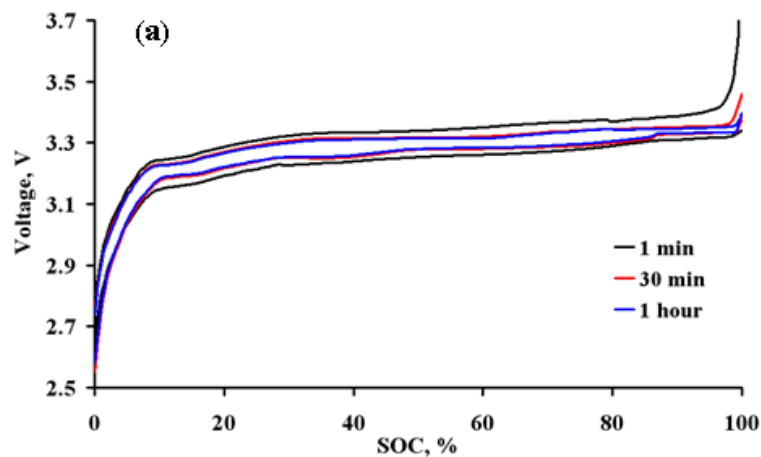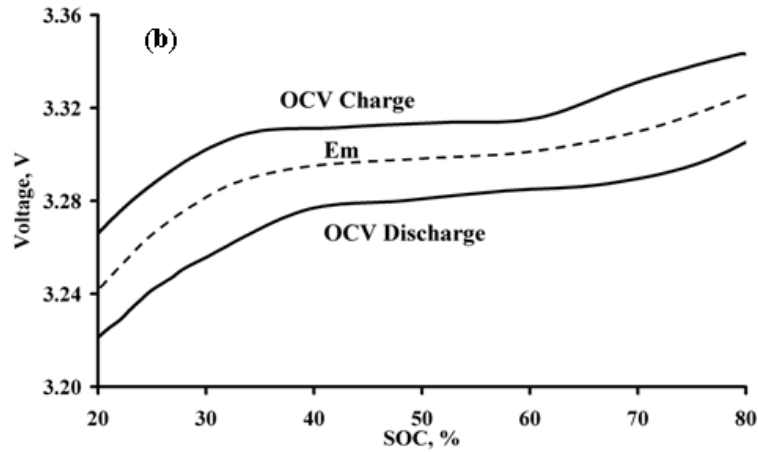
Figure 5.6 Typical hysteresis effect of the Lithium Iron Phosphate cell.
(a) 1 I_t-rate of charge and discharge with different resting duration.
(b). The hysteresis effect of the cell after 1 hour of relaxation.

From the results of OCV measured with 1 hour of relaxation duration, a discrepancy was found between the OCV measured during charging and discharging. This discrepancy existed even when a much longer relaxation time was given and this is called the hysteresis effect. Figure 5.6(b) demonstrates the hysteresis effect of the LFP cell tested. A common compromise to the hysteresis gap is to adopt the average value E_m, of the OCV for both charging and discharging. In doing so, the accuracy in predicting the electrical and thermal behavior will be reduced. In this study, the hysteresis voltage (V_h) in Equation 5-6 and Equation 5-7 was adopted to compensate for the errors in using E_m and to improve the accuracy of prediction.

$$V_{oc\_charging} = E_m + V_{h\_charging} \qquad (5\text{-}6)$$

$$V_{oc\_discharging} = E_m - V_{h\_discharging} \qquad (5\text{-}7)$$

5.4.2 Constant current validation

Experimental validations of electrical and thermal behavior of the battery model under different I_t-rate of discharge are shown in Figure 5.7 and Figure 5.8.
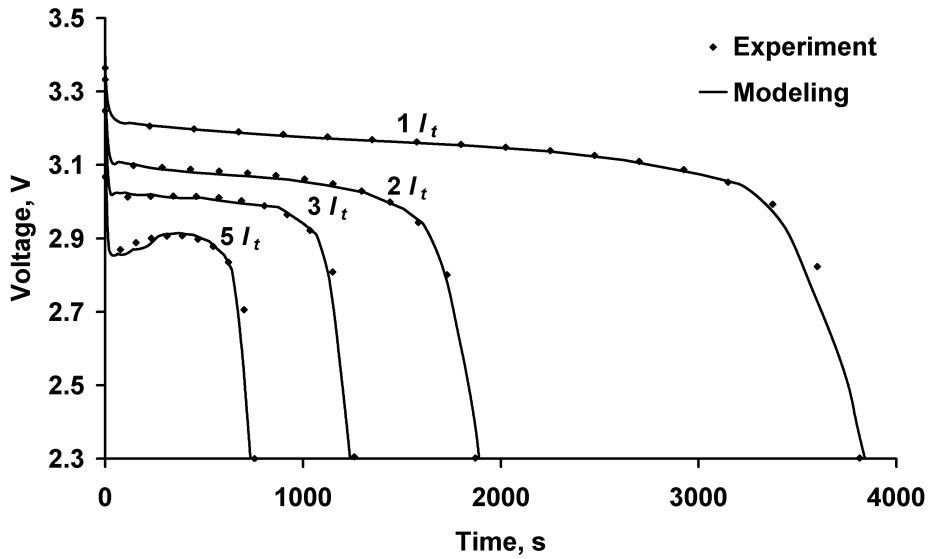
Figure 5.7 Voltage prediction results of 1-3 I_t constant current discharge test.
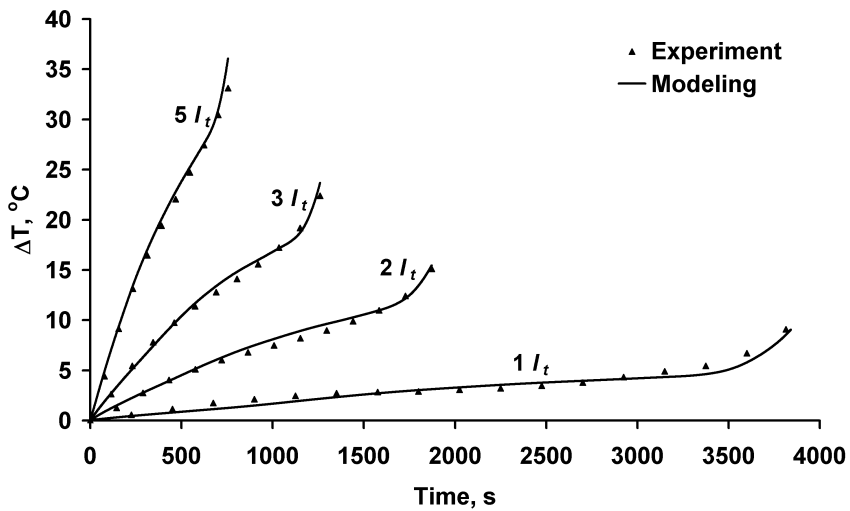
Figure 5.8 Temperature rise of the cell at different I_t- rates of discharge.

The battery model exhibits good accuracy in predicting the electrical behavior of the cell under steady-state conditions. The averaged relative error of the cell voltage for 1, 2, 3 and 5 I_t-rates are 0.3%, 0.3%, 0.8% and 1.3%, respectively. The sudden drop of the battery voltage for a period of 260s during 5 I_t-rate of discharge is due to the polarization effect of the solid phase and the electrolyte. Large concentration gradients of Li-ions are developed in the active material and electrolyte interface at high I_t-rate of discharging and the Li-ions need some time to travel from the negative electrode to the positive

139

electrode (Nyman et al., 2010).

Comparisons of simulated and measured surface temperature of the pouch cell showed that the battery model produced a good estimation of the thermal behavior of the cell at various I_t-rates under natural convection cooling. The averaged relative errors of the cell surface temperature for 1, 2, 3 and 5 I_t-rates are 14.9%, 7.9%, 5.5% and 5.8%, respectively. The maximum surface temperature of the cell at 5 I_t-rates is about 61 $^{\mathrm{o}}$C and exceeds the optimum operating temperature limit of the cell. Hence, a proper cooling system is recommended for high I_t-rates of discharging or charging to reduce the thermal aging of the cell.

Comparisons of simulated and measured heat generated in the pouch cell at various I_t-rates of discharge are depicted in Figure 5.9.
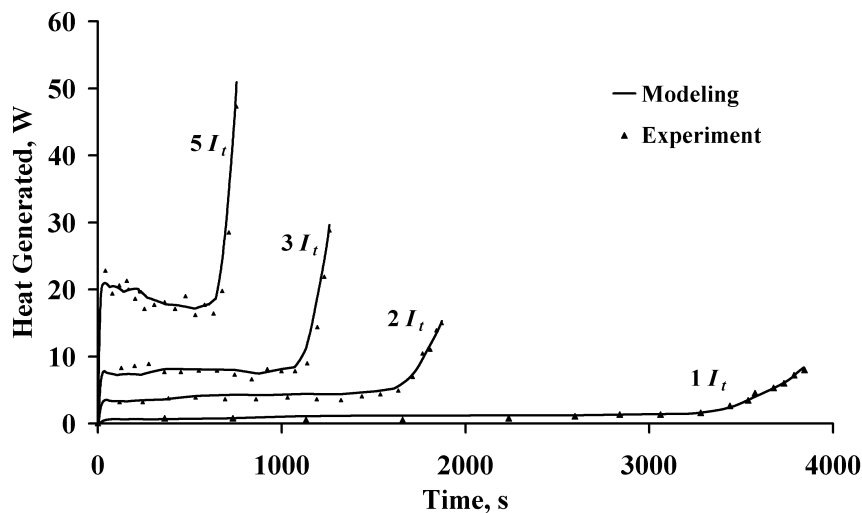
Figure 5.9 Comparison between simulation results and experimental data of the pouch cell heat generated at different constant current discharge rates.

Heat generated from the cell is positively correlated to discharge current and capacity of the cell. Average heat generated in the cell at 1, 2, 3 and 5 I_t-rates are about 1.51 W, 4.79 W, 9.02 W and 20.5 W, respectively. Modeling results of the heat generated agreed well with the experimental data obtained

from the accelerating rate calorimeter. Some deviation of the experimental data with simulation results is noted around the middle portions of the curves. The effect is also evident in the temperature graph in Figure 5.8. Slightly lower temperatures were measured on the cell surface as compared to the simulation results.

The heat dissipated from the cell was using a heat flux sensor and the results are shown in Figure 5.10. The maximum rate of cooling from the cell for 1, 2, 3 and 5 I_t rates at the end of the discharging process are 2.58 W, 5.25 W, 6.91 W and 10.58 W respectively.
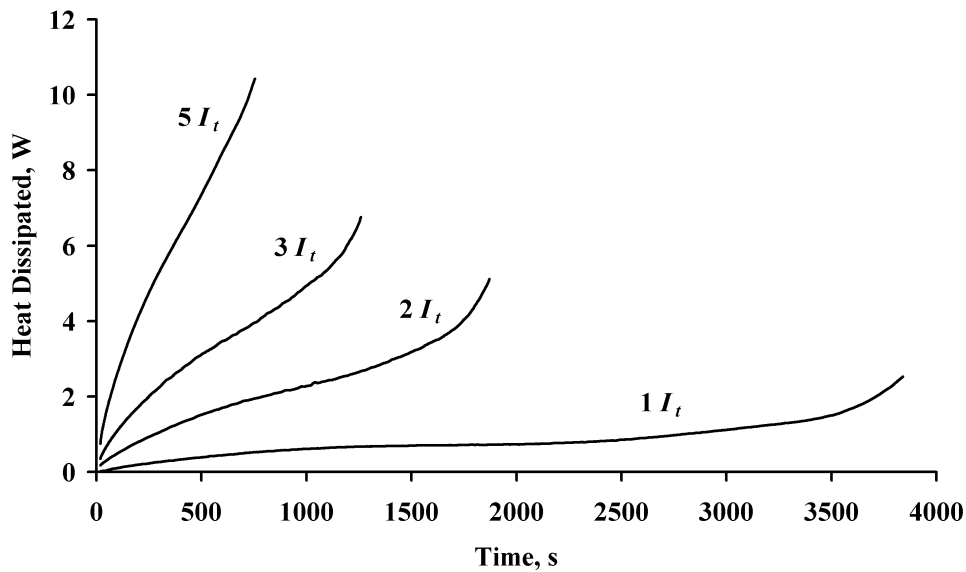
Figure 5.10 Rate of cooling from the cell through natural convection at different I_t-rates of constant current discharge.

As shown in Figure 5.9 and Figure 5.10, natural convection is effective to dissipate about 30% of the heat generated from the cell and most of the heat generated is kept inside the cell. The ratio of average rate of cooling by natural convection to heat generated in the cell is reduced from 58% for 1 I_t-rate of constant current discharge to 29% at 5 I_t-rate of constant current discharge. Hence, for a high current discharging process, forced convection is desirable to dissipate the intensive heat generated and prolong the calendar life of the

141

cell.

Figure 5.11 shows the internal temperature distribution of the pouch cell at the end of 5 I_t-rate of constant current discharge for h = 10 Wm^{-2}K^{-1} (natural convection) and 100 Wm^{-2}K^{-1} (forced air convection). The maximum internal temperature region of the pouch cell is located at the center of the cell. About 2.7 ^{o}C of temperature difference between the center of the cell and the battery surface was found when the heat transfer coefficient is 10 Wm^{-2}K^{-1} is applied on the battery surface as shown in Figure 5.11(a). On the other hand, about 6.3 ^{o}C of temperature difference between the center of the cell and the battery surface when the heat transfer coefficient is 100 Wm^{-2}K^{-1} as shown in Figure 5.11(b).
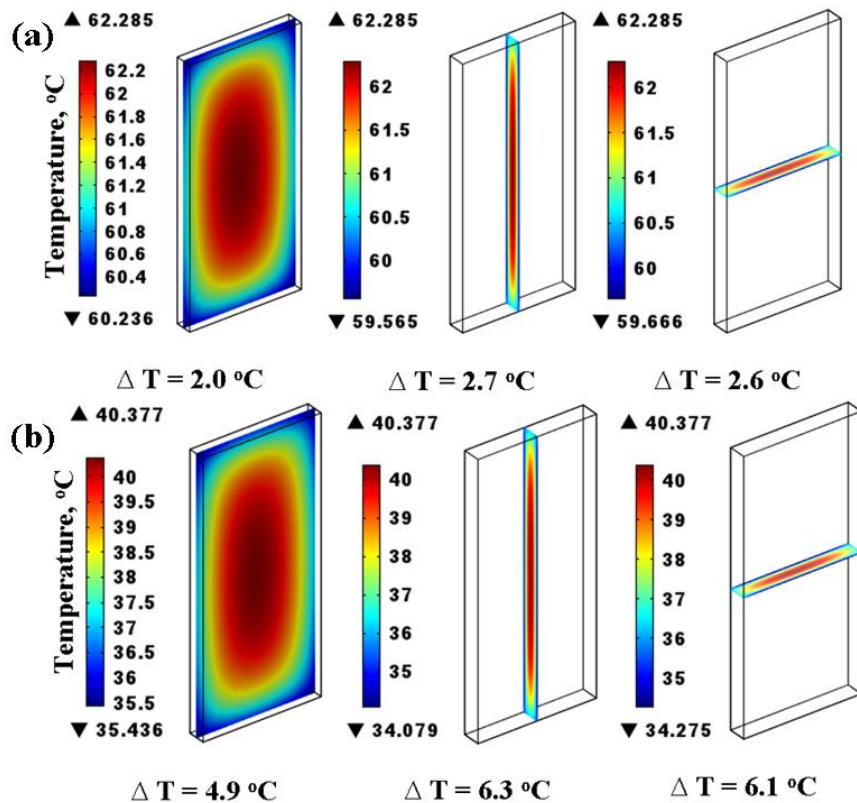
Figure 5.11 Predicted variation of internal temperature of the cell across the thickness at the end of 5-I_t discharge. (a) h = 10 Wm^{-2}K^{-1}. (b) h = 100 Wm^{-2}K^{-1}.

As compared to the excellent thermal conductivity of the aluminum casing, the active material of the cell is a poor thermal conductor. Although the current collectors of the cell are made of copper and aluminum, the porous electrodes and separator are poor thermal conductors, which prevent the heat generated from the cell to be effectively dissipated to the outer environment. Hence, the safety of the battery cannot be ensured by examining only the surface temperature. Compared to the cylindrical cell, a pouch cell with a large flat surface is more favorable for thermal management. However, strong forced convection will increase the temperature gradient across the cell and accelerate thermal aging. Hence, enhancing the thermal conductivity of the porous electrode, electrolyte, filler and decreasing the thickness of the separator is more effective in improving cooling (Chen et al., 2006).

5.4.3 Validation of dynamic behavior

In order to further validate the battery model, 5 I_t-rate of pulse charging-discharging was performed on the pouch cell. The simulated and experimental values are compared in Figure 5.12.
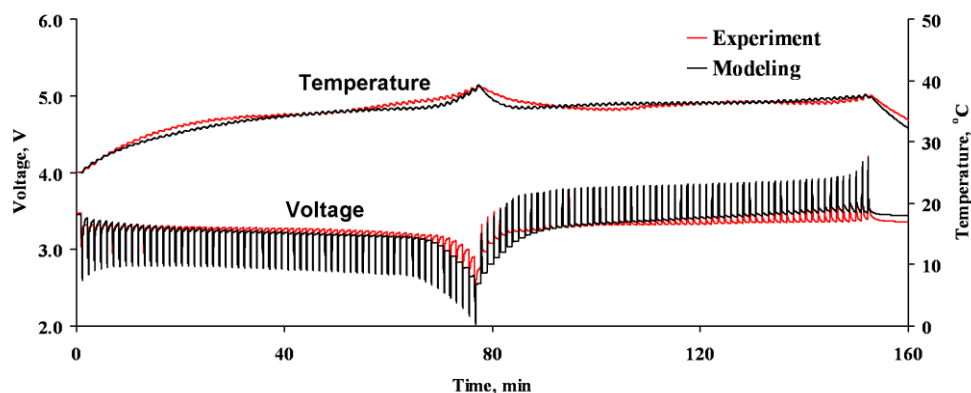
Figure 5.12 Comparison between simulated and experimental results for 5 I_t-rate of pulse discharging and charging for the pouch cell.

The simulation results agreed well with the experimental data, except during the end of the discharging and charging process. The cause of the

discrepancy can be explained by the slight error in the estimation of the model parameters at the end of discharging. The proposed battery model regenerated voltage response of the cell with the averaged relative error of 3.2%. Besides, the accuracy of the thermal model is satisfactory. Averaged relative error of 1.7% was obtained. The close agreement of the simulation results with experimental data on the Lithium Iron Phosphate pouch cell indicates that the proposed battery model does give an accurate prediction of the electrical and thermal behavior of the LFP cell in the steady state as well as the dynamic state.

5.4.4 Thermal response of the battery pack

To check if the battery model can perform well in real life application, the UDDS and US06 tests (Figure 4.5) were used to investigate the thermal response of the battery pack. The overall duration of the UDDS test is 1369 s with a peak velocity of 91 kmh^{-1} while the overall duration of the US06 test is 600 s with a peak velocity of 129 kmh^{-1}. As shown in Figure 5.13 and Figure 5.14, the battery pack is able to complete 8.3 cycles of the UDDS test and 4.5 cycles of the US06 test before reaching the cutoff voltage of 64.4 V.
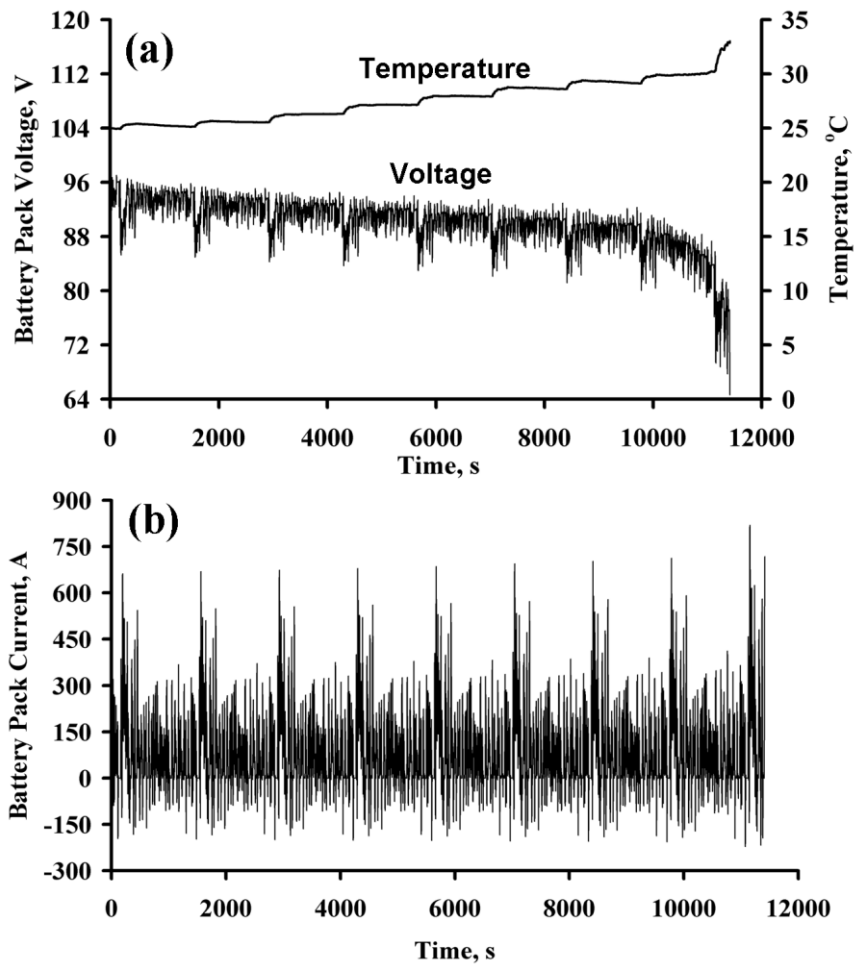
Figure 5.13 Electrical and thermal responses of the battery pack to the UDDS test at 25 ^{o}C under natural convection.

Figure 5.14 Electrical and thermal responses of the battery pack to the US06 test at 25 $^{\circ}$C under natural convection.

The maximum current withdrawn from the battery pack is 818 A during the end of the cycle. On the other hand, the charging current into the battery pack during regenerative braking is 217 A as shown in Figure 5.13(b). As shown in Figure 5.13(a), the temperature of the battery pack increased constantly during the cycle and reached the maximum at the end of the cycle. The average temperature of the cell at the end of the UDDS test is about 33 $^{\circ}$C with natural convection cooling and the temperature of the cells is within the optimum operating temperature limit of the Li-ion battery. An average of 5.2 kJ of heat is generated by a single cell in the battery pack during the UDDS test cycle. Throughout the UDDS cycle, 88.81 MJ of energy is utilized to

146

propel the vehicle to the targeted speed while 9.85 MJ of energy is recovered through regenerative braking. The average temperature of the cells at the end of the US06 test could reach 52.3 ^{o}C. As shown in Figure 5.14(b), the maximum current withdrawn from the battery pack is 2003 A during the acceleration to pick up the desired velocity. On the other hand, the charging current into the battery pack during regenerative braking is 538 A, which is about 2 I_t-rate of pulse charging. The simulation results predict that more heat is generated during the aggressive US06 driving cycle as compared to the less aggressive UDDS test cycle for which an average 11.5 kJ of heat is generated per cell throughout the test. And about 75.53 MJ of energy is used to drive the vehicle while 7.4 MJ of energy is recovered through regenerative braking. Therefore, an active battery thermal management system is needed for EVs which operated in aggressive driving conditions, to remove the excessive heat generated from the cells and prevent the heated cells from thermal runaway. Besides, the battery thermal management system also helps to prolong the cycle life of the cell by ensuring that the cells operated within the optimum temperature range and maintaining the temperature uniformity of the cells in the battery pack.

5.5 Summary

A battery model has been developed which is capable of modeling the electrical and thermal behavior of LFP cells under different operating conditions with good accuracy. The battery model was validated using a constant current discharge and 5 I_t-rate of pulse current charge and discharge. The results of model showed good agreement with experimental results of voltage and temperature over a wide range of temperature and SOC of the

pouch cell. The LFP cell shows a more noticeable hysteresis effect as compared to Cobalt, Manganese and Nickel cathode systems. However, the hysteresis effect can be minimized by prolonging the resting duration before the OCV of the cell is measured. The heat generated from the cell is positively correlated with the I_t-rates. Natural convection cooling is capable of dissipating only 30% of the heat generated in the cell, and most of the heat is kept inside the cell. This is explained by the poor thermal conductivity of the active material. Therefore, using active cooling or improving the thermal conductivity of the electrodes, electrolyte, filler and decreasing the thickness of the separator can effectively dissipate the heat generated and reduce the thermal aging of the cell. Lastly, the validated battery model was used to investigate the thermal behavior of the EV battery pack under the UDDS and US06 tests. At the end of the US06 cycle, the average surface temperature of the cell could reach 52.3 ^{o}C. Hence, a well designed active thermal management system is desired for the EV battery pack to prolong the cycle life of the cell and ensure the safety and reliable operation of the battery pack.

CHAPTER 6

BORON NITRIDE COATING

6.1 Introduction

Insulation of the battery body is extremely important for a battery so that the positive and negative terminals are insulated. Good insulation is desirable to prevent any short circuit and sparks that occurring when the cells are closely packed. In general, insulation material for the battery body is made of polymer such as Polyvinyl Chloride (PVC) or Polyethylene Terephthalate (PET) and heat shrink wrapped around the battery body as shown in Figure 6.1.

Figure 6.1 Various types of heat shrink wrapping for Li-ion battery.

The thickness of the insulating film is about 0.2 to 0.3 mm. The polymer insulator must endure temperature changes during charging and discharging, and corrosive environments which could cause the insulator to degrade, fracture or soften. These conditions are expected to be very challenging for the reliability of the polymer insulator. Additionally, the polymer insulator with its poor thermal conductivity, and high thermal contact resistance between the polymer insulator and battery metal casing, prevents the heat generated in the battery being effectively transferred to the surroundings. The heat transfer

from the battery occurs by conduction across the actual contact area of the metal casing and polymer insulator and through conduction or radiation across the air gaps at the interfaces (Incropera et al., 2007). The actual contact area is normally very small for rough surfaces. In addition, an imperfect heat shrink process may introduce air bubbles trapped between the battery metal casing and the insulator, leading to localized hot spots. During high I_t-rates of charging and discharging, the heat generated would be retained inside the cell. This is caused by thermal contact resistance between battery casing and polymer insulator, thus forming a large temperature gradient inside the cell under strong convection process (Shi et al., 2006). Therefore, it is important to investigate this insulator issue.

The properties of the metal surface could be changed by applying a layer of coating. The coating material properties could have an excellent thermal conductivity, good thermal insulating properties, electrically conductive or non-conductive (Rudolph, 1993). Boron Nitride has a layered structure which is similar to graphite (Lipp et al., 1989), and possesses a good thermal conductivity, good electrical insulation, low dielectric constant and good thermal stability up to 1000 $^{\circ}$C in air (Rudolph, 1993). Boron Nitride also shows chemical inertness, high corrosion and erosion resistance. Due to the above advantages, Boron Nitride has been used widely as a release agent and protective coatings for dies/molds, the glass making process, metal processing, sintering, welding, brazing, etc. Properties of Boron Nitride are shown in Table 6.1.

Table 6.1 Properties of Boron Nitride (Accuratus, 2013).

Properties	Value
Crystal structure	Hexagonal
Color	White
Density, kgm^{-3}	1900
Maximum used temperature, ^{o}C	1800
Hardness, $kgmm^{-2}$	15-24
Elastic modulus, GPa	46.9
Thermal Expansion Coefficient (10^{-6}) $(^{o}C^{-1})$	Parallel 11.9 Perpendicular 3.1
Thermal conductivity, $Wm^{-1}K^{-1}$	Parallel 30 Perpendicular 33
Specific heat, $Jkg^{-1}K^{-1}$	1610
Dielectric breakdown strength , $ac-kVmm^{-1}$	Parallel 95 Perpendicular 79
Vol resistivity, Ωcm	Parallel $> 10^{14}$ Perpendicular $> 10^{15}$

There are various methods used to produce Boron Nitride coatings such as chemical vapor deposition (CVD) (Li et al., 2011; Gallet et al., 2004 and Ye et al., 2012), plasma assisted chemical vapor deposition (PACVD) (Konyashin et al., 1997; Kim et al., 1996 and McKenzie et al., 1996), physical vapor deposition (PVD) (Djouadi et al., 2004; Bello et al., 2005 and Jensen and Sorensen, 1996), and spin coating (Husain et al., 2013). However, studies on the Boron Nitride coating on the battery casing are rare. Moreover, most of the studies on the thermal analysis of Li-ion battery did not take the effect of the polymer insulator into account (Jeon and Baek, 2011, Cai and White, 2011, Forgez et al., 2010, Chen et al., 2006 and Sato, 2011).

The Taguchi technique can be used to dramatically improve the process, quality, product characteristics and simultaneously reduce the product development time and cost (Ross, 1988, Chen et al., 2010 and Turgut et al., 2012). The principles of robust design are based on statistical methods to identify and quantitatively estimate the various parameters that affecting the design. Besides, the optimum parameters determined in the laboratory can be

reproduced in actual production (Kotcioglu et al., 2013). A full factorial design, which requires measuring all the design parameters, is costly and time consuming. However, by implementing the Taguchi method, only a certain combination of parameters according to an orthogonal array needs to be calculated and the target of the Taguchi method is to create a better parameter group and shorten the design period (Chen et al., 2010). Hence, the Taguchi method will be utilized to optimize the coating parameters effectively.

In the present study, the feasibility of replacing the polymer insulator of the cell with a Boron Nitride coating will be investigated. The Taguchi method with an orthogonal array L_9 (3^4) is used to optimize the coating parameters of the battery casing. Two factors, surface roughness of casing and coating thickness, which affect the coating quality, are investigated. The target performance measure is used to determine the main control factors that largely affect the coating performance. The significance and contribution of each factor is analyzed using Analysis of Variance (ANOVA). A confirmation test will be performed to validate the experimental design. Lastly, the influence of the conventional polymer insulator and Boron Nitride coating on the internal cell temperature distribution under various I_t-rates of constant current charging with forced convection will be discussed.

6.2 Model development

6.2.1 Experimental setup and procedures

The most important assessment of coating performance is the adhesion strength. The coating studies were conducted using commercial 18650 Li-ion battery casings. The battery casings were flattened and cut into specimens of 2 cm x 2 cm. The thickness of the casing was 0.3 mm. The samples were

152

polished with 300-1200 μm emery papers into different categories of surface roughness. Next, samples were ultrasonically cleaned using water for 10 min, followed by ethanol washing. Mean absolute deviation of the sample surface roughness (R_a) was measured using a profilometer (Talysurf-120). Boron Nitride refractory paint (Alfa Aesar) was coated on the sample by spraying in the horizontal direction on the first layer and the vertical direction on the second layer to yield a uniform coating as shown in Figure 6.2.
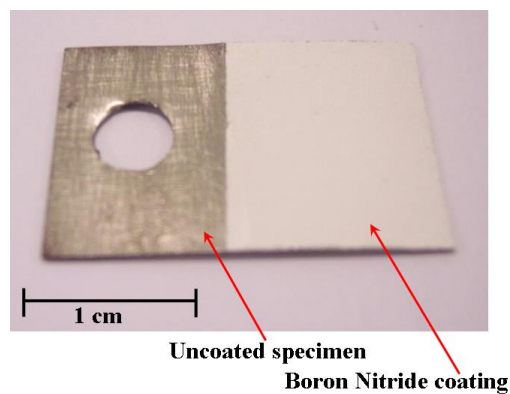
Figure 6.2 Coated specimen.

The samples were dried in open air for 12 hours. The thickness of the coating was measured with the cross section of the sample using Scanning Electron Microscope (SEM) (JEOL JSM-5600 LV). Besides, the surface topology of the samples was also characterized using SEM and illustrated in Figure 6.3.
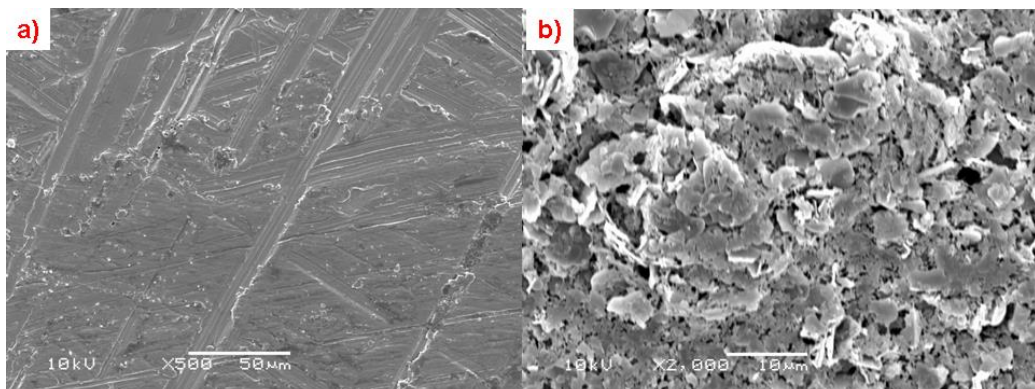
Figure 6.3 (a) Typical SEM micrograph of uncoated specimen at magnification of 500X. (b) Typical SEM micrograph of coated specimen at magnification of 2000X.

The left side of Figure 6.3 shows the surface topology of the polished specimen. Scratch lines were formed on the surface by emery papers. On the other hand, the right side of Fig. 3 shows the surface topology of the specimen coated with Boron Nitride. No pores were formed on the coated specimen and the specimen was fully protected by Boron Nitride coating. Adhesion measurements were conducted using a Nanoscratch tester (CSM Instruments). Additionally, a current leakage test was carried out by subjecting the sample to an open circuit voltage of $0 - 60$ V as shown in Figure 6.4. The purpose of the current leakage test is to assess the quality of coating and ensure that no leakage current flow across the coated specimen. In addition, it is also used to determine the minimum coating thickness required for a given voltage before the insulation effect breakdown.
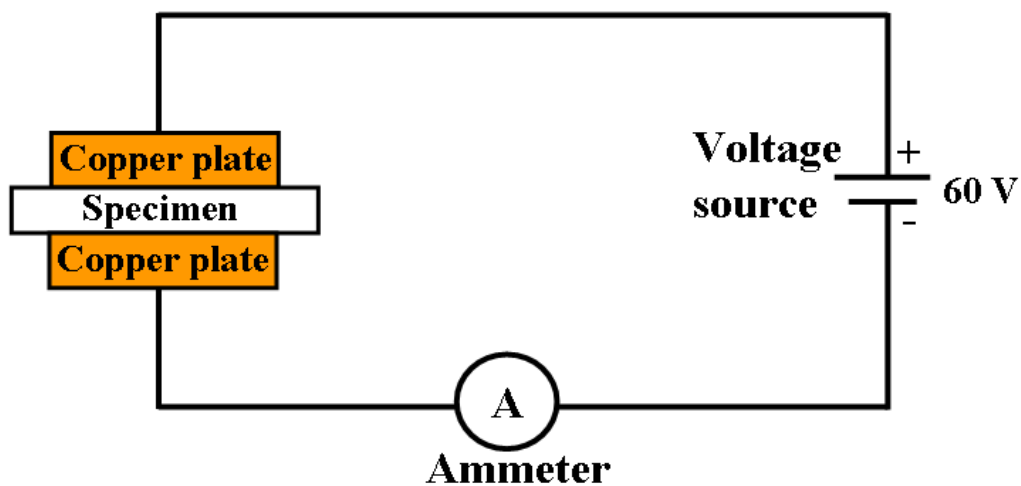
Figure 6.4 Current leakage test.

6.2.2 Design of experiments

Defining the quality characteristic is very important to the success of the design of experiment (DOE). The quality characteristic should be defined in term of quantifiable units. Besides, the quality characteristic is defined so that potential interactions between factors are minimized and additivity is assured

(Belavendram, et al., 1995). Additionally, the parameters are selected in such a way that the influence of the noise factors on the variation of the system performance is reduced. In this study, the parameters to be examined are surface roughness and coating thickness. The Taguchi parameters and level are tabulated in Table 6.2.

Table 6.2 The parameters and their levels used in the experiments.

Parameters	Level		
	1	2	3
A: Surface roughness, μm	0.05 – 0.10	0.11 - 0.30	0.31 - 0.53
B: Coating thickness, mm	0.09 - 0.10	0.25 - 0.26	0.35 - 0.36

To evaluate the effects of the parameters on performance (adhesion strength) and to optimize the parameters, an orthogonal array L_9 (3^4) as shown in Table 6.3 is selected for the DOE.

Table 6.3 Orthogonal array for L_9 (3^4) for coating experiment and SNR values.

Experiment No.	A	B	AB	$\bar{y}$, mN	S/N ratio (η)	Leakage, A
1	1	1	1	20.00	26.02	0
2	1	2	2	24.67	27.84	0
3	1	3	3	95.17	39.57	0
4	2	1	2	24.50	27.78	0
5	2	2	3	38.23	31.65	0
6	2	3	2	122.00	41.73	0
7	3	1	3	29.33	29.35	0
8	3	2	1	48.33	33.68	0
9	3	3	2	156.67	43.90	0

A L_9 (3^4) orthogonal array allows four 3-level factors to be considered in nine experiments. The DOE as follows: the first column was assigned to surface roughness (A), the second column was assigned to coating thickness (B) and the third column was assigned to (AB) to estimate the interaction between surface roughness and coating thickness. The experiments were performed for each combination of parameters and its level and repeated three times to obtain the average value of adhesion strength.

6.2.3 Analysis of the S/N ratio

There are two performance measures for Taguchi method analysis, which are noise performance measure (NPM) and target performance measure (TPM) (Belavendram, 1995). NPM is a measure of the variation of the response and to identify the control factors that largely affect variation and it is termed as variability control factors (Belavendram, 1995). The noise factors are external factors that will influence the outcome of the experimental results, but it is difficult to control in the field or the levels are expensive to control (Belavendram, 1995). The TPM is a measure of the mean response and to identify the control factors that largely affect the mean and it is termed as target control factors (Belavendram, 1995). In this study, the experimental observations are further transformed into a signal-to-noise (S/N) ratio. S/N ratio is the ratio of the mean (signal) to standard deviation (noise) and is used to evaluate the optimal parameters by taking the mean and variability into account (Belavendram, 1995). Three types of standard S/N ratios are generally used such as "nominal the best", "smaller the best" and "larger the best" (Belavendram, 1995). Since the coating thickness and surface roughness of the casing are proportional to the manufacturing cost, "nominal the best" is selected. "Nominal the best" as in Equation 6-1 is chosen to obtain the optimum coating parameters (Belavendram, 1995).

$$\eta = 10 \, log_{10} \left(\frac{\bar{y}^2}{\sigma^2} \right) \tag{6-1}$$

Where $\bar{y}$ represents the average experimental results (y) of the adhesion strength under experimental conditions, while σ represents the variance of the experimental results y.

6.2.4 Analysis of Variance

ANOVA is a key technique for analyzing the effect of categorical factors on a response (Bendell et al., 1989). ANOVA is used to analyze the results of the orthogonal array of experiments by partitioning variability into identifiable sources of variation. Besides, the significant effect of a factor on the adhesion strength and the variation attributed to each factor can be rapidly identified, thus reducing the time required for experimental work (Bendell et al., 1989). The influential degree of each factor on the adhesion strength can be determined through the percentage of contribution of the design parameters.

6.2.5 Thermal model

The thermal model of the 18650 LFP cell is shown in Figure 3.4. The battery consists of several layers of electrodes and separator wounded spirally into a cylinder. The cavity in the center of the cell is fully filled with electrolyte $LiPF_6$. In this study, the spiral wound region is assumed to be a single active material domain and the thermal conductivity is considered anisotropic because the thermal conductivity of the cell in the axial direction is higher than the radial direction (Chen et al., 2006). The thermal conductivity of the cell in radial and axial direction is defined as in Equation 3-31. The thermal conductivity of the active material in the cell in x, y and z direction is defined as in Equation 3-32. The total density of the active material in the cell is expressed in Equation 3-33. The total heat capacity of the active material in the cell is expressed in Equation 3-34. The physical and thermal properties of the 18650 cell are presented in Table 3.1. The general energy equation used to model the heat conduction of the cell is defined in Equation 6-2 (Fang et al., 2010).

$$\rho_{eff} C_{p,eff} \frac{dT}{dt} = \nabla \cdot k_{T,eff} \nabla T + Q_{gen} \qquad (6\text{-}2)$$

With the boundary conditions at the outer surface of the cell is defined by Newton's cooling law and thermal radiation as in Equation 3-26. Heat generated of the cell during constant current charging at increasing state of charge is measured using accelerating rate calorimeter (ARC, THT). The charging of the single cell was carried out using 3 and 5 I_t-rates of constant current charging. The heat generated data were then input into the thermal model to predict the internal temperature of the cell. In the numerical modeling, the thermal resistance film gap for the imperfection of polymer insulator wrapping is assumed to be 0.3 mm based on a worst case scenario. The typical heat transfer coefficient for liquid cooling is within 100-20000 $Wm^{-2} K^{-1}$ (Incropera et al., 2007). In the current study, a moderate liquid condition with h = 500 $Wm^{-2} K^{-1}$ is used in the modeling to compare the thermal performance of the cell using polymer insulator and Boron Nitride coating.

6.2.6 Numerical modeling

The thermal model of the 18650 cell, together with appropriate boundary conditions was solved with commercial finite element solver, COMSOL Multiphysics 4.3. Triangular element was used to mesh the geometry and direct solver PARDISO was chosen with a relative convergence tolerance of 10^{-6} for the modeling. All computations were carried out on a computer with a 3.40 GHz Quad core processor and 32 GB Random Access Memory (RAM). In addition, the grid independent test was carried out to refine the gird size of the model until the simulation results are not affected by further refinement of the mesh and error of the results is less than 5%.

6.3 Results and discussion

6.3.1 Analysis of the S/N ratio

The average S/N values obtained for each experiment are presented in Table 6.4 and Figure 6.5.

Table 6.4 Average S/N ratios for adhesion strength.

Control factors	Average S/N ratios		
	A	B	AB
Level 1	27.51	25.32	30.37
Level 2	32.64	27.30	31.95
Level 3	31.34	38.88	29.17
Delta	4.50	13.56	2.78
Rank	2	1	
Characteristic type	Nominal the best		
Optimum	A2	B3	
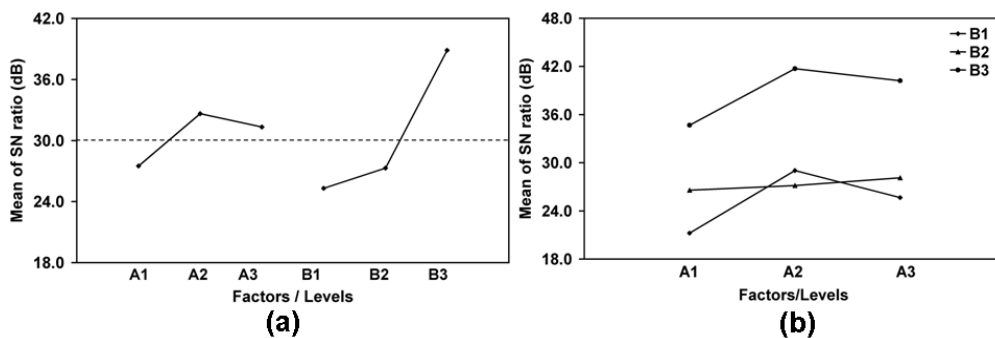
Figure 6.5 (a) The effect of design parameters on adhesion strength.
(b) Interaction graph of design parameter of A and B.

As shown in the Figure 6.5(a), the larger slope means that the effect of the control factor on the performance characteristic is more significant. Besides, the largest S/N ratios for each control factor provide an optimum performance. The effect of A is 5.13 dB while the effect of B is 13.56 dB. This also means that the coating thickness plays a more important role than the surface roughness in affecting the adhesion strength. Increasing the thickness of the coating to 0.35-0.36 mm will lead to improving of adhesion strength by 400% under experimental conditions. On the other hand, increasing the surface roughness of the sample to 0.53 μm will only lead to increasing of adhesion strength by 68% under experimental conditions. Based on the "nominal the

159

best" transformation, the recommended optimal level of surface roughness is A2 (0.11-0.30 μm) and B3 (0.35-0.36 mm) for coating thickness. The interaction of factors A and B is illustrated in Figure 6.5(b). Analysis of these interactions shows that there is a strong interaction on level 2 of factors A and B. Average S/N ratios for interaction AB on level 2 is 31.95 dB. On the other hand, the control factors have relatively weak interaction among each other on level 1 and level 3 but they do have an effect on the adhesion strength. As shown in Table 4, average S/N ratio of interaction AB at level 1 and level 3 is 30.37 dB and 29.17 dB respectively and lower than interaction AB at level 2.

6.3.2 Analysis of Variance

The results of the analysis are presented in Table 6.5.

Table 6.5 Results of the analysis of variance.

Source	Sum of squares, SS	Degree of freedom, df	Variance, V	F-test	Contribution, %
A	4468.84	2	2234.42	34.41	7.21
B	53454.01	2	26727.00	411.56	88.61
AB	953.68	2	476.84	7.34	1.37
Error	1298.82	20	64.94	1.00	2.81
Total	60175.34	26	2314.44	-	100.00
Mean	104119.34	1	-	-	-
Total sum of squares	164294.689	27	-	-	-

F-test of 99% confidence is used as a reference tool to identify the significant factors that affect the performance characteristics in this study. An alpha-error of 1%, $\alpha = 0.01$, $v1 = 2$ and $v2 = 20$ is determined from the F-table and $F_{0.01,2,20} = 5.85$. Since factor A (34.41) and B (411.56) is much larger than 5.85, it can be inferred that factor A and B are significant. Moreover, interaction of A and B with F-ratio of 7.34 showed that interaction between A and B is significant and interdependent. Coating thickness was found to be the most significant parameter affecting the adhesion strength (88.61%). The

contribution of surface roughness is about 7.21%. The contribution due to error provides an estimate of the sufficiency of the experiments. The error is referred to the unknown or uncontrolled factors. Hence, the contribution of the error can be employed as an effective tool to evaluate the sufficiency or insufficiency of the experiment. Since the contribution of error in this study is about 2.8%, which is low enough to indicate that the experiment is sufficient and no important factors have been overlooked.

6.3.3 Confirmation tests

The optimum parameters are determined through the S/N ratio analysis and F-test in the ANOVA analysis. Next, a confirmation test was planned to predict and validate the improvements of the adhesion strength using the optimum parameters A2 and B3. This combination was found in the orthogonal array experiment (Trial number 9). The predicted mean of response (PV) can be calculated from Equation 6-3 (Belavendram, 1995):

$$PV = \bar{y} + \left(A2 - \bar{y}\right) + \left(B3 - \bar{y}\right) \qquad (6\text{-}3)$$

The predicted mean of response is 124.09 mN. A confirmation run that generates adhesion strength close to 124.09 mN would verify the assumptions of the Taguchi method. Three experiments were carried out to verify the adhesion strength at optimum level of A2 and B3 and the values obtained were 123 mN, 125 mN and 129 mN with an average value of 125.67 mN. This suggests that the implementation of the Taguchi method in optimizing the coating parameters is successful.

6.3.4 Thermal analysis of the battery

Figure 6.6 shows the experimental results of the heat generated of the 18650 cell during 3 and 5 I_t-rates of constant current charging. The maximum heat generated of the cell is 2.79 W and 4.89 W respectively for 3 and 5 I_t-rates of constant current charging. In addition, the effect of Boron Nitride coating on the temperature distribution across the 18650 LFP cell under moderate liquid cooling condition with h = 500 $Wm^{-2} K^{-1}$ were investigated.
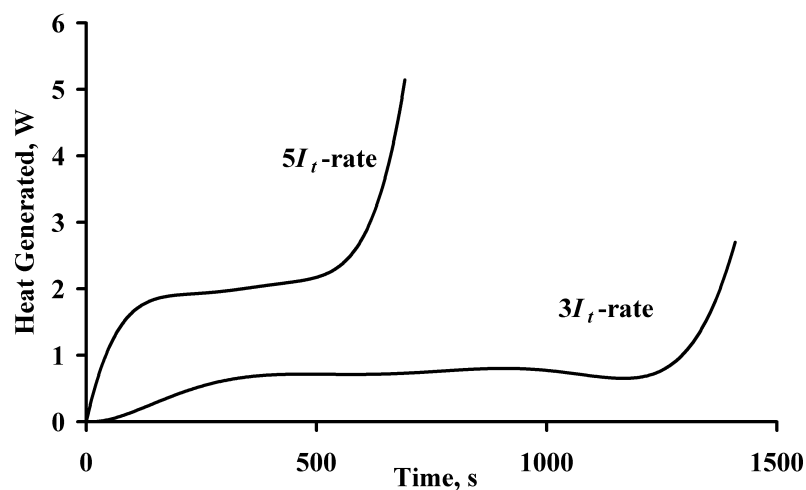
Figure 6.6 Heat generated of the cell at 3 and 5 I_t-rates of constant current charging.

Figure 6.7 shows the temperature distribution across the cell with conventional polymer insulator and battery casing coated with Boron Nitride at the end of the charging process.
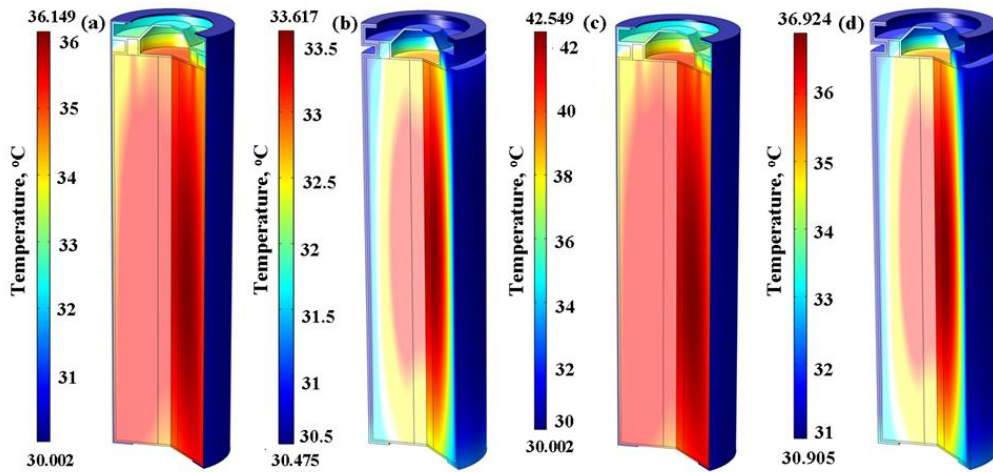
Figure 6.7 Internal temperature distribution of the 18650 cell. (a) 3 I_t-rate of constant current charging with polymer insulator. (b). 3 I_t-rate of constant current charging with Boron Nitride coating. (c) 5 I_t-rate of constant current charging with polymer insulator. (d). 5 I_t-rate of constant current charging with Boron Nitride coating.

The maximum temperature is situated in the active material region near the center cavity. As shown in Figure 6.7(a) and Figure 6.7(b), the maximum temperature of the cell during 3 I_t-rate of constant current charging is effectively suppressed from 36.1 ^{o}C to 33.6 ^{o}C when the battery casing is coated with Boron Nitride. As shown in Figure 6.7(c) and Figure 6.7(d), for 5 I_t-rate of constant current charging, the temperature of the cell could reach 42.5 ^{o}C with conventional polymer insulator while the maximum temperature of the battery casing coated with Boron Nitride is only 36.9 ^{o}C. The optimum operating temperature of Li-ion battery is within 25 ^{o}C to 40 ^{o}C for optimum performance and calendar life (Peseran, 2002). Hence, internal temperature of the cell casing coated with Boron Nitride is still within the optimum operating temperature of the Li-ion battery. Polymer insulator creates a thermal resistive film and prevents the heat generated from the cell being effectively transferred to the outer environment and a large temperature gradient was developed inside the cell. According to Arrhenius law (equation 6-3) (Kuper et al., 2009), when the temperature of the cell is increased by 10 ^{o}C to 15 ^{o}C, the life cycle

163

of the cell will decrease by about 30% to 50%. For a long period of operation, the internal resistance of the cell will increase and thus reducing the total charging capacity of the cell. Besides, the cell is more prone to thermal explosion at high temperature (Kuper et al., 2009).

$$k_{aging} = exp(-\frac{E_a}{RT})$$ (6-3)

This is a significant adverse effect and should be accounted for the thermal management design of the Li-ion battery. The boron nitride coating will enhance the heat transfer from the cell to the surroundings and also ensure good thermal contact between the battery and the cold plate or cooling fin while maintaining adequate electric insulation.

A worth noting issue is the cost of the Boron Nitride coating, which may be higher than the polymer insulation. However, the cost increment according to the lab scale study is minimal ($< 5\%$) as compared to the cost of battery. The cost may be reduced during mass production stage. A cost effectiveness analysis may show that it is worthwhile to have Boron Nitride coating on batteries, especially fast charging battery.

6.4 Summary

In this study, the influence of the battery casing surface roughness and coating thickness of the Boron Nitride was optimized by the Taguchi experimental design method. The optimum parameters combination of casing surface roughness, coating thickness and the interaction of the parameters was obtained using analysis of S/N ratio and analysis F-test. The "Nominal the best" criteria was chosen to optimize the parameters to yield a minimum manufacturing cost and can be easily implemented in practice. The significance of the factor and the contributions on the performance

characteristic were determined using ANOVA. All the parameters are considered to be within 99% confidence level. The optimum combination of parameters is with surface roughness of 0.11-0.30 μm and the coating thickness of 0.35-0.36 mm. It is shown that the surface roughness of casing and coating thickness are correlated and they play a significant effect on the adhesion strength. At a high I_t-rate of charging, the conventional polymer insulation may create a substantial temperature gradient inside the cell. This is not favored from the perspective of thermal management and cycle life of the cell. Moreover, the cell is more prone to thermal aging and thermal explosion as compared to the battery casing coated with Boron Nitride. In addition, battery surface coated with Boron nitride also enables the cold plate to be attached directly to the battery casing for effective heat transfer.

CHAPTER 7

AIR COOLING SYSTEM WITH AIR FLOWING PARALLEL TO CYLINDRICAL CELLS

7.1 Introduction

After investigating the thermal behavior of a unit cell in the last chapter, the next step is to construct a thermal management system for a group of cells in a battery pack. In this study, the performance of an air-cooled battery pack made up of cylindrical 38120 cells was investigated, where the cooling air flows in the spaces between the cylinders parallel to the axis of the cells. The battery heat generation was characterized using an accelerating rate calorimeter under constant current charging. Average heat generated in the cell at 3 I_t-rate was used in the steady state simulation to investigate the temperature distribution of the cells in the battery pack under different cooling conditions. The heat transfer correlation is subsequently deduced from the simulation results and compared with open literature. Finally, experimental testing of the battery pack at different charging rates was carried out to validate the mathematical model.

7.2 Battery pack design

A battery pack consisting of twenty-four pieces of commercial LFP cells with an electric configuration of 12S2P (12 cells in series and 2 cells in parallel) was developed for the current study as shown in Figure 7.1.
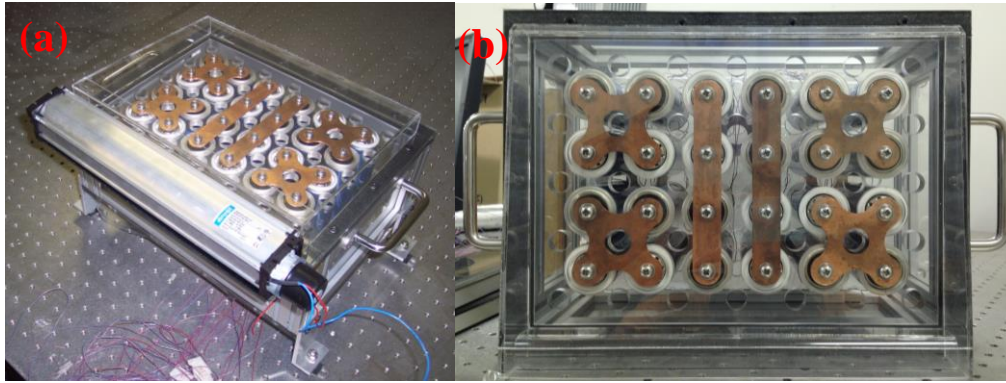
Figure 7.1 (a). Overview of battery pack. (b). Top view of battery pack.

The nominal voltage and capacity of the battery pack were 38.4 V and 16 Ah, respectively. Specifications of the LFP cell used in the modeling are summarized in Table 4.1. The cells were attached to copper bus bars with screws to form the battery array. The arrangement of the batteries in the pack was based on a close-pack structure. The spacing between the cells was 5 mm and 15.50 mm diameter venting holes were created on the holding plate in between four cells to allow cooling air to flow uniformly over the cell surfaces. The pack casing was made of aluminum and plexiglass. Anti-vibration rubber mounts were attached at the bottom of the battery pack to insulate the cells from possible vibration that will be harmful to the electrical connection of the battery pack. Tapered intake and exhaust plenums were used to direct the cooling air flow uniformly to each row of cells.

A constant flow rate of air was provided to the cells through the tangential blower. Cooling air was constricted when its flows through the venting holes and expanded to the cell surfaces. Similarly, constriction and expansion of cooling air occurred again when the cooling air flow out to the exhaust plenum through venting holes in the holding plate. The process of constriction and expansion will induce a pressure drop along the flow path. Besides,

constriction and expansion of cooling air will also result in significant cooling effects at both terminals of the cell (Sabbah et al., 2008).

7.3 Numerical and experimental procedures

7.3.1 Numerical procedures

Computation Fluid Dynamic (CFD) software-ANSYS-CFX was used to complement the experimental study and understand the flow field that is difficult to be observed in the experiment. The governing equations used to solve the time dependent three-dimensional flow problems which involve heat transfer are the continuity equation, momentum equation, energy equation and equation of state given in Equations 7-1 to 7-7 (Versteeg and Malalasekera, 1999). The momentum equations are also known as the Navier-Stokes equations.

Continuity equation:

$$\frac{\partial \rho}{\partial t} + \nabla \cdot (\rho \mathbf{u}) = 0 \tag{7-1}$$

X-momentum:

$$\frac{\partial (\rho u)}{\partial t} + \nabla \cdot (\rho u \mathbf{u}) = -\frac{\partial P}{\partial x} + \nabla \cdot (\mu \nabla u) + S_{Mx} \tag{7-2}$$

Y-momentum:

$$\frac{\partial (\rho v)}{\partial t} + \nabla \cdot (\rho v \mathbf{u}) = -\frac{\partial P}{\partial y} + \nabla \cdot (\mu \nabla v) + S_{My} \tag{7-3}$$

Z-momentum:

$$\frac{\partial (\rho w)}{\partial t} + \nabla \cdot (\rho w \mathbf{u}) = -\frac{\partial P}{\partial z} + \nabla \cdot (\mu \nabla w) + S_{Mz} \tag{7-4}$$

According to the first law of thermodynamics, the rate of change of energy of a fluid particle is equal to the rate of heat addition to the fluid

particle plus the rate of work done on the particle (Versteeg and Malalasekera, 1995). This yield the following equation:

$$\frac{\partial(\rho i)}{\partial t} + \nabla \cdot (\rho i \mathbf{u}) = -p \nabla \cdot \mathbf{u} + \nabla \cdot (k \nabla T) + \Phi + S_i \qquad (7\text{-}5)$$

Four unknown thermodynamic variables (ρ, P, i and T) from the five partial differential equations: mass conservation, x-, y- and z-momentum equations and energy equation can be obtained through thermodynamic equilibrium. Equations of state relate the other variables to the two state variables. For a perfect gas the following equations provide the link between the variables (Versteeg and Malalasekera, 1995).

$$P = \rho RT \qquad (7\text{-}6)$$

$$h_f = \int_{T_{ref}}^{T_f} C_{pf} dT_f \qquad (7\text{-}7)$$

7.3.2 SST turbulence model

The SST turbulence model is employed to predict the flow behavior in the present study. The SST model has proven to be stable and numerically robust and has a good predictive capability to give a good compromise between accuracy and robustness. Besides, the SST model has been designed to give accurate predictions of the onset and the amount of flow separation under adverse pressure gradients by the inclusion of transport effects into the formulation of the eddy-viscosity. The superior performance of the SST model is validated by a large number of studies (Huang et al., 1997). The SST model is also recommended for high accuracy boundary layer simulations. In free shear flows, the SST model is identical to the k-ε model. In addition, the SST model has been developed to overcome deficiencies in the k-ω and BSL k-ω model. One of the advantages is the near-wall treatment for low-Reynolds

number computations. The SST model also incorporates a slight modification to the eddy viscosity for better prediction of the turbulent shear stress. The details of the SST model can found in Sparrow et al., 2009, Menter et al., 2003 and Lee et al, 2013. The transport equations for the SST model are given below:

$$\frac{\partial(\rho k)}{\partial t} + \frac{\partial(\rho U_i k)}{\partial x_i} = \tilde{P}_k - \beta^* \rho k \omega + \frac{\partial k}{\partial x_i}\left[(\mu + \sigma_k \mu_t)\frac{\partial k}{\partial x_i}\right] \qquad (7\text{-}8)$$

$$\frac{\partial(\rho \omega)}{\partial t} + \frac{\partial(\rho U_i \omega)}{\partial x_i} = \alpha \rho S^2 - \beta \rho \omega^2 + \frac{\partial}{\partial x_i}\left[(\mu + \sigma_\omega \mu_t)\frac{\partial \omega}{\partial x_i}\right]$$
$$+ 2(1 - F_1)\rho \sigma_{\omega 2}\frac{1}{\omega}\frac{\partial k}{\partial x_i}\frac{\partial \omega}{\partial x_i} \qquad (7\text{-}9)$$

where the blending function F_1 is defined by:

$$F_1 = tanh\left\{\left\{min\left[max\left(\frac{\sqrt{k}}{\beta^* \omega y}, \frac{500v}{y^2 \omega}\right), \frac{4\rho \sigma_{\omega 2} k}{CD_{k\omega} y^2}\right]\right\}^4\right\} \qquad (7\text{-}10)$$

where y is the distance to the nearest wall.

F_1 is equal to zero away from the surface (k-ε model) and switches over to one inside the boundary layer (k-ω model)

$$CD_{k\omega} = max\left(2\rho \sigma_{\omega 2}\frac{1}{\omega}\frac{\partial k}{\partial x_i}\frac{\partial \omega}{\partial x_i}, 10^{-10}\right).$$

The energy equation for the cell is given by:

$$mC_p\frac{dT_c}{dt} = \nabla(\lambda_c \nabla T_c) + Q_{gen} \qquad (7\text{-}11)$$

A steady state conjugate heat transfer simulation was performed to predict the thermal performance of the battery pack with all the time derivative terms in Equations 7-1 to 7-5 equal to zero. The cylindrical 38120 LFP cell was modeled with a uniform volumetric heat source and anisotropic thermal

conductivity. A heat generation rate of 4 W (corresponding to the average heat generation rate during 3 I_t-rate of charging) per cell was used for the steady state simulation. The heat generated in each cell in the battery pack was assessed to be uniform. The contact resistances at the cell terminals were not modeled in this study.

The CAD model of the battery pack used for the simulation and cooling air flow path is shown in Figure 7.2.
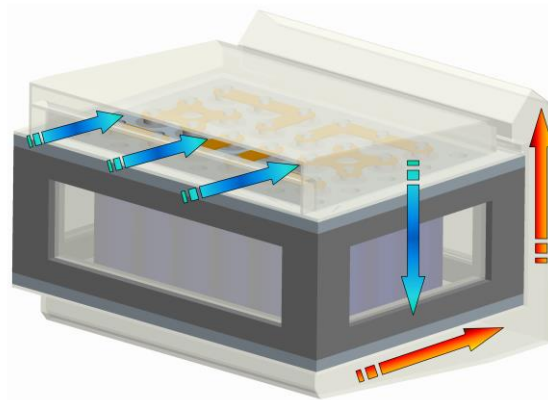
Figure 7.2 Battery pack CAD model and cooling air flow path.

A hybrid meshing was adopted to discretize the battery pack domain into 58511496 elements using ANSYS ICEM CFD 14.0 SP1. The coolant was air which was assumed to be an ideal gas. Since, the tangential blower of the battery pack operated in blowing mode, the intake of the battery pack was given a mass flow boundary condition while the pressure boundary condition was assigned to the outlet. The intake air temperature was kept at 30 ^{o}C. The confining walls on the top, side and bottom of the battery pack were specified as no slip, adiabatic wall boundary conditions. Heat loss through the battery pack casing in the CFD analysis is assumed negligible. The Shear Stress Transport (SST) turbulence model was selected for this study. This model will provide accurate prediction from laminar to turbulent flow and near-wall boundary conditions. Besides, it also utilized automatic wall treatment for

maximum accuracy in wall shear and heat transfer predictions as well as capturing the streamline curvature (Ansys, 2010). The computational domain was initialized with ambient conditions at 1 atmospheric pressure. CFX solver was used to solve the governing equations for the conservation of mass, momentum and energy. All simulations were executed with a high resolution scheme to achieve an accurate solution. A tight convergence criterion with an RMS of 1.0×10^{-6} is applied to the continuity, momentum and energy equations (H-energy and T-energy) for all case studies. It was also ensured that there is no domain imbalance in momentum and energy. All simulations were computed on the 8 node-HP cluster. In addition, grid independence tests were carried out to refine the grid size until the simulation results were not affected by any further refinement of the mesh and the relative error of the results (cell temperature and pressure drop across the battery pack) is kept within 5%. Total computation time is about 52 hours 20 minutes.

In an actual charging process, a battery may not reach thermal steady state because of the short charging time, especially during fast charging when high current is involved. The common sense may lead to the idea that a comprehensive three dimensional transient modeling is more straightforward and powerful to capture the temperature distribution and evolution within the battery pack. 3D transient modeling can be conducted by importing the transient heat generation rate as a function of time into the CFD model. However, 3D transient modeling for a large battery pack is a tedious and time-consuming undertaking because of the complex air flow dynamics and the conjugate heat transfer between various cells and the air flow in the battery pack. A steady state CFD simulation takes about 52 hours 20 minutes for each

172

run on the 8-nodes-HP cluster and the computing time and results file size for the 3D transient simulation may build up to an unacceptable level, making it impractical for the current study. Therefore, in this study, the steady state modeling focuses on the investigation of temperature distribution and uniformity of the cells in the battery pack. Then, a correlation of Nu number to Re number was developed based on the steady state simulations to evaluate the cooling effectiveness of the battery pack thermal management system in transient state. The effective heat transfer coefficient derived from the steady state modeling was assigned to the surfaces of each cell to account for the convective heat transfer there. This simplified method is based on the fact that there is only a small change in the air temperature and only a minor difference in temperature among the cells.

7.3.3 Experimental setup and parameter extraction

Commercial 38120 LFP cells with a capacity of 8 Ah were used in the experimental study. The charge and discharge processes of the cell were performed using a battery cycler (Maccor Instrument 4000). The specific heat capacity of a single cell was measured using an adiabatic accelerating rate calorimeter (THT ARC). Heat generated in a single cell during constant current charging at increasing state of charge was measured using the ARC. The charging of the single cell and the battery pack were carried out using three different charging rates, namely 1, 3 and 5 I_t-rates. The charging current for 1, 3 and 5 I_t-rates is 8, 24 and 20 A, respectively. The tangential blower of the battery pack was set to operate at its maximum flow rate ($\dot{m} = 30 \, \text{gs}^{-1}$). The air flow rate was measured by a digital air velocity meter (TSI, velociCalc 9565-P). A differential pressure transducer (Gems sensor, 5266 series) was

connected to the pressure taps at the intake and exhaust plenum to measure the pressure drop across the battery pack. The cells were fully discharged to 2.0 V before the charging experiment started. The battery pack was placed in a temperature chamber (Weiss, T1500) and the chamber temperature was set to 30 ^{o}C. The experiment was initiated after the cells had achieved an equilibrium temperature of 30 ^{o}C. Twenty seven T-type thermocouples were used in the experiment. Two thermocouples were attached to the intake and exhaust plenum of the battery pack to measure the intake and exhaust air temperatures. One thermocouple was placed outside the battery pack to measure the environment temperature in the chamber. While the temperature of the cell surfaces was measured using twenty four thermocouples attached to the center of the cell body. Measurements of battery surface temperature during different charging rates were done at an ambient temperature of 30 ^{o}C for air cooling of 30 gs^{-1}. A HP 34970A data acquisition system was used to record the temperature readings. All the tests were repeated three times and the average value was taken. The experimental results were compared with numerical results under similar cooling conditions.

7.3.4 Data processing

The steady state of heat transfer from the cells to the air in the battery pack can be expressed as follows (Sahin et al., 2004):

$$\dot{Q}_{total} = \dot{Q}_{conv} + \dot{Q}_{rad} + \dot{Q}_{loss} \qquad (7\text{-}12)$$

$$\dot{Q}_{conv} = \dot{m}C_p\left(T_{out} - T_{in}\right) \qquad (7\text{-}13)$$

Besides, the rate of convective heat transfer from the cells can also be expressed as

$$\dot{Q}_{conv} = \bar{h} A_{ext} \left[T_s - \left(\frac{T_{out} + T_{in}}{2} \right) \right] \qquad (7\text{-}14)$$

The battery casing is made of highly polished Aluminum and the emissivity is low. Therefore, the radiation heat loss was neglected. In the simulation, the battery pack was assumed well insulated and no leakage occurred. Therefore, Equation 7-12 can be further reduced to

$$\dot{Q}_{total} = \dot{Q}_{conv} \qquad (7\text{-}15)$$

The steady state heat transfer rate through the air is equal to the heat loss of the cells, and the average convective heat transfer coefficient can be deduced via Equation 7-16 (Sahin et al., 2004).

$$\bar{h} = \frac{\dot{Q}_{conv}}{A_{ext} \left[\bar{T}_s - \left(\frac{T_{out} + T_{in}}{2} \right) \right]} \qquad (7\text{-}16)$$

The Reynolds number for the cooling air is calculated using Equation 7-17 (Sahin et al., 2004):

$$Re = \frac{\rho U_{\infty} D}{\mu_{\infty}} \qquad (7\text{-}17)$$

The mass flow rate of cooling air, $\dot{m}$ is based on the measured mean velocity of the air supply by the tangential blower and is given by

$$\dot{m} = \rho A_{duct} U_{\infty} \qquad (7\text{-}18)$$

where

$$A_{duct} = WH \qquad (7\text{-}19)$$

The Nusselt number and ideal fan power are calculated using Equation 7-20 and Equation 7-21 (Wiberg and Lior, 2004 and Kays and London, 1964), respectively.

$$Nu = \frac{hD}{k} \tag{7-20}$$

$$P = \Delta P \dot{V} \tag{7-21}$$

The Nusselt number calculated from the CFD model is then correlated with the Reynolds number Re according to Equation 7-22 for different flow rate of cooling air (Wiberg and Lior, 2004). *C* and *n* were determined for various Re through least-mean-squares fit,

$$Nu = C\,Re^{n} \tag{7-22}$$

The correlation is then used to predict the average surface temperature change of the cell under various charging rate.

7.4 Results and discussion

7.4.1 Heat generation in the cell

In order to show the accuracy of the measurements, uncertainty analysis was preformed according to the method suggested by Moffat (Moffat, 1988). The uncertainties in this study were determined by the root-sum-square method. The results are shown in Table below. Average uncertainty measurement of the battery body temperature in the accelerating rate calorimeter and battery pack is about 1.03% and 2.21%, respectively.

Table 7.1 Average uncertainties analysis of the variables.

Properties	Average uncertainty, %
Specific heat capacity, %	2.43
ΔT_{batt}, ^{o}C (in ARC)	1.03
ΔT_{batt}, ^{o}C (in battery pack)	2.21
Heat generation, W	3.31
A_{duct}, m^2	2.27
Fan power ,W	4.29
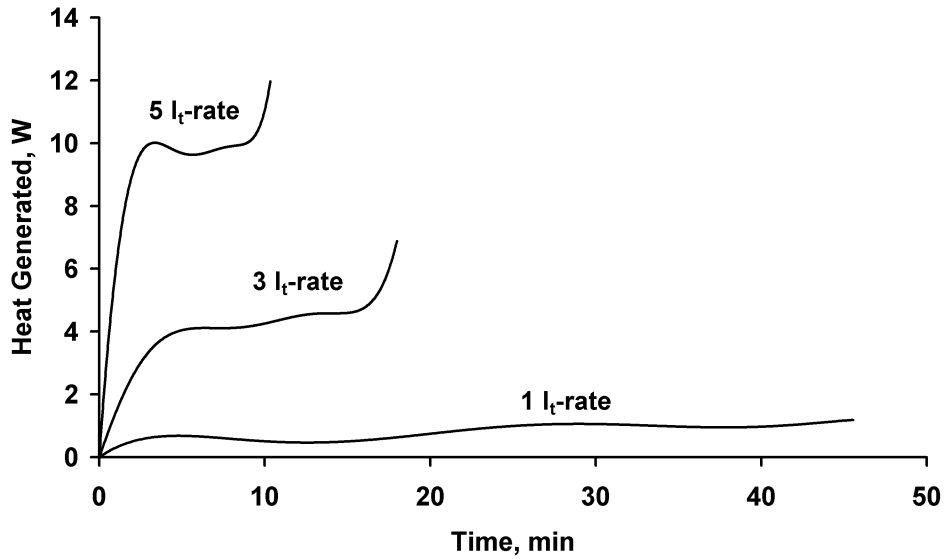
Figure 7.3 Heat generated in the cell during various I_t-rate of constant current charging.

Figure 7.3 shows the heat generated in the cell measured in the ARC from 0 to 100% SOC at 1, 3 and 5 I_t-rates of constant current charging. A sharp increase in the heat generated in the cell was found at 90% SOC or greater. This is due to a sudden increase in the ohmic heat towards the end of the charging process. As shown in Figure 7.3, the average heat generated in the cell at 1, 3 and 5 I_t-rates are about 0.84 W, 4.28 W and 9.48 W respectively.
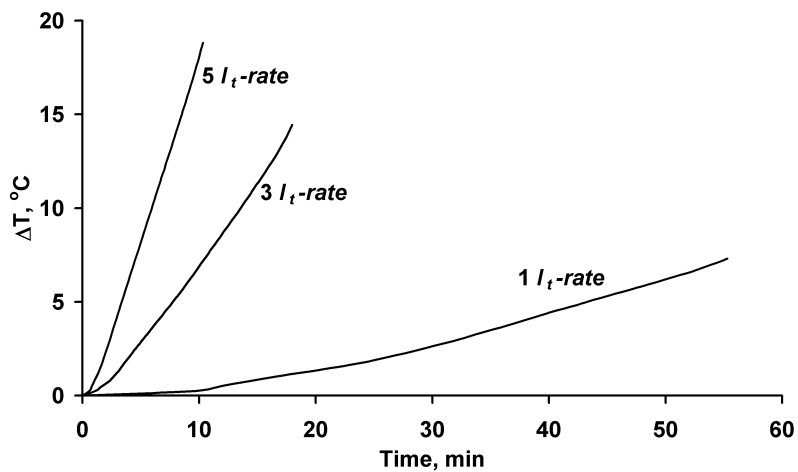
Figure 7.4 Experimental cell surface temperature at various I_t-rates of constant current charging.

As shown in Figure 7.4, the temperature rise at the cell surface in the adiabatic calorimeter is about 7.3 ^{o}C, 14.4 ^{o}C and 18.8 ^{o}C for 1, 3 and 5 I_t-rates, respectively. The ambient temperature in Singapore is about 30 ^{o}C and at 1 I_t rate of charging, the cell surface temperature may reach 37.3 ^{o}C without cooling. Even though the surface temperature of the cell is within the optimum operating temperature range for the Li-ion battery, the internal temperature of the cell may exceed the optimum operating temperature limit. According to previous studies, large thermal resistance of the active material in the large cylindrical battery will cause about 5 ^{o}C of temperature difference between the center and the surface of the cell at the end of 3 I_t-rate of discharging with heat generation of 14W and subjected to natural convection cooling (h = 8 $Wm^{-2}K^{-1}$). Although the internal resistance of the cell is reduced at high temperatures, thermal aging of the cell is more severe and the cycle life span of the cell is also reduced (Jin et al., 2014 and Kuper et al., 2009). Hence, an active thermal management system is needed to prolong the cycle life of the cell and optimize the cell performance by operating the battery between 0 ^{o}C to 40 ^{o}C.

7.4.2 Fluid flow analysis results

For the battery pack thermal management system design, steady state CFD simulations were performed using a mass flow rate of 5 to 75 gs^{-1} at 30 ^{o}C. High resolution of the mesh and fluid-thermal CFD model is important to capture the flow field and conjugate heat transfer in the battery pack. The typical velocity contour plot of the battery pack with the mass flow rate of 40 gs^{-1} is shown in Figure 7.5.
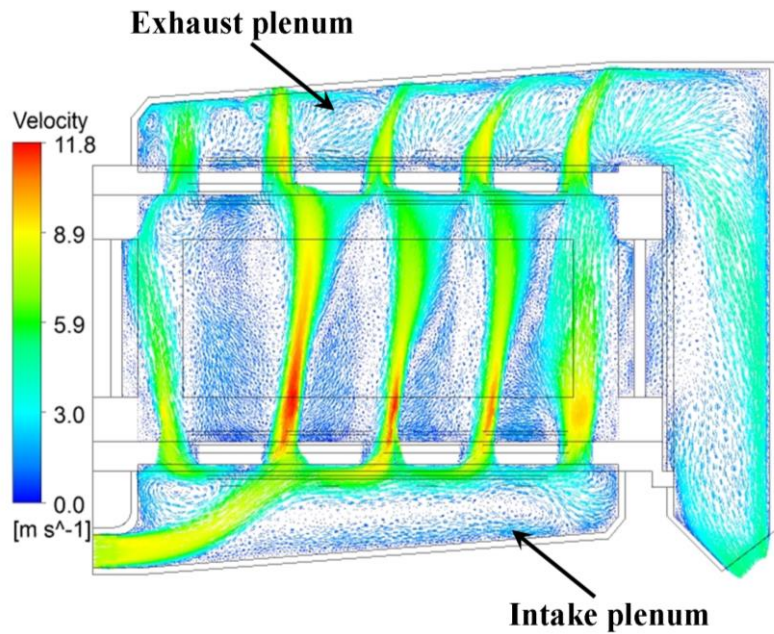
Figure 7.5 Velocity contour of airflow through the intake plenum, battery compartment and exhaust plenum.

The cooling air is rapidly accelerated into the battery pack through the narrow intake plenum and venting holes, creating local high entrance velocities and a large entrance pressure drop. The cooling air is also rapidly accelerated to the battery compartment due to the large contraction in the face area of the venting hole, resulting in high heat transfer coefficients on the battery surfaces.

In order to achieve uniform parallel air distribution, the air intake and exhaust plenum need to be designed carefully to obtain a uniform air flow to the battery compartment and minimize parasitic pressure drop. The recirculation flow and turbulence must be minimized. Moreover, the intake plenum design must be able to keep the inflow streamlined. A streamline plot of the cooling air, which could provide qualitative analysis of the cooling air distribution in the battery pack is shown in Figure 7.6.
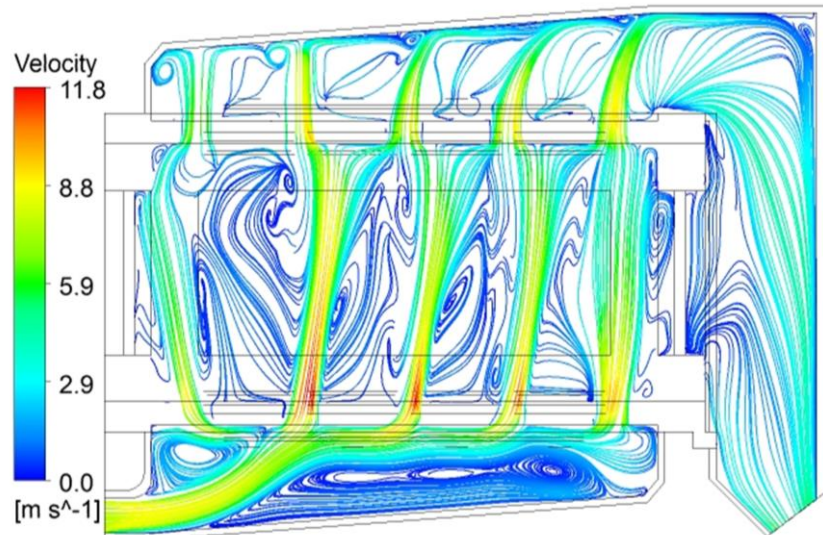
Figure 7.6 Surface streamline plot of air flow path in the battery pack.

The flow of cooling air has reasonable streamlines except at the front end of the intake plenum and corner of the battery compartment. Chamfers at the end of the intake plenum and taper design help to divert more flow to the last row of the cells and reduce creation of local turbulence that will cause an additional pressure drop. Cooling air is supplied by the tangential blower to the battery compartment through the venting holes. After picking up waste heat from all the cells, the warmed air is the discharged to the exhaust manifold through venting holes and recombines in the exhaust plenum. Air exits the battery pack through tapered exhaust manifold and finally dumped out to the outer environment.

7.4.3 Temperature variation analysis

Figure 7.7 shows the average temperature average temperature of the cells in the battery pack for mass flow rates of 5 to 75 gs^{-1}. The highest temperature was achieved at a mass flow rate of 5gs^{-1} and gradually reduced to 33.2 ^{o}C at a mass flow rate of 75 gs^{-1}. At a flow rate of 40 gs^{-1}, the average temperature of the cell is reduced to 35.7 ^{o}C. The variations of the cell are about 6 ^{o}C for mass flow rate of 5 gs^{-1} and are gradually reduced to about 1.5 ^{o}C at 75 gs^{-1} as

shown in Fig. 7.7. At 40 gs^{-1} the average variation of the cells surface temperature is about 1.7 ^{o}C and this is within the allowable limits.
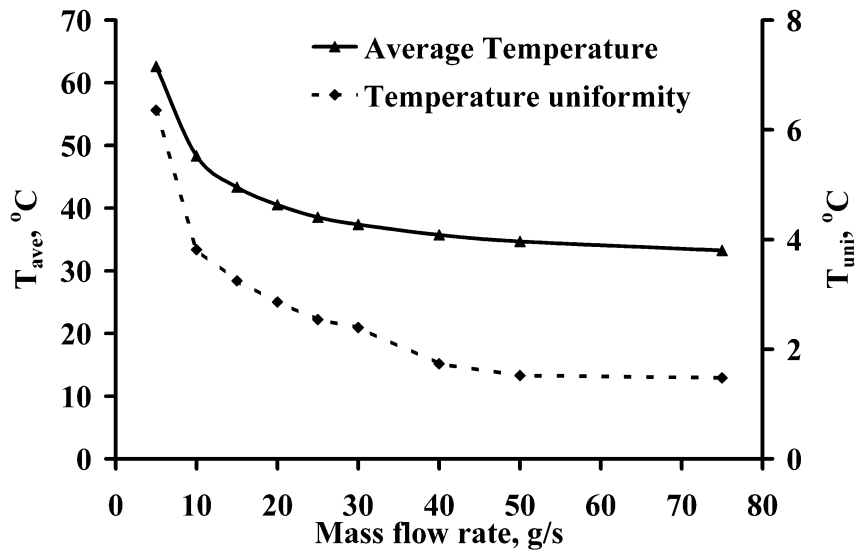
Figure 7.7 Average surface temperature and variation of cells temperature in the battery pack for mass flow rate of 5 - 75gs^{-1}.

Overview of the surface temperature distribution of the cells in the battery pack is shown in Figure 7.8, while the internal temperature distribution of the cells is shown in Figure 7.9. Average difference of cell core temperature and surface temperature is about 2.6 ^{o}C. The maximum cell core temperature at 40gs^{-1} of cooling air is about 39.2 ^{o}C. The cell in the center and front end of the battery pack is hotter than the cell on the side. This is due to lack of air flow to the end of battery pack and concentrating of heat at the center of the battery pack. Moreover, the highest temperature also occurs at the end of the cell body which is located in the slot on the holding plate and block the cooling air reached the cell surfaces. The simulation results confirm that the designed air cooling system is capable to maintain the battery temperature within the desired range.
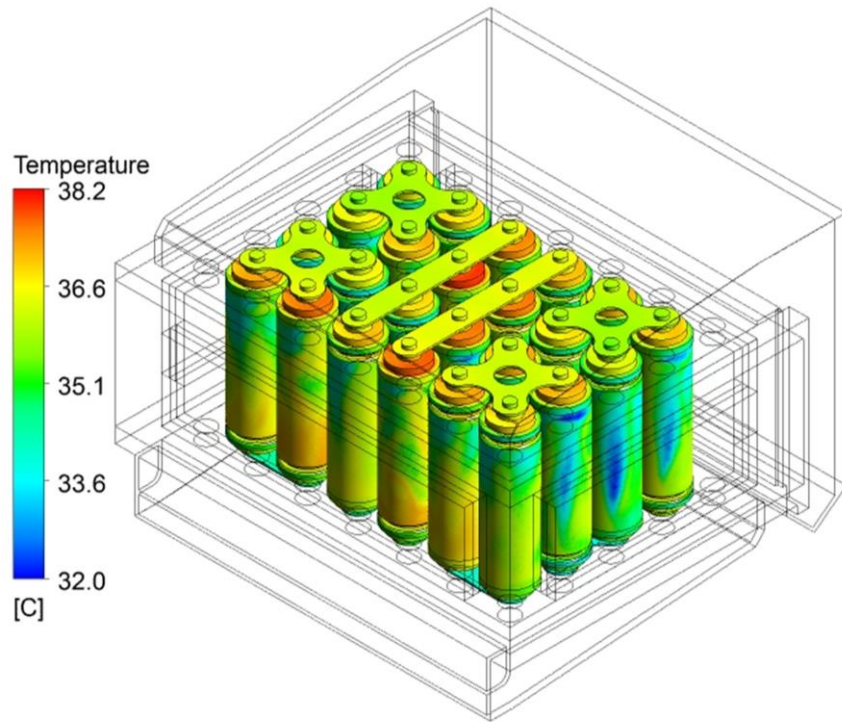
Figure 7.8 Temperature distribution of the cells in the battery pack.
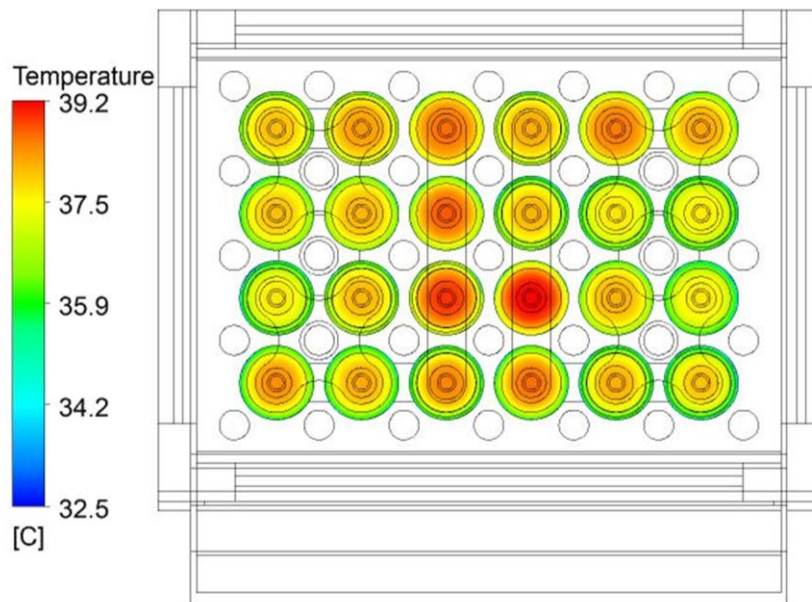
Figure 7.9 Internal temperature of the cells in the battery pack.

Figure 7.10 shows the correlation of the average Nusselt number for the current study.
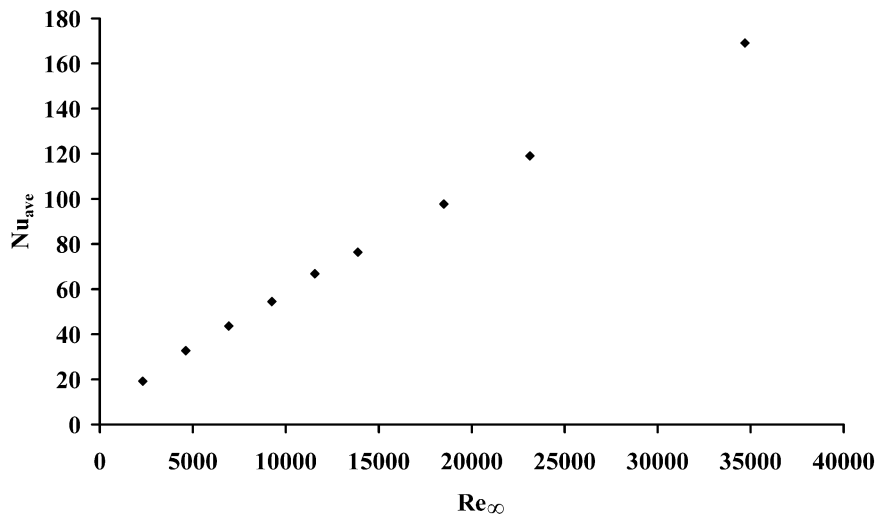
Figure 7.10 Overall Nu of the current study.

The average Nu along the cell surface is seen to increase with Re_∞ as expected. The average Nu for 30 gs^{-1} of cooling air is about 76.4 while for 75 gs^{-1} the Nu is about 169. Forced convection cooling requires parasitic power to overcome the flow resistance induced by narrow gaps between the cells in the battery pack. Figure 7.11 shows the measured and simulated ideal fan power consumption for various flow rates.
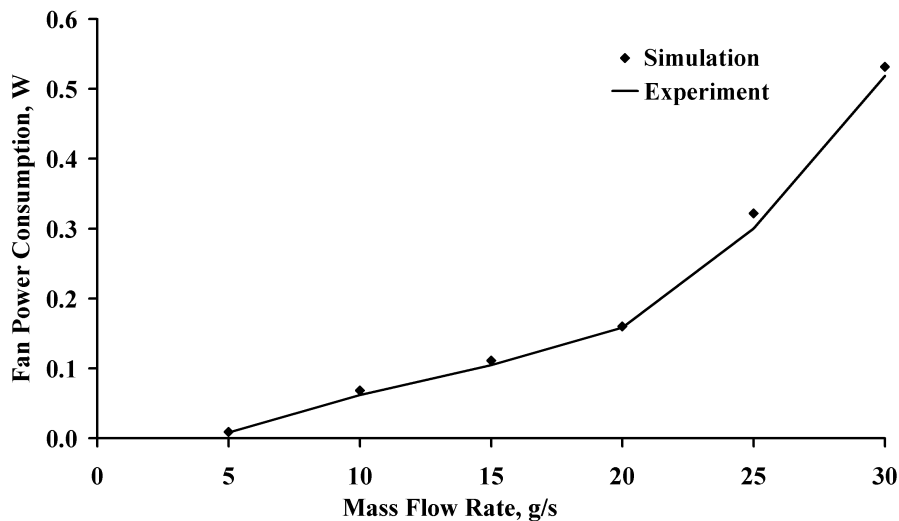
Figure 7.11 Experimental and simulated fan power consumption.

The measurement of the pressure drop in the battery pack is validated until the top limit of the tangential blower which is about 30 gs^{-1}. At 30 gs^{-1}, 0.53 W of fan power is needed to maintain the final temperature of the cells

183

within the safety limit. Minor leakage occurring in the battery pack may have contributed to the slight deviation of experimental measured fan power and simulation results. The averaged relative error is 5.03%.

Correlations of Nu with Re of the current study which determined via a least-mean-squared fit can be represented by Equation 7-23 with R-square of 0.9985.

$$Nu = 0.0374\, Re^{0.8014} \tag{7-23}$$

Figure 7.12 compares the new correlation with correlations of heat transfer for a cylinder in the axial flow direction found in the open literature. Wiberg and Lior's (Wiberg and Lior, 2004) correlation is based on a single cylinder placed downstream of a circular disc 1/3D in diameter and centered on the cylinder axis, parallel to the cylinder front surface. The examined flows were in the Reynolds number range of 8.9 x 10^4 to 6.17 x 10^5. On the other hand, Sparrow and Geiger (Sparrow and Geiger, 1985) derived the heat transfer coefficient for a circular disk facing a uniform air flow for a Reynolds number range from 5000 to 50000 using the naphthalene sublimation technique. Ota and Kon's (Ota and Kon, 1977) correlation is based on the heat transfer characteristics of reattached and redeveloped regions for longitudinal incompressible air flow along a blunt circular cylinder in a Reynolds number range from 24900 to 53600. The average Nusselt numbers for above-mentioned studies are tabulated in Table 7.2.

Table 7.2 Heat transfer correlations from open literature.

Authors	Re	C	e
Wiberg and Lior (Wiberg and Lior, 2004)	89000 - 61700000	0.070	0.734
Sparrow and Geiger (Sparrow and Geiger, 1985)	5000- 500000	0.927	0.5
Ota and Kon (Ota and Kon, 1977)	24900 - 53600	0.109	0.701
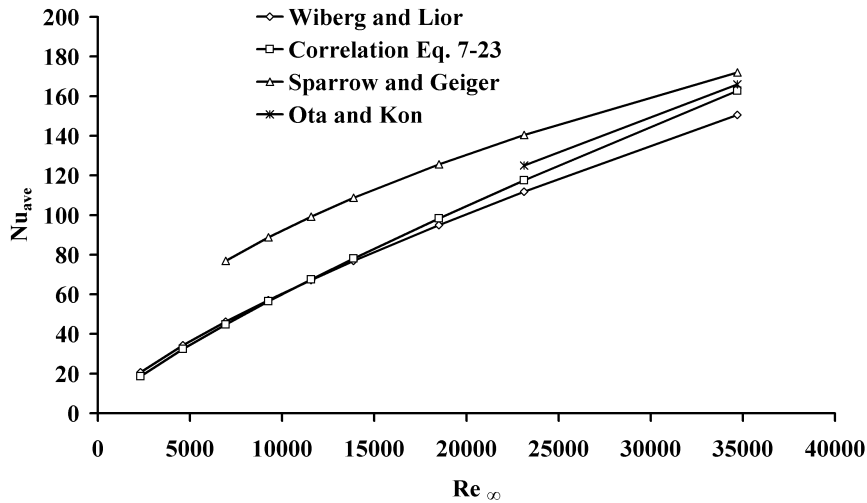
Figure 7.12 Comparison of heat transfer characteristics with open literature.

As shown in Figure 7.12, Sparrow & Geiger's and Ota & Kon's correlations do not result in reliable predictions. Although, the examined Reynolds number range for Wiberg and Lior is higher than that for the current study, the results agree well with the current study. The possible explanation could be because the flow of cooling air is through a circular disk which is similar to the current battery pack design with venting holes on the holding plate. On the other hand, the other authors' correlations are based on the direct impingement of cooling air on a circular body. From the above comparisons, it is found that the developed correlation is reasonable and would be applied to the following transient simulations of the battery pack.

7.4.4 Transient simulation and model validation

In this section, simplified transient simulations were performed to evaluate the temperature rise in the battery pack. In the numerical modeling, heat generation in the cell as a function of time of the cell obtained from the ARC measurement (Figure 7.3) was imported into the battery domains as transient heat sources. Heat conduction within the batteries is governed by the energy Equation 7-11, and the heat transfer coefficient given by Equation 7-23

was assigned to the battery surfaces as effective convective heat transfer boundaries. The simulations were performed for different charging rates and the average surface temperatures of the twenty four cells were plotted in Figure 7.13.
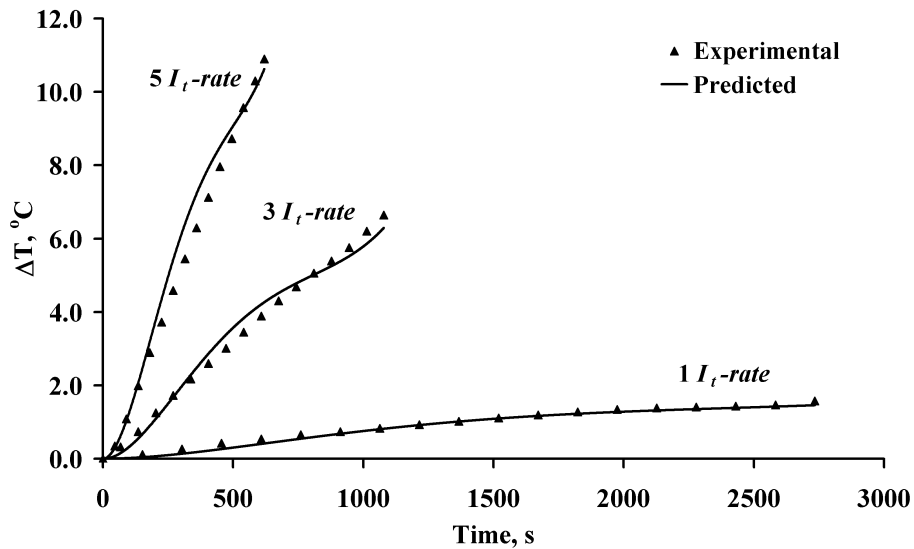
Figure 7.13 Comparison of the experimental and modeling results.

Additionally, an experimental testing of the battery pack was done to validate the developed mathematical model at various charging rates. Figure 7.13 shows the comparison of experimental data and numerical prediction of the average rise of cell temperature in the battery pack at $\dot{m} = 30$ gs^{-1}. The figure shows good quantitative and qualitative agreement between experimental data and numerical prediction with averaged relative error of 13.1%, 13.7% and 13.6% respectively for 1, 3 and 5 I_t-rates of constant current charging. Both experimental and numerical results showed a trend of increasing average cell surface temperature versus time. From the experiments, the variations of average cell temperature in the battery pack are about 1.6 $^{\circ}$C, 2.6 $^{\circ}$C and 3.4 $^{\circ}$C for 1, 3 and 5 I_t-rates of constant current charging, respectively, confirming the findings from the simplified transient modeling that there is minor temperature difference among the cells. Although the

internal temperature of the cell may exceed 40 $^{\circ}$C during 3 I_t-rate of constant charging, the Li-ion cell can tolerate high temperature temporarily [Kuper et al., 2009]. Sudden increase of the cell temperature occurred when the SOC of the cell reached 90%. Remaining charging time is less than 2 minutes. Hence, 30 gs^{-1} of air flow rates and the current design of battery thermal management system is still capable of handling constant current charging till 3 I_t-rate. On the other hand, at 5 I_t-rate of charging, the maximum temperature rises of the cell is about 11.6 $^{\circ}$C, which exceeds the top ideal operating temperature limit of Li-ion batteries. Therefore, a more powerful tangential blower is recommended in this situation, especially for fast charging applications.

7.5 Summary

In this study, CFD analysis was utilized to analyze the air cooling of a battery pack comprising 38120 cells. The simulation was able to predict the hot spots and cold spots within the battery pack. The simulation results demonstrate that an increasing of cooling air flow rate will result in the increase of heat transfer coefficient and pressure drop. A correlation of Nusselt number to Reynolds number was developed based on the steady state numerical simulations and compared with the correlations from the open literature. In general, the developed correlations show a similar trend with most of the correlations in open literature. Finally, the numerical model was validated by a series of experiments done for active air cooling. The numerical results showed good agreement with the experimental results at various I_t-rates of constant current charging. For charging at 5 I_t-rate, a more powerful fan was required to keep the cell temperature at optimum range. This method provides a simple way to estimate thermal performance of the battery pack

thermal management system when the size of battery pack is large and full

transient simulation is not viable.

CHAPTER 8

AIR COOLING SYSTEM WITH COOLING FINS

8.1 Introduction

The thermal management systems presently installed on most EVs is only suitable for low charging rate and little attention has been paid to the temperature uniformity within the battery pack. Moreover, the thermal system design is less elaborate and overheating of the batteries is commonly found. In this study, conceptual designs of the 18650 cell battery module with cooling fins are proposed. Two different types of cooling fin were investigated which are the plate fin and the helical fin. A Taguchi method with orthogonal array L_{16} $(4^2 2^2)$ was used to optimize the cooling fin design. Mass flow rate, fin thickness, number of fins/number of turns and fin material are the parameters investigated which affect the performance of the cooling fins. The target performance measure was used to determine the main control factors that greatly affect the performance of the cooling fins. The significance and contribution of each factor were analyzed using Analysis of Variance (ANOVA). Then, a grey relational analysis (GRA) with an assigned weightage for each control factor was used to determine the optimum design for the finned battery module. Finally, regression analysis was used to develop the correlation of the Nusselt number, Colburn factor, temperature uniformity and friction factor to the Reynolds number for the cooling fins.

Finally, experimental studies of the cooling fins were investigated using a wind tunnel. The temperature rises of the cooling fins were measured under different cooling conditions. The experimental results are then compared with the simulation results to validate the developed correlation.

8.2 Battery module designs

A battery module forms a basic unit of a battery pack. The battery module interior and cell arrangement must be properly planned and designed to maintain the smallest variation of temperature from cell to cell in a battery module. It is important to ensure that all the batteries in the module possess similar charging and discharging behavior. A battery module consisting of 36 pieces of commercial LFP cells with an electric configuration of 12S3P (12 cells in series and 3 cells in parallel) was developed for the current study as shown in Figure 8.1. The module housing is made of plexiglass widows to provide insulation for the battery as well as rigid structure and housing for the connectors and cells.
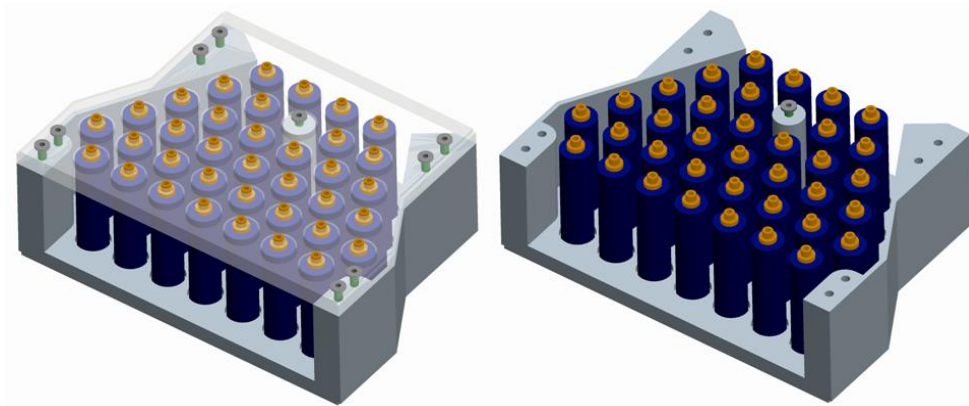
Figure 8.1 CAD model of the unfinned battery module.

The cooling fin serves two major roles. First it will act as a homogenizer to reduce the variation of cell temperature and second to increase the rate of cooling from the cells to the air. The trapezoidal shape based on the staggered arrangement of the batteries can alleviate the problem of higher temperature at the downstream of the cell that is commonly found in the regular aligned and staggered arrangements. The number of batteries is gradually reduced in the flow direction and the flow channel area is also gradually narrowed down. Thus, the coolant speed is increased resulting in higher cooling rates along the

190

flow direction which tends to compensate for the rise in air temperature along the flow direction. It is believed that this kind of configuration could reduce the non-uniformity of battery temperature commonly found in a cuboids-shaped pack.

8.2.1 Plate fin

A plate-fin battery module is made of layers of sheet metal to increase the heat transfer area of the battery module. The batteries are slotted into the metal tubing. The hole at the top end is used to secure the module housing and hold the battery rigidly to the connectors. The batteries are represented by blue colored cylinders. Figure 8.2 illustrates the plate fin battery module design.

(a)   (b)   (c)
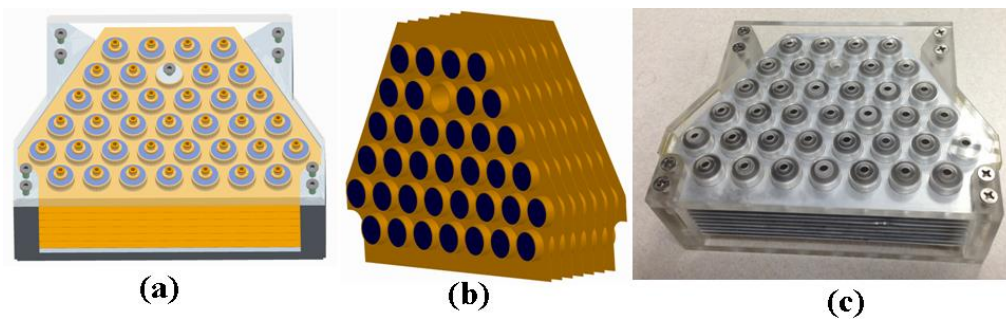
Figure 8.2 CAD model and fabricated plate fin battery module.

8.2.2 Helical fin

The second concept makes use of helical fins. A flat strip of metal is helically wound on a single tube like threads on a screw. Helical fins use less material as compared to plate fins. A single damaged battery can be replaced easily. On the other hand, cells with helical fins can be positioned nearer to one another to produce more compact staggered arrangement, which is not possible with plate fins. Figure 8.3 shows the battery module design with helical fins.
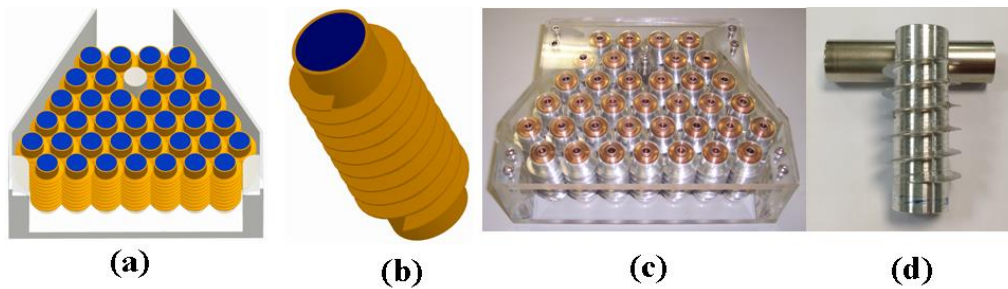
Figure 8.3 CAD model and fabricated helical fin battery module.

8.3 Design of experiments

8.3.1 Taguchi method

In the current study, the Taguchi method was used to determine the parameters that will improve the cooling performance, cost and weight of the battery module and derive an optimized battery module design. Different orthogonal arrays were chosen for this optimization study.

Instead of a full factorial analysis which requires 64 runs of the simulation, the orthogonal array L_{16}, which comprises two four-level factor and two two-level factors and a total of 16 runs, is used to optimize the plate and helical cooling fins. The Noise Factor which is also known as the uncontrollable factor was not considered in the analysis. The factor level for cooling fins is shown in Table 8.1 while the design of experiments for cooling fins is shown in Table 8.2. Four control factors were considered in this study, namely are mass flow rate of cooling air, number of fins /number of turns, fin thickness and fin material.

Table 8.1 The parameters and their levels used in the design of experiments.

Factor	Code	Levels				Units
		1	2	3	4	
Mass flow rate	A	15	20	25	30	gs^{-1}
Number of fins/ Number of turns	B	5	9	11	15	-
Fin thickness	C	0.5	0.2	-	-	mm
Fin material	D	Copper	Aluminum	-	-	Type

Table 8.2 Orthogonal array L_{16} (4^2 2^2) for cooling fins design.

Exp No.	Factor			
	A	B	C	D
1	1	1	1	1
2	1	2	1	1
3	1	3	2	2
4	1	4	2	2
5	2	1	1	2
6	2	2	1	2
7	2	3	2	1
8	2	4	2	1
9	3	1	2	1
10	3	2	2	1
11	3	3	1	2
12	3	4	1	2
13	4	1	2	2
14	4	2	2	2
15	4	3	1	1
16	4	4	1	1

8.3.2 Analysis of the S/N ratio

In this study, the experimental observations are further transformed into a signal-to-noise (S/N) ratio. The S/N ratio is used to evaluate the optimal parameters by taking the mean and variability into account. The S/N ratio is the ratio of the mean (Signal) to the standard deviation (Noise) and it depend on the quality characteristics of the product to be optimized. Three types of standard S/N ratios are generally used, namely "Nominal the best", "Smaller the best" and "Larger the best". The equation used for calculating S/N ratios are as follows:

Larger the best:

$$\eta = -10\log_{10}\left(\frac{1}{n}\sum_{i=1}^{n}\frac{1}{Y_i^2}\right)$$
(8-1)

Smaller the best:

$$\eta = -10\log_{10}\left(\frac{1}{n}\sum_{i=1}^{n}Y_i^2\right)$$
(8-2)

Nominal the best:

$$\eta = -10\log_{10}\left(\frac{1}{n}\sum_{i=1}^{n}\frac{\mu^2}{\sigma^2}\right) \tag{8-3}$$

Four different types of the responses, such as specific performance, temperature uniformity, pressure drop and weight of the cooling fin were used to evaluate the effect of each control factor. The evaluation criteria for the responses are shown below:

➢ Specific performance-Larger the best.

➢ Temperature uniformity- Smaller the best.

➢ Pressure drop-Smaller the best.

➢ Mass of the fin – Smaller the best.

The specific performance of the cooling fin design for battery module is defined by Equation 8-4 (Smith, 2005):

$$\dot{Q}_{spec} = \frac{\dot{Q}}{V\Delta\theta} \tag{8-4}$$

$\dot{Q}$ Amount of heat generated, W

V Volume of the cooling fin, m^3

$\Delta\theta$ Change of temperature, K

The friction factor of the battery module is defined by Equation 8-5 (Kays and London, 1964):

$$\frac{\Delta p}{P_1} = \frac{G^2}{2}\frac{\rho_{air,in}}{P_1}\left[\left(1+\sigma^2\right)\left(\frac{\rho_{air,out}}{\rho_{air,in}}-1\right) + f\frac{A_{ext}}{A_c}\left(\frac{\rho_{air,m}}{\rho_{air,in}}\right)\right]$$

$$f = \frac{A_c}{A_{ext}}\frac{\rho_{air,in}}{\rho_{air,m}}\left[\frac{2\Delta p \cdot \rho_{air,in}}{G_{air}^2}-\left(1+\sigma^2\right)\left(\frac{\rho_{air,out}}{\rho_{air,in}}-1\right)\right] \tag{8-5}$$

A_c Free flow area, m^2

A_{ext} Total heat transfer area, m^2

$\rho_{air,in}$ Inlet air density, kgm^{-3}

$\rho_{air,out}$ Outlet air density, kgm^{-3}

Δp Pressure drop, Pa

G_{air} Mass flux of air based on minimum flow area,($\frac{\dot{m}}{A_c}$) kgm^{-2} s^{-1}.

σ Contraction ratio of the cross-sectional area, (A_c/A_{fr})

A_c/A_{ext} Ratio of free flow area to total heat transfer area can be define as r_h/L

r_h hydraulic radius, mm

L Length of the battery module, mm

8.3.3 Analysis of Variance

Analysis of variance (ANOVA) is a method of partitioning variability into identifiable sources and the associated degrees of freedom in an experiment. It decomposes the variability in the response variable amongst the different factors. It is an important technique for analyzing the effect of categorical factors on a response. The concept of conserving the total sum of squares and total degrees of freedom is emphasized. Pure sum of squares is calculated for factors to establish the contribution ratios. Depending upon the type of analysis, it may be important to determine:

 (a) The significant effect of the factor on the response, and/or

 (b) The variability in the response variable attributable to each factor.

Analysis of variance is used in analysis of the data and the basic formulas are provided (Belavendram, 1995):

Total sum of squares, ST:

$$ST = \sum Y^2 \tag{8-6}$$

Sum of squares due to mean, Sm:

$$Sm = n\bar{y}^2 \tag{8-7}$$

Factor A sum of squares, SA:

$$SA = \frac{[TotalofA_1]^2}{n_1} + \frac{[TotalofA_2]^2}{n_2} - \frac{[TotalofA]^2}{n_1 + n_2} \tag{8-8}$$

Factor B sum of squares, SB:

$$SB = \frac{[TotalofB_1]^2}{n_1} + \frac{[TotalofB_2]^2}{n_2} - \frac{[TotalofB]^2}{n_1 + n_2} \tag{8-9}$$

Error sum of squares, Se:

$$Se = ST - Sm - SA - SB \tag{8-10}$$

Pure sum of squares factor A or B, SA' or SB' etc:

$$SA' = SA - v_A \sigma^2 \tag{8-11}$$

where v_a = degrees of freedom of factor A.

Percentage of the pure sum of squares of a source to the total sum of squares, ρ:

$$\rho A = \frac{SA'}{St} \times 100\% \tag{8-12}$$

The influential degree of each factor in the performance of the cooling fins can be determined through the percentage of contribution of the control factors. The F-test of 95% confidence was used as a reference tool to identify the significant factor that affects the performance characteristics in this study. The error in the analysis is refers to the uncontrolled factors and it is normally used to evaluate the sufficiency and insufficiency of the experiment.

8.3.4 Grey Relational Analysis

Grey relational analysis (GRA) uses the information from the grey system to dynamically evaluate the design parameters qualitatively. This method is

developed based on the level of similarity and variability of all design parameters to develop their relation (Tsai et al., 2003). The GRA will assist in the decision making process and generate reports for the selection of the design parameters.

The first step in GRA is to normalize the results to the range between 0 and 1. This process is known as the generation of the grey relation. The expectation goal can be described as follows (Wu, 1996):

Larger the best:

$$x_i(k) = \frac{X_i(k) - \min X_i(k)}{\max X_i(k) - \min X_i(k)} \qquad (8\text{-}13)$$

Smaller the best:

$$x_i(k) = \frac{\max X_i(k) - X_i(k)}{\max X_i(k) - \min X_i(k)} \qquad (8\text{-}14)$$

Nominal the best

$$x_i(k) = \frac{X_i(k) - X_0(k)}{\max X_i(k) - X_0(k)} \qquad (8\text{-}15)$$

where

$x_i(k)$ Value after the grey relational generation.

$X_i(k)$ Original value for the kth response.

$\min X_i(k)$ Minimum value of $X_i(k)$ for the kth response.

$\max X_i(k)$ Maximum value of $X_i(k)$ for the kth response.

$X_0(k)$ Ideal sequence for the response.

The next step in GRA is to compute the Grey Relational Coefficient (GRC) $\xi_i(k)$. The grey coefficient is given by

$$\xi_i(k) = \frac{\Delta_{min} + \psi \Delta_{max}}{\Delta_{0i}(k) + \psi \Delta_{max}} \qquad (8\text{-}16)$$

where

$$\Delta_{0i} = \left\| x_0(k) - x_i(k) \right\|, \Delta_{\min} = \min_{\forall j \in i} \min_{\forall k} \left\| x_0(k) - x_j(k) \right\|,$$

$$\Delta_{\max} = \max_{\forall j \in i} \max_{\forall k} \left\| x_0(k) - x_j(k) \right\| \; \Delta_{0i} = \text{Deviation of the absolute value } x_0(k)$$

and $x_i(k)$, $x_0(k) = 1$

Ψ Distinguishing coefficient with $0 \leq \Psi \leq 1$, generally is 0.5

$\Delta_{\min}$ Smallest value of Δ_{0i}, 0

$\Delta_{\max}$ Largest value of Δ_{0i}, 1

The last step in GRA is to calculate Grey Relational Grade (GRG). GRG is defined as:

$$\gamma_i = \frac{1}{\sum\limits_{k=1}^{n} w_k} \sum_{k=1}^{n} w_k \xi_i(k) \tag{8-17}$$

where

γ_i Overall grey relational grade for i^{th} experiment.

w_k Normalized weight value of kth performance characteristic.

8.3.5 Weightage for the response

The weightage used to determine the optimum design for the finned battery module is shown in the table below:

Table 8.3 Response weightage.

Weightage,	Response			
	Specific performance, Q_{spec}	Pressure drop, Δp	Temperature uniformity, ΔT	Mass of the fin, m
w	0.4	0.2	0.2	0.2

8.3.6 Regression Analysis

Regression analysis was used to investigate the relationships between variables. The goal of regression analysis is to determine the values of parameters for a function that causes the function to best fit a set of observed

198

data. Data have to be assembled on the underlying variable of interest and the regression is employed to estimate the quantitative effect of the causal variables upon the variables that they influence to study on each case. The degree of confidence was used to determine the statistical significance of the estimated relationship.

There are two types of regression analyses, namely linear regression and multiple regressions. In a linear regression model, the dependent variable is assumed to be a linear function of one or more independent variables plus an error introduced to account for all other factors. A common method of estimation for the regression model is the ordinary least squares method. While multiple regressions are a technique that allows additional factors to enter the analysis separately so that the effect of each can be estimated, it is valuable for quantifying the impact of various simultaneous influences upon a single dependent variable. Furthermore, because of omitted variables bias with simple regression, multiple regressions are often essential even when the investigator is only interested in the effects of one of the independent variables (Navidi, 2008).

Simple linear regression involves one independent variable: x_i, and two parameters, β_0 and β_1:

$$y_i = \beta_0 + \beta_1 x_i + e_i, \qquad i = 1,...,n. \tag{8-18}$$

Multiple linear regressions with several independent variables or functions of independent variables:

$$y_i = \beta_0 + \beta_1 x_i + \beta_2 x_i^2 + e, \qquad i = 1,...,n. \tag{8-19}$$

e_i Error term

Sum of squared residuals, SSE:

$$SSE = \sum_{i=1}^{N} e_i^2 \tag{8-20}$$

The formula for the least squares estimates:

$$\hat{\beta}_1 = \frac{\sum (x_i - \bar{x})(y_i - \bar{y})}{\sum (x_i - \bar{x})^2} \quad \text{and} \quad \hat{\beta}_0 = \bar{y} - \hat{\beta}_1 \bar{x} \tag{8-21}$$

8.3.7 Data processing

The equivalent thermal circuit for the cooling fin is illustrated in Figure 8.4. Effectiveness, efficiency, Colburn factor, Nusselt number and Reynolds number used to characterize the performance of the cooling fins and flow characteristic in the battery module are given in equations below:
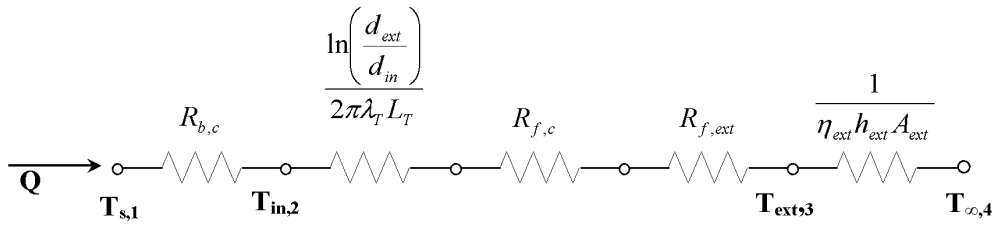
Figure 8.4 Equivalent thermal circuit for cooling fin installed on the battery.

Q Amount of heat generated, W

$R_{b,c}$ Battery body contact resistance, KW^{-1}

$R_{f,c}$ Fin contact resistance, KW^{-1}

$R_{f,ext}$ Air side fouling resistance, KW^{-1}

k_T Tube thermal conductivity, $Wm^{-1} K^{-1}$

h_{ext} Convective heat transfer coefficient, $Wm^{-2} K^{-1}$

η_{ext} Surface efficiency

A_{ext} Total heat transfer area, m^2

in Interior

ext Exterior

Overall heat transfer resistance $(UA)^{-1}$

$$\frac{1}{UA} = \frac{1}{\eta_{ext} h_{ext} A_{ext}} + R_{f,ext} + R_c + \frac{\ln\left(\dfrac{d_{ext}}{d_{in}}\right)}{2\pi\lambda_T L_T} + R_{b,c} \qquad (8\text{-}22)$$

Assumptions:

i. The contact resistance of the tube to the fin is negligible,

$R_{f,c} = 0$ K W^{-1}

ii. Clean air is used, resulting in negligible fouling resistance,

$R_{f,ext} = 0$ K W^{-1}

iii. Perfect contact between battery and fins, $R_{b,c} \approx 0$ K W^{-1}

The heat transfer coefficient (Sparrow and Samie, 1985) is defined as,

$$h_{ext} = \frac{Q_{gain}}{\left(\bar{T}_s - T_\infty\right)\left(A_{tot}\right)} \qquad (8\text{-}23)$$

$$A_{tot} = A_b + \eta A_{fin}$$

where

Q_{gain} Actual heat transfer, energy gained by air, W

A_b Unfinned surface area, m^2

A_{fin} Fin area, m^2

T_∞ Freestream temperature, K

$\bar{T}_s$ Average surface temperature of the cooling fin, K

The rate of heat transfer by air (Sparrow and Samie, 1985) is,

$$Q_{gain} = \dot{m} C_{p,air}\left(T_{out} - T_\infty\right) \qquad (8\text{-}24)$$

where

$\dot{m}$ Mass flow rate of air, kgs^{-1}

$C_{P,air}$ Specific heat of air, Jkg^{-1} K^{-1}

T_{out} Outlet temperature, K

The surface efficiency of the cooling fin is given by.

$$\eta_{ext} = 1 - \left(1 - \eta_{fin}\right)\left(\frac{A_{fin}}{A_{ext}}\right) \tag{8-25}$$

The efficiency of the cooling fin is calculated by using Schmidt approximation (Schmidt, 1949) as:

$$\eta_{fin,Schmidt} = \frac{\tanh\left(m \cdot l^*\right)}{m \cdot l^*} \tag{8-26}$$

where

$$m = \sqrt{\frac{2 \cdot h_{ext}}{t_{fin} \cdot k_{fin}}} \tag{8-27}$$

k_{fin} Fin thermal conductivity, Wm^{-1} K^{-1}

t_{fin} Thickness of the fin, m

The parameter l^* for plate fin and helical fin are given in Equations 8-28 and 8-29, respectively.

Plate fin (Baehr and Stephan, 2006):

$$l^* = \left(0.64\sqrt{S_2\left(S_1 - 0.2S_2\right)} - \left(\frac{d_{ext}}{2}\right)\right)\left(1 + 0.35\ln\left(1 + \frac{0.64\sqrt{S_2\left(S_1 - 0.2S_2\right)} - \left(\frac{d_{ext}}{2}\right)}{d_{ext}/2}\right)\right) \tag{8-28}$$

S_1 Transverse length of bank, m

$S2$ Longitudinal length of bank, m

Helical fin (Huisseune et al., 2010) :

$$l^* = \left(\frac{D_{fin}}{2} - \frac{d_{ext}}{2}\right)\left(1 + \frac{t_{fin}}{D_{fin} - d_{ext}}\right)\left(1 + 0.35\ln\left(\frac{D_{fin}}{d_{ext}}\right)\right) \tag{8-29}$$

8.3.8 Correlations of the parameters

Correlations of average Nusselt number, J factor, average friction factor and variation of temperature across the optimized battery module for the flow across the plate fin were given as follows:

$$\overline{Nu}_D = C\overline{\text{Re}}_D^n \qquad (8\text{-}30)$$

$$\overline{J} = C\overline{\text{Re}}_D^n \qquad (8\text{-}31)$$

$$\overline{f} = C\overline{\text{Re}}_D^n \qquad (8\text{-}32)$$

$$\frac{\Delta T}{T_\infty} = C\overline{\text{Re}}_D^n \qquad (8\text{-}33)$$

where

$$Nu = \frac{h_{ext} \cdot d_{ext}}{k_{air}} \qquad (8\text{-}34)$$

k_{air} \qquad Thermal conductivity of air, $Wm^{-1}\,K^{-1}$

$$Re = \frac{d_{ext} \cdot G_{air}}{\mu_{air}} \qquad (8\text{-}35)$$

μ_{air} \qquad Dynamic viscosity of air, $kg\,m^{-1}s^{-1}$

d_{ext} \qquad External diameter of tube, m

$$Pr = \frac{\mu_{air} \cdot C_{p\,air}}{k_{air}} \qquad (8\text{-}36)$$

$$j = \frac{Nu}{Re\,Pr^{1/3}} \qquad (8\text{-}37)$$

In order to perform the regression analysis, Equations 8-31 to 8-33 were transformed into the following equations:

$$\ln\left(\overline{Nu}_D\right) = \ln C + n\ln \overline{\text{Re}}_D \qquad (8\text{-}38)$$

$$\ln\left(\overline{J}\right) = \ln C + n\ln \overline{\text{Re}}_D \qquad (8\text{-}39)$$

$$\ln\left(\overline{f}\right) = \ln C + n \ln \overline{\mathrm{Re}_D} \tag{8-40}$$

$$\ln\left(\frac{\Delta T}{T_\infty}\right) = \ln C + n \ln \overline{\mathrm{Re}_D} \tag{8-41}$$

The correlations were determined via a least mean squares fit with 95% confidence interval.

96 sets of numerical analysis were carried out to investigate the effects of the different number of fins/number of turns, fin thickness and mass flow rate of air on the average Nusselt number, average friction factor, average J factor and variation of cell temperature across the battery module.

$$\overline{Nu}_D = f_1\left(\frac{F_p - \delta}{D_0}, \frac{F_p}{D_h}; \frac{F_p}{P_t}, Re\right) \tag{8-42}$$

$$\overline{f} = f_2\left(\frac{F_p - \delta}{D_0}, \frac{F_p}{D_h}; \frac{F_p}{P_t}, Re\right) \tag{8-43}$$

$$\overline{J} = f_3\left(\frac{F_p - \delta}{D_0}, \frac{F_p}{D_h}; \frac{F_p}{P_t}, Re\right) \tag{8-44}$$

$$\frac{\Delta T}{T_\infty} = f_4\left(\frac{F_p - \delta}{D_0}, \frac{F_p}{D_h}; \frac{F_p}{P_t}, Re\right) \tag{8-45}$$

δ Fin thickness, mm

F_p Fin pitch, mm

D_0 Outer diameter of the tube, mm

D_h Hydraulic diameter, mm

P_t Transverse tube pitch, mm

There are various forms of correlations used. Therefore, similar forms as found in previous research works were used to correlate the data (Xie, et al., 2009 and Wang, 2000). Correlations of average Nusselt number, J

factor, average friction factor and variation of temperature of the flow across the plate fin can be defined in the follow equations.

$$\overline{Nu}_D = a\overline{\mathrm{Re}}_D^n \left(\frac{F_p - \delta}{D_0}\right)^x \left(\frac{F_p}{D_h}\right)^y \left(\frac{F_p}{P_t}\right)^z \tag{8-46}$$

$$\overline{f} = a\overline{\mathrm{Re}}_D^n \left(\frac{F_p - \delta}{D_0}\right)^x \left(\frac{F_p}{D_h}\right)^y \left(\frac{F_p}{P_t}\right)^z \tag{8-47}$$

$$\overline{J} = a\overline{\mathrm{Re}}_D^n \left(\frac{F_p - \delta}{D_0}\right)^x \left(\frac{F_p}{D_h}\right)^y \left(\frac{F_p}{P_t}\right)^z \tag{8-48}$$

$$\frac{\Delta T}{T_\infty} = a\overline{\mathrm{Re}}_D^n \left(\frac{F_p - \delta}{D_0}\right)^x \left(\frac{F_p}{D_h}\right)^y \left(\frac{F_p}{P_t}\right)^z \tag{8-49}$$

In order to perform the multiple regression analysis, Equations 8-46 to 8-49 are transformed into the following equations:

$$\ln\left(\overline{Nu_D}\right) = \ln a + n\ln\overline{\mathrm{Re}}_D + x\ln\left(\frac{F_p - \delta}{D_0}\right) + y\ln\left(\frac{F_p}{D_h}\right) + z\ln\left(\frac{F_p}{P_t}\right) \tag{8-50}$$

$$\ln\left(\overline{f}\right) = \ln a + n\ln\overline{\mathrm{Re}}_D + x\ln\left(\frac{F_p - \delta}{D_0}\right) + y\ln\left(\frac{F_p}{D_h}\right) + z\ln\left(\frac{F_p}{P_t}\right) \tag{8-51}$$

$$\ln\left(\overline{J}\right) = \ln a + n\ln\overline{\mathrm{Re}}_D + x\ln\left(\frac{F_p - \delta}{D_0}\right) + y\ln\left(\frac{F_p}{D_h}\right) + z\ln\left(\frac{F_p}{P_t}\right) \tag{8-52}$$

$$\ln\left(\frac{\Delta T}{T_\infty}\right) = \ln a + n\ln\overline{\mathrm{Re}}_D + x\ln\left(\frac{F_p - \delta}{D_0}\right) + y\ln\left(\frac{F_p}{D_h}\right) + z\ln\left(\frac{F_p}{P_t}\right) \tag{8-53}$$

The correlations were determined via a least mean squares fit with 95% confidence interval.

8.4 Numerical procedures

ANSYS-CFX software was used in this work to solve the Navier-Stokes equations using a fully conservative, finite element (cell vertex numeric) method. Steady state conjugate heat transfer simulations were performed to

predict the thermal performance of the cooling fins. The fluid flow in the cooling fin is assumed incompressible. The cylindrical 18650 LFP cell was modeled with a uniform volumetric heat source and anisotropic thermal conductivity. A heat generation rate of 5 W per cell was assumed in the current study. The cells in the battery module were idealized with uniform rate of cooling. The contact resistances of the cell casing to the internal wall of the cooling fins tube were neglected in this study. The numerical modeling procedures are described in sections 7.3.1 and 7.3.2.

Hybrid meshing was adopted to discretize the battery pack domain using ANSYS ICEM CFD 14.0 SP1. Air was used for the simulation and assumed to be an ideal gas. The mass flow boundary condition was assigned to the inlet of the battery module as given in Table 8.1 and Table 8.2, and the air inlet temperature was 30 $^{\circ}$C. At the outlet of the battery module, an average static pressure of 0 Pa was assigned. The confining walls of the battery module on the top, side and bottom were specified as no slip, adiabatic wall boundaries. The Shear Stress Transport (SST) turbulence model was used for this study. This model provides accurate predictions from laminar to turbulent flow and near-wall boundary conditions. The computational domain was initialized with ambient conditions at 1 atmospheric pressure. CFX solver was used to solve the governing equations for the conservation of mass, momentum and energy. All simulations were executed with a high resolution scheme to achieve an accurate solution. A tight convergence criterion with RMS 1.0×10^{-6} was applied to the continuity, momentum and energy equations (H-energy and T-energy) for all case studies. It is also ensured that no domain imbalance is present in the momentum and energy equations. All simulations were

computed on 8-node HP clusters. In addition, grid independent tests were carried out to refine the grid size of the battery module until the simulation results were not affected by further refinement of the mesh and the error of the results was kept within 5%.

8.5 Results and discussion

8.5.1 Unfinned battery module

The numerical simulation results of the unfinned battery module temperature distribution with 5 W of heat generated per cell, and the velocity streamlines are shown in Figure 8.5.
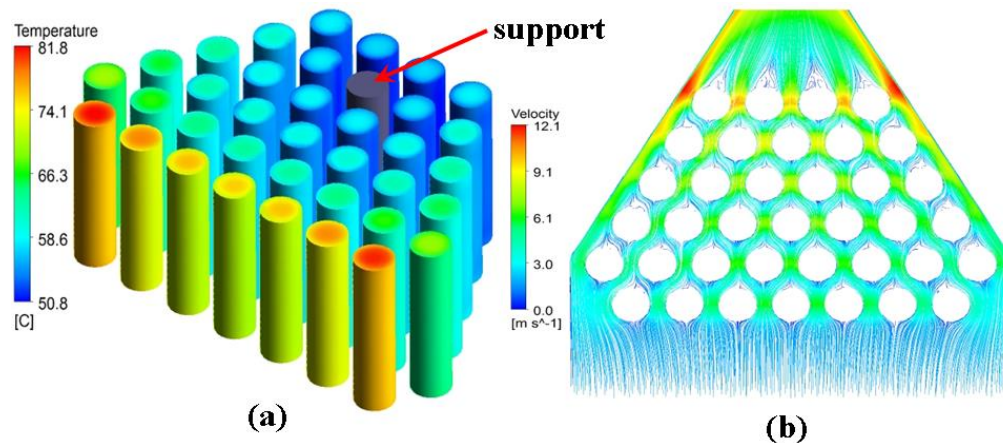
Figure 8.5 (a) Temperature distribution of the cells. (b) Surface streamline of the flow around the cell.

Figure 8.5(a) shows the temperature distribution of the cells with heat generation of 5 W per cell when subjected to cooling with ambient air at mass flow rate of $30gs^{-1}$ and inlet temperature of 30 ^{o}C. The highest temperature attained by the cells is 81.8 ^{o}C which is located at the 1st row. The average temperature of the cell surface is about 59.3 ^{o}C and variation of the cell surface temperature in the battery module is 25.5 ^{o}C. Banks of the cells act as vortex generators and depending on the location of the cells, different turbulence levels are experienced by the each row of the cells. Therefore, heat transfer for cells in inner rows is considerably higher than the heat transfer of

the cells in the first row. The temperature of the cells at the first row is always higher as shown in the Figure 8.5(a) (Zukauskas and Ulinskas, 1988). The factor that determines the rate of heat transfer from the cells is the turbulence level of the incoming fluid. Increasing turbulence level from 1% to 15% will increase the heat transfer by an average of 40% (Zukauskas and Ulinskas, 1988). Heat transfer from the first row of the cell in a bank is 60% of the heat transfer from the third row after the flow begins to stabilize (Zukauskas and Ulinskas, 1988).

Figure 8.5(b) shows the flow field in the battery module. The highest velocity is located at the side of the end row of the cells, which is about 12.1 ms^{-1}. Heat transfer from a cell is closely related to the fluid flow characteristics. Laminar boundary layer is formed at the front side of the cells. Away from the stagnation point, the boundary layer increases, leading to increase in thermal resistance and the cooling rate is decreased. Therefore, in the trapezoidal shape, the flow velocity is increased to balance the heat transfer rate downstream. At a low Reynolds number (Re), the cell is completely immersed in the flow and the boundary layer separates at the rear side of the cell only. Inertial force starts to play an important role and the boundary layer separate from the surface at the middle surface of the cell as the Re is increased. At high Re (Re > 1.5 x 10^5) a critical flow regime is reached and the boundary layer becomes turbulent and the separation point shifts back to the rear side of the cell (Zukaukas et al., 1987). Recirculation flow occurred at the rear side of the cell and the temperature at the rear side is higher.

8.5.2 Plate fin

8.5.2.1 Taguchi method analysis

The Taguchi method was used to study the effects of mass flow rate, fin number, fin thickness and fin materials on the performance of the plate fin battery module. The factors used to perform the numerical simulations and the levels are given in Table 8.1 and Table 8.2. The results of the simulations are shown in Table 8.4. The results are transformed into S/N (signal to noise) ratios according to the characteristic of the response either "smaller the best", "nominal the best" or "larger the best" as shown in Table 8.5 to Table 8.7.

Table 8.4 Design of experiment and collected response data.

| No | Parameters | | | | Response | | | |
	A	B	C	D	Specific Performance, Q_{spec}, Wm^{-3}K^{-1}	Pressure drop ΔP, Pa	Variation, ΔT, K	Mass, kg
1	1	1	1	1	1197.79	38.11	1.48	1.64
2	1	2	1	1	1231.73	40.71	1.76	1.90
3	1	3	2	2	1547.44	37.66	3.46	0.48
4	1	4	2	2	1621.56	40.11	3.77	0.51
5	2	1	1	2	1518.10	66.04	1.85	0.50
6	2	2	1	2	1575.19	70.74	2.20	0.57
7	2	3	2	1	1964.76	65.47	1.94	1.60
8	2	4	2	1	2061.87	69.82	2.22	1.70
9	3	1	2	1	2051.63	96.59	1.24	1.44
10	3	2	2	1	2306.33	99.25	1.56	1.55
11	3	3	1	2	1921.52	116.64	2.07	0.61
12	3	4	1	2	1927.77	134.74	2.29	0.69
13	4	1	2	2	2383.53	137.80	1.69	0.44
14	4	2	2	2	2703.00	143.58	2.06	0.47
15	4	3	1	1	2249.02	169.66	1.23	2.02
16	4	4	1	1	2253.87	197.28	1.44	2.28

Table 8.5 Average S/N ratio for the specific performance.

TPM	Average S/N ratio for specific performance			
	mass flow rate	number of fins	fin thickness	material
Level 1	62.84	64.75	64.55	65.39
Level 2	64.93	65.41	66.23	65.39
Level 3	66.22	65.59	-	-
Level 4	67.57	65.81	-	-
difference	4.73	1.07	1.68	0.00
Rank	1	3	2	4
Characteristic type	**Larger the best**			
Optimum	**A4**	**B4**	**C2**	**either**

Table 8.6 Average S/N ratio for the pressure drop

TPM	Average S/N ratio for pressure drop			
	mass flow rate	number of fins	fin thickness	material
Level 1	-31.85	-37.63	-38.95	-38.37
Level 2	-36.65	-38.07	-37.79	-38.37
Level 3	-40.89	-38.44	-	-
Level 4	-44.10	-39.36	-	-
difference	12.26	1.73	1.16	0.00
Rank	1	2	3	4
Characteristic type	**Smaller the best**			
optimum	**A1**	**B1**	**C2**	**either**

Table 8.7 Average S/N ratio for the variation of batteries temperature.

TPM	Variation of batteries temperature			
	mass flow rate	number of fins	fin thickness	material
Level 1	-7.66	-3.80	-4.88	-3.97
Level 2	-6.22	-5.48	-6.44	-7.36
Level 3	-4.81	-6.17	-	-
Level 4	-3.96	-7.21	-	-
difference	3.70	3.41	1.56	3.39
Rank	1	2	4	3
Characteristic type	**Smaller the best**			
optimum	**A4**	**B1**	**C1**	**D1**

Table 8.8 Average S/N ratio for mass of the plate fin.

TPM	Mass of plate fin			
	mass flow rate	number of fin	fin thickness	material
Level 1	0.56	1.46	-0.59	-4.85
Level 2	0.56	0.52	1.27	5.54
Level 3	0.13	0.094	-	-
Level 4	0.13	-0.70	-	-
difference	0.44	2.15	1.86	10.39
Rank	4	2	3	1
Characteristic type	**Smaller the best**			
optimum	**A1**	**B1**	**C2**	**D2**

The highest S/N ratios at all levels of the parameters indicate optimum performance. From Table 8.5, "larger the best" was used to characterize the specific performance of the plate fin. The optimum design parameters are (A) 30 gs^{-1} (level 4) for mass flow rate, (B) 15 (level 4) for number of fins, (C) 0.2 mm (level 2) for fin thickness and (D) either copper of aluminum fin. The specific performance of the plate fin is proportional to the mass flow rate, number of fins and fin thickness while the effect of fin material is not significant for specific performance. "Smaller the best" was used to characterize pressure drop across the plate fin. The optimum design parameters for pressure drop are (A) 15 gs^{-1} (level 1), (B) 5 (level 1) for number of fins and (C) 0.2 mm (level 2) for fin thickness as shown in Table 8.6. Lower mass flow rate, number of fins and fin thickness will result in lower pressure drop, while fin material does not affect the pressure drop. "Smaller the best" was used to characterize the variation of the battery temperature. The optimum design parameters for the variation of the battery temperature are (A) 30 gs^{-1} (level 4) for mass flow rate, (B) 5 (level 1) for number of fins, (C) 0.5 mm (level 1) for fin thickness and (D) copper fin (level 1) as shown in Table 8.7. Lower mass flow rate and fin thickness will result in high non-uniformity of the battery module temperature. Higher number of fins will also increase the variation of the battery module temperature. Copper with high thermal conductivity will give better uniformity than aluminum fin. "Smaller the best" was used to characterize the mass of the plate fin, the optimum design parameters for mass of plate fin are (A) 15 gs^{-1} (level 1) for mass flow rate, (B) 5 (level 1) for number of fins, (C) 0.2 mm (level 2) for fin thickness and (D) aluminum fin (level 2)

211

as shown in Table 8.8. Number of fins, fin thickness and fin material are the major factors which affect the mass of the plate fin. Obviously, aluminum with lower density is the best choice for plate fins.

8.5.2.2 Grey Relational Analysis

Grey relational analysis (GRA) was used to optimize the design parameters by maximizing the specific performance, minimizing the pressure drop, non-uniformity of the battery module temperature and mass of the plate fin. The results of the simulations were first normalized to the range of 0 and 1 according to section 8.3.4 as shown in Table 8.9. The results of the grey relational coefficient and grey relational grade are tabulated in Table 8.10. The grey relational grade (GRG) graph according to the L_{16} orthogonal experiment plan is shown in Table 8.11.

Table 8.9 Normalized response values.

| Exp No. | Parameters | | | | Normalized Response | | | |
	A	B	C	D	Specific Performance, Q_{spec}, $Wm^{-3}K^{-1}$	Pressure drop ΔP, Pa	Variation, ΔT, K	Mass, kg
1	1	1	1	1	0.000	0.997	0.903	0.349
2	1	2	1	1	0.023	0.981	0.791	0.209
3	1	3	2	2	0.232	1.000	0.125	0.975
4	1	4	2	2	0.282	0.985	0.000	0.958
5	2	1	1	2	0.213	0.822	0.757	0.968
6	2	2	1	2	0.251	0.793	0.618	0.926
7	2	3	2	1	0.510	0.826	0.720	0.370
8	2	4	2	1	0.574	0.798	0.613	0.314
9	3	1	2	1	0.567	0.631	0.998	0.454
10	3	2	2	1	0.736	0.614	0.872	0.398
11	3	3	1	2	0.481	0.505	0.672	0.905
12	3	4	1	2	0.485	0.392	0.583	0.863
13	4	1	2	2	0.788	0.373	0.818	1.000
14	4	2	2	2	1.000	0.336	0.676	0.983
15	4	3	1	1	0.698	0.173	1.000	0.140
16	4	4	1	1	0.702	0.000	0.917	0.000
Ideal sequence					1.000	1.000	1.000	1.000

Table 8.10 Grey relational coefficients and grey relational grade values.

| Exp No. | Grey relational coefficient | | | | Grey Relational Grade | Orders |
	Specific Performance, Q_{spec}, $Wm^{-3}K^{-1}$	Pressure drop ΔP, Pa	Variation, ΔT, K	Mass, kg		
1	0.333	0.994	0.838	0.434	0.587	10
2	0.338	0.963	0.705	0.387	0.547	16
3	0.394	1.000	0.364	0.952	0.621	6
4	0.410	0.970	0.333	0.922	0.609	7
5	0.388	0.738	0.673	0.940	0.626	3
6	0.400	0.707	0.567	0.871	0.589	9
7	0.505	0.742	0.641	0.442	0.567	12
8	0.540	0.713	0.564	0.422	0.556	13
9	0.536	0.575	0.995	0.478	0.624	5
10	0.655	0.564	0.796	0.454	0.625	4
11	0.491	0.503	0.604	0.840	0.586	11
12	0.493	0.451	0.545	0.785	0.553	15
13	0.702	0.443	0.733	1.000	0.716	2
14	**1.000**	**0.430**	**0.607**	**0.967**	**0.801**	**1**
15	0.624	0.377	1.000	0.368	0.598	8
16	0.626	0.333	0.858	0.333	0.555	14

Table 8.11 Average grey relational grade for combination of all responses.

| TPM | Combination of all responses | | | |
	mass flow rate	number of fins	fin thickness	material
Level 1	0.59	0.64	0.58	0.58
Level 2	0.58	0.64	0.64	0.64
Level 3	0.60	0.60	-	-
Level 4	0.67	0.57	-	-
difference	0.083	0.072	0.060	0.055
Rank	4	1	3	2
Characteristic type	**Larger the best**			
optimum	**A4**	**B2**	**C2**	**D2**

Grey relational analysis was used to determine the best design parameters of the plate fin. Specific performance is the critical factor in determining the plate fin design followed by pressure drop, temperature variation of battery module and mass of plate fin. Therefore, the weighting value for specific performance, pressure drop, temperature variation of battery module and mass of the fin are 0.4, 0.2, 0.2 and 0.2, respectively. The most ideal candidate for the optimal design parameters are (A) mass flow rate 30 gs^{-1} (level 4), (B) 9 fins (level 2), (C) 0.2 mm thickness of the

fin (level 2) and (D) aluminum fin (level 2) corresponding to Order 1 as shown in Table 8.10 and Table 8.11.

8.5.2.3 Analysis of Variance and F-Test

Analysis of variance (ANOVA) was used to analyze the variation of design parameters such as mass flow rate, number of fins, fin thickness, fin material and the associated degrees of freedom. The influence of the design parameters to each response was investigated. In this analysis, 5% of error in the classification of the significance of the design parameters was taken into consideration. Hence $\alpha = 0.05$, $v1 = 3$ for mass flow rate and fin number, $v1 = 1$ for fin thickness and fin material, $v2 = 7$ for error calculated with 17 degrees of freedom were used for the F-test. For design parameters mass flow rate and number of fins $F_{0.05, 3, 7} = 4.3469$. Fin thickness and fin material $F_{0.05, 1, 7} = 5.5914$. The results of ANOVA analysis of the responses are shown in the following tables:

Table 8.12 Analysis of variance for the specific performance.

Source	Sq	DF	Mq	F-ratio	Rho, %
Mass flow rate	2139892.83	3	713297.61	130.66	78.17
Number of fins	80529.06	3	26843.02	4.92	2.94
Fin thickness	477879.02	1	477879.02	87.54	17.46
Material	883.61	1	883.61	0.16	0.03
Error	38214.60	7	5459.23	1.00	1.40
St	2737399.12	15	182493.27	-	100.00
Mean	58198277.94	1	-	-	-
ST	60935677.06	16	-	-	-

Table 8.13 Analysis of variance for the pressure drop.

Source	Sq	DF	Mq	F-ratio	Rho, %
Mass flow rate	34516.71	3	11505.57	293.41	91.53
Number of fins	1575.53	3	525.18	13.39	4.18
Fin thickness	1289.40	1	1289.40	32.88	3.42
Material	54.69	1	54.69	1.39	0.15
Error	274.49	7	39.21	1.00	0.73
St	37710.82	15	2514.05	-	100.00
Mean	145198.00	1	-	-	-
ST	182908.82	16	-	-	-

Table 8.14 Analysis of variance for the variation temperature.

Source	Sq	DF	Mq	F-ratio	Rho, %
Mass flow rate	2.33	3	0.78	53.20	30.85
Number of fins	1.66	3	0.55	37.85	21.95
Fin thickness	0.81	1	0.81	55.62	10.75
Material	2.65	1	2.65	181.50	35.09
Error	0.10	7	0.01	1.00	1.35
St	7.56	15	0.50	-	100.00
Mean	65.07	1	-	-	-
ST	72.63	16	-	-	-

Table 8.15 Analysis of variance for mass of plate fin.

Source	Sq	DF	Mq	F-ratio	Rho, %
Mass flow rate	0.13	3	0.04	8.64	1.96
Number of fins	0.18	3	0.06	11.81	2.68
Fin thickness	0.25	1	0.25	50.06	3.79
Material	6.08	1	6.08	1202.17	91.03
Error	0.04	7	0.01	1.00	0.53
St	6.68	15	0.45	-	100.00
Mean	21.18	1	-	-	-
ST	27.86	16	-	-	-

The degree of influence of each design parameter is determined by the percent contribution and F-test in the ANOVA analysis. As shown in Table 8.12, mass flow rate and fin thickness influence the specific performance of the plate fin the most which contributed about 95.6%. The pressure drop of the plate fin is heavily affected by mass flow rate (91.53%) as shown in Table 8.13. Next, mass flow rate, number of fins and fin material are the major factors affecting the uniformity of the batteries module temperature. The contributions of the mass flow rate, number of fins and fin material are 30.85%, 21.95% and 35.09%, respectively, as shown in Table 8.14. Lastly, the analysis results show the most significant design parameters affecting the mass of the plate fin is fin material which contributed about 91.03% as shown in Table 8.15.

8.5.2.4 Optimized design

The temperature contour and velocity streamline plot of the optimized Aluminum plate fin are shown in Figure 8.6.

(a)   (b)
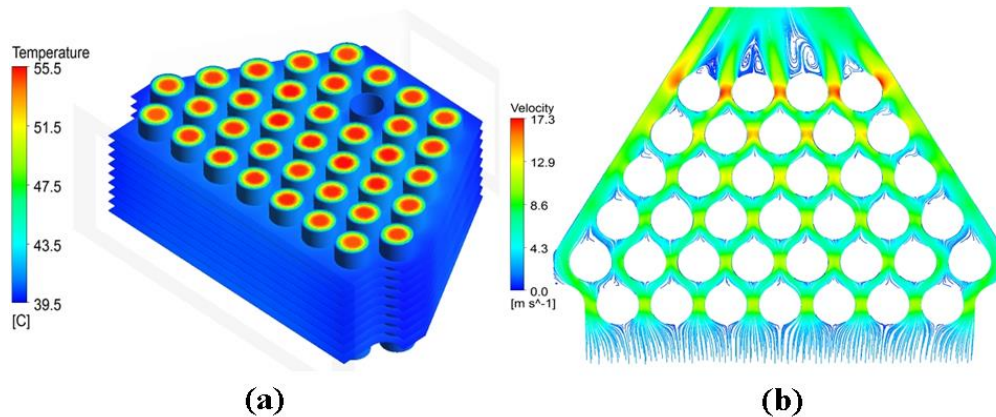
Figure 8.6 (a) Temperature distribution of the cells. (b) Surface streamline of the flow around the cells.

Figure 8.6(a) shows the temperature distribution of the optimized plate fin design. Both ends of the cells are thermally insulated, therefore the maximum temperature of the trapezoidal staggered arrangement cell is located at the center of the cells which is about 55.5 $^{\circ}$C. However, the cell center temperature might be lower in the real application as the copper connector connected to the terminal of the cell will help to transfer the heat from the cells in the axial direction. The cell body is at the same temperature as the fin at a relatively minimum temperature which is about 39.5 $^{\circ}$C. About 9.5 $^{\circ}$C of temperature rise is found when cooling the battery module with 30 $^{\circ}$C ambient air. The variation of the surface temperature of the cells is 1.74 $^{\circ}$C. Figure 8.6(b) shows the flow field in the battery module. As the cooling air approach the front side of the cell, the pressure of the cooling air rise to the stagnation point value from the free stream value. The cooling air is forced to move along the tube surface by the high pressure forces and boundary layers are developed on the both sides of the

216

tube. However, the viscous forces will counteract the pressure force and the cooling air cannot flow to the rear surface of the tube and boundary layer separation occurs. This process will develop two shear layers, the inner layers which are in contact with the tube surface moves slower than the outer layer. As a result, the shear layers roll up and recirculation flow at the rear of the tube and it depends on the Reynolds numbers. The temperature will increase substantially compared to the front side of the tube (Sunden, 2011 and Zukauskas and Ulinskas, 1988). In the trapezoidal arrangement, the cooling air flows from the bottom to the top and increases along the flow direction due to the gradual decrease of the flow area. Although the temperature of the cooling air rises along the direction of flow, the increasing of the flow velocity will increase the heat transfer rate which tends to help maintain a more uniform temperature distribution of the cells in the module. The highest velocity is found at the center in between the end row of the tubes which is 17.3 ms^{-1}. Vortices are developed at the rear end of the last row due to high velocity at the outlet.

8.5.2.5 Performance characterization

The heat transfer and flow characteristic of the optimized design in terms of Reynolds number and Nusselt number for the aluminum plate fin are shown in Figure 8.7.
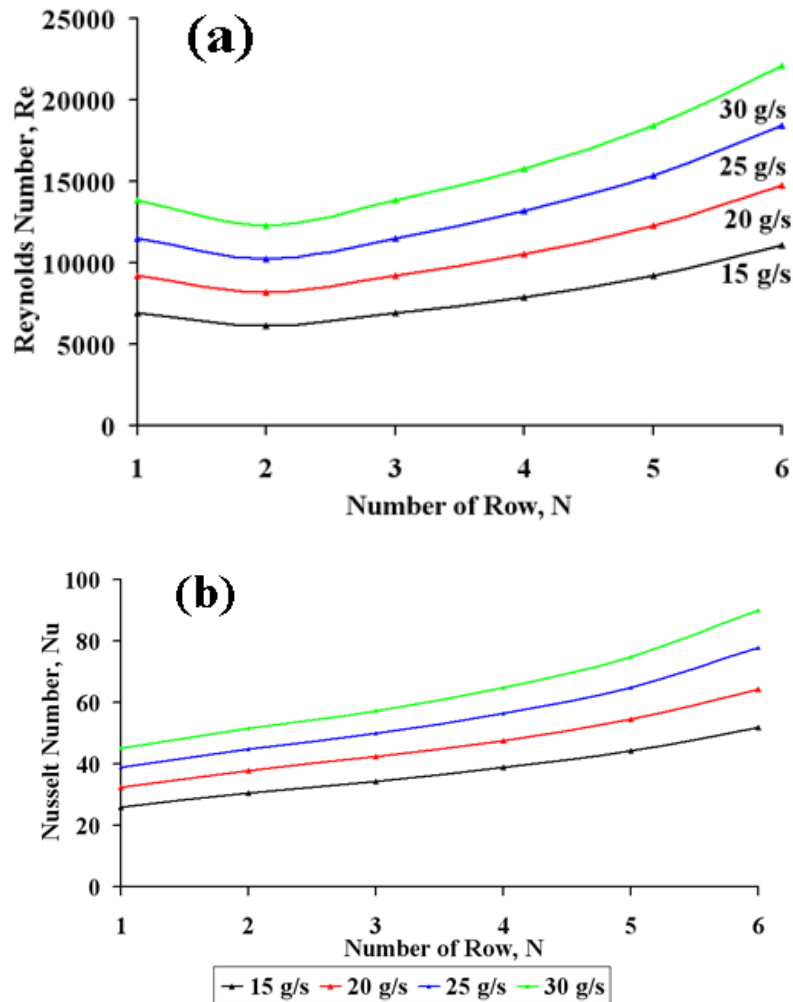
Figure 8.7 Performance of the optimized cooling fin at each row.
(a). Reynolds number. (b) Nusselt number.

Figure 8.7(a) shows the variation of the Reynolds number across the battery module. The Reynolds number is increased with the row number, which is caused by decreasing of the flow area in the trapezoidal shape. Besides, the heat transfer rate is also increasing across the cell bank as presented in Figure 8.7(b).

The results of the regression analysis for an average Nusselt number, average J factor, average friction factor and variation of temperature for the aluminum plate fin are shown in Table 8.16 to Table 8.19, respectively. The regression equations are shown in Equations 8-54 to 8-57.

Table 8.16 Regression statistics of the average Nusselt number.

Predictor	Coefficient	Standard Error	T	P	Lower 95%	Upper 95%
Constant	-4.484	0.0414	-108.362	0.0001	-4.662	-4.306
$Ln\overline{Re}_D$	0.857	0.0044	194.040	0.0000	0.838	0.876
S = 0.00229		R = 99.99%		R-Sq = 99.99%		R-Sq(adj) = 99.99%

Table 8.17 Regression statistics of the average J factor.

Predictor	Coefficient	Standard Error	T	P	Lower 95%	Upper 95%
Constant	-4.219	0.0414	-101.942	9.62e-5	-4.397	-4.040
$Ln\overline{Re}_D$	-0.143	0.0044	-32.320	0.000956	-0.162	-0.124
S = 0.00229		R = 99.90%		R-Sq = 99.80%		R-Sq(adj) = 99.71%

Table 8.18 Regression statistics of the average friction factor.

Predictor	Coefficient	Standard Error	T	P	Lower 95%	Upper 95%
Constant	-3.867	0.179	-21.663	0.00212	-4.635	-3.099
$Ln\overline{Re}_D$	-1.059	0.0191	-55.521	0.000324	-1.141	-0.977
S = 0.00987		R = 99.97%		R-Sq = 99.94%		R-Sq(adj) = 99.90%

Table 8.19 Regression statistics of the temperature variation.

Predictor	Coefficient	Standard Error	T	P	Lower 95%	Upper 95%
Constant	1.664	0.0783	21.242	0.00221	1.327	2.001
$Ln\overline{Re}_D$	-0.688	0.00836	-82.238	0.000148	-0.724	-0.652
S = 0.00229		R = 99.99%		R-Sq = 99.97%		R-Sq(adj) = 99.96%

$$\overline{Nu}_D = 0.0113\overline{Re}_D^{0.857} \tag{8-54}$$

$$\overline{J} = 0.0147\overline{Re}_D^{-0.143} \tag{8-55}$$

$$\frac{\overline{f}}{Re} = 0.0209\overline{Re}_D^{-1.059} \tag{8-56}$$

$$\frac{\Delta T}{T_{in}} = 5.28\overline{Re}_D^{-0.688} \tag{8-57}$$

As can be seen from Table 8.16- Table 8.19, the R-square for the $\overline{Nu}_D$, $\overline{J}$, $\overline{f}$ and $\Delta T/T_{in}$ are 99.9%, 99.8%, 99.9% and 99.9%, respectively, which indicate very good correlation with Re_D with variations of ±0.01 %, ±0.2 %, ±0.06% and ±0.03%, respectively. The errors of prediction for the average

219

Nusselt number, friction factor, J factor and variation of temperature are 0.1%, 0.7%, 0.1% and 8.7%, respectively.

The results of the multiple regression analysis for the average Nusselt number, average J factor, average friction factor and variation of temperature for Aluminum fin are shown in Table 8.20 to Table 8.24, respectively. The regression equations for the aluminum plate fins are shown in Equations 8-58 to 8-61.

Table 8.20 Regression statistics of the average Nusselt number.

Predictor	Coefficient	Standard Error	T	P	Lower 95%	Upper 95%
Constant	-3.164	0.0779	-40.649	6.007e-36	-3.321	-3.007
$Ln\overline{Re}_D$	0.8561	0.00286	299.814	4.935e-73	0.850	0.862
$Ln\left(\dfrac{F_p - \delta}{D_0}\right)$	-0.2285	0.0451	-5.064	8.200e-06	-0.320	-0.138
$Ln\left(\dfrac{F_p}{D_h}\right)$	-0.7916	0.0578	-13.687	2.846e-17	-0.908	-0.675
$Ln\left(\dfrac{F_p}{P_t}\right)$	0.7847	0.0656	11.967	2.832e-15	0.652	0.917
S = 0.00512	R = 99.98%		R-Sq = 99.96%		R-Sq(adj) = 99.95%	

Table 8.21 Regression statistics of the average friction factor.

Predictor	Coefficient	Standard Error	T	P	Lower 95%	Upper 95%
Constant	-3.089	0.168	-18.353	5.839e-22	-3.429	-2.750
$Ln\overline{Re}_D$	-0.0532	0.00618	-8.613	6.550e-11	-0.0656	-0.0407
$Ln\left(\dfrac{F_p - \delta}{D_0}\right)$	0.335	0.0976	3.435	0.00132	0.138	0.532
$Ln\left(\dfrac{F_p}{D_h}\right)$	-0.0172	0.125	-0.137	0.891	-0.269	0.235
$Ln\left(\dfrac{F_p}{P_t}\right)$	0.253	0.142	1.786	0.0811	-0.0327	0.539
S = 0.00111	R = 99.87%		R-Sq = 99.74%		R-Sq(adj) = 99.71%	

Table 8.22 Improved regression statistics of the average friction factor.

Predictor	Coefficient	Standard Error	T	P	Lower 95%	Upper 95%
Constant	-3.111	0.0602	-51.706	4.846e-41	-3.232	-2.990
$Ln\overline{\text{Re}}_D$	-0.0532	0.00611	-8.710	3.945e-11	-0.0655	-0.0409
$Ln\left(\dfrac{F_p - \delta}{D_0}\right)$	0.347	0.0484	7.168	6.481e-09	0.249	0.444
$Ln\left(\dfrac{F_p}{P_t}\right)$	0.235	0.0518	4.544	4.273e-05	0.131	0.340
S = 0.0110		R = 99.87%		R-Sq = 99.74%		R-Sq(adj) = 99.72%

Table 8.23 Regression statistics of the average J factor.

Predictor	Coefficient	Standard Error	T	P	Lower 95%	Upper 95%
Constant	-2.899	0.0779	-37.236	2.354e-34	-3.057	-2.742
$Ln\overline{\text{Re}}_D$	-0.144	0.00286	-50.397	7.010e-40	-0.150	-0.138
$Ln\left(\dfrac{F_p - \delta}{D_0}\right)$	-0.229	0.0451	-5.064	8.201e-06	-0.320	-0.138
$Ln\left(\dfrac{F_p}{D_h}\right)$	-0.792	0.0578	-13.687	2.846e-17	-0.908	-0.675
$Ln\left(\dfrac{F_p}{P_t}\right)$	0.785	0.0656	11.967	2.832e-15	0.652	0.917
S = 0.00512		R = 99.89%		R-Sq = 99.78%		R-Sq(adj) = 99.76%

Table 8.24 Regression statistics of the variation of temperature.

Predictor	Coefficient	Standard Error	T	P	Lower 95%	Upper 95%
Constant	-1.467	0.614	-2.392	0.0212	-2.705	-0.230
$Ln\overline{\text{Re}}_D$	-0.653	0.0225	-29.035	6.957e-30	-0.699	-0.699
$Ln\left(\dfrac{F_p - \delta}{D_0}\right)$	2.810	0.356	7.904	6.494e-10	2.093	3.527
$Ln\left(\dfrac{F_p}{D_h}\right)$	1.307	0.456	2.867	0.00639	0.388	2.226
$Ln\left(\dfrac{F_p}{P_t}\right)$	-3.810	0.517	-7.373	3.727e-09	-4.852	-2.768
S = 0.0404		R = 98.52 %		R-Sq = 97.06 %		R-Sq(adj) = 96.79%

$$\overline{Nu}_D = a\overline{Re}_D^{\,n}\left(\frac{F_p - \delta}{D_0}\right)^x \left(\frac{F_p}{D_h}\right)^y \left(\frac{F_p}{P_t}\right)^z \tag{8-58}$$

with $a = 0.0422$, $n = 0.856$, $x = -0.229$, $y = -0.792$, $z = 0.785$

$$\overline{f} = a\overline{Re}_D^{\,n}\left(\frac{F_p - \delta}{D_0}\right)^x \left(\frac{F_p}{P_t}\right)^z \tag{8-59}$$

with $a = 0.0446$, $n = -0.0532$, $x = 0.347$, $z = 0.235$

$$\overline{J} = a\overline{Re}_D^{\,n}\left(\frac{F_p - \delta}{D_0}\right)^x \left(\frac{F_p}{D_h}\right)^y \left(\frac{F_p}{P_t}\right)^z \tag{8-60}$$

with $a = 0.0551$, $n = -0.144$, $x = -0.229$, $y = -0.792$, $z = 0.785$

$$\frac{\Delta T}{T_\infty} = a\overline{Re}_D^{\,n}\left(\frac{F_p - \delta}{D_0}\right)^x \left(\frac{F_p}{D_h}\right)^y \left(\frac{F_p}{P_t}\right)^z \tag{8-61}$$

with $a = 0.231$, $n = -0.653$, $x = 2.810$, $y = 1.307$, $z = -3.810$

The R-square for the average Nusselt number plot for the Aluminum plate fins are 99.9% as shown in Table 8.20, which indicates a very good correlation with a variation of ±0.04%. The p-value for the average friction factor plot for Aluminum plate fin is > 0.05 to correlate $\left(\frac{F_p}{D_h}\right)^y$ as shown in Table 8.21. Therefore, p-value approach and critical value approach tests are used as an evaluation criterion to retain or omit the $\left(\frac{F_p}{D_h}\right)^y$ term. The test results are shown in Table 8.25. Through both tests, $\left(\frac{F_p}{D_h}\right)^y$ is statistically insignificant at a significant level of 0.05 and can be omitted.

Table 8.25 Evaluation criteria for the parameter.

Evaluation criteria	Significant
p-value approach	TDIST (8.06,43,2)=3.9E-10 $P < 0.05$
Critical value approach	TINV(0.05, 43) = 2.0167 $t = |-8.06|>2.0167$

New analysis was carried out, and the p-value of all the parameters was found statistically significant to correlate the friction factor as shown in Table 8.22 with a variation of ±0.26%. As can be seen from Table 8.23 and Table 8.24, the R-square for average J factor and variation of cell temperature are 99.8% and 97.1%, respectively, which indicates very good correlation, with variations of ±0.2% and ±2.9%, respectively. The best fit curves for the $\overline{Nu}_D$, $\overline{J}$, $\overline{f}$ and $\Delta T / T_{in}$ for the aluminum plate fin are shown in Figure 8.8.
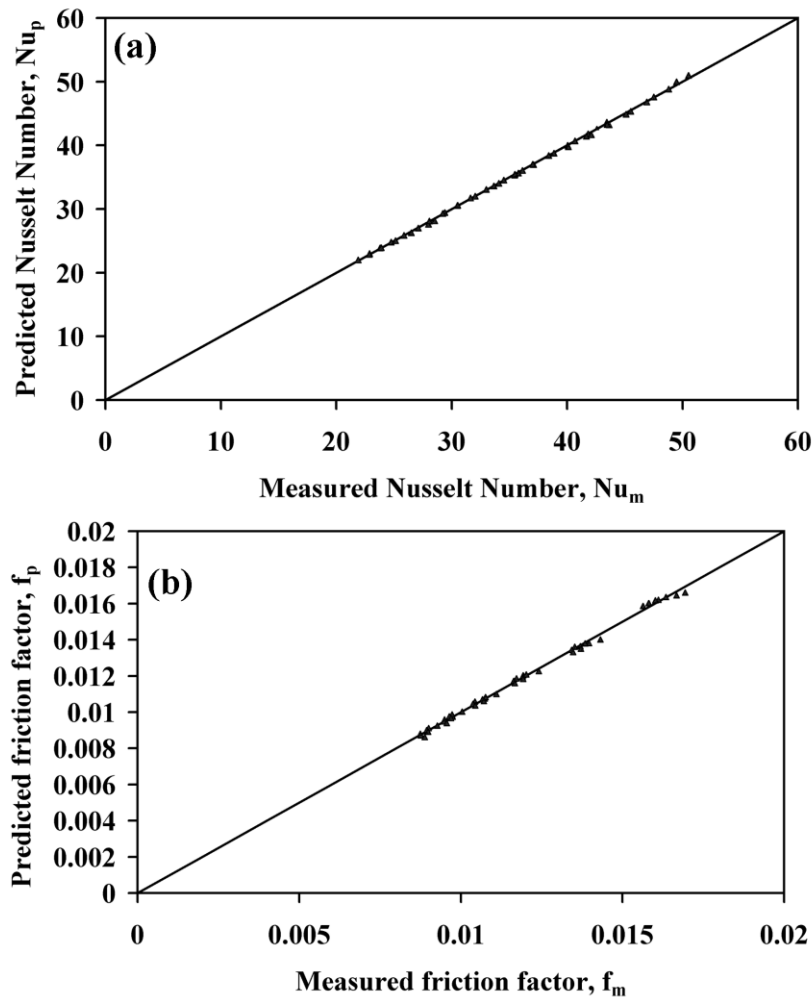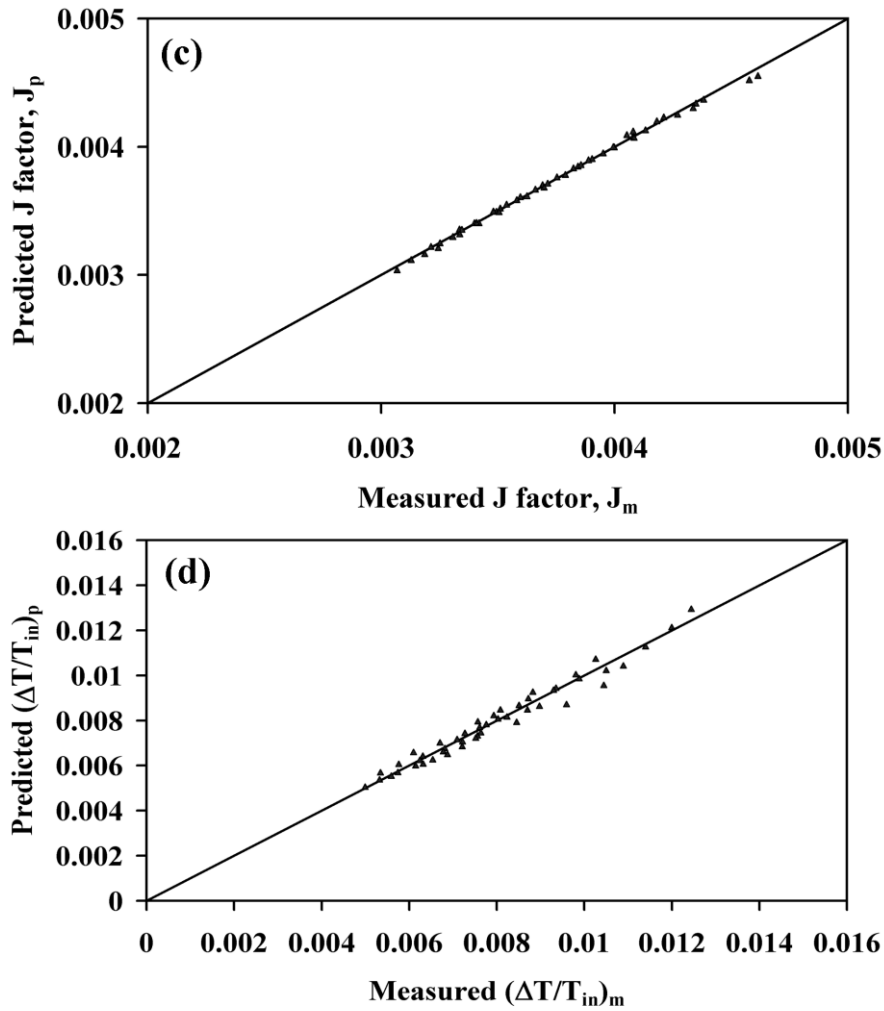
Figure 8.8 Comparison of the correlation with simulation data for aluminum fin. (a) Nusselt number. (b) Friction factor. (c) J factor. (d) $\Delta T/T_{in}$.

The maximum error of using the developed correlation to predict the measured data for the average Nusselt number, friction factor, J factor and variation of temperature for the aluminum fins are 1.4%, 2.8%, 1.3% and 8.9%, respectively. The overall maximum error is less than 10%. Hence, the correlations developed in Equations 8-58 to 8-61 give good predictions of the average Nusselt number, Friction factor, J factor and variation of temperature of the plate fin battery module.

8.5.2.6 Comparison of the finned and unfinned battery module

Comparison of the variation of cell temperature, average Nusselt number and fan power consumption of finned and unfinned battery module are shown in Figure 8.9.
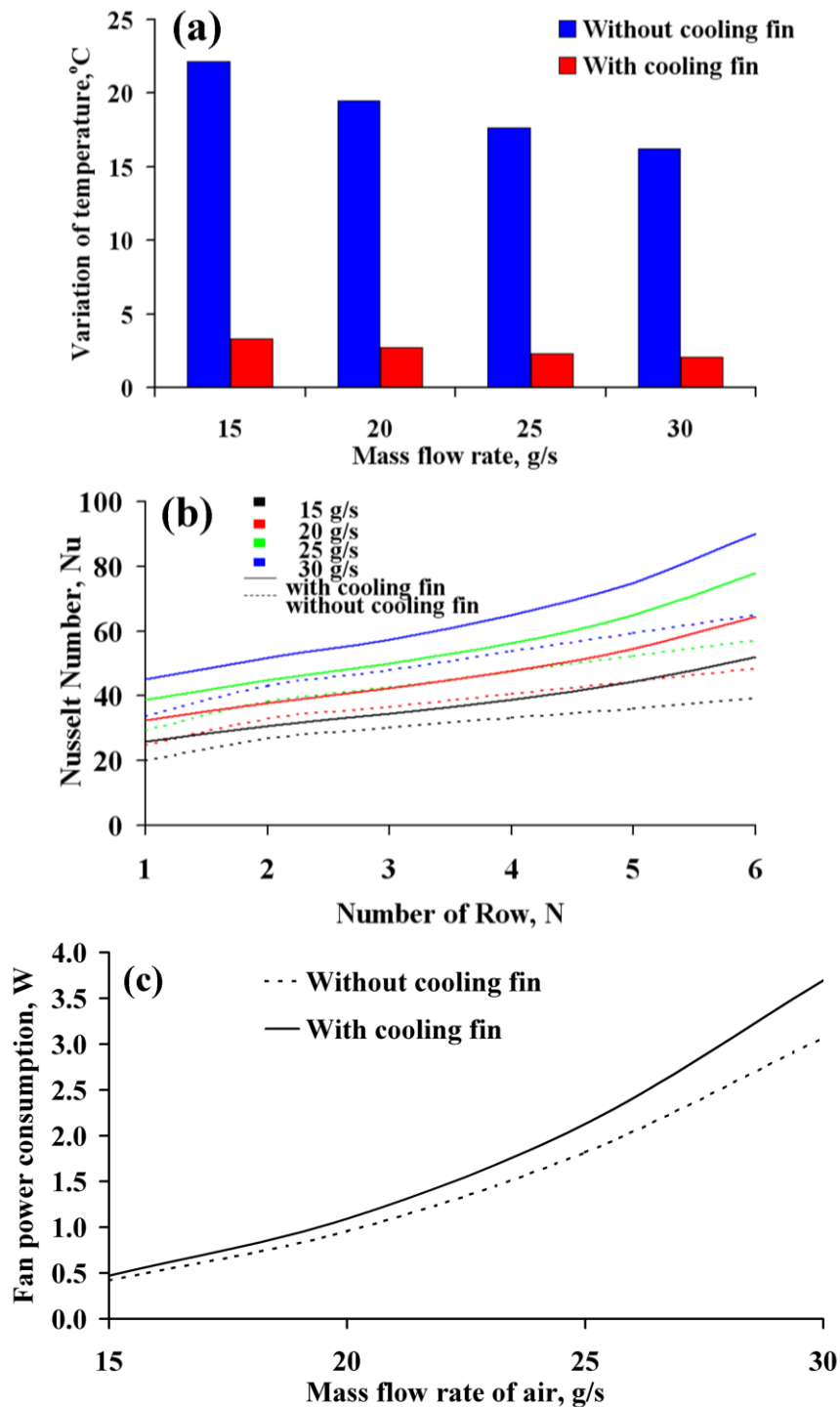
Figure 8.9 Comparison of finned and unfinned battery module. (a). Variation of temperature. (b). Nusselt number. (c). Fan power consumption.

The variation temperature of the unfinned battery module is higher than the battery module with the plate fins installed. The variation of temperature is decreased with the mass flow rate of cooling air. Besides, the variation of temperature for the unfinned battery module at 15 gs^{-1} of air flow are about 22 $^{\circ}$C, while the variation of temperature for the plate fin battery module is about 3.3 $^{\circ}$C and this is within the tolerable variation temperature range of the battery module. Although the average Nusselt numbers of the unfinned and finned battery module are progressively increased with the number row, the average Nusselt number for the unfinned battery module is lower than the finned battery module. At a low mass flow rate of cooling air (15 gs^{-1}), the fan power consumption of the finned battery module is about 12.6% higher than the unfinned module. When the mass flow rate of cooling air is doubled, there is only a 7.8% increase of the fan power consumption. Therefore, plate fins can increase the heat transfer from the battery cells and maintain temperature uniformity within the battery module.

8.5.3 Helical fin

8.5.3.1 Taguchi method analysis

The Taguchi method was also used to study the effects of mass flow rate, number of turns, fin thickness and fin materials on the performance of the helical fin battery module. The factors used to perform the numerical simulations and the levels are given in Table 8.1 and Table 8.2. The results of the simulation are shown in Table 8.26. The results are transformed into S/N (signal to noise) ratios according to the characteristic of the response either "smaller the best", "nominal the best" or "larger the best" as shown in Table 8.27 to Table 8.30.

Table 8.26 Design of experiment and collected response data.

No	Parameters				Response			
	A	B	C	D	Specific Performance, Q_{spec}, Wm^{-3}K^{-1}	Pressure drop ΔP, Pa	Variation, ΔT, K	Mass, kg
1	1	1	1	1	1192.28	47.84	7.60	1.63
2	1	2	1	1	1201.22	51.24	9.92	1.91
3	1	3	2	2	1415.24	56.11	8.88	0.48
4	1	4	2	2	1531.12	59.24	9.28	0.51
5	2	1	1	2	1509.38	83.74	5.71	0.49
6	2	2	1	2	1525.45	90.20	7.37	0.58
7	2	3	2	1	1814.34	99.46	6.67	1.59
8	2	4	2	1	1985.62	104.72	7.08	1.70
9	3	1	2	1	1716.66	140.32	3.94	1.42
10	3	2	2	1	2006.58	148.55	4.80	1.53
11	3	3	1	2	1943.41	156.19	6.31	0.62
12	3	4	1	2	1837.78	166.64	6.86	0.71
13	4	1	2	2	1979.58	201.51	3.54	0.43
14	4	2	2	2	2341.58	214.35	4.29	0.46
15	4	3	1	1	2143.03	220.68	4.96	2.05
16	4	4	1	1	2150.58	241.45	5.43	2.33

Table 8.27 Average S/N ratio for the specific performance.

TPM	Average S/N ratio for specific performance			
	mass flow rate	number of turns	fin thickness	material
Level 1	62.46	63.93	64.34	64.783
Level 2	64.59	64.67	65.24	64.792
Level 3	65.45	65.15	-	-
Level 4	66.65	65.40	-	-
difference	4.19	1.47	0.90	0.01
Rank	1	2	3	4
Characteristic type	Larger the best			
Optimum	**A4**	**B4**	**C2**	**either**

Table 8.28 Average S/N ratio for the pressure drop

TPM	Average S/N ratio for pressure drop			
	mass flow rate	number of turns	fin thickness	material
Level 1	-34.56	-40.27	-41.02	-41.13
Level 2	-39.48	-40.84	-41.23	-41.13
Level 3	-43.67	-41.42	-	-
Level 4	-46.81	-41.99	-	-
difference	12.25	1.72	0.21	0.00
Rank	1	2	3	4
Characteristic type	Smaller the best			
optimum	**A1**	**B1**	**C1**	**either**

Table 8.29 Average S/N ratio for the variation of batteries temperature.

TPM	Variation of batteries temperature			
	mass flow rate	number of turns	fin thickness	material
Level 1	-18.97	-13.91	-16.42	-15.64
Level 2	-16.49	-15.89	-15.12	-15.89
Level 3	-14.56	-16.34	-	-
Level 4	-13.06	-16.94	-	-
difference	5.91	3.04	1.30	0.25
Rank	1	2	3	4
Characteristic type	**Smaller the best**			
optimum	**A4**	**B1**	**C2**	**D1**

Table 8.30 Average S/N ratio for mass of the helical fin.

TPM	Mass of helical fin			
	mass flow rate	number of turns	fin thickness	material
Level 1	0.57	1.54	-0.68	-4.86
Level 2	0.57	0.525	1.34	5.53
Level 3	0.10	0.061	-	-
Level 4	0.10	-0.79	-	-
difference	0.46	2.34	2.02	10.39
Rank	4	2	3	1
Characteristic type	**Smaller the best**			
optimum	**A1**	**B1**	**C2**	**D2**

The highest S/N ratios at all levels of the parameters indicate optimum performance. From Table 8.27, "larger the best" is used to characterize the specific performance of the helical fin, the optimum design parameters are (A) 30 gs^{-1} (level 4) for mass flow rate, (B) 15 (level 4) for number of turns, (C) 0.2 mm (level 2) for fin thickness and (D) either copper or aluminum fin. The specific performance of the helical fin is proportional to the mass flow rate, number of turns and fin thickness while the effect of fin material is not significant. "Smaller the best" is used to characterize pressure drop across the helical fin, the optimum design parameters for pressure drop are (A) 15 gs^{-1} (level 1), (B) 5 (level 1) for number of turns, (C) 0.5 mm (level 1) for fin thickness and (D) either copper or aluminum fin as shown in Table 8.28. Lower mass flow rate, number of turns and fin thickness will result in lower pressure drop, while fin material does not affect the pressure

drop. "Smaller the best" is used to characterize the variation of the battery temperature, the optimum design parameters are (A) 30 gs^{-1} (level 4) for mass flow rate, (B) 5 (level 1) for number of turns, (C) 0.2 mm (level 2) for fin thickness and (D) copper fin (level 1) as shown in Table 8.29. Lower mass flow rate and fin thickness will result in highly non-uniformity of the battery temperature. Higher number of turns will also increase the variation of the battery temperature. Copper with high thermal conductivity will give better uniformity than aluminum. "Smaller the best" is used to characterize the mass of the helical fin, the optimum design parameters for mass of helical fin are (A) 15 gs^{-1} (level 1) for mass flow rate, (B) 5 (level 1) for number of turns, (C) 0.2 mm (level 2) for fin thickness and (D) aluminum fin (level 2) as shown in Table 8.30. Number of turns, fin thickness and fin material are the major factors which affect the mass of the helical fin. Hence, Aluminum is the best choice.

8.5.3.2 Grey Relational Analysis

Grey relational analysis (GRA) was used to optimize the design parameters by maximizing the specific performance, minimizing the pressure drop, non-uniformity of the battery module temperature and mass of the helical fin. The results of the simulation are first normalized in the range of 0 and 1 according to section 8.3.4 as shown in Table 8.31. The results of the grey relational coefficient and grey relational grade are tabulated in Table 8.32. The grey relational grade (GRG) graph according to the L$_{16}$ orthogonal experiment plan is shown in Table 8.33.

Table 8.31 Normalized response values.

Exp No.	Parameters				Normalized Response			
	A	B	C	D	Specific Performance, Q_{spec}, $Wm^{-3}K^{-1}$	Pressure drop ΔP, Pa	Variation, ΔT, K	Mass, kg
1	1	1	1	1	0.000	1.000	0.364	0.369
2	1	2	1	1	0.008	0.982	0.000	0.221
3	1	3	2	2	0.194	0.957	0.163	0.973
4	1	4	2	2	0.295	0.941	0.100	0.955
5	2	1	1	2	0.276	0.815	0.661	0.967
6	2	2	1	2	0.290	0.781	0.400	0.922
7	2	3	2	1	0.541	0.733	0.510	0.391
8	2	4	2	1	0.690	0.706	0.446	0.332
9	3	1	2	1	0.456	0.522	0.938	0.479
10	3	2	2	1	0.709	0.480	0.803	0.420
11	3	3	1	2	0.654	0.440	0.566	0.900
12	3	4	1	2	0.562	0.386	0.480	0.855
13	4	1	2	2	0.685	0.206	1.000	1.000
14	4	2	2	2	1.000	0.140	0.882	0.982
15	4	3	1	1	0.827	0.107	0.778	0.147
16	4	4	1	1	0.834	0.000	0.704	0.000
Ideal sequence					1.000	1.000	1.000	1.000

Table 8.32 Grey relational coefficients and grey relational grade values.

Exp No.	Grey relational coefficient				Grey Relational Grade	Orders
	Specific Performance, Q_{spec}, $Wm^{-3}K^{-1}$	Pressure drop ΔP, Pa	Variation, ΔT, K	Mass, kg		
1	0.333	1.000	0.440	0.442	0.554	11
2	0.335	0.966	0.333	0.391	0.506	16
3	0.383	0.921	0.374	0.949	0.657	4
4	0.415	0.895	0.357	0.918	0.646	5
5	0.408	0.729	0.596	0.937	0.668	3
6	0.413	0.696	0.454	0.865	0.607	7
7	0.522	0.652	0.505	0.451	0.532	14
8	0.618	0.630	0.474	0.428	0.537	13
9	0.479	0.511	0.890	0.490	0.593	8
10	0.632	0.490	0.717	0.463	0.575	9
11	0.591	0.472	0.536	0.833	0.608	6
12	0.533	0.449	0.490	0.775	0.562	10
13	0.614	0.386	1.000	1.000	0.750	2
14	**1.000**	**0.368**	**0.809**	**0.966**	**0.786**	**1**
15	0.743	0.359	0.693	0.370	0.541	12
16	0.751	0.333	0.628	0.333	0.511	15

Table 8.33 Average grey relational grade for combination of all responses.

TPM	Combination of all responses			
	mass flow rate	number of turns	fin thickness	material
Level 1	0.591	0.641	0.570	0.544
Level 2	0.586	0.619	0.635	0.660
Level 3	0.584	0.585	-	-
Level 4	0.647	0.564	-	-
difference	0.063	0.077	0.065	0.117
Rank	4	2	3	1
Characteristic type	**Larger the best**			
optimum	**A4**	**B1**	**C2**	**D2**

Grey relational analysis was used to determine the best design parameters of the helical fin. Specific performance is the critical factor in determining the helical fin design followed by pressure drop, temperature variation of battery and mass of helical fin. Therefore, the weighting value for specific performance, pressure drop, variation of battery temperature and mass of the fin were 0.4, 0.2, 0.2 and 0.2, respectively. The most ideal candidate for the optimal design parameters are (A) mass flow rate 30 gs^{-1} (level 4), (B) 5 turns of fin (level 1), (C) 0.2 mm thickness of fin (level 2) and (D) aluminum fin (level 2) corresponding to Order 1 in the orders as shown in Table 8.32 and Table 8.33.

8.5.3.3 Analysis of Variance and F-Test

Analysis of Variance (ANOVA) was used to analyze the variation of design parameters such as mass flow rate, number of turns, fin thickness, fin material and the associated degrees of freedom. The influence of the design parameters to each response will be investigated. In this analysis, 5% of error in the classification of the significance of the design parameters was taken into consideration. Hence $\alpha = 0.05$, $v1 = 3$ for mass flow rate and number of turns, $v1 = 1$ for fin thickness and fin material, $v2 = 7$ for error calculated with 17 degrees of freedom are used for the F-test. For design parameters mass flow

rate and number of turns $F_{0.05,\,3,\,7} = 4.3469$. For fin thickness and fin material $F_{0.05,\,1,\,7} = 5.5914$. The results of the ANOVA analysis of the responses are illustrated in the Table 8.34 to Table 8.37.

Table 8.34 Analysis of variance for the specific performance.

Source	Sq	DF	Mq	F-ratio	Rho, %
Mass flow rate	1405929.95	3.00	468643.32	41.79	79.68
Number of turns	175380.38	3.00	58460.13	5.21	9.94
Fin thickness	103620.33	1.00	103620.33	9.24	5.87
Material	1004.68	1.00	1004.68	0.09	0.06
Error	78497.81	7.00	11213.97	1.00	4.45
St	1764433.16	15.00	117628.88	-	100.00
Mean	50033833.76	1.00	-	-	-
ST	51798266.92	16.00	-	-	-

Table 8.35 Analysis of variance for the pressure drop.

Source	Sq	DF	Mq	F-ratio	Rho, %
Mass flow rate	62515.93	3.00	20838.64	1251.97	97.58
Number of turns	1319.69	3.00	439.90	26.43	2.06
Fin thickness	71.03	1.00	71.03	4.27	0.11
Material	43.16	1.00	43.16	2.59	0.07
Error	116.51	7.00	16.64	1.00	0.18
St	64066.32	15.00	4271.09	-	100.00
Mean	270978.13	1.00	-	-	-
ST	335044.44	16.00	-	-	-

Table 8.36 Analysis of variance for the variation of temperature.

Source	Sq	DF	Mq	F-ratio	Rho, %
Mass flow rate	42.82	3.00	14.27	95.56	78.23
Number of turns	8.64	3.00	2.88	19.29	15.79
Fin thickness	2.02	1.00	2.02	13.50	3.68
Material	0.21	1.00	0.21	1.43	0.39
Error	1.05	7.00	0.15	1.00	1.91
St	54.73	15.00	3.65	-	100.00
Mean	658.24	1.00	-	-	-
ST	712.98	16.00	-	-	-

Table 8.37 Analysis of variance for the mass of helical fin.

Source	Sq	DF	Mq	F-ratio	Rho, %
Mass flow rate	0.16	3.0	0.05	8.64	2.28
Number of turns	0.21	3.0	0.07	11.81	3.12
Fin thickness	0.30	1.0	0.30	50.06	4.41
Material	6.11	1.0	6.11	1017.67	89.58
Error	0.04	7.0	0.01	1.00	0.62
St	6.83	15.0	0.46	-	100.00
Mean	21.30	1.0	-	-	-
ST	28.12	16.0	-	-	-

The degree of influence of each design parameter was determined by percent contribution and F-test in the ANOVA analysis. As shown in Table 8.34, mass flow rate and fin thickness influence the specific performance of the helical fin the most with a contribution of about 79.68%. The pressure drop of the helical fin is heavily affected by mass flow rate (97.58%) as shown in Table 8.35. Next, mass flow rate, number of turns and fin thickness are the major factors affecting the temperature uniformity. The contributions of the mass flow rate, number of turns and fin thickness are 78.23%, 15.79% and 3.68%, respectively as shown in Table 8.36. Lastly, the analysis results show that the most significant design parameters affecting the mass of the helical fin is fin material which contributed about 89.58% as shown in Table 8.37. However, due to limitations of machining technology, a fin thickness of 0.5 mm was chosen for the experimental study.

8.5.3.4 Optimized design

The temperature contour and velocity streamline plot of the optimized Aluminum helical fin are shown in Figure 8.10.
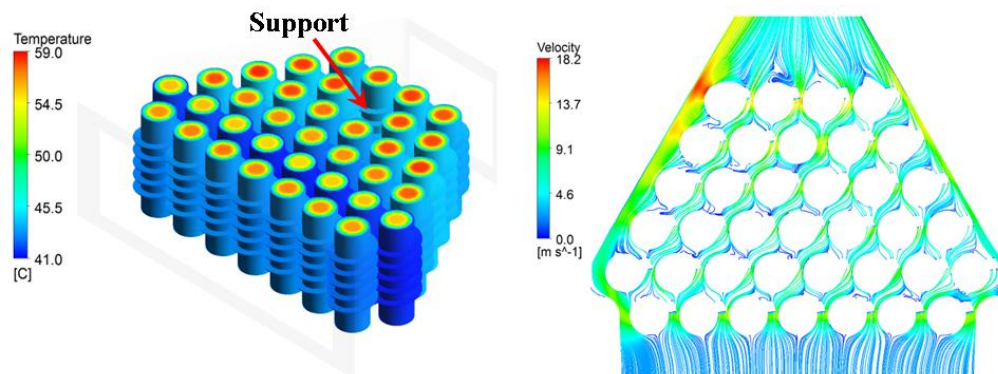
Figure 8.10 (a) Temperature distribution of the cells. (b) Surface streamline of the flow around the fin.

Figure 8.10(a) shows the temperature distribution of the optimized helical fin design. Both ends of the cells are thermally insulated, therefore

the maximum temperature of the trapezoidal staggered arrangement of cell is located at the center of the cells which is about 53.3 $^{\circ}$C. This is due to the poor thermal conductivity of the battery in the radial direction. The cell body is at the same temperature with the fin at a relatively minimum temperature of about 46.2 $^{\circ}$C. About 16.2 $^{\circ}$C of temperature rise is found when cooling the battery module with 30 $^{\circ}$C of ambient air. The variation of the surface temperature of the cells is 3.5 $^{\circ}$C. Figure 8.10 (b) shows the flow field in the battery module. The flow field in the finned module is similar to explanation as in section 8.5.2.4. The highest velocity is found at the top sides near the wall which is 18.1 ms^{-1}. As shown in Figure 8.10 (b), vortices are developed at the rear end of the last row due to high velocity at the outlet.

8.5.3.5 Performance characterization

The heat transfer and flow characteristic of the optimized design in term of Reynolds number and Nusselt number for aluminum helical fin are shown in Figure 8.11.
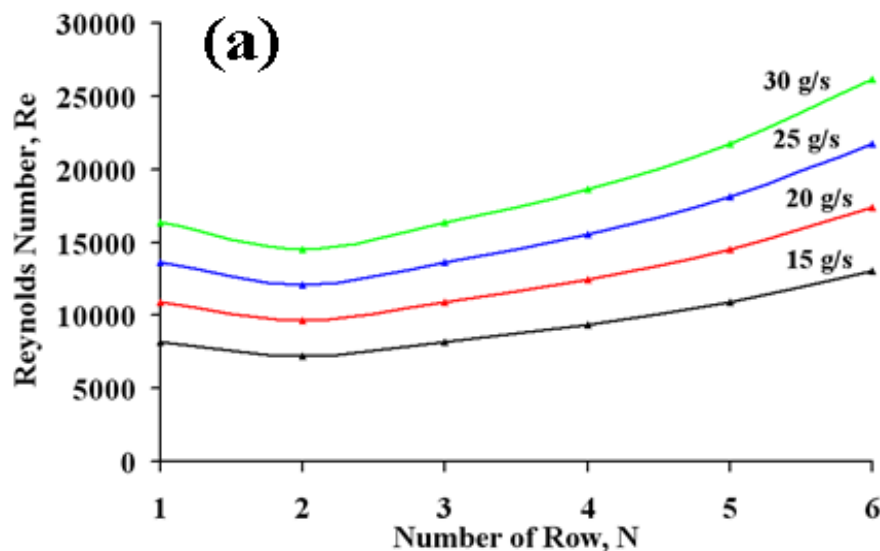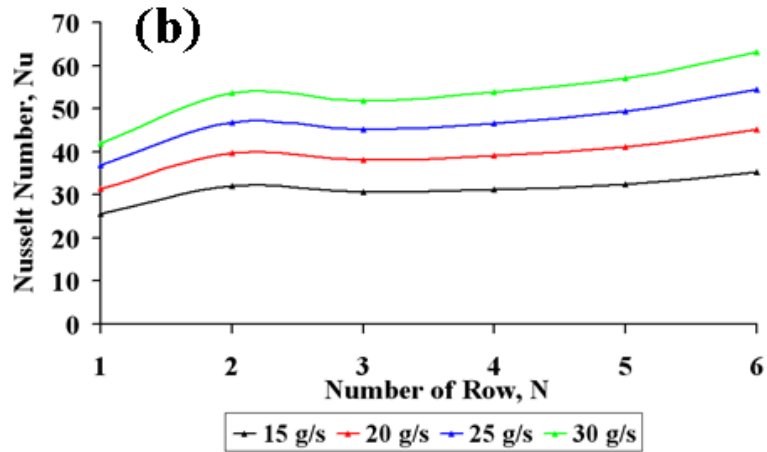
Figure 8.11 Performance of the optimized cooling fin at each row.
(a). Reynolds number. (b) Nusselt number.

Figure 8.11(a) shows the variation of the Reynolds number across the battery module. The Reynolds number increases with the row number, which is caused by decreasing of the flow area in the trapezoidal shape. Besides, the Nusselt number across the cell bank is also increased as shown in Figure 8.11(b).

The results of the regression analysis for the average Nusselt number, average J factor, average friction factor and variation of temperature for the aluminum helical fins are shown in Table 8.38 to Table 8.41, respectively. The regression equations are given in Equations 8-62 to 8-65.

Table 8.38 Regression statistics of the average Nusselt number.

Predictor	Coefficient	Standard Error	T	P	Lower 95%	Upper 95%
Constant	-4.246	0.0726	-58.480	0.000293	-4.559	-3.934
$Ln\overline{Re}_D$	0.810	0.00762	106.340	8.842e-5	0.777	0.843
S = 0.003942		R = 99.99%		R-Sq = 99.98%		R-Sq(adj) = 99.97%

Table 8.39 Regression statistics of the average J factor.

Predictor	Coefficient	Standard Error	T	P	Lower 95%	Upper 95%
Constant	-3.981	0.0726	-54.822	0.000333	-4.293	-3.668
$Ln\overline{Re}_D$	-0.190	0.00762	-24.955	0.00160	-0.223	-0.157
S = 0.003942		R = 99.84%		R-Sq = 99.68%		R-Sq(adj) = 99.52%

Table 8.40 Regression statistics of the average friction factor.

Predictor	Coefficient	Standard Error	T	P	Lower 95%	Upper 95%
Constant	-3.813	0.0797	-47.813	0.000437	-4.156	-3.470
$Ln\overline{Re}_D$	-0.0637	0.00837	-7.620	0.0168	-0.0997	-0.0278
S = 0.004329		R = 98.32%		R-Sq = 96.67%		R-Sq(adj) = 95.01%

Table 8.41 Regression statistics of the variation of temperature.

Predictor	Coefficient	Standard Error	T	P	Lower 95%	Upper 95%
Constant	5.790	0.241	23.998	0.00173	4.752	6.829
$Ln\overline{Re}_D$	-1.032	0.0253	-40.790	0.000601	-1.141	-0.924
S = 0.0131		R = 99.94%		R-Sq = 99.88%		R-Sq(adj) = 99.82%

$$\overline{Nu}_D = 0.0143\overline{Re}_D^{0.810} \tag{8-62}$$

$$\overline{J} = 0.0187\overline{Re}_D^{-0.190} \tag{8-63}$$

$$\overline{f} = 0.0221\overline{Re}_D^{-0.0637} \tag{8-64}$$

$$\frac{\Delta T}{T_{in}} = 327.159\overline{Re}_D^{-1.032} \tag{8-65}$$

As can be seen from Table 8.38 - Table 8.41, the R-square for the $\overline{Nu}_D$, $\overline{J}$, $\overline{f}$ and $\Delta T/T_{in}$ are 99.9%, 99.7%, 99.7% and 99.9%, respectively, which indicate very good correlation with Re_D with variations of ±0.02%, ±0.3%, ±3.3% and ±0.1%, respectively. The errors of predicted data and simulated data for average Nusselt number, J factor, friction factor and variation of temperature are 0.1%, 0.3%, 0.3% and 0.9%, respectively.

The results of the multiple regression analysis for the average Nusselt number, J factor, friction factor and variation of temperature for Aluminum fins are shown in Table 8.42 to Table 8.46 respectively. The regression equations for aluminum helical fins are shown in Equations 8-66 to 8-69.

Table 8.42 Regression statistics of the average Nusselt number.

Predictor	Coefficient	Standard Error	T	P	Lower 95%	Upper 95%
Constant	0.451	0.967	0.466	0.643	-1.498	2.4
$Ln\overline{Re}_D$	0.853	0.0227	37.583	1.60e-34	0.807	0.899
$Ln\left(\dfrac{F_p-\delta}{D_0}\right)$	-5.868	1.254	-4.681	2.86e-05	-8.396	-3.34
$Ln\left(\dfrac{F_p}{D_h}\right)$	-3.208	0.629	-5.10	7.30e-06	-4.477	-1.940
$Ln\left(\dfrac{F_p}{P_t}\right)$	6.832	1.365	5.007	9.9e-06	4.080	9.584
S = 0.0407		R = 98.74%		R-Sq = 97.50%		R-Sq(adj) = 97.27%

Table 8.43 Regression statistics of the average friction factor.

Predictor	Coefficient	Standard Error	T	P	Lower 95%	Upper 95%
Constant	-4.919	0.391	-12.570	5.414e-16	-5.708	-4.130
$Ln\overline{Re}_D$	-0.0252	0.00919	-2.741	0.00888	-0.0437	-0.00666
$Ln\left(\dfrac{F_p-\delta}{D_0}\right)$	6.514	0.508	12.835	2.652e-16	5.491	7.538
$Ln\left(\dfrac{F_p}{D_h}\right)$	0.343	0.255	1.346	0.185	-0.171	0.857
$Ln\left(\dfrac{F_p}{P_t}\right)$	-5.872	0.553	-10.629	1.313e-13	-6.987	-4.758
S = 0.0165		R = 99.92%		R-Sq = 99.85%		R-Sq(adj) = 99.84%

Table 8.44 Improved regression statistics of the average friction factor.

Predictor	Coefficient	Standard Error	T	P	Lower 95%	Upper 95%
Constant	-4.407	0.0941	-46.851	3.44e-39	-4.597	-4.218
$Ln\overline{Re}_D$	-0.0251	0.00927	-2.703	0.00974	-0.0437	-0.00637
$Ln\left(\dfrac{F_p-\delta}{D_0}\right)$	5.838	0.0703	83.055	5.27e-50	5.696	5.979
$Ln\left(\dfrac{F_p}{P_t}\right)$	-5.135	0.0755	-68.067	3.13e-46	-5.287	-4.983
S = 0.0166		R = 99.92%		R-Sq = 99.84%		R-Sq(adj) = 99.83%

Table 8.45 Regression statistics of the average J factor.

Predictor	Coefficient	Standard Error	T	P	Lower 95%	Upper 95%
Constant	0.717	0.967	0.741	0.463	-1.233	2.666
$Ln\overline{\mathrm{Re}}_D$	-0.147	0.0227	-6.488	7.119e-08	-0.193	-0.102
$Ln\left(\dfrac{F_p - \delta}{D_0}\right)$	-5.868	1.254	-4.681	2.858e-05	-8.396	-3.340
$Ln\left(\dfrac{F_p}{D_h}\right)$	-3.208	0.629	-5.10	7.299e-06	-4.477	-1.940
$Ln\left(\dfrac{F_p}{P_t}\right)$	6.832	1.365	5.007	9.9e-06	4.080	9.584
S = 0.0407	R = 96.91%		R-Sq = 93.91%		R-Sq(adj) = 93.34%	

Table 8.46 Regression statistics of the variation of temperature.

Predictor	Coefficient	Standard Error	T	P	Lower 95%	Upper 95%
Constant	9.511	0.761	12.502	6.5e-16	7.977	11.045
$Ln\overline{\mathrm{Re}}_D$	-0.974	0.0179	-54.511	2.52e-41	-1.01	-0.938
$Ln\left(\dfrac{F_p - \delta}{D_0}\right)$	-9.086	0.987	-9.208	9.93e-12	-11.075	-7.096
$Ln\left(\dfrac{F_p}{D_h}\right)$	-2.617	0.495	-5.285	3.96e-06	-3.616	-1.619
$Ln\left(\dfrac{F_p}{P_t}\right)$	9.237	1.074	8.600	6.82e-11	7.071	11.403
S = 0.0320	R = 99.46 %		R-Sq = 98.92 %		R-Sq(adj) = 98.82%	

$$\overline{Nu}_D = a\overline{\mathrm{Re}}_D^{\,n}\left(\frac{F_p - \delta}{D_0}\right)^x\left(\frac{F_p}{D_h}\right)^y\left(\frac{F_p}{P_t}\right)^z \tag{8-66}$$

with $a = 1.570$, $n = 0.853$, $x = -5.868$, $y = -3.208$, $z = 6.832$

$$\overline{f} = a\overline{Re}_D^{\,n}\left(\frac{F_p - \delta}{D_0}\right)^x\left(\frac{F_p}{P_t}\right)^z \tag{8-67}$$

with $a = 0.0122$, $n = -0.0251$, $x = 5.838$, $z = -5.135$

$$\overline{J} = a\overline{\mathrm{Re}}_D^{\,n}\left(\frac{F_p - \delta}{D_0}\right)^x\left(\frac{F_p}{D_h}\right)^y\left(\frac{F_p}{P_t}\right)^z \tag{8-68}$$

with $a = 2.047$, $n = -0.147$, $x = -5.868$, $y = -3.208$, $z = 6.832$

$$\frac{\Delta T}{T_{\infty}} = a\overline{Re}_D^{\ n}\left(\frac{F_p - \delta}{D_0}\right)^x \left(\frac{F_p}{D_h}\right)^y \left(\frac{F_p}{P_t}\right)^z \tag{8-69}$$

with $a = 13507.284$, $n = -0.974$, $x = -9.086$, $y = -2.617$, $z = 9.237$

The R-square for the average Nusselt number plot for Aluminum helical fin are 98.7% as shown in Table 8.42, which indicates a very good correlation with a variation of ±1.3%. From the p-values (see page 227) shown in Table 8.25, $\left(\dfrac{F_p}{D_h}\right)^y$ is statistically insignificant at a significant level of 0.05 and can be omitted. New analysis was carried out, and the p-value of all the parameters was found statistically significant to correlate the average friction factor as shown in Table 8.44 with a variation of ±0.08%. As can be seen from Table 8.45 and Table 8.46, the R-square for average J factor and variation of cell temperature are 96.9% and 99.5%, respectively, which indicates very good correlation, with variations of ±3.1% and ±0.5%, respectively. The best fit curves for the average Nusselt number, friction factor, J factor and variation of cell temperature for aluminum helical fin are shown in Figure 8.12.
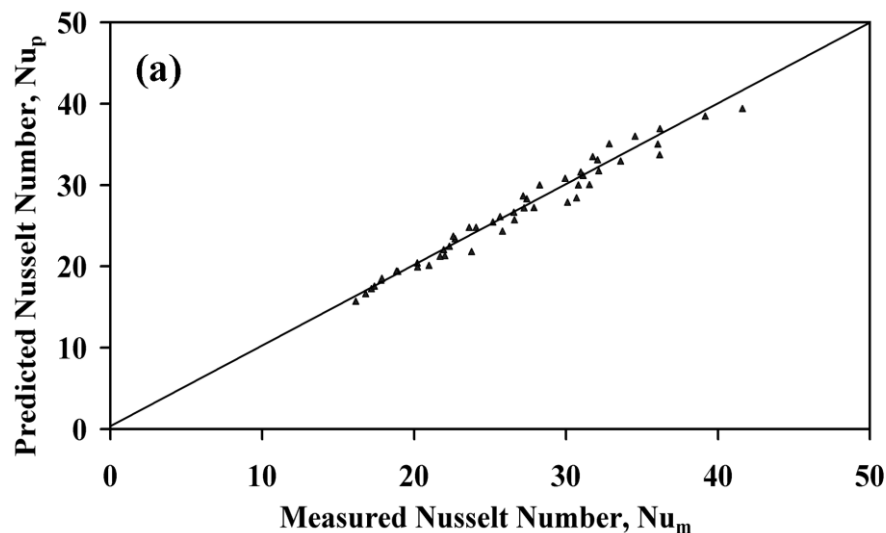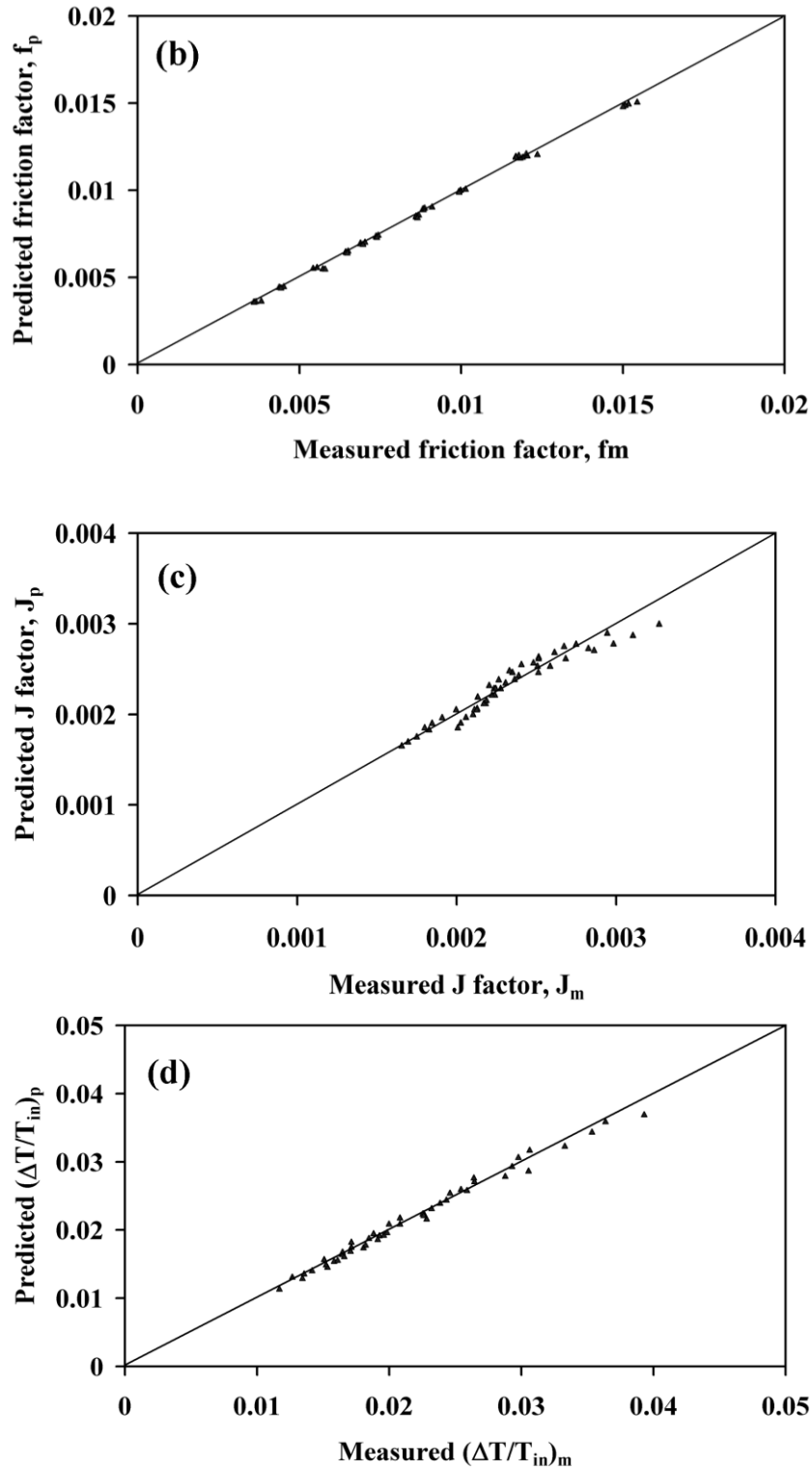
Figure 8.12 Comparison of the correlation with simulation data for Aluminum
fin. (a) Nusselt number. (b) Friction factor. (c) J factor. (d) $\Delta T/T_{in}$.

The maximum error of using developed correlation to predict the
measured data for the average Nusselt number, friction factor, J factor and
variation of temperature for aluminum fin are 1.4%, 2.8%, 1.3% and 8.9%

respectively. The average error of predicted data and simulated data for the average Nusselt number, friction factor, J factor and variation of temperature is 3.2%, 1.2%, 3.2% and 2.5% respectively. Hence, the correlation developed as in Equations 8-66 to 8-69 give a good prediction of the $\overline{Nu}_D$, $\overline{J}$, $\overline{f}$ and $\Delta T/T_{in}$ of the helical fin battery module.

8.5.3.6 Comparison of helical fin and unfinned battery module

Comparison of the variation of cell temperature, average Nusselt number and fan power consumption of the helical fin and unfinned battery module is shown in Figure 8.13.
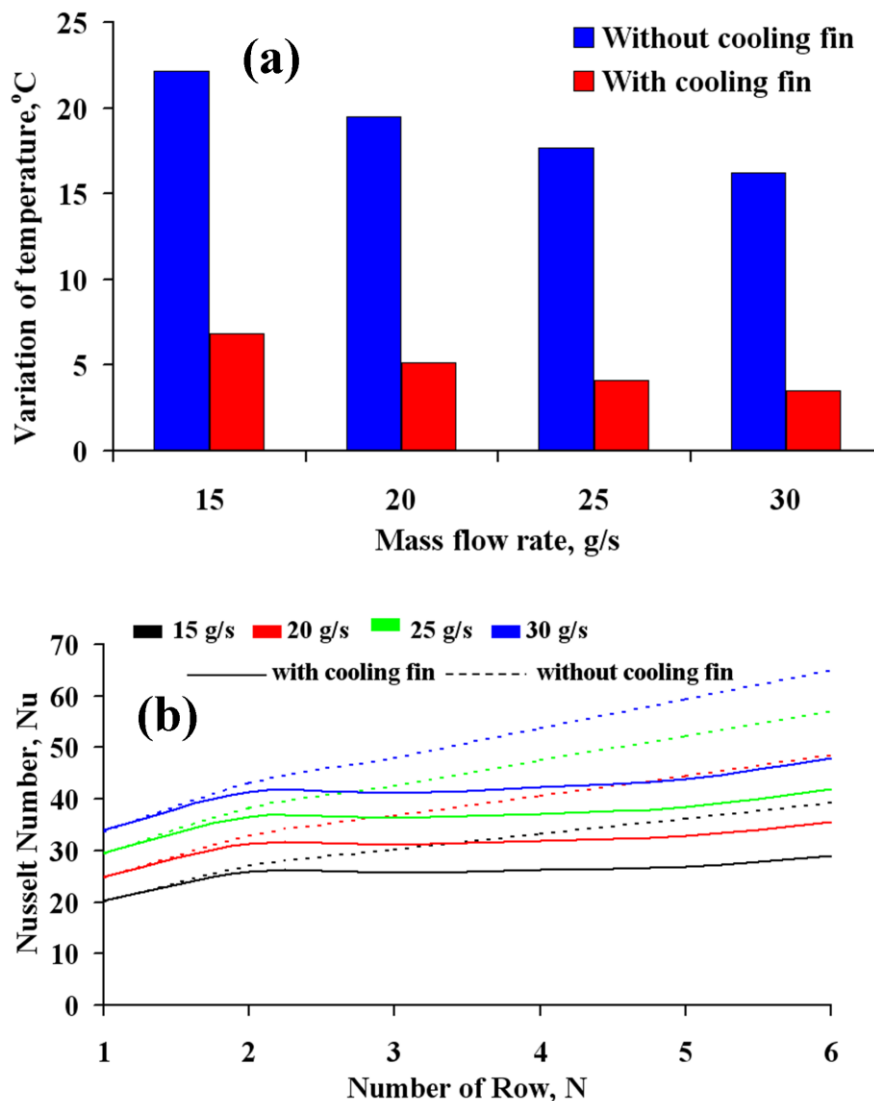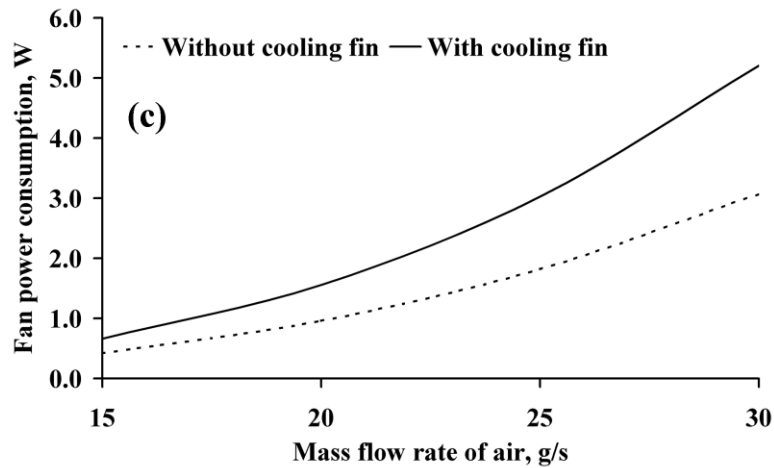
Figure 8.13 Comparison of finned and unfinned battery module. (a). Variation of temperature. (b). Average Nusselt number. (c). Fan power consumption.

The variation of temperature in the unfinned battery module is higher than the battery module with helical fin installed. The variation of temperature is decreased with the mass flow rate of cooling air. Besides, the variation of temperature for the unfinned battery module at 15 gs^{-1} of air flow are about 22 ^{o}C, while the variation of temperature for the helical finned battery module is about 6.8 ^{o}C. In order to keep the temperature uniformity of the helical fin module below 5 ^{o}C, the mass flow rate of cooling rate needs to further increase to 25 gs^{-1} and this is higher compared to the plate finned module. Although the average Nusselt number of the unfinned battery module and the helical fin battery module is progressively increased with the number row. At the first three rows, the Nusselt number for the helical-finned battery module is higher than the unfinned battery module. On the other hand, at the fourth to sixth rows, average Nusselt number of the helical-finned battery module is less than the unfinned battery module. Due to the staggered arrangement of the cooling fins, the fan power consumption of the helical-finned battery module is higher than an unfinned module. The fan power consumption at 30 gs^{-1} is about 50% higher than for the unfinned battery module. Hence, helical fins

242

cannot be closely packed in the battery module; it will increase the pressure loss and become parasitic pressure drops and does not increase the heat transfer.

8.6 Experimental procedures

The test rig consists of a closed loop wind tunnel as shown in Figure 8.14.

1. Air inlet	2. Honey comb straightener.
3. T/C inlet temperature.	4. Pressure tap (inlet)
5. Test section (battery module)	6. Pressure tap (outlet)
7. T/C outlet temperature.	8. Setting means.
9. T/C battery module temperature.	10. Power supply for heaters.
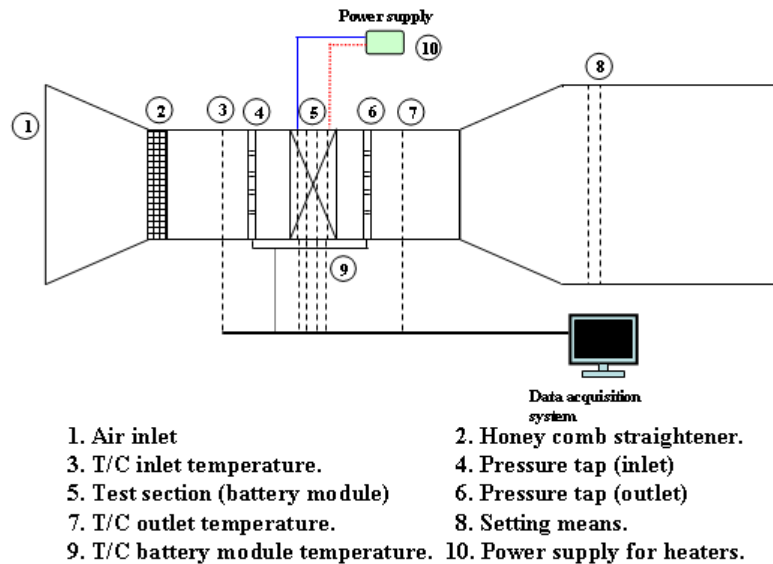
Figure 8.14 Experimental setup on the wind tunnel.

The air velocity in the wind tunnel was measured using a digital air velocity transducer (TSI, 8465 series). The pressure drop over the battery module was measured using a differential pressure transducer (Gems sensor, 5266 series). The fan of the wind tunnel was driven by a frequency controller, which allowed setting an air mass flow rate to a maximum of 0.9 kgs^{-1}

(corresponding to a maximum velocity of 7.9 ms^{-1} at the inlet of the test section). Hotwire measurements were performed to confirm these local velocity measurements and the uniform inlet flow conditions. The heating effect of the batteries was simulated using tubular cartridge heaters. The power rating of each of the heaters is set at approximately 5 W. The heaters were inserted into the center of copper rods which were machined to the size of the 18650 cell. The cartridge heaters were coated with a layer of thermal paste (Electrolube HTSP) to make sure there was no air gap present between the surfaces of the cartridge heaters and the copper rods. The silicone-based heat transfer compound will enhance the heat transfer from the cartridge heater to the copper body. The copper rods were then coated with thermal paste and inserted into the aluminum tube with the plate fins and helical fins. The plate fin consisted of 9 layers of aluminum fins while the helical fin consisted of 5 turns of the fin. The purpose of the fin design is to allow more efficient removal of heat generated from the battery by the air flow, thereby cooling down the battery module. The test setup of the battery module in the wind tunnel is shown in Figure 8.15.
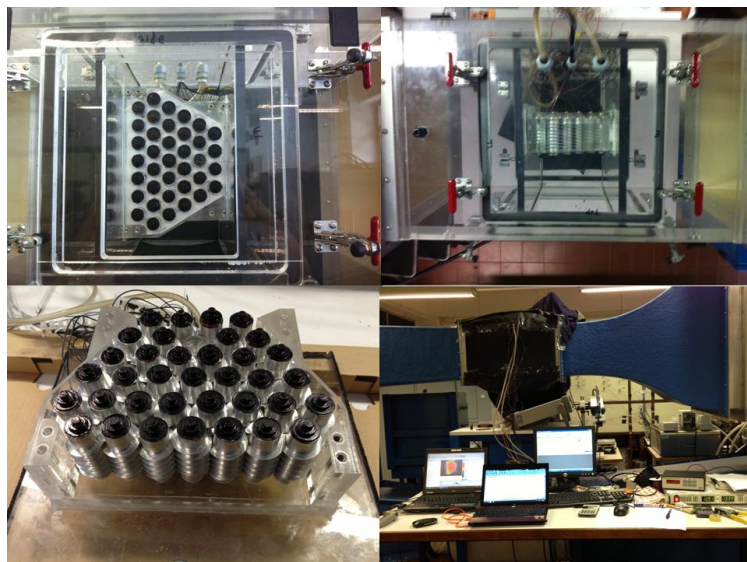
Figure 8.15 Test section of the battery module in the wind tunnel.

All temperatures were measured using calibrated T-type thermocouples and infrared camera. The thermocouples were calibrated in a dry box calibrator (Isotech Fast-Cal, Low complete series) to within ±0.1 $^{\circ}$C deviation before being used in the experiments. Two thermocouples were placed at the upstream and three thermocouples at the downstream of the test section to measure the incoming and exit air temperature. Due to the non-uniformity of the temperature profile at the downstream of the test section, extra thermocouples were needed and an averaged value was used in the calculations. A HP 34970A data acquisition system was used to record the temperature readings. The infrared thermography system was used to monitor the temperature of the cooling fins. Infrared camera (VarioCAM, Jenoptik Inc) is a modern thermographic system for precise, prompt and non-contact measurement of the surface temperature of the cooling fins. Besides, the camera equipped with a digital color video camera for photographic documentation with long wave infrared spectral range of 7.5 μm to 14 μm. The maximum resolution of the infrared camera is 640 x 480 pixels. The emissivity setting of the infrared camera is crucial to the accuracy of the temperature readings taken during the experiment. The emissivity value set on the IR camera was 0.95. The temperature resolution of the infrared camera was 0.08 K at 303 K. The auto focusing lens embedded within the camera helps to capture bright and high contract thermal images of the cooling fins. The temperature range of the infrared camera is 233K to 1473 K. The infrared images were analyzed with the software of IRBIS® Remote 3 Professional. A summary of the measurement equipment and their accuracies are summarized in Table 8.47.

Table 8.47 Measurement equipments and their accuracies.

Measurement equipment	Accuracy
Air velocity transducer, %	± 2.0
Differential pressure transducer, %	± 1.0
T-type thermocouple, ^{o}C	± 0.1
Infrared camera, K	± 1.5

In order to determine the heat transferred to the cooling air, the steady state heat gain q by air can be calculated using Equation 8-24. On the other hand, the amount of heat loss that was dissipated via other means such as natural convection, radiation and conduction through the housing of the battery module were experimentally determined by using the equation below:

$$Q_{loss} = \frac{Q_{in} - Q_{gain}}{Q_{in}} x100\% \tag{8-70}$$

$$Q_{in} = VI \qquad V = \text{Voltage, V} \quad I = \text{Current, A} \tag{8-71}$$

The input power Q_{in} was supplied via 1.5 kW programmable DC power supply (Amrel SPS60-25-V029). It was found the heat loss is less than 15% when the mass flow rate of cooling air was more than 20 gs^{-1}.

The measurements were performed under steady state conditions for different mass flow rates of air. The steady state regime was verified by monitoring the temperature variation of the cooling fins. Once the steady state was reached, thermocouple reading and infrared images were taken and the measurements were then averaged. All the tests were repeated three times and the average values were taken. Then, the experimental results were compared with the numerical results under similar cooling condition. The testing of the cooling fins was carried out with the mass flow rate of air in the range of 0.008-0.032 kgs^{-1} at 28 ^{o}C to 30 ^{o}C.

In order to show the accuracy of the measurements, a thorough uncertainty analysis was performed according to the method suggested by

Moffat (Moffat, 1988). The uncertainties in this study were determined by the root-sum-square method (Moffat, 1988). The errors estimated on the thermodynamic properties of air are tabulated in Table 8.48 (Huisseune et al., 2010).

Table 8.48 Uncertainties on the thermodynamic properties of air.

Properties	Uncertainty
Dynamic viscosity, μ (%)	2.00
Density, ρ (%)	0.02-0.1
Specific heat capacity, C_p (%)	2.00
Thermal conductivity, k (%)	2.00

8.7 Results and discussion

8.7.1 Plate fin

8.7.1.1 Uncertainty of calculations

The uncertainties for most of the calculated variables for plate fin are shown in Table 8.49. The averaged relative uncertainty for Nusselt number and friction factor are 2.01 % and 3.37 %, respectively.

Table 8.49 Average uncertainties of the variables.

Properties	Average uncertainty, (%)
Heat transfer rate of air, Q_{air} (W)	2.85
ΔT_{air} ($^o C$)	2.00
ΔT_{fin} ($^o C$)	5.29
Reynolds number based on velocity in the minimum cross section (Re_c)	2.00
Nusselt number, Nu	2.01
Friction factor, f	5.14
Colburn j-factor, j	2.83
Prandtl number	3.46

8.7.1.2 Infrared imaging

The temperature distributions on the surfaces of the battery module measured by the infrared imaging device under different mass flow rates of cooling air are shown in Figure 8.16.
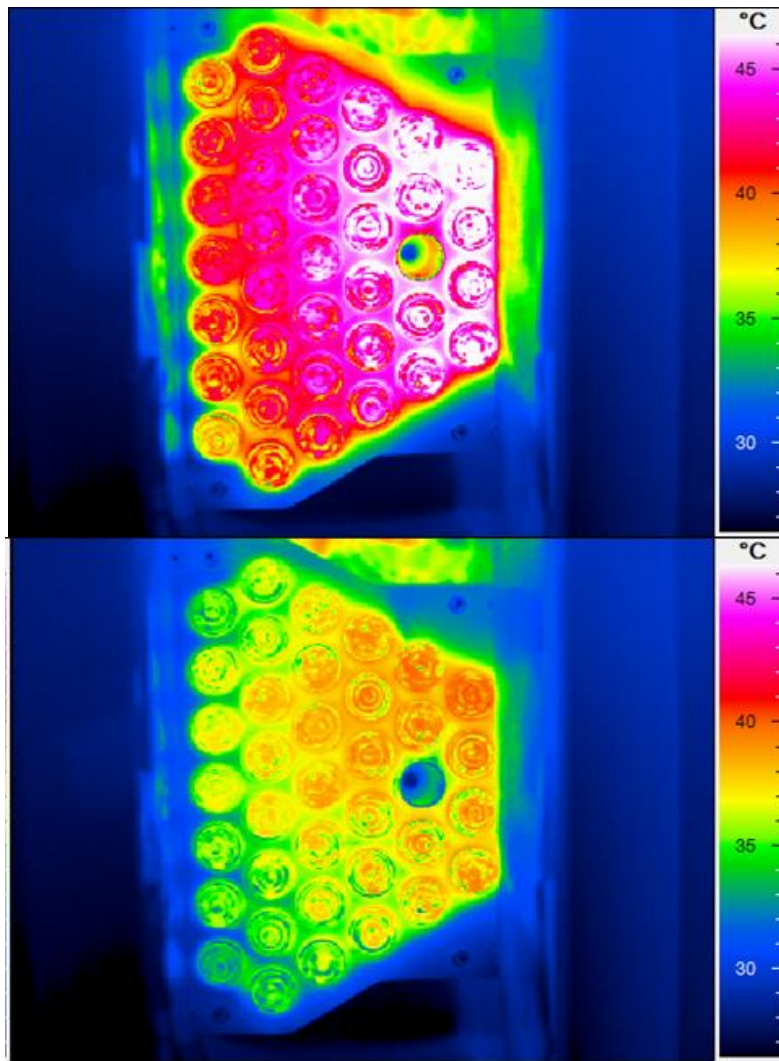
Figure 8.16 Infrared image of the battery module. Top: Air flow rate of 14 gs^{-1}.
Bottom: Air flow rate of 29 gs^{-1}..

The temperature distribution in the battery module is fairly uniform. As shown in Figure 8.16 at the low mass flow rate of cooling air, about half of the battery pack registered temperatures of about 45 ^{o}C.

At the higher mass flow rate of 29 gs^{-1}, the region of high temperature is reduced tremendously. The cells at the downstream are hotter than the cells located in the upstream of the battery module. The highest temperature of the cell could reach to about 38 ^{o}C. The heat transfer coefficient of the cooling air is proportional to the mass flow rate. At higher flow rate the cooling is also increased and more heat is removed from the battery module through

248

convection cooling. Hence the temperature of the battery module is much lower at a high flow rate of cooling air.

8.7.1.3 Experimental validation

The correlations for the average Nusselt number, friction factor, J factor and variation of temperature in Equations 8-54 to 8-57 for the optimized plate fin were then verified with the experimental study. The comparisons of the correlations are shown in Figure 8.17.
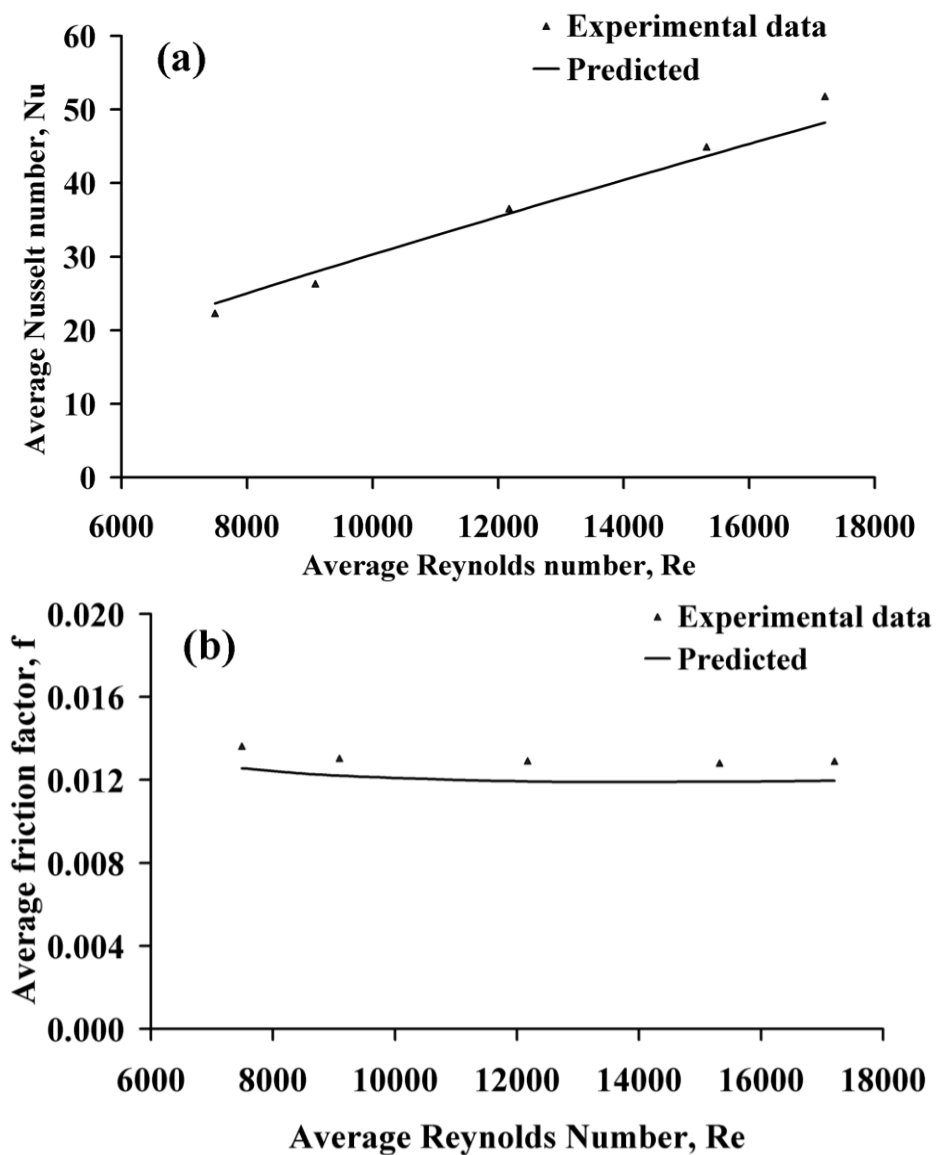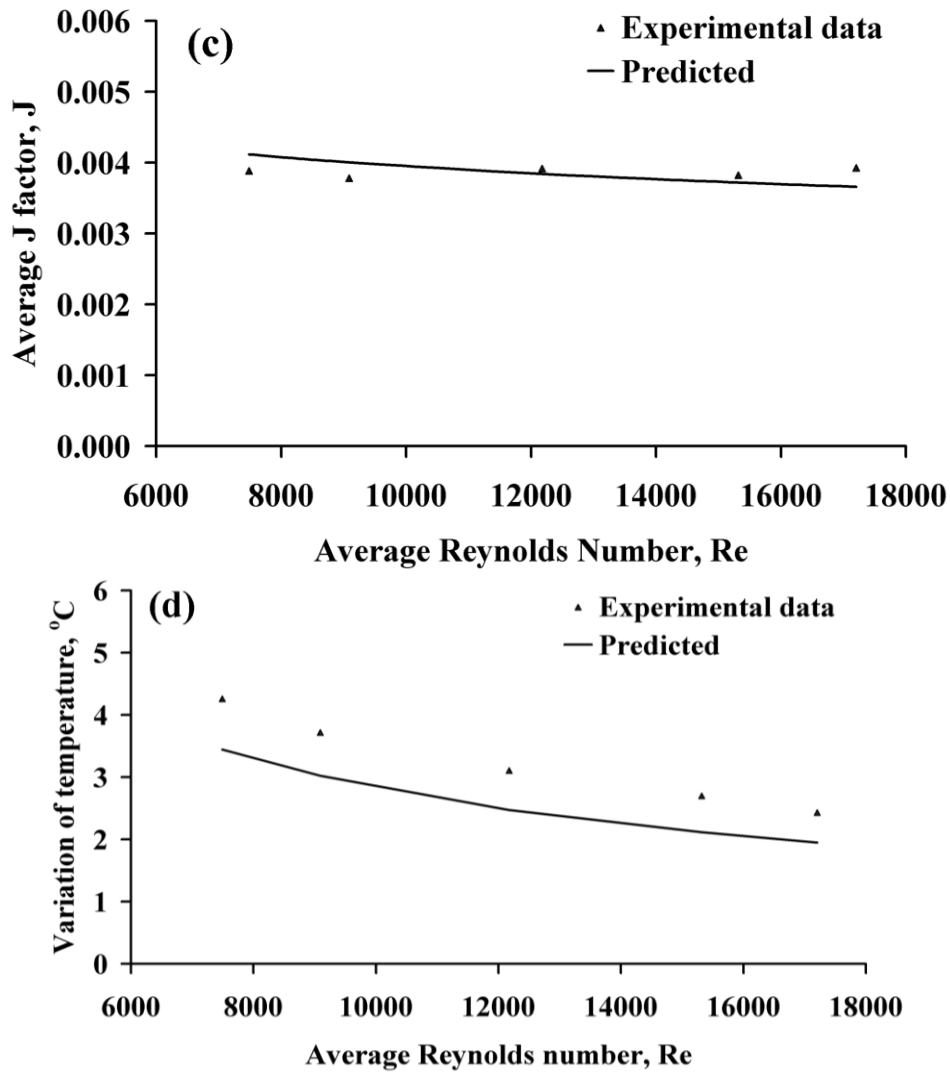
Figure 8.17 Comparison of the experimental data and correlation (a) $\overline{Nu}_D$.
(b) $\overline{f}$. (c) $\overline{J}$. (d) $\Delta T/T_{in}$.

The figures show good qualitative and qualitative agreement between experimental data and numerical prediction with averaged relative error of 4.7%, 10.9%, 5.7% and 19.0%, respectively, for the average Nusselt number, friction factor, J factor and variation of temperature. Both experimental and numerical results show an increasing trend for the average Nusselt number versus Reynolds number. On the other hand, experimental and numerical results show a decreasing trend for average friction factor, J factor and variation of cell temperature versus average Reynolds number. Surface roughness of the plate fin which is one of the factors that contributed to the

high friction factor, was measured in the experiment. However, the accuracy of the pressure drop measurement could be improved by using a narrower range of differential pressure transducers. The relative error of prediction of the variation of cell temperature appears large due to its small magnitude. The actual the temperature difference between the correlation and experimental data is less than 1 ^{o}C.

8.7.2 Helical fin

8.7.2.1 Uncertainty of calculations

The uncertainties for most of the calculated variables for the helical fin are given in Table 8.50. The averaged relative uncertainty for Nusselt number and friction factor are 2.10% and 2.67%, respectively.

Table 8.50 Average uncertainties of the variables.

Properties	Average uncertainty, (%)
Heat transfer rate of air, Q_{air} (*W*)	3.55
ΔT_{air} (^oC)	2.81
ΔT_{fin} (^oC)	5.03
Reynolds number based on velocity in the minimum cross section (Re_c)	2.00
Nusselt number, *Nu*	2.10
Friction factor, *f*	2.67
Colburn j-factor, *j*	2.90
Prandtl number	3.46

8.7.2.2 Infrared imaging

The temperature distributions on the surface of the battery module for different mass flow rates of cooling air measured by the infrared imaging device are shown in Figure 8.18.
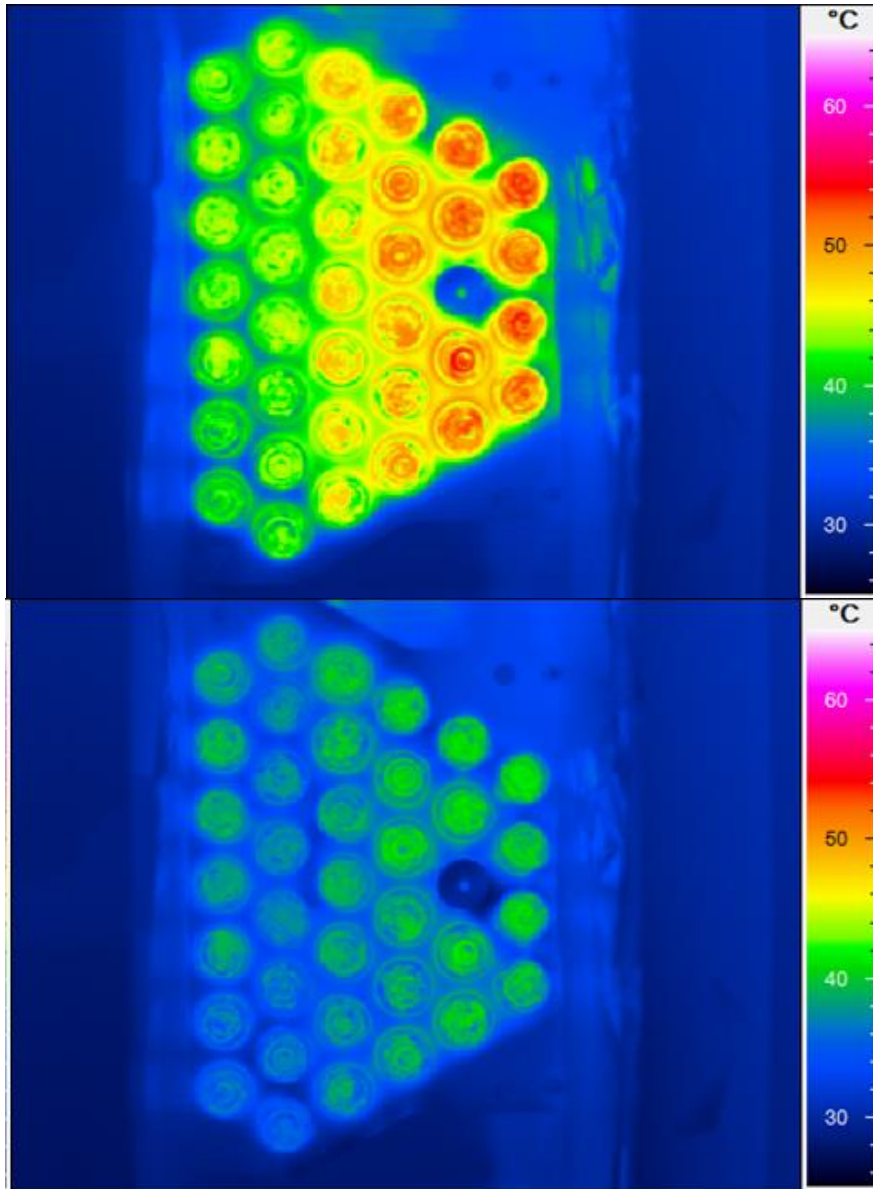
Figure 8.18 Infrared image of the battery module. Top: Air flow rate of 14 gs^{-1}. Bottom: Air flow rate of 29 gs^{-1}.

The temperature distribution in the helical fin battery module is fairy uniformed. As shown in Figure 8.18 at the low mass flow rate of cooling air, about half of the battery pack registered temperatures of about 48 $^{\circ}$C. At the higher mass flow rate of 29 gs^{-1}, the region of high temperature is reduced tremendously. The cells located downstream are hotter than the cells located upstream in the battery module. The highest temperature the cell could reach was about 37 $^{\circ}$C. At higher flow rate of cooling air the cooling rate is also increased and more heat is removed from the battery module through

convection cooling. Hence the temperature of the helical fin battery module is much lower than that for the plate fin.

8.7.2.3 Experimental validation

The correlations for the average Nusselt number, friction factor, J factor and variation of temperature in Equations 8-62 to 8-65 for the optimized plate fin were then verified with the experimental study. The comparisons of the correlations are shown in Figure 8.19.
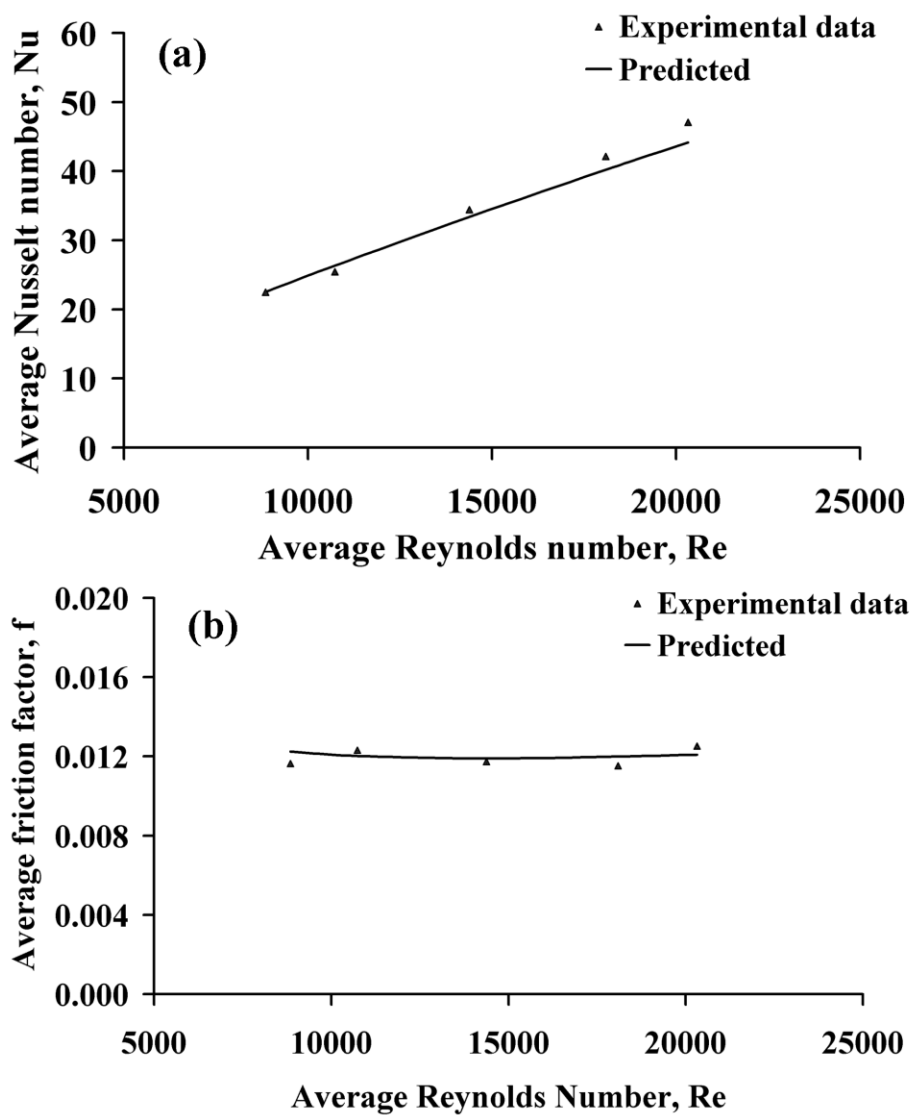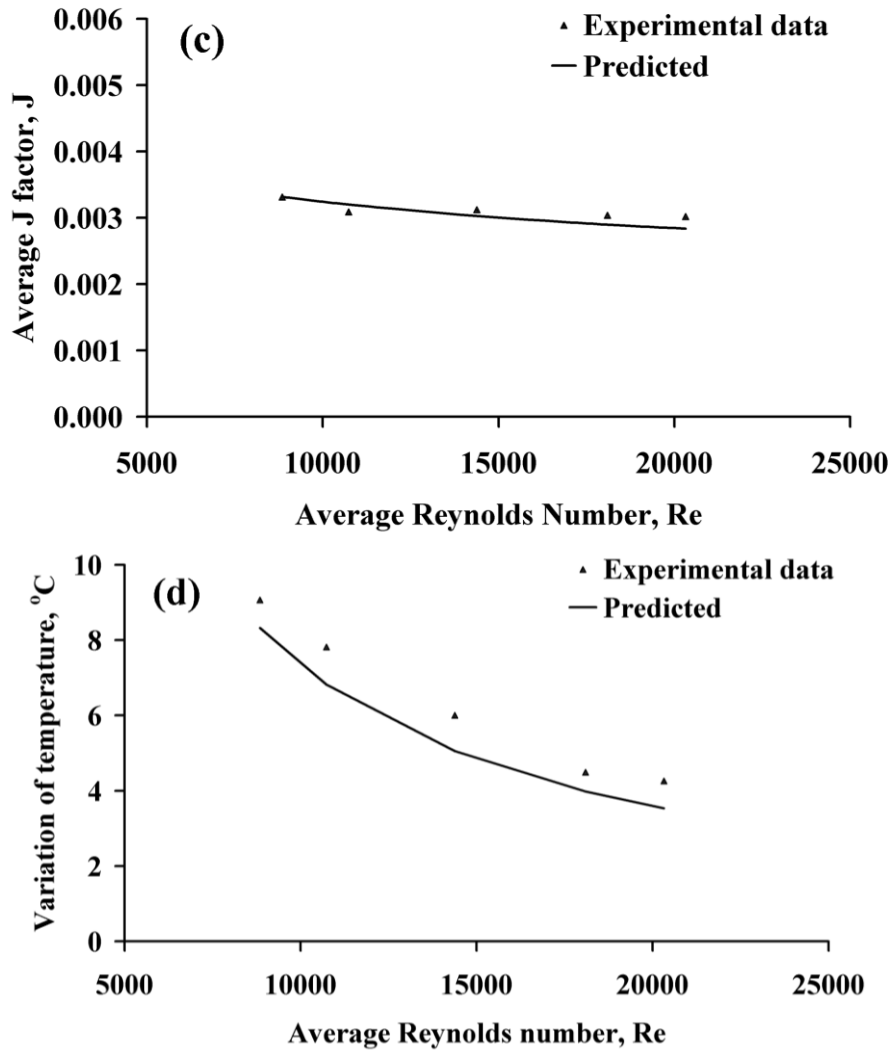
Figure 8.19 Comparison of the experimental data and correlation (a) $\overline{Nu}_D$. (b) $\overline{f}$. (c) $\overline{J}$. (d) $\Delta T/T_{in}$.

The figures show good qualitative and qualitative agreement between experimental data and numerical prediction with averaged relative error of 3.5%, 3.3%, 3.5% and 13.0%, respectively, for average Nusselt number, friction factor, J factor and variation of temperature. Both experimental and numerical results show an increasing trend of average Nusselt number versus average Reynolds number. On the other hand, experimental and numerical results show a decreasing trend of average friction factor, J factor and variation of cell temperature versus average Reynolds number. The average friction factor of the helical fin battery module is higher than that for the plate

254

fin battery module. The error of prediction of the variation of cell temperature is higher than that for the average Nusselt number. This is probably due to insufficient resolution of the infrared camera images. Besides, the temperature difference between the correlation and experimental data is less than 1 $^{\circ}$C.

8.8 Summary

This chapter presents the numerical study of the novel air cooling fin designed for EV battery thermal management. Two types of cooling fins were studied, namely plate fins and helical fins. The batteries are arranged in the module in a trapezoidal shape to attempt to balance the temperature downstream and upstream. The Taguchi method was used to optimize the design of the cooling fins. All design parameters for the finned battery module including mass flow rate, number of fins, fin thickness and mass were formed to be significant factors contributing to the evaluation of responses such as specific performance, pressure drop, variation of the battery surface temperature within the module and the mass of the fins. The most significant factors affecting the specific performance of the plate fins were mass flow rate of cool air and fin thickness. The pressure drop across the plate fin module was mainly affected by mass flow rate. Uniformity of battery temperature in the plate-finned module is affected by fin material, followed by mass flow rate, fin number and fin thickness. Fin material is the main factor determining the mass of the plate fin battery module. The optimum design parameters for the plate fins were mass flow rate 30 gs^{-1}, 9 fins per module, 0.2 mm fin thickness and made of Aluminum. On the other hand, the most significant factors affecting the specific performance of the helical-finned module were mass flow rate of cool air and the number of turns in the helical fin. Similar to plate

fins, pressure drop across the helical fin module was mainly affected by the mass flow rate. Uniformity of battery temperature in the helical fin was affected by the mass flow rate and number of turns in the helical fin. Fin material was the main criteria determining the mass of the helical-finned battery module. The optimum design parameters for the helical fins were mass flow rate 30 gs^{-1}, 5 turn of helical fin, 0.2 mm fin thickness and made of Aluminum. However, as compared to the plate fin, the performance of the helical fin is poorer than the plate fin. The fan power consumption of the helical fin was much higher than for the plate fin, but the cell temperature uniformity and heat transfer ability are lower than for the plate fin. This is due to the fin high limit and constrained by the physical dimension of the battery module design.

Experimental data and correlations show good agreement qualitatively and quantitatively. The experimental results showed an increasing trend of average Nusselt number with the mass flow rate of cooling air. On the other hand, average friction factor, J factor and average variation of temperature within the battery module decrease with the increase in mass flow rate of cooling air. Plate fins showed more promising results than helical fins with higher heat transfer and lower pressure drop. Hence, cooling of the battery module could be achieved by using plate fins with minimum fan power consumption.

CHAPTER 9

LIQUID COOLING SYSTEMS

9.1 Introduction

Most mechanical and electronic equipment such as engine, motor, battery pack, microprocessor, etc dissipate large amounts of heat during their operation. Ineffective cooling will give rise to excessive costs due to shortened life expectancy of the equipment. In order to increase the efficiency of the operation and prolong the life time of the equipment, a cooling system that is able to provide effective cooling and reduce the non-uniformity of the temperature is needed. In this study, liquid cold plates for the Li-ion battery pack are proposed. The liquid cold plate is particularly suitable for the prismatic and pouch cells which have large and flat surfaces. Two different types of cooling fins within the cold plate are investigated, namely droplet fin and variable droplet fin. A Taguchi method with orthogonal array L_{36} $(3^6 2^1)$ was used to optimize the cooling fin design. Mass flow rate, fin spacing in transverse and longitudinal directions, the hydraulic diameter of the fin and number of zones for the fin are the parameters that affect the performance of the cooling fin, are investigated. The target performance measure was used to determine the main control factors that largely affect the performance of the liquid cold plate. The significance and contribution of each factor were analyzed using Analysis of Variance (ANOVA). Then, grey relational analysis (GRA) with an assigned weightage for each control factor was used to determine the optimum design for the liquid cold plate. Finally, regression analysis was used to develop the correlation between Nusselt number, Colburn factor, temperature uniformity, friction factor and the Reynolds number for the

liquid cold plate. Finally, experimental studies of the cooling fins were carried out. The temperature rises of the cooling fins were measured under different mass flow rate of cooling water. The experimental results are then compared with the simulation results to validate the developed correlation.

9.2 Design of the Liquid cold plate

Various types of liquid cold plate have been used to provide cooling for the prismatic and pouch cell in the Li-ion battery pack such as folded fin, straight channel and oblique. Liquid cold plates can offer a higher heat transfer coefficient and a more uniform temperature distribution among the cells as compared to air cooling. In this chapter, novel and high performance liquid cold plates were developed to cool fast charging battery packs which have extensive heat generation. There are two different types of the liquid cold plate design which contained optimized droplet shape with uniform distribution and zonal distribution. As compared to conventional straight fin channel with a similar channel width and dimension, these types of design enhanced the heat transfer performance and temperature distribution at the downstream section of the conventional straight channel without the need for an increase in pumping power.

9.2.1 Straight channel fin

Conventional straight fins comprise a flat base surface with flat straight fins extruded from the base surface. Multiple straight fins with constant fin length formed multiple channels on the base surface. A liquid flows through the channels of the straight fin and enhances the heat transfer from the base surface. The fluid flow loses a significant amount of energy when flow along

the channel. However, as the cooling fluid gained heat along the flow direction and thermal boundary layers are developed as shown in Figure 9.1.
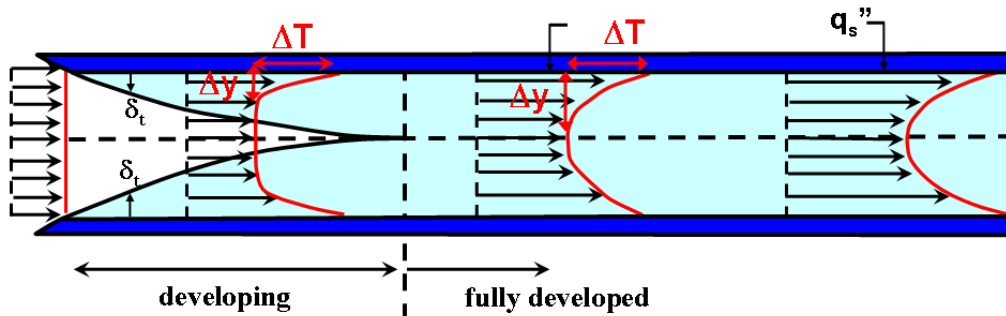
Figure 9.1 Boundary layer development of conventional straight channel.

The straight channel fin has a larger temperature gradient $\Delta T/\Delta y$ at the entrance region and a relatively smaller $\Delta T/\Delta y$ for the fully developed region. The cooling fluid starts to lose its cooling capacity along the flow direction and the downstream temperature is always higher than the upstream temperature. This will lead to high non-uniformity of the temperature on the cooling surface and affect the life time of the equipment. This phenomenon is more obvious when the cooling surface is long or the cooling surface required long cooling fins. Figure 9.2 illustrates the straight channel fin.

Figure 9.2 Straight channel fin.

9.2.2 Uniform distributed droplet fin

The first concept is using uniformly distributed droplet fin to change the flow conditions in the cold plate. The motivation of this novel design is to streamline the inflow and reinitialize the thermal entrance effect throughout the cold plate and enhance the mixing of the fluid. Besides, the present

invention provides an improved heat transfer performance and reduced the flow resistance compared to the conventional circular pin fin. A cooling fin comprised a flat surface having numerous streamlined droplet fins perpendicular and extruding from the base surface. The droplet fin has a sharp leading edge at the upstream and a round trailing edge at the downstream. The novel and aerodynamic shapes of the droplet fins are staggered to increase the heat transfer performance. High surface area to volume ratio of the droplet fin structure improved the heat transfer and reduced the flow resistance as compared to the straight fin and conventional circular pin fin. Figure 9.3 illustrates the thermal boundary layer of the droplet fin.
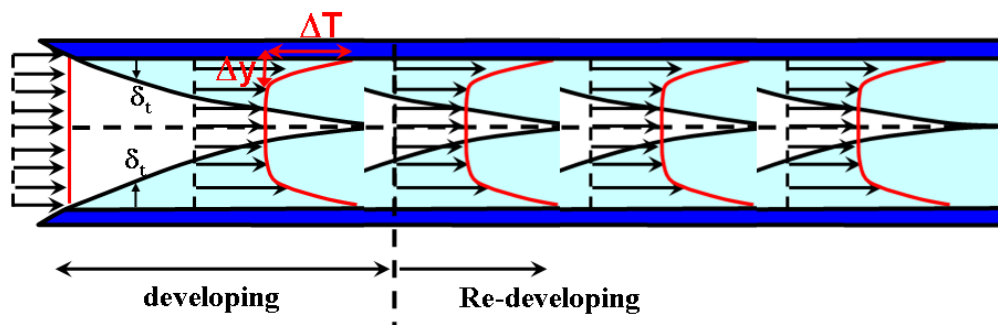
Figure 9.3 Thermal boundary layer of droplet fin.

The characteristics of the thermal boundary layer redevelopment an droplet fins are shown in Figure 9.3. The flow path is disrupted and causing the hydrodynamic boundary layer redevelopment at the leading edge of the next droplet fin of the next downstream section. The temperature gradient $\Delta T/\Delta y$ remained steep throughout the entire length of the cold plate. Hence, the heat transfer coefficient could remain almost constant, unlike the conventional straight channel, where the heat transfer coefficient is decreasing along the flow direction. A schematic diagram and actual realization of a droplet fin cold plate are shown in Figure 9.4.
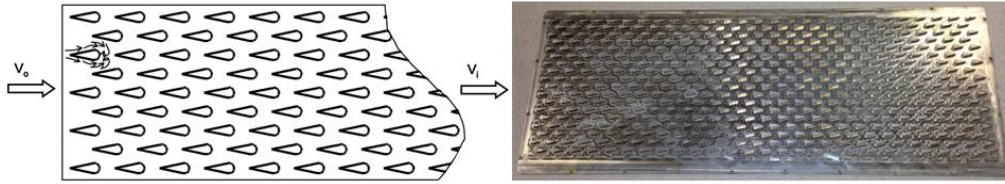
Figure 9.4 Uniform distributed droplet fin.

Referring to Figure 9.4, a cooling plate comprised numerous droplet fins arranged in a staggered fashion and extruded from the base plate of the cooling plate. The droplet fins comprised round trailing edge on the downstream, sharp leading edge at the upstream and a streamlined body.

As shown on the left of Figure 9.4, the fluid flow from the left to the right direction as indicated by the arrows. The inlet velocity of the fluid prior to flowing to the cooling fin as indicated by V_o, while the outlet velocity of the fluid is indicated by V_i. The sharp leading edge of the droplet fin will first streamline the incoming flow and lead the flow through a streamlined body and go to the round trailing edge and creates a turbulent wake on the downstream side of the droplet fin to provide enhanced heat transfer between the fin and the fluid. The stagnation points, excess turbulence which will cause a large pressure drop, commonly found on the circular pin fins are eliminated by the present invention. Circular pin fins become inefficient when dealing with high flow rates or highly turbulent incoming flow. The fluid does not easily flow through the rows of circular pin fins and become highly disordered. This will cause greater pressure drop and increase the power consumption of the system. On the other hand, the typical characteristic of the turbulence wakes that are normally found at the downstream of the circular fin that enhance the heat transfer are maintained. The convergent spacing between the droplet fins help to generate the turbulence that is needed to ensure that the

261

fluid remains in contact with the droplet fin body to result better heat transfer between droplet fin and cooling medium. Besides, the present invention is designed to break the thermal boundary layer and enhance the mixing of the fluid. The fluid flow is streamlined by the present invention to achieve minimum pressure loss and the effect is obvious when dealing with highly turbulent incoming flows or high flow rates. Hence, a relatively smaller fan or pump can be used to drive the system and cost savings can be achieved.

Referring to Figure 9.4, the droplet fins have spacing to hydraulic diameter ratio of less than 3 and fin length to hydraulic diameter ratio in between 1.5 to 1 to maintain the effectiveness of the heat transfer rate. High surface area to volume ratio of the cooling fin structure improves the heat transfer and the streamlined shape across the plate allows higher cooling rate with less fan or pumping power required and flow resistance is reduced tremendously.

9.2.3 Zonal distributed droplet fin

The second concept is using a zonal distributed droplet fin to change the downstream flow conditions in the cold plate. The motivation of this novel design is to improve the heat transfer performance and reduce the non-uniformity of downstream temperature, which is commonly found in conventional long cold plates. A cooling fin comprises a flat surface having numerous perpendicular droplet fins extruded therefrom. The droplet fins are staggered and the fin's length is progressively decreased or the fin's density is progressively increased in the flow direction of the cooling fluid to increase the heat transfer performance at the downstream section and solve the problem of non-uniformity in temperature to some extent. Although the cooling fluid

temperature rises along the direction of flow, fin density is also increased to balance the heat transfer between the upstream and downstream. Hence, the temperature at the downstream can be uniformly controlled. For long cooling surfaces, there is a necessity to use variable droplet fin configurations with optimum and uniform heat transfer rates at low pressure drops. A schematic diagram and actual realization of a droplet fin cold plate are shown in Figure 9.5.
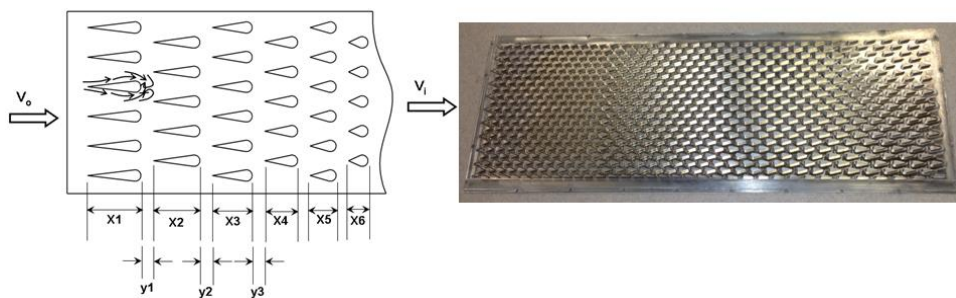
Figure 9.5 Zonal distributed droplet fin.

Figure 9.5 illustrates a cold plate comprising numerous droplet fins with increasing fin density along the flow direction. The droplet fins are staggered, extruded from the base plate of the cold plate and the fin density is increased along the flow direction. The droplet fins comprised a round trailing edge on the downstream end, a sharp leading edge at the upstream and a streamlined body.

As shown in the left figure in Figure 9.5, the operating method of the droplet fin with increasing fin density is illustrated. Fluid flows from the left to the right of the cold plate as indicated by the arrows. The inlet velocity of the fluid prior to flowing to the cooling fin as indicated by V_o, while the outlet velocity of the fluid is indicated by V_i. The droplet fins are arranged in such a way that few rows of droplet fins have a length of X1 are classified as a zone. Zone Y1 have a few rows of fin with a length of X1 and the droplet fin in the

second zone Y2 have a shorter length X2 (< X1) and the droplet fin in the third zone Y3 has a shorter length of X3 (< X2). The length of the droplet fin becomes shorter with a constant hydraulic diameter D_h to increase the heat transfer area at the downstream section resulting in high temperature uniformity along the cold plate.

Having higher fin density in the downstream section to ensure the fluid cooling capacity remains substantially constant and cooling effectiveness is not diminished downstream. High turbulence cooling flow in the space between the droplet fins will generate high heat transfer coefficients and create of an abrupt cooling effect along the flow path with the variation of fin density. The uniqueness of the droplet fin with increasing fin density, along the cold plate will achieve a highly efficient cooling design.

For the conventional straight channel or pin fin cold plate with constant fin dimensions, the cold plate becomes inefficient when the cooling surface is long. The variation of temperature across the cooling surface becomes very large. The cooling effectiveness is significantly diminished at the downstream section and higher flow rates of cooling fluid is needed to achieve a more uniform temperature distribution, resulting in greater power consumption.

9.3 Design of experiment

9.3.1 Taguchi method

In the current study, the Taguchi's method was used to optimize the droplet fin cold plate. Instead of a full factorial analysis which requires 1458 runs of the simulation, the orthogonal array L_{36} which comprises one two-level factor and six three level factors and a total 36 runs was used to optimize the design of the cooling fins. Noise factor which is also known as uncontrollable

factor was not considered in the analysis. The factor level for uniformly

distributed droplet fins is shown in Table 9.1 while the design of experiments

is shown in Table 9.3. On the other hand, the factor level for zonal distributed

droplet fin is shown in Table 9.2 and the design of experiments is shown in

Table 9.4. There were six control factors for uniformly distributed droplet fins

and seven control factors were considered for the zonal distributed droplet fins.

The control factors for uniformly distributed droplet fins are direction of flow,

mass flow rate of liquid, fin thickness, fin length, transverse and longitudinal

spacing. The control factors for zonal distributed droplet fins are direction of

flow, mass flow rate of liquid, fin thickness, fin length, number of zones,

transverse and longitudinal spacing. The cooling fins were machined from an

aluminum blocks.

Table 9.1 The parameters and their levels used in the uniformly distributed
droplet fins.

Factor	Code	Levels			Units
		1	2	3	
Flow direction	A	Forward	Reverse	-	-
Mass flow rate	B	40	60	80	gs^{-1}
Fin thickness	C	3	4	5	mm
Fin length	D	12	15	18	mm
Transverse spacing	E	9	11	13	mm
Longitudinal spacing	F	-3	0	3	mm

Table 9.2 The parameters and their levels used in the zonal distributed droplet fin.

Factor	Code	Levels			Units
		1	2	3	
Flow direction	A	Forward	Reverse	-	-
Mass flow rate	B	40	60	80	gs^{-1}
Fin thickness	C	3	4	5	mm
Fin length	D	12	15	18	mm
Transverse spacing	E	9	11	13	mm
Longitudinal spacing	F	-3	0	3	mm
Number of zones	G	2	3	4	-

Table 9.3 Orthogonal array L_{36} ($3^5\,2^1$) for uniform distributed droplet fin.

Exp No.	Factor					
	A	B	C	D	E	F
1	1	1	1	1	1	1
2	1	2	2	2	2	2
3	1	3	3	3	3	3
4	1	1	1	1	1	2
5	1	2	2	2	2	3
6	1	3	3	3	3	1
7	1	1	1	2	3	1
8	1	2	2	3	1	2
9	1	3	3	1	2	3
10	1	1	1	3	2	1
11	1	2	2	1	3	2
12	1	3	3	2	1	3
13	1	1	2	3	1	3
14	1	2	3	1	2	1
15	1	3	1	2	3	2
16	1	1	2	3	2	1
17	1	2	3	1	3	2
18	1	3	1	2	1	3
19	2	1	2	1	3	3
20	2	2	3	2	1	1
21	2	3	1	3	2	2
22	2	1	2	2	3	3
23	2	2	3	3	1	1
24	2	3	1	1	2	2
25	2	1	3	2	1	2
26	2	2	1	3	2	3
27	2	3	2	1	3	1
28	2	1	3	2	2	2
29	2	2	1	3	3	3
30	2	3	2	1	1	1
31	2	1	3	3	3	2
32	2	2	1	1	1	3
33	2	3	2	2	2	1
34	2	1	3	1	2	3
35	2	2	1	2	3	1
36	2	3	2	3	1	2

Table 9.4 Orthogonal array L_{36} ($3^6 \, 2^1$) for zonal distributed droplet fin.

Exp No.	Factor						
	A	B	C	D	E	F	G
1	1	1	1	1	1	1	1
2	1	2	2	2	2	2	2
3	1	3	3	3	3	3	3
4	1	1	1	1	1	2	2
5	1	2	2	2	2	3	3
6	1	3	3	3	3	1	1
7	1	1	1	2	3	1	2
8	1	2	2	3	1	2	3
9	1	3	3	1	2	3	1
10	1	1	1	3	2	1	3
11	1	2	2	1	3	2	1
12	1	3	3	2	1	3	2
13	1	1	2	3	1	3	2
14	1	2	3	1	2	1	3
15	1	3	1	2	3	2	1
16	1	1	2	3	2	1	1
17	1	2	3	1	3	2	2
18	1	3	1	2	1	3	3
19	2	1	2	1	3	3	3
20	2	2	3	2	1	1	1
21	2	3	1	3	2	2	2
22	2	1	2	2	3	3	1
23	2	2	3	3	1	1	2
24	2	3	1	1	2	2	3
25	2	1	3	2	1	2	3
26	2	2	1	3	2	3	1
27	2	3	2	1	3	1	2
28	2	1	3	2	2	2	1
29	2	2	1	3	3	3	2
30	2	3	2	1	1	1	3
31	2	1	3	3	3	2	3
32	2	2	1	1	1	3	1
33	2	3	2	2	2	1	2
34	2	1	3	1	2	3	2
35	2	2	1	2	3	1	3
36	2	3	2	3	1	2	1

9.3.2 Analysis of the S/N ratio

In this study, the experimental observations were further transformed into signal-to-noise (S/N) ratios as described in section 8.3.2 to evaluate the optimal parameters. The responses used to evaluate the control factors are specific performance, pressure drop and temperature uniformity. The evaluation criteria for the responses are shown below:

> ➢ Specific performance-Larger the best.

> ➢ Pressure drop-Smaller the best.

> ➢ Temperature uniformity- Smaller the best.

9.3.3 Grey Relational Analysis

Grey relational analysis (GRA) was then combined with the Taguchi method (also known as Taguchi-Grey method) to determine the optimal factors from the 36 simulations.

9.3.4 Weightage for the response

The weightage used to determine the optimum design of the cooling fins is shown in the table below:

Table 9.5 Response weightage.

Weightage,	Response		
	Specific performance, Q_{spec}	Pressure drop, Δp	Temperature uniformity, ΔT
w	0.35	0.3	0.35

9.3.5 Regression Analysis

Regression analysis in section 8.3.6 was used to develop the correlation of the Nusselt number, friction factor and temperature uniformity to the Reynolds number section 8.3.8.

9.3.6 Performance characterization

The hydraulic diameter is defined as the ratio of volume available for the flow to the total wetted surface area inside the cooling fin region. This ratio is more appropriate to characterize the different configurations of the cooling fins.

$$D_h = \frac{4V_f}{A_f} \qquad (9\text{-}1)$$

V_f Total fluid volume inside the cooling fin.

A_f Total convective heat transfer area in contact with the fluid.

Average convective heat transfer coefficient is defined as:

$$h_{ave} = \frac{q}{T_{w,ave} - T_{f,ave}} \qquad (9\text{-}2)$$

q Heat flux on the heated surface.

$T_{w,ave}$ Average temperature of cooling fin.

$T_{f,ave}$ Arithmetic average temperature of inlet temperature and outlet temperature of cooling fluid.

9.4 Numerical procedures

Commercial CFD software ANSYS-CFX software was used to solve the Navier-Stokes equations using a fully conservative, finite elements (cell vertex numeric) method. A steady state conjugate heat transfer simulations were performed to predict the thermal performance of the cooling fins and the fluid flow over the cooling fins was assumed incompressible. A uniform heat flux of 350W was applied on the based surface of the cooling fins. The contact resistances of the heater to the based of the cooling fins were neglected in this study. The numerical modeling procedures of the cooling fins in the ANSYS-CFX software are described section 7.3.1 and 7.3.2.

A hybrid meshing was adopted to discretize the battery pack domain using ANSYS ICEM CFD 14.0 SP1. Water was used for the simulation. The mass flow boundary condition was assigned to the inlet of the cooling fins as in Table 9.1 and Table 9.2 and the inlet temperature of water was 30 $^{\circ}$C. At the outlet of the cooling fin, average static pressure of 0 Pa was assigned. The confining walls of the cooling fin on the top, side and bottom were specified as no slip, adiabatic walls. The Shear Stress Transport (SST) turbulence model was selected for this study. The computational domain was initialized with ambient conditions at one atmospheric pressure. All simulations were executed with a high resolution scheme to achieve an accurate solution. A tight convergence criterion with RMS 1.0 x 10^{-6} is applied to continuity, momentum and energy equations (H-energy and T-energy) for all the cases studied. It was also ensured that no domain imbalance was present in the momentum and energy equations. All simulations were computed on 8 nodes HP clusters. In addition, grid independent tests were carried out to refine the grid size such that the error of the results was kept within 5%. Finally, an experimental validation of the optimized cooling fin was conducted.

9.5 Results and discussion

9.5.1 Straight channel

The numerical simulation results of the temperature distribution and velocity vector in a straight channel are shown in Figure 9.6.
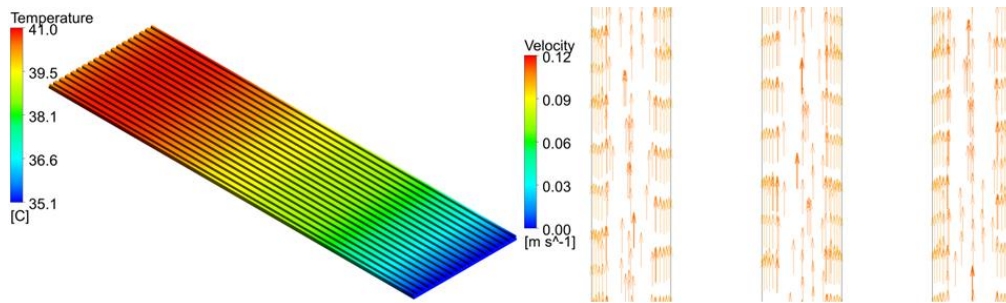
Figure 9.6 (a) Temperature distribution of the straight channel. (b) Velocity
vector of the flow in the straight channel at a mass flow rate of
20gs^{-1}.

Figure 9.6(a) shows the temperature distribution in the straight channel cold plate at steady state. The inlet temperature of the water was 30 $^{\text{o}}$C and mass flow rate was 20 gs^{-1}. The temperature of the straight channel cold plate increased gradually toward the downstream and the highest temperature is 41 $^{\text{o}}$C. The average temperature of the cold plate is about 39.1 $^{\text{o}}$C and variation of the straight channel cold plate is about 5.9 $^{\text{o}}$C. As shown in Figure 9.6(b) the flow of the water in the straight channel is unidirectional and thermal boundary layer is slow developed along the flow direction. The average velocity in the channel is about 0.1 ms^{-1}. Heat transfer of the straight channel is closely related to the fluid flow characteristics. At higher flow rates, the variation of temperature will be reduced, but the pressure loss will be increased.

9.5.2 Uniformly distributed droplet fin

9.5.2.1 Taguchi method analysis

The Taguchi method was used to study the effects of direction of flow, mass flow rate of liquid, fin thickness, fin length, transverse and longitudinal spacing on the performance of the uniformly distributed droplet fin. The factors used to perform the numerical simulations and the levels are given in

Table 9.1 and Table 9.3. The results of the simulations are shown in Table 9.6.

The results are transformed into S/N ratios as shown in Table 9.7 to Table 9.9.

Table 9.6 Design of experiment and collected response data.

No	Parameters						Response		
	A	B	C	D	E	F	Specific Performance Q_{spec}, Wm^{-3} K^{-1}	Pressure drop ΔP, Pa	Variation ΔT, K
1	1	1	1	1	1	1	317739.16	23.98	8.1
2	1	2	2	2	2	2	327000.86	26.01	7.1
3	1	3	3	3	3	3	334739.73	31.15	6.7
4	1	1	1	1	1	2	291310.52	17.02	8.6
5	1	2	2	2	2	3	313104.47	22.45	7.5
6	1	3	3	3	3	1	361178.48	42.05	6.1
7	1	1	1	2	3	1	269103.30	13.73	8.7
8	1	2	2	3	1	2	304744.71	24.90	7.2
9	1	3	3	1	2	3	387909.05	44.85	6.3
10	1	1	1	3	2	1	262956.32	12.92	8.8
11	1	2	2	1	3	2	339486.99	27.85	7.1
12	1	3	3	2	1	3	380984.94	45.06	6.5
13	1	1	2	3	1	3	227230.59	11.59	9.0
14	1	2	3	1	2	1	362969.52	53.35	6.4
15	1	3	1	2	3	2	387896.45	31.39	6.7
16	1	1	2	3	2	1	250726.82	15.18	8.5
17	1	2	3	1	3	2	331397.89	32.36	6.9
18	1	3	1	2	1	3	403193.42	34.53	6.9
19	2	1	2	1	3	3	237464.05	12.25	8.7
20	2	2	3	2	1	1	339163.44	46.25	6.0
21	2	3	1	3	2	2	355741.98	29.78	6.4
22	2	1	2	2	3	3	227349.66	10.71	8.1
23	2	2	3	3	1	1	314408.01	36.37	6.0
24	2	3	1	1	2	2	410774.65	39.17	6.0
25	2	1	3	2	1	2	243356.56	18.62	7.8
26	2	2	1	3	2	3	286023.75	17.27	7.7
27	2	3	2	1	3	1	433509.22	56.31	5.5
28	2	1	3	2	2	2	234448.31	15.82	7.9
29	2	2	1	3	3	3	274313.61	15.93	7.8
30	2	3	2	1	1	1	471113.93	79.93	5.3
31	2	1	3	3	3	2	216015.33	12.06	8.4
32	2	2	1	1	1	3	335374.75	24.02	7.0
33	2	3	2	2	2	1	415406.30	49.96	5.0
34	2	1	3	1	2	3	240208.89	15.49	8.4
35	2	2	1	2	3	1	334720.25	23.96	6.5
36	2	3	2	3	1	2	347240.92	36.93	5.8

Table 9.7 Average S/N ratio for the specific performance.

TPM	Average S/N ratio for specific performance					
	A	B	C	D	E	F
Level 1	110.14	107.96	110.20	110.62	110.24	110.58
Level 2	109.79	110.13	109.97	110.00	109.95	109.83
Level 3	-	111.80	109.72	109.27	109.70	109.48
difference	0.35	3.84	0.48	1.35	0.55	1.11
Rank	**6**	**1**	**5**	**2**	**4**	**3**
Characteristic type	**Larger the best**					
Optimum	**A1**	**B3**	**C1**	**D1**	**E1**	**F1**

Table 9.8 Average S/N ratio for the pressure drop.

TPM	Average S/N ratio for pressure drop					
	A	B	C	D	E	F
Level 1	-28.23	-23.27	-26.94	-29.75	-29.35	-30.20
Level 2	-28.08	-28.78	-28.15	-28.06	-28.05	-27.80
Level 3	-	-32.41	-29.38	-26.66	-27.06	-26.47
difference	0.15	9.13	2.44	3.09	2.29	3.73
Rank	**6**	**1**	**4**	**3**	**5**	**2**
Characteristic type	**Smaller the best**					
Optimum	**A2**	**B1**	**C1**	**D3**	**E3**	**F1**

Table 9.9 Average S/N ratio for the variation of temperature.

TPM	Average S/N ratio for variation of temperature					
	A	B	C	D	E	F
Level 1	-17.32	-18.49	-17.35	-16.80	-16.82	-16.41
Level 2	-16.65	-16.80	-16.82	-16.88	-16.99	-17.04
Level 3		-15.65	-16.78	-17.27	-17.14	-17.50
difference	0.67	2.84	0.57	0.47	0.32	1.09
Rank	**3**	**1**	**4**	**5**	**6**	**2**
Characteristic type	**Smaller the best**					
Optimum	**A2**	**B3**	**C3**	**D1**	**E1**	**F1**

The highest S/N ratios at all levels of the parameters indicate optimum performance. From Table 9.7, "larger the best" is used to characterize the specific performance of the uniformly distributed droplet fin, the optimum design parameters are (A2) forward flow, (B3) mass flow rate of 80 gs^{-1}, (C1) fin thickness 3 mm, (D1) fin length 12 mm, (E1) transverse spacing of fins 9 mm and (F1) longitudinal spacing of fins -3 mm. The specific performance of the cooling fin is proportional to all of the factors investigated. "Smaller the best" was used to characterize pressure drop

across the plate fin, the optimum design parameters for pressure drop are (A2) forward flow, (B1) mass flow rate of 20 gs^{-1}, (C1) fin thickness 3mm, (D3) fin length 18 mm, (E3) transverse spacing of fins 13 mm and (F1) longitudinal spacing of fins -3 mm as shown in Table 9.8. Lower mass flow rate, sharp leading edge of the fin, smaller thickness and longer fin, large transverse spacing and short longitudinal spacing will result in lower pressure drop. "Smaller the best" was used to characterize the variation of the temperature across the cooling fins, the optimum design parameters for variation of temperature are (A2) forward flow, (B3) mass flow rate of 80 gs^{-1}, (C3) fin thickness 5mm, (D1) fin length 12 mm, (E1) transverse spacing of fins 9 mm and (F1) longitudinal spacing of fins -3 mm as shown in Table 9.9. Mass flow rate and longitudinal spacing are the two main factors affecting the temperature uniformity across the cooling fins.

9.5.2.2 Grey Relational Analysis

The grey relational analysis method was used to optimize the design parameters by maximizing the specific performance, minimizing the pressure drop and temperature variation across the cooling fins. The results of the simulation were first normalized in the range of 0 and 1 as shown in Table 9.10. The results of the grey relational coefficient and grey relational grade are tabulated in Table 9.11. The grey relational grade graph according to the L$_{36}$ orthogonal experiment plan is shown in Table 9.12.

Table 9.10 Normalized response values.

No	Parameters						Normalized Response		
	A	B	C	D	E	F	Specific Performance Q_{spec}, Wm^{-3} K^{-1}	Pressure drop ΔP, Pa	Variation ΔT, K
1	1	1	1	1	1	1	0.399	0.808	0.235
2	1	2	2	2	2	2	0.435	0.779	0.465
3	1	3	3	3	3	3	0.465	0.705	0.564
4	1	1	1	1	1	2	0.295	0.909	0.099
5	1	2	2	2	2	3	0.381	0.830	0.377
6	1	3	3	3	3	1	0.569	0.547	0.708
7	1	1	1	2	3	1	0.208	0.956	0.084
8	1	2	2	3	1	2	0.348	0.795	0.444
9	1	3	3	1	2	3	0.674	0.507	0.680
10	1	1	1	3	2	1	0.184	0.968	0.060
11	1	2	2	1	3	2	0.484	0.752	0.480
12	1	3	3	2	1	3	0.647	0.504	0.620
13	1	1	2	3	1	3	0.044	0.987	0.000
14	1	2	3	1	2	1	0.576	0.384	0.642
15	1	3	1	2	3	2	0.674	0.701	0.584
16	1	1	2	3	2	1	0.136	0.935	0.123
17	1	2	3	1	3	2	0.452	0.687	0.521
18	1	3	1	2	1	3	0.734	0.656	0.534
19	2	1	2	1	3	3	0.084	0.978	0.090
20	2	2	3	2	1	1	0.483	0.487	0.732
21	2	3	1	3	2	2	0.548	0.724	0.635
22	2	1	2	2	3	3	0.044	1.000	0.227
23	2	2	3	3	1	1	0.386	0.629	0.745
24	2	3	1	1	2	2	0.763	0.589	0.754
25	2	1	3	2	1	2	0.107	0.886	0.313
26	2	2	1	3	2	3	0.274	0.905	0.339
27	2	3	2	1	3	1	0.853	0.341	0.875
28	2	1	3	2	2	2	0.072	0.926	0.281
29	2	2	1	3	3	3	0.229	0.925	0.299
30	2	3	2	1	1	1	1.000	0.000	0.923
31	2	1	3	3	3	2	0.000	0.981	0.161
32	2	2	1	1	1	3	0.468	0.808	0.489
33	2	3	2	2	2	1	0.782	0.433	1.000
34	2	1	3	1	2	3	0.095	0.931	0.169
35	2	2	1	2	3	1	0.465	0.809	0.623
36	2	3	2	3	1	2	0.514	0.621	0.785

Table 9.11 Grey relational coefficients and grey relational grade values.

Exp No.	Grey relational coefficient			Grey Relational Grade	Orders
	Specific Performance, Q_{spec}, $Wm^{-3}K^{-1}$	Pressure drop ΔP, Pa	Variation ΔT, K		
1	0.454	0.723	0.395	0.514	36
2	0.470	0.694	0.483	0.541	21
3	0.483	0.629	0.534	0.545	18
4	0.415	0.846	0.357	0.524	32
5	0.447	0.747	0.445	0.536	23
6	0.537	0.525	0.631	0.566	11
7	0.387	0.920	0.353	0.535	25
8	0.434	0.709	0.474	0.530	28
9	0.605	0.503	0.610	0.576	10
10	0.380	0.940	0.347	0.537	22
11	0.492	0.669	0.490	0.544	19
12	0.586	0.502	0.568	0.555	15
13	0.343	0.975	0.333	0.529	29
14	0.541	0.448	0.583	0.528	30
15	0.605	0.626	0.546	0.591	6
16	0.367	0.886	0.363	0.521	33
17	0.477	0.615	0.511	0.530	27
18	0.653	0.592	0.518	0.587	7
19	0.353	0.957	0.355	0.535	26
20	0.492	0.493	0.651	0.548	16
21	0.525	0.645	0.578	0.580	9
22	0.344	1.000	0.393	0.558	14
23	0.449	0.574	0.662	0.561	12
24	0.679	0.549	0.670	0.637	4
25	0.359	0.814	0.421	0.517	35
26	0.408	0.841	0.431	0.546	17
27	0.772	0.432	0.800	0.680	3
28	0.350	0.871	0.410	0.527	31
29	0.393	0.869	0.416	0.544	20
30	**1.000**	**0.333**	**0.866**	**0.753**	**1**
31	0.333	0.962	0.374	0.536	24
32	0.484	0.722	0.494	0.559	13
33	0.696	0.469	1.000	0.734	2
34	0.356	0.879	0.376	0.520	34
35	0.483	0.723	0.570	0.586	8
36	0.507	0.569	0.699	0.593	5

Table 9.12 Average grey relational grade for combination of all responses.

TPM	Combination of all responses					
	A	B	C	D	E	F
Level 1	0.54	0.53	0.56	0.58	0.564	0.589
Level 2	0.58	0.55	0.59	0.57	0.565	0.55
Level 3		0.62	0.54	0.55	0.562	0.549
difference	0.04	0.087	0.045	0.026	0.003	0.039
Rank	**5**	**1**	**2**	**4**	**6**	**3**
Characteristic type	**Larger the best**					
Optimum	**A2**	**B3**	**C2**	**D1**	**E2**	**F1**

Specific performance is the critical factor determining the cooling fin design followed by pressure drop and temperature variation across the cooling fin. Therefore, the weighting value for specific performance, pressure drop and temperature variation are 0.35, 0.3 and 0.35 respectively. The optimal design parameters are (A2) forward flow, (B3) mass flow rate of 80 gs^{-1}, (C2) fin thickness 4 mm, (D1) fin length 12 mm, (E2) transverse spacing of fins 11 mm and (F1) longitudinal spacing of fins -3 mm corresponding to Order 1 as shown in Table 9.10.

9.5.2.3 Analysis of Variance and F-Test

Analysis of variance (ANOVA) was used to analyze the effect of each factor on the responses such as specific performance, pressure drop and variation of temperature. In this analysis, 5% of error in the classification of the significance of the design parameters was taken into consideration. Hence $\alpha = 0.05$, $v1 = 1$ for flow direction, $v2$-$v6 = 2$ for mass flow rate, fin thickness, fin, transverse and longitudinal spacing of the fins for error calculated with 24 degrees of freedom were used for the F-test. For design parameter flow direction $F_{0.05, 1, 24} = 4.26$ and for the rest of the factors $F_{0.05, 1, 24} = 3.4$. The results of the ANOVA analysis of the responses are illustrated in the following tables:

Table 9.13 Analysis of variance for the specific performance.

Source	Sq	DF	Mq	F-ratio	Rho, %
Flow direction	521662733.68	1	521662734	6.13	0.35
Mass flow rate	$1.16 \, x10^{11}$	2	$5.82 \, x10^{10}$	684.15	77.94
Fin thickness	1562563849	2	781281924	9.18	1.05
Fin length	16265724649	2	$8.13 \, x10^{9}$	95.56	10.89
Transverse spacing	2190329748	2	$1.10 \, x10^{9}$	12.87	1.47
Longitudinal spacing	10372063848	2	$5.19 \, x10^{9}$	60.93	6.94
Error	2042639850.47	24	85109994	1.00	1.37
St	$1.49 \, x10^{11}$	35	$4.27 \, x10^{9}$	-	100.00
Mean	$3.72 \, x10^{12}$	1	-	-	-
ST	$3.87 \, x10^{12}$	36	-	-	-

Table 9.14 Analysis of variance for the pressure drop.

Source	Sq	DF	Mq	F-ratio	Rho, %
Flow direction	25.79	1	25.79	1.12	0.30
Mass flow rate	4865.78	2	2432.89	105.30	56.78
Fin thickness	571.55	2	285.78	12.37	6.67
Fin length	839.70	2	419.85	18.17	9.80
Transverse spacing	341.79	2	170.90	7.40	3.99
Longitudinal spacing	1370.80	2	685.40	29.67	16.00
Error	554.50	24	23.10	1.00	6.47
St	8569.91	35	244.85	-	100.00
Mean	30697.53	1	-	-	-
ST	39267.44	36	-	-	-

Table 9.15 Analysis of variance for the variation of temperature.

Source	Sq	DF	Mq	F-ratio	Rho, %
Flow direction	2.29	1	2.29	83.27	5.33
Mass flow rate	33.21	2	16.61	605.01	77.43
Fin thickness	1.49	2	0.74	27.12	3.47
Fin length	1.01	2	0.50	18.33	2.35
Transverse spacing	0.35	2	0.17	6.29	0.80
Longitudinal spacing	3.89	2	1.95	70.95	9.08
Error	0.66	24	0.03	1.00	1.54
St	42.89	35	1.23	-	100.00
Mean	1840.82	1	-	-	-
ST	1883.72	36	-	-	-

The degree of the influence of each design parameter is determined by percent contribution and F-test in the ANOVA analysis. As shown in Table 9.13, mass flow rate, fin length and longitudinal spacing are the primary factors influence the specific performance of the cooling fins which contributed about 95.77%. The pressure drop of the cooling fin is affected

by mass flow rate (56.78%), longitudinal spacing (16.00%), fin length (9.87%) and fin thickness (6.67%) as shown in Table 9.14. On the other hand, contributions of flow direction of fluid in the pressure drop are insignificant. Lastly, mass flow rate (77.43%), longitudinal spacing (9.08%), and flow direction (5.33%) are the major factors affecting the temperature uniformity across the cooling fin as shown in Table 9.15.

9.5.2.4 Optimized design

The temperature contour and velocity streamline plot of the optimized cooling fin at a mass flow rate of 40 gs^{-1} are shown in Figure 9.7.
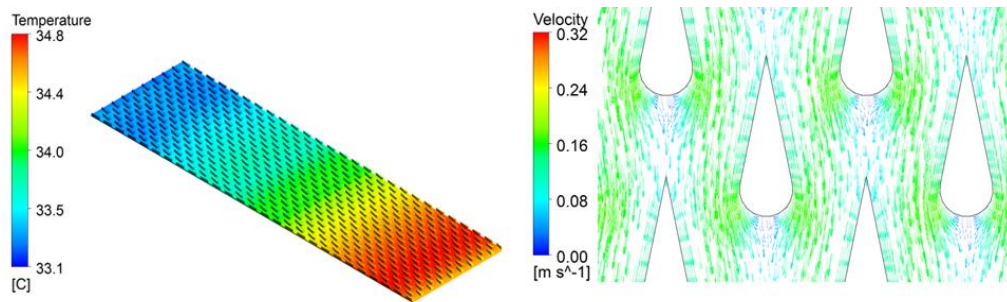
Figure 9.7 (a) Temperature distribution of the cooling fin. (b) Velocity vector of the flow around the uniform distributed droplet fin.

Figure 9.7(a) shows the temperature distribution of the optimized cooling fin design. The temperature of the cooling fin is progressively increased to 34.8 ^{o}C along the flow path. The temperature difference across the cooling fin is about 1.7 ^{o}C. Figure 9.7(b) shows the flow field in the cooling fins. As the cooling liquid approach the sharp leading edge of the droplet fin, the flows is streamlined by the fin body and go a round the trailing edge and creates a turbulent wake on the downstream side. The turbulent wake at the trailing edge of the cooling fin will enhance the mixing and increase the heat transfer rate. Besides, any development of the thermal boundary layer will be broken up by the sharp leading edge. The maximum velocity is near the round trailing edge which is about 0.16 ms^{-1}.

9.5.2.5 Performance characterization

The results of the regression analysis for the average Nusselt number, average friction factor and variation of temperature for the cooling fin are shown in Table 9.16 to Table 9.18, respectively. The regression equations are given in Equations 9-1 to 9-3.

Table 9.16 Regression statistics of the average Nusselt number.

Predictor	Coefficient	Standard Error	T	P	Lower 95%	Upper 95%
Constant	-1.792	0.157	-11.428	0.00144	-2.291	-1.293
Ln Re	0.679	0.0193	35.161	5.058e-05	0.618	0.741
S = 0.0246	R = 99.88%		R-Sq = 99.76%		R-Sq(adj) = 99.68%	

Table 9.17 Regression statistics of the average friction factor.

Predictor	Coefficient	Standard Error	T	P	Lower 95%	Upper 95%
Constant	0.558	0.055	10.135	0.00205	0.383	0.733
Ln Re	-0.140	0.00678	-20.638	0.000249	-0.162	-0.118
S = 0.00862	R = 99.65%		R-Sq = 99.30%		R-Sq(adj) = 99.07%	

Table 9.18 Regression statistics of the temperature variation of the cell.

Predictor	Coefficient	Standard Error	T	P	Lower 95%	Upper 95%
Constant	1.135	0.216	5.257	0.0134	0.448	1.823
Ln Re	-0.801	0.0266	-30.106	8.05e-05	-0.886	-0.716
S = 0.0338	R = 99.83%		R-Sq = 99.67%		R-Sq(adj) = 99.56%	

$$\overline{Nu} = 0.167\, Re^{0.679} \tag{9-3}$$

$$\overline{f} = 1.747\, Re^{-0.140} \tag{9-4}$$

$$\frac{\Delta T}{T_{in}} = 3.112\, Re^{-0.801} \tag{9-5}$$

The R-square for the average Nusselt number as shown in Table 9.16 is 99.7%, which indicates very good correlation between the average Nusselt number and Reynolds number. On the other hand, the R-square for friction factor as shown in Table 9.17 is 99.3%, which also indicates very good correlation between the average friction factor and Reynolds number. The R-

square for the variation of cooling fin temperature to the free stream temperature is 99.7% as shown in Table 9.18, which indicates a very good correlation with the variation of cooling fin temperature to the Reynolds number with a variation of ±0.3%.

The results of the multiple regression analysis for the average Nusselt number, average friction factor and variation of temperature for various sizes of droplet shapes of cooling fin are shown in Table 9.19 to Table 9.21 respectively. The regression equations for the cooling fins are shown in Equations 9-4 to 9-6, respectively. The variables used are shown in Figure 9.8.

P : Perimeter of fin   **H: Height of fin**
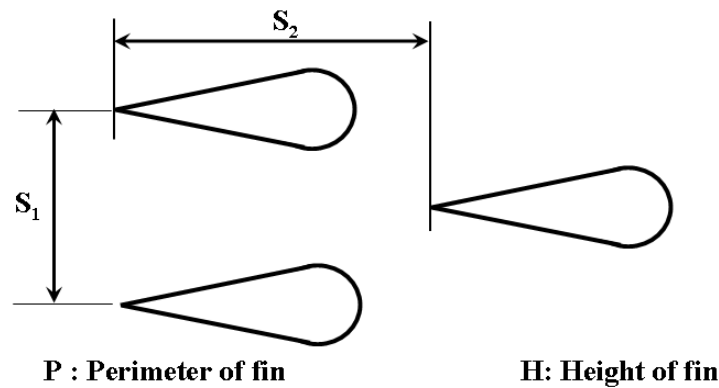
Figure 9.8 Parameter of the droplet fin.

Table 9.19 Regression statistics of the average Nusselt number.

Predictor	Coefficient	Standard Error	T	P	Lower 95%	Upper 95%
Constant	1.593	0.869	1.833	0.0898	-0.285	3.471
$Ln\,Re$	0.326	0.102	3.193	0.00707	0.106	0.547
$Ln\left(S_1/P\right)$	-0.692	0.208	-3.325	0.00548	-1.141	-0.242
$Ln\left(S_2/P\right)$	-1.012	0.118	-8.541	1.085e-6	-1.267	-0.756
$Ln\left(H/P\right)$	1.20	0.244	4.924	0.000278	0.673	1.726
S = 0.0893		R = 95.06%		R-Sq = 90.36%		R-Sq(adj) = 87.40%

Table 9.20 Regression statistics of the average friction factor.

Predictor	Coefficient	Standard Error	T	P	Lower 95%	Upper 95%
Constant	0.964	1.563	0.617	0.548	-2.413	4.341
$Ln\,Re$	-1.250	0.184	-6.804	1.256e-5	-1.647	-0.853
$Ln\left(\dfrac{S_1}{P}\right)$	1.171	0.374	3.129	0.00798	0.363	1.979
$Ln\left(\dfrac{S_2}{P}\right)$	0.520	0.213	2.440	0.0298	0.0596	0.980
$Ln\left(\dfrac{H}{P}\right)$	-0.435	0.438	-0.993	0.339	-1.382	0.511
S = 0.161		R = 93.65%		R-Sq = 87.71%		R-Sq(adj) = 83.92%

Table 9.21 Improved regression statistics of the average friction factor.

Predictor	Coefficient	Standard Error	T	P	Lower 95%	Upper 95%
Constant	1.885	1.258	1.499	0.156	-0.812	4.583
$Ln\,Re$	-1.307	0.175	-7.483	2.953e-6	-1.682	-0.932
$Ln\left(\dfrac{S_1}{P}\right)$	0.865	0.212	4.074	0.00114	0.410	1.320
$Ln\left(\dfrac{S_2}{P}\right)$	0.549	0.211	2.602	0.0209	0.0964	1.001
S = 0.161		R = 93.15%		R-Sq = 86.77%		R-Sq(adj) = 83.94%

Table 9.22 Regression statistics of the variation of temperature.

Predictor	Coefficient	Standard Error	T	P	Lower 95%	Upper 95%
Constant	-1.748	0.703	-2.486	0.0273	-3.267	-0.229
$Ln\,Re$	-0.276	0.0827	-3.340	0.00532	-0.455	-0.0975
$Ln\left(\dfrac{S_1}{P}\right)$	0.432	0.168	2.568	0.0234	0.0686	0.796
$Ln\left(\dfrac{S_2}{P}\right)$	0.775	0.0958	8.090	1.978e-6	0.568	0.982
$Ln\left(\dfrac{H}{P}\right)$	-0.512	0.197	-2.598	0.0221	-0.938	-0.0862
S = 0.0722		R = 93.51%		R-Sq = 87.44%		R-Sq(adj) = 83.59%

$$\overline{Nu} = 4.92\,Re^{0.326}\left(\frac{S_1}{P}\right)^{-0.692}\left(\frac{S_2}{P}\right)^{-1.01}\left(\frac{H}{P}\right)^{1.20} \tag{9-6}$$

$$\frac{\bar{f}}{Re} = 6.589\,Re^{-1.307}\left(\frac{S_1}{P}\right)^{0.865}\left(\frac{S_2}{P}\right)^{0.549} \tag{9-7}$$

$$\frac{\Delta T}{T_\infty} = 0.174\,Re^{-0.276}\left(\frac{S_1}{P}\right)^{0.432}\left(\frac{S_2}{P}\right)^{0.775}\left(\frac{H}{P}\right)^{-0.512} \tag{9-8}$$

The R-square for the average Nusselt number for cooling fin are 90.4% as shown in Table 9.19, which indicates a significant correlation with a variation of ±9.6%. The p-value for the average friction factor is > 0.05 to correlate $\left(\dfrac{H}{P}\right)^z$ as shown in Table 9.20. Hence, this term is omitted. A new analysis was carried out, and the p-value of all the parameters was found to be statistically significant to correlate the friction factor as shown in Table 9.21 with a variation of ±12.3%. The R-square for the variation of cooling fin temperature to the free stream is 87.7% as shown in Table 9.22. This indicates significant acceptable correlation with a variation of ±12.6%.

9.5.2.6 Comparison of uniformly distributed droplet fin and straight channel

Comparisons of the thermal resistance, variation of cooling fin temperature, average Nusselt number and fan power consumption for uniform distributed droplet fin and equal flow channel width of the straight channel cooling fin are shown in Figure 9.9.

Although the average Nusselt number of the droplet fin and straight channel fin progressively increases with the mass flow rate, the average Nusselt number of the straight channel is lower than the droplet fin. The Nusselt number for the uniform distributed droplet fin at a mass flow rate of 20 gs^{-1} is about 300% higher than the straight channel fin. The thermal resistance of the droplet fin is about 25% lower than the straight channel fin. The variation of temperature is decreased with the mass flow rate of cooling water. Besides, the variation of temperature for the droplet fin at 20 gs^{-1} is about 3 ^{o}C, while the variation of temperature for the straight channel fin is

about 6 ^{o}C. At a low mass flow rate of cooling water flow (20 gs^{-1}), the pumping power consumption of the straight channel and droplet fin is the same. At higher mass flow rate (80 gs^{-1}), the pumping power consumption of the droplet fin is 7.3% less than straight channel fin. Hence, uniform distributed droplet fin could offer higher cooling capacity than the straight channel fin with similar pumping power consumption.
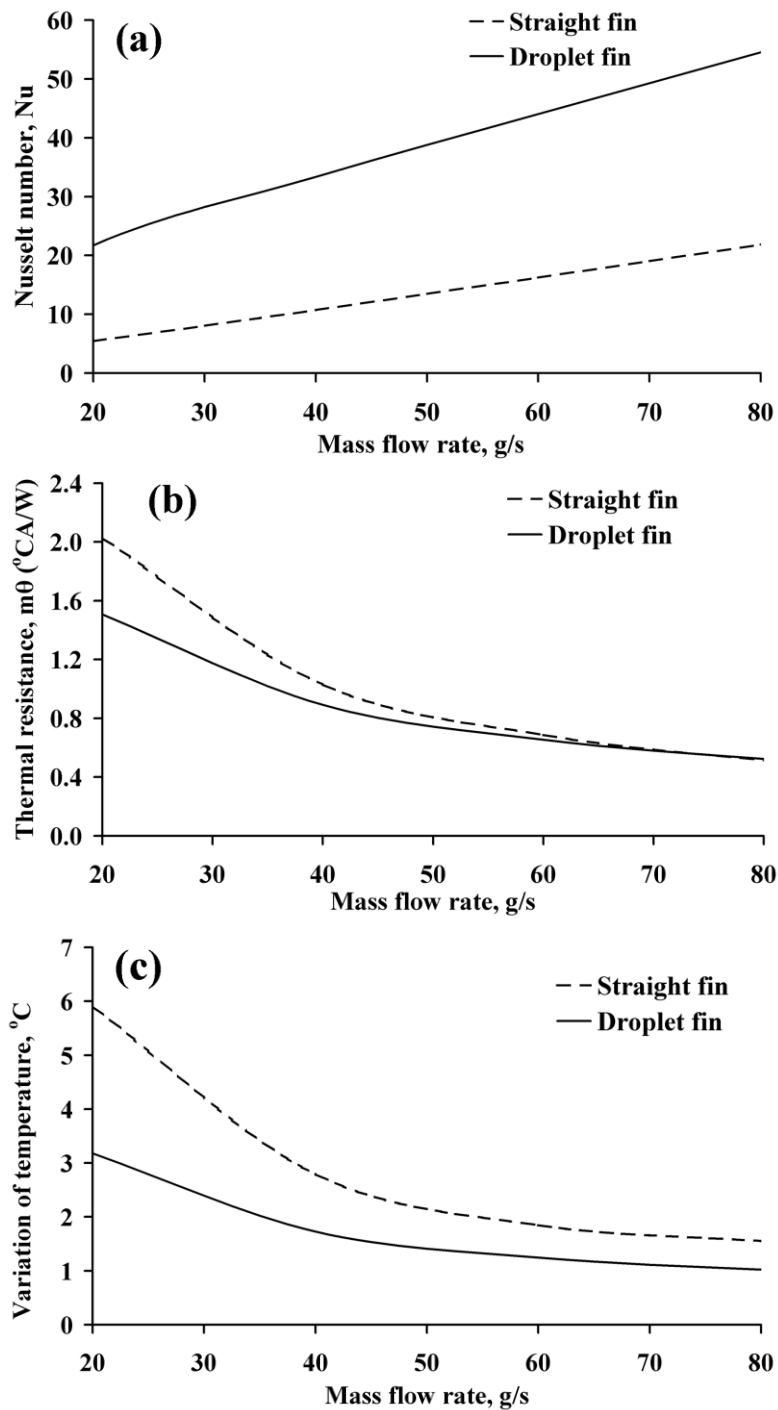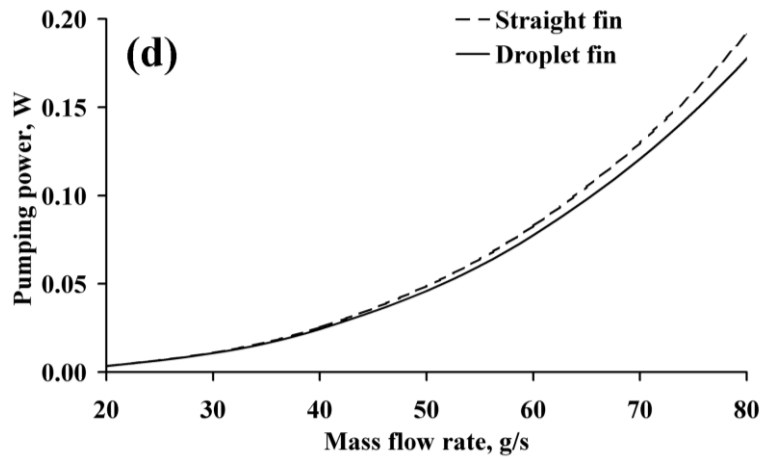
Figure 9.9 Comparison of uniform distributed droplet fin and straight channel fin. (a) Nu. (b) Thermal resistance. (c) $\Delta T/T_{in}$. (d) Pumping power.

9.5.3 Zonally distributed droplet fin

9.5.3.1 Taguchi method analysis

The Taguchi method was used to study the effects of direction of flow, mass flow rate of liquid, fin thickness, fin length, transverse and longitudinal spacing of the fins and also the number of zones on the performance of the zonal distributed droplet fin cold plate. The factors used to perform the numerical simulations and the levels are given in Table 9.2 and Table 9.4. The results of the simulations are shown in Table 9.23. The results are transformed into S/N ratios as shown in Table 9.24 to Table 9.26.

Table 9.23 Design of experiment and collected response data.

No	A	B	C	D	E	F	G	Specific Performance Q_{spec}, Wm^{-3} K^{-1}	Pressure drop ΔP, Pa	Variation ΔT, K
1	1	1	1	1	1	1	1	336083.22	33.84	6.5
2	1	2	2	2	2	2	2	341475.25	30.32	6.2
3	1	3	3	3	3	3	3	350562.29	35.04	6.1
4	1	1	1	1	1	2	2	301463.98	19.98	7.5
5	1	2	2	2	2	3	3	326253.54	25.06	6.7
6	1	3	3	3	3	1	1	354909.49	42.05	6.1
7	1	1	1	2	3	1	2	282142.67	16.58	7.0
8	1	2	2	3	1	2	3	317700.14	28.46	6.3
9	1	3	3	1	2	3	1	410564.15	52.82	5.7
10	1	1	1	3	2	1	3	276061.50	15.50	7.4
11	1	2	2	1	3	2	1	358892.64	33.73	5.9
12	1	3	3	2	1	3	2	398494.38	51.41	5.6
13	1	1	2	3	1	3	2	234096.84	12.64	8.0
14	1	2	3	1	2	1	3	388213.35	77.98	5.0
15	1	3	1	2	3	2	1	409292.32	35.96	5.8
16	1	1	2	3	2	1	1	264210.18	19.20	6.9
17	1	2	3	1	3	2	2	349383.18	39.47	5.8
18	1	3	1	2	1	3	3	419139.03	37.82	6.3
19	2	1	2	1	3	3	3	249266.96	14.22	7.4
20	2	2	3	2	1	1	1	363631.41	65.83	4.6
21	2	3	1	3	2	2	2	374097.73	33.25	5.3
22	2	1	2	2	3	3	1	233365.13	12.04	7.4
23	2	2	3	3	1	1	2	332611.99	46.08	4.6
24	2	3	1	1	2	2	3	437436.12	46.14	5.0
25	2	1	3	2	1	2	3	254895.21	22.50	6.4
26	2	2	1	3	2	3	1	298601.06	18.96	6.6
27	2	3	2	1	3	1	2	461576.78	71.73	4.2
28	2	1	3	2	2	2	1	248306.77	19.72	6.3
29	2	2	1	3	3	3	2	284091.77	16.97	6.6
30	2	3	2	1	1	1	3	509093.72	113.83	4.1
31	2	1	3	3	3	2	3	227535.83	14.24	6.8
32	2	2	1	1	1	3	1	350820.60	27.37	6.2
33	2	3	2	2	2	1	2	430492.40	61.66	4.1
34	2	1	3	1	2	3	2	251168.01	18.05	6.9
35	2	2	1	2	3	1	3	356746.68	28.41	5.4
36	2	3	2	3	1	2	1	364084.55	42.49	4.8

Table 9.24 Average S/N ratio for the specific performance.

TPM	Average S/N ratio for specific performance						
	A	B	C	D	E	F	G
Level 1	110.52	108.35	110.62	111.10	110.67	111.03	110.31
Level 2	110.24	110.57	110.38	110.41	110.38	110.26	110.37
Level 3		112.21	110.14	109.62	110.08	109.84	110.45
difference	0.28	3.85	0.48	1.48	0.59	1.19	0.15
Rank	5	1	4	2	7	3	6
Characteristic type	Larger the best						
Optimum	A2	B3	C2	D1	E3	F2	G1

Table 9.25 Average S/N ratio for the pressure drop.

TPM	Average S/N ratio for pressure drop						
	A	B	C	D	E	F	G
Level 1	-29.68	-24.86	-28.26	-31.65	-31.05	-32.29	-29.63
Level 2	-29.65	-30.39	-29.69	-29.56	-29.62	-29.22	-29.55
Level 3		-33.75	-31.05	-27.79	-28.32	-27.49	-29.82
difference	0.03	8.89	2.79	3.87	2.73	4.81	0.27
Rank	7	1	4	3	5	2	6
Characteristic type	Smaller the best						
Optimum	A2	B1	C1	D3	E3	F3	G2

Table 9.26 Average S/N ratio for the variation of temperature.

TPM	Average S/N ratio for variation of temperature						
	A	B	C	D	E	F	G
Level 1	-16.03	-16.92	-15.93	-15.19	-15.26	-14.61	-15.57
Level 2	-14.95	-15.23	-15.33	-15.42	-15.44	-15.50	-15.35
Level 3		-14.33	-15.22	-15.87	-15.77	-16.36	-15.55
difference	1.09	2.59	0.71	0.68	0.52	1.76	0.22
Rank	3	1	5	4	6	2	7
Characteristic type	Smaller the best						
Optimum	A2	B3	C2	D1	E1	F1	G2

The highest S/N ratios at all levels of the parameters indicate optimum performance. From Table 9.24, "larger the best" was used to characterize the specific performance of the zonal distributed droplet fin, the optimum design parameters are (A2) forward flow, (B3) mass flow rate of 80 gs^{-1}, (C2) fin thickness 4 mm, (D1) fin length 12 mm, (E3) transverse spacing of fins 13 mm, (F2) longitudinal spacing of fins 0 mm and (G1) the number of zones 2. The specific performance of the cooling fin is proportional to all of the factors investigated. "Smaller the best" was used to characterize

pressure drop across the plate fin, the optimum design parameters for pressure drop are (A2) forward flow, (B1) mass flow rate of 40 gs^{-1}, (C1) fin thickness 3 mm, (D3) fin length 18 mm, (E3) transverse spacing of fins 13 mm, (F3) longitudinal spacing of fins 3 mm and (G2) the number of zones 3 as shown in Table 9.25. The pressure drop of the zonal distributed droplet fin is insensitive to the direction of flow. "Smaller the best" was used to characterize the variation of the temperature across the cooling fin, the optimum design parameters for variation of temperature are (A2) forward flow, (B3) mass flow rate of 80 gs^{-1}, (C2) fin thickness 4mm, (D1) fin length 12 mm, (E1) transverse spacing of fins 9 mm, (F1) longitudinal spacing of fins -3 mm and (G2) the number of zones 3 as shown in Table 9.26. Mass flow rate and longitudinal spacing are the two main factors affecting the temperature uniformity across the cooling fins.

9.5.3.2 Grey Relational Analysis

Grey relational analysis method was used to optimize the design parameters for the cooling fins. The results of the simulation were first normalized in the range of 0 and 1 as shown in Table 9.27. The results of the grey relational coefficient and grey relational grade are tabulated in Table 9.28. The grey relational grade graph according to the L$_{36}$ orthogonal experiment plan is shown in Table 9.29.

Table 9.27 Normalized response values.

No	Parameters							Response		
	A	B	C	D	E	F	G	Specific Performance Q_{spec}, Wm^{-3} K^{-1}	Pressure drop ΔP, Pa	Variation ΔT, K
1	1	1	1	1	1	1	1	0.386	0.786	0.393
2	1	2	2	2	2	2	2	0.405	0.820	0.476
3	1	3	3	3	3	3	3	0.437	0.774	0.490
4	1	1	1	1	1	2	2	0.263	0.922	0.131
5	1	2	2	2	2	3	3	0.351	0.872	0.341
6	1	3	3	3	3	1	1	0.452	0.705	0.480
7	1	1	1	2	3	1	2	0.194	0.955	0.258
8	1	2	2	3	1	2	3	0.320	0.839	0.442
9	1	3	3	1	2	3	1	0.650	0.599	0.604
10	1	1	1	3	2	1	3	0.172	0.966	0.168
11	1	2	2	1	3	2	1	0.467	0.787	0.543
12	1	3	3	2	1	3	2	0.607	0.613	0.612
13	1	1	2	3	1	3	2	0.023	0.994	0.000
14	1	2	3	1	2	1	3	0.571	0.352	0.768
15	1	3	1	2	3	2	1	0.646	0.765	0.560
16	1	1	2	3	2	1	1	0.130	0.930	0.291
17	1	2	3	1	3	2	2	0.433	0.731	0.572
18	1	3	1	2	1	3	3	0.681	0.747	0.450
19	2	1	2	1	3	3	3	0.077	0.979	0.164
20	2	2	3	2	1	1	1	0.483	0.472	0.872
21	2	3	1	3	2	2	2	0.521	0.792	0.689
22	2	1	2	2	3	3	1	0.021	1.000	0.166
23	2	2	3	3	1	1	2	0.373	0.666	0.867
24	2	3	1	1	2	2	3	0.745	0.665	0.760
25	2	1	3	2	1	2	3	0.097	0.897	0.426
26	2	2	1	3	2	3	1	0.252	0.932	0.370
27	2	3	2	1	3	1	2	0.831	0.414	0.967
28	2	1	3	2	2	2	1	0.074	0.925	0.446
29	2	2	1	3	3	3	2	0.201	0.952	0.363
30	2	3	2	1	1	1	3	1.000	0.000	0.991
31	2	1	3	3	3	2	3	0.000	0.978	0.320
32	2	2	1	1	1	3	1	0.438	0.849	0.467
33	2	3	2	2	2	1	2	0.721	0.512	1.000
34	2	1	3	1	2	3	2	0.084	0.941	0.301
35	2	2	1	2	3	1	3	0.459	0.839	0.668
36	2	3	2	3	1	2	1	0.485	0.701	0.829

Table 9.28 Grey relational coefficients and grey relational grade values.

Exp No.	Grey relational coefficient			Grey Relational Grade	Orders
	Specific Performance, Q_{spec}, $Wm^{-3}K^{-1}$	Pressure drop ΔP, Pa	Variation ΔT, K		
1	0.449	0.700	0.452	0.525	36
2	0.456	0.736	0.488	0.551	20
3	0.470	0.689	0.495	0.545	25
4	0.404	0.865	0.365	0.529	34
5	0.435	0.796	0.431	0.542	27
6	0.477	0.629	0.490	0.527	35
7	0.383	0.918	0.403	0.550	21
8	0.424	0.756	0.473	0.541	29
9	0.588	0.555	0.558	0.568	12
10	0.377	0.936	0.375	0.544	26
11	0.484	0.701	0.522	0.563	14
12	0.560	0.564	0.563	0.562	15
13	0.339	0.988	0.333	0.532	33
14	0.538	0.436	0.684	0.558	18
15	0.585	0.680	0.532	0.595	10
16	0.365	0.877	0.413	0.535	32
17	0.468	0.650	0.539	0.547	24
18	0.610	0.664	0.476	0.579	11
19	0.351	0.959	0.374	0.542	28
20	0.492	0.486	0.797	0.597	9
21	0.510	0.706	0.617	0.606	7
22	0.338	1.000	0.375	0.550	22
23	0.444	0.599	0.789	0.611	6
24	0.663	0.599	0.676	0.648	4
25	0.356	0.830	0.466	0.537	31
26	0.401	0.880	0.442	0.559	17
27	0.748	0.460	0.937	0.728	2
28	0.351	0.869	0.474	0.549	23
29	0.385	0.912	0.440	0.562	16
30	**1.000**	**0.333**	**0.982**	**0.794**	**1**
31	0.333	0.959	0.424	0.553	19
32	0.471	0.768	0.484	0.565	13
33	0.642	0.506	1.000	0.726	3
34	0.353	0.894	0.417	0.538	30
35	0.480	0.757	0.601	0.606	8
36	0.493	0.626	0.745	0.621	5

Table 9.29 Average grey relational grade for combination of all responses.

TPM	Combination of all responses						
	A	**B**	**C**	**D**	**E**	**F**	**G**
Level 1	0.550	0.540	0.572	0.592	0.583	0.609	0.563
Level 2	0.605	0.567	0.602	0.579	0.577	0.57	0.587
Level 3		0.625	0.56	0.561	0.572	0.554	0.582
difference	0.055	0.085	0.044	0.031	0.010	0.055	0.024
Rank	**2**	**1**	**4**	**5**	**7**	**3**	**6**
Characteristic type	**Larger the best**						
Optimum	**A2**	**B3**	**C2**	**D1**	**E1**	**F1**	**G2**

Specific performance and variation of temperature, followed by pressure are the factors determining the cooling fin design. Therefore, the weighting values for specific performance, pressure drop and temperature variation are 0.35, 0.3 and 0.35, respectively. The optimal design parameters are (A2) forward flow, (B3) mass flow rate of 80 gs^{-1}, (C2) fin thickness 4 mm, (D1) fin length 12 mm, (E1) transverse spacing of fins 9 mm, (F1) longitudinal spacing of fins -3 mm and the number of zones in the cooling fin is 3 corresponding to Order 1 as shown in Table 9.28.

9.5.3.3 Analysis of Variance and F-Test

Analysis of Variance (ANOVA) was used to analyze the effect of each factor on the responses. In this analysis, 5% of error in the classification of the significance of the design parameters was taken into consideration. Hence α = 0.05, $v1 = 1$ for flow direction, $v2$-$v6 = 2$ for mass flow rate, fin thickness, fin length, transverse and longitudinal spacing of the fin and the number of zones. 22 degrees of freedom were used for error calculated in F-test. For design parameter flow direction $F_{0.05, 1, 24} = 4.3$ and for the rest of the factors $F_{0.05, 1, 24} = 3.44$. The results of the ANOVA analysis of the responses are illustrated in the following tables:

Table 9.30 Analysis of variance for the specific performance.

Source	Sq	DF	Mq	F-ratio	Rho, %
Flow direction	230611592.73	1	230611593	1.47	0.13
Mass flow rate	$1.29\,x10^{11}$	2	$6.46\,x10^{10}$	410.93	74.58
Fin thickness	1811974055	2	905987028	5.76	1.05
Fin length	21954492413	2	$1.10\,x10^{10}$	69.78	12.66
Transverse spacing	2912211156	2	$1.46\,x10^{9}$	9.26	1.68
Longitudinal spacing	13092097158	2	$6.55\,x10^{9}$	41.61	7.55
Error	609083648	2	304541824	1.94	0.35
St	3460662498.42	22	157302841	1.00	2.00
Mean	$1.73\,x10^{11}$	35	$4.95\,x10^{9}$	-	100.00
ST	$4.10\,x10^{12}$	1	-	-	-

Table 9.31 Analysis of variance for the pressure drop.

Source	Sq	DF	Mq	F-ratio	Rho, %
Flow direction	119.59	1.00	119.59	1.43	0.72
Mass flow rate	6874.90	2.00	3437.45	41.18	41.30
Fin thickness	1176.14	2.00	588.07	7.04	7.07
Fin length	2145.41	2.00	1072.70	12.85	12.89
Transverse spacing	847.02	2.00	423.51	5.07	5.09
Longitudinal spacing	3507.64	2.00	1753.82	21.01	21.07
Error	137.00	2.00	68.50	0.82	0.82
St	1836.64	22.00	83.48	1.00	11.03
Mean	16644.34	35.00	475.55	-	100.00
ST	45606.77	1.00	-	-	-

Table 9.32 Analysis of variance for the variation of temperature.

Source	Sq	DF	Mq	F-ratio	Rho, %
Flow direction	4.12	1.00	4.12	63.55	11.45
Mass flow rate	19.58	2.00	9.79	150.94	54.39
Fin thickness	1.46	2.00	0.73	11.22	4.04
Fin length	1.26	2.00	0.63	9.71	3.50
Transverse spacing	0.60	2.00	0.30	4.59	1.65
Longitudinal spacing	7.51	2.00	3.75	57.90	20.86
Error	0.05	2.00	0.02	0.36	0.13
St	1.43	22.00	0.06	1.00	3.96
Mean	35.99	35.00	1.03	-	100.00
ST	1312.56	1.00	-	-	-

The degree of influence of each design parameter was determined by percent contribution and F-test in the ANOVA analysis. As shown in Table 9.30, mass flow rate, fin length and longitudinal spacing of the fins are the primary factors influencing the specific performance of the cooling fins which contributed about 94.79%. Flow direction and the number of zones

do not affect the specific performance of the cooling fin. The pressure drop of the cooling fin is affected by mass flow rate (41.30%), longitudinal spacing (21.07%), fin length (12.89%), fin thickness (7.07%) and transverse spacing of the fins as shown in Table 9.31. On the other hand, contributions of flow direction of fluid and the number of zones in the pressure drop are insignificant. Lastly, mass flow rate (54.39%), longitudinal spacing (20.86%), and flow direction (11.45%) are the major factors affecting the temperature uniformity across the cooling fins as shown in Table 9.32. The effect of the number of zones can not be clearly shown in the ANOVA analysis, probably because the range of the mass flow rate selected is too wide and in the turbulence region.

9.5.3.4 Optimized design

The temperature contour and velocity streamline plot of the optimized cooling fins at a mass flow rate of 40 gs^{-1} are shown in Figure 9.10.
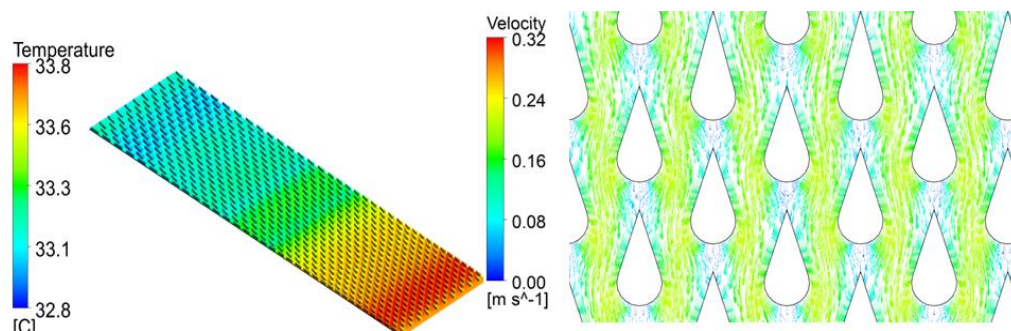
Figure 9.10 (a) Temperature distribution of the zonal distributed droplet fin.
(b) Velocity vector of the zonal distributed droplet fin.

Figure 9.10(a) shows the temperature distribution of the optimized cooling fin design. The temperature of the cooling fin is progressively increased to 33.8 ^{o}C along the flow path. The temperature difference across the cooling fin is about 1.0 ^{o}C. Therefore, excluding thermal resistance across the heated surface and cooling fins, there will not be a serious

293

temperature different across the upstream and downstream of the cooling fins. Figure 9.10(b) shows the flow field in the cooling fins. A similar flow trend is observed for the boundary between two zones of the large droplet fin and small droplet fin. A turbulence wake is also observed at the end of the round trailing edge of the droplet fin. The flow around the droplet is streamlined and no chaotic flow is observed. The maximum velocity is near the round trailing edge which is about 0.16 ms^{-1}.

9.5.3.5 Performance characterization

The results of the regression analysis for the average Nusselt number, average friction factor and temperature uniformity for the cooling fin are shown in Table 9.33 to Table 9.35, respectively. The regression equations are given in Equations 9-7 to 9-9.

Table 9.33 Regression statistics of the average Nusselt number.

Predictor	Coefficient	Standard Error	T	P	Lower 95%	Upper 95%
Constant	-1.829	0.166	-11.006	0.00161	-2.358	-1.300
Ln Re	0.695	0.0210	33.010	6.111e-5	0.628	0.762
S = 0.0267	R = 99.86%		R-Sq = 99.73%		R-Sq(adj) = 99.63%	

Table 9.34 Regression statistics of the average friction factor.

Predictor	Coefficient	Standard Error	T	P	Lower 95%	Upper 95%
Constant	0.271	0.114	2.369	0.0986	-0.0930	0.635
Ln Re	-0.152	0.0145	-10.483	0.00185	-0.198	-0.106
S = 0.0117	R = 99.46%		R-Sq = 98.93%		R-Sq(adj) = 98.58%	

Table 9.35 Regression statistics of the temperature variation.

Predictor	Coefficient	Standard Error	T	P	Lower 95%	Upper 95%
Constant	1.947	0.260	7.498	0.00492	1.121	2.773
Ln Re	-0.997	0.0329	-30.326	7.88e-5	-1.102	-0.892
S = 0.0418	R = 99.84%		R-Sq = 99.67%		R-Sq(adj) = 99.57%	

$$\overline{Nu} = 0.161 Re^{0.695} \tag{9-9}$$

$$\overline{f} = 1.311 Re^{-0.152} \tag{9-10}$$

$$\frac{\Delta T}{T_{in}} = 7.006 \, Re^{-0.997} \qquad (9\text{-}11)$$

The R-square for the average Nusselt number as shown in Table 9.33 is 99.7%, which indicates very good correlation between the average Nusselt number and Reynolds number. On the other hand, the R-square for the average friction factor as shown in Table 9.34 is 98.9%, which also indicates very good correlation between average friction factor and Reynolds number. The R-square for the variation of cooling fin temperature to the free stream temperature is 99.7% as shown in Table 9.35, which indicates a very good correlation with the variation of cooling fin temperature to the Reynolds number with a variation of ±0.3%.

9.5.3.6 Comparison of zonally distributed droplet fin and straight channel

Comparisons of the thermal resistance, variation of cooling fin temperature, average Nusselt number and fan power consumption for zonal distributed droplet fin and equal flow channel width of the straight channel cooling fin are shown in Figure 9.11.
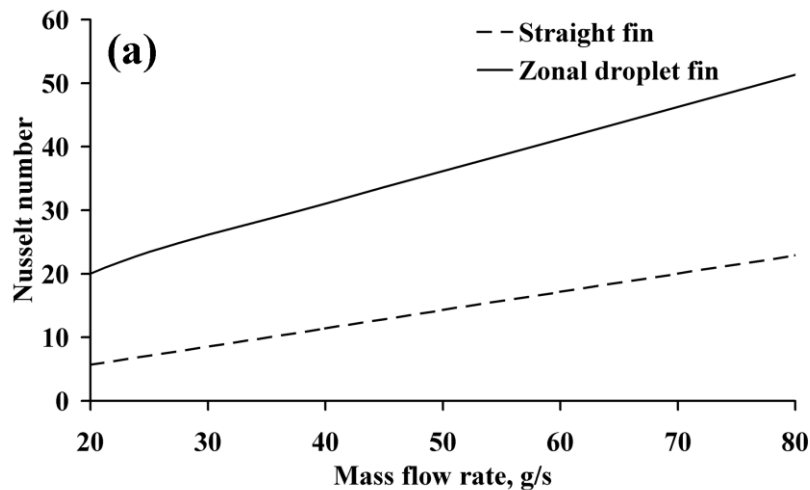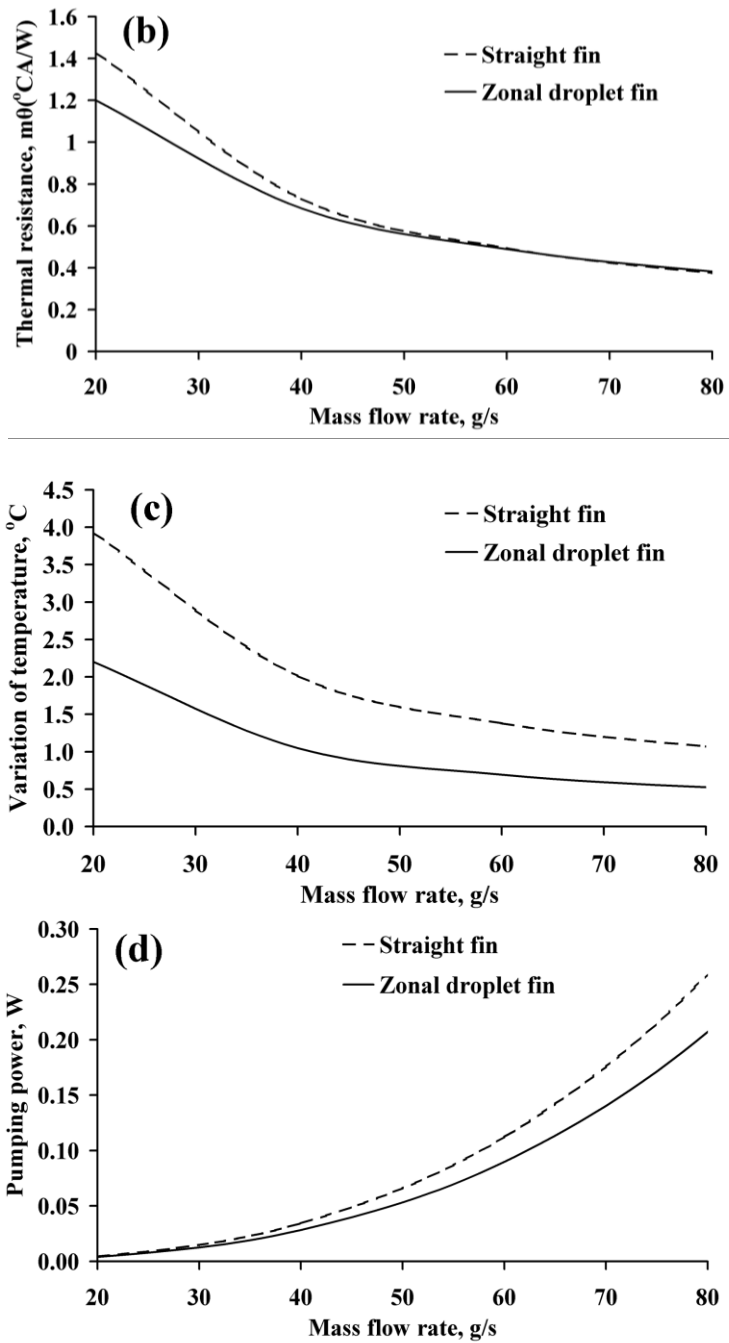
Figure 9.11 Comparison of uniformly distributed droplet fin and straight channel fin. (a) Nusselt number. (b) Thermal resistance. (c) Variation of temperature. (d) Pumping power.

The average Nusselt number of the zonal distributed droplet fin and straight channel fin progressively increases with the mass flow rate. Besides, the average Nusselt number of the straight channel is lower than the droplet fin. Compared to the straight fin, the Nusselt number for the zonal distributed

droplet fin at a mass flow rate of 20 gs^{-1} is about 270% higher than the straight channel fin. The thermal resistance of the droplet fin is about 40% lower than the straight channel fin. The variation of temperature is decreased with the mass flow rate of cooling water. Besides, the variation of temperature for the zonally-distributed droplet fin at 20 gs^{-1} is about 2.2 ^{o}C, while the variation of temperature for the straight channel fin is about 4 ^{o}C. At a low mass flow rate of cooling water flow (20 gs^{-1}), the pumping power consumption of the straight channel and the zonally-distributed droplet fin is same. At a higher mass flow rate (80 gs^{-1}), the pumping power consumption of the zonally-distributed droplet fin is 8% less than the straight channel fin. Hence, zonally-distributed droplet fin could offer higher cooling capacity and better temperature uniformity than straight channel fin with similar pumping power consumption.

9.6 Experimental procedures

The experimental test rig of the straight channel, uniformly-distributed droplet fin and zonally-distributed droplet fin are shown in Figure 9.12.
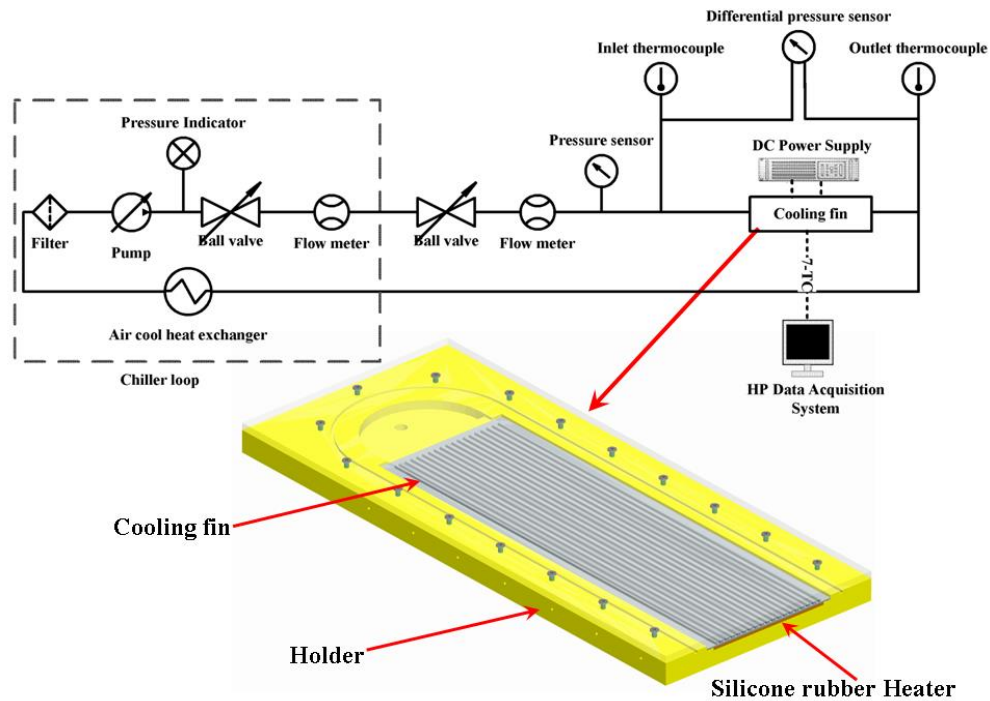
Figure 9.12 Experimental setup.

The water flow in the test rig was measured using vortex flow meter (Kobold, DVZ). The pressure drop over the cooling fins was measured using a differential pressure transducer (ABB, 266DSH). The cooling water was supplied by a chiller (Shelton, SAEAC-1), which allowed settings of water flow rate to a maximum of 13 $l$min^{-1} and water temperature of 5 $^{\circ}$C to 30 $^{\circ}$C. The heating of the cooling fin was simulated using silicone rubber heater. The power rating of the heater was set to approximately 350 W. The heater was attached to the bottom of the cooling fin. One layer of ultra thin thermal conductive pad (T-global technology, TG4040) with thickness of 0.5 mm and thermal conductivity of 4 Wm^{-1}K^{-1} to make sure there is no air gap present between the surfaces of the silicone rubber heater and the cooling fins. The thermal conductive pad will enhance the heat transfer from the silicone rubber heater to the aluminum cooling fins. The test setup of the cooling fins is shown in Figure 9.13.

Figure 9.13 Cooling fins in testing.

The temperature of the cooling fin and water inlet and outlet were measured using calibrated K-type thermocouples. The thermocouples were calibrated in a dry box calibrator (Isotech Fast-Cal, Low complete series) to within ±0.1 ^{o}C deviation before being used in the experiments. Two thermocouples were placed at the inlet and outlet of the chiller to measure the inflow and outflow of the water temperature from the test rig. HP 34970A data acquisition system was used to record the temperature readings. A summary of the measurement equipment and their accuracies are summarized in Table 9.36.

Table 9.36 Measurement equipments and their accuracies.

Measurement equipment	Accuracy
Flowmeter, %	± 2.5
Differential pressure transducer, %	±0.06
K-type thermocouple, ^{o}C	± 0.1

In order to determine the heat being transferred to the cooling water, the steady state heat gain q by water can be calculated using Equation 8-24. On the other hand, the amount of heat loss that was dissipated via other means such as natural convection, radiation and conduction through the holder of the cooling fins can be calculated using Equations 8-70 to 8-71. The input power Q_{in} was supplied via 1.5 kW programmable DC power supply (Amrel SPS60-25-V029). It was found the heat loss is less than 8% when the mass flow of cooling water more than 20 gs^{-1}.

The measurements were performed under steady state conditions for different flow rate of water. The steady state regime was verified by monitoring the temperature variation of the cooling fins. Once the steady state was reached, thermocouple readings were taken and the measurements were then averaged. All the tests were repeated three times and the average value was taken. Then, the experimental results were compared with numerical results under similar cooling condition. The testing of the cooling fins is carried out under the mass flow rate of water of 0.010-0.100 kgs^{-1} at 25 $^{\circ}$C.

In order to show the quality of the measurements, a thorough uncertainty analysis was performed according to the method suggested by Moffat (Moffat, 1988). The uncertainties in this study were determined by the root-sum-square method (Moffat, 1988). The errors estimated on the thermodynamic properties of water are tabulated in Table 9.37 (Huisseune et al., 2010).

Table 9.37 Uncertainties on the thermodynamic properties of water.

Properties	Uncertainty
Dynamic viscosity, μ (%)	1.0
Density, ρ (%)	0.001
Specific heat capacity, C_p (%)	0.1
Thermal conductivity, k (%)	1.8

9.7 Results and discussion

9.7.1 Straight channel and uniform distributed droplet fin

9.7.1.1 Uncertainties of calculations

The average relative uncertainties for most of the calculated variables for the droplet fin are in Table 9.38. The straight channel average relative uncertainty for average Nusselt number is 1.8% and 1.3% for average friction factor. On the other hand, the uniform distributed droplet fin average relative uncertainty for average Nusselt number and average friction factor is 1.8% and 1.4% respectively.

Table 9.38 Average uncertainties of the variables.

Properties	Average uncertainty, (%)	
	Straight channel	Uniform distributed droplet
Heat transfer rate of water, Q_{water} (W)	2.86	2.83
ΔT_{water} (^{o}C)	2.86	2.83
ΔT_{fin} (^{o}C)	2.47	3.36
Reynolds number based on velocity in the minimum cross section (Re_c)	1.00	1.00
Nusselt number, Nu	1.83	1.81
Friction factor, f	1.29	1.42

9.7.1.2 Experimental validation

The correlations for the Nusselt number, friction factor and variation of temperature given in Equations 9-3 to 9-5 for the optimized droplet fin were then verified with the experiments. The comparisons of the correlations for the straight channel and uniformly-distributed droplet fin are shown in Figure 9.14.

Figure 9.14 shows good qualitative and qualitative agreement between experimental data and numerical prediction. The averaged relative error for straight channel average Nusselt number, average friction factor and variation of temperature are 6.7%, 4.3% and 18.8% respectively. On the other hand, the averaged relative error for uniform distributed droplet fin average Nusselt number, friction factor and variation of temperature are 6.2%, 4.7% and 17.1%, respectively. Both experimental and numerical results for straight channel and uniform distributed droplet fin shows an increasing trend of average Nusselt number versus mass flow rates. Average Nusselt of uniform distributed droplet fin is about 242% higher than a straight channel at a mass flow rate of 20 gs^{-1}. On the other hand, experimental and numerical results show a decreasing trend of the average friction factor and variation of cooling fin temperature versus mass flow rates. As mentioned before, the relative error of prediction of the fin temperature uniformity (Figure 9.14(c)) is relatively

higher due to the small values involved; the temperature difference of the

correlation and experimental data is about 1 ^{o}C.
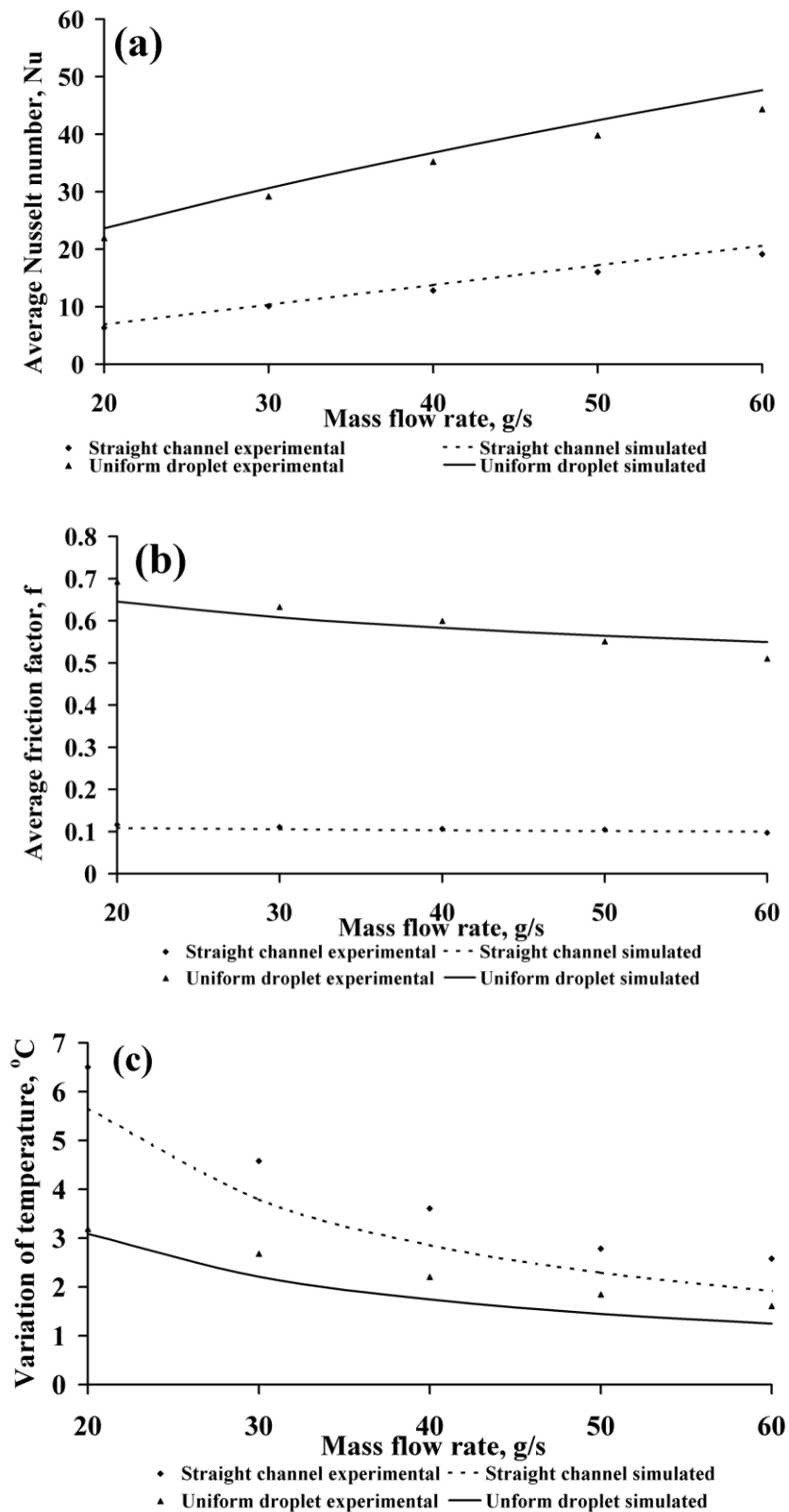
Figure 9.14 Comparison of the experimental data and correlation (a) Average
        Nusselt number. (b) Average friction factor. (d) Variation of
        temperature.

9.7.2 Straight channel and zonally-distributed droplet fin

9.7.2.1 Uncertainties of calculations

The average relative uncertainties for most of the calculated variables for the straight channel and the zonally-distributed droplet fin are shown in Table 9.39. The straight channel average relative uncertainty for average Nusselt number is 1.80% and 2.56% for average friction factor. On the other hand, the uniformly-distributed droplet fin average relative uncertainty for average Nusselt number and average friction factor is 1.81% and 2.46% respectively.

Table 9.39 Average uncertainties of the variables.

Properties	Average uncertainty, (%)	
	Straight channel	**Uniformly distributed droplet**
Heat transfer rate of water, Q_{water} (W)	2.85	2.78
ΔT_{water} (^{o}C)	1.86	1.81
ΔT_{fin} (^{o}C)	2.67	3.04
Reynolds number based on velocity in the minimum cross section (Re_c)	1.00	1.00
Nusselt number, Nu	1.80	1.80
Friction factor, f	2.56	2.46

9.7.2.2 Experimental validation

The correlations for the Nusselt number, friction factor and variation of temperature for the optimized zonally-distributed droplet fin given in Equations 9-9 to 9-11 are then verified with the experiments. The comparisons of the correlations are shown in Figure 9.15.
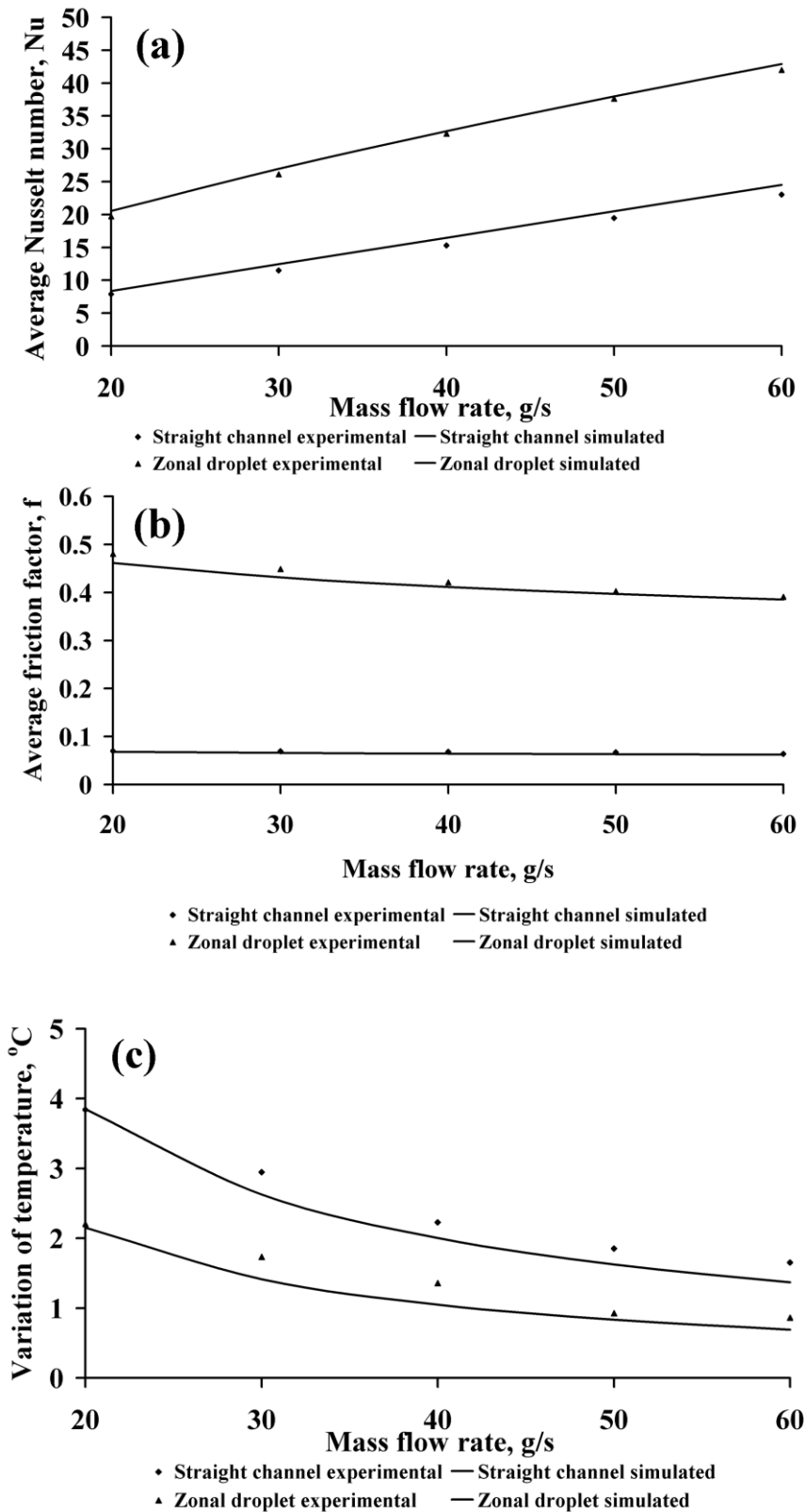
Figure 9.15 Comparison of the experimental data and correlation (a) Average Nusselt number. (b) Average friction factor. (c) Variation of temperature.

Figure 9.15 shows good qualitative and qualitative agreement between experimental data and numerical prediction. The averaged relative error for straight channel average Nusselt number, average friction factor and variation of temperature are 6.8%, 4.3% and 10.1% respectively. On the other hand, the averaged relative error for the average Nusselt number, friction factor and variation of temperature for the zonally-distributed droplet fin are 2.4%, 2.6% and 14.7%, respectively. Both experimental and numerical results for straight channel and zonally-distributed droplet fin show an increasing trend of average Nusselt number versus mass flow rates. Average Nusselt of the zonally-distributed droplet fin is about 145% higher than a straight channel at a mass flow rate of 20 gs^{-1}. On the other hand, experimental and numerical results show a decreasing trend of average friction factor and also variation of cooling fin temperature versus mass flow rates. As shown in Figure 9.15(c), the error of prediction of the variation of cooling fin temperature is higher than Nusselt number.

9.8 Summary

This chapter presents a numerical study of the liquid cold plate with a novel droplet fin design for EV battery thermal management. Two types of designs were investigated namely the uniformly-distributed droplet fin and the zonally-distributed droplet fin. The droplet fins have a sharp leading edge and a round trailing edge to streamline the incoming flow and create a turbulence wake at the trailing edge. Taguchi method was used to optimize the design of the cooling fins. All design parameters for the cooling fin such as direction of flow, mass flow rate, transverse spacing, longitudinal spacing, fin length, fin thickness and number of zones are determined to be significant factors

contributing to the evaluation of responses such as specific performance, pressure drop, variation temperature across the cooling fins. The most significant factors affecting the specific performance of the uniformly-distributed droplet fins are mass flow rate, fin length and longitudinal spacing. The pressure drop across the uniformly-distributed droplet fin is mainly affected by the mass flow rate. Temperature uniformity of the cooling fin is affected by the mass flow rate and longitudinal spacing of the fin. The optimum design parameters for the uniformly-distributed droplet fin are forward flow, mass flow rate 40 gs^{-1}, fin thickness 4 mm, fin length 12 mm, transverse spacing of the fins 9 mm and longitudinal spacing of the fins -3 mm. On the other hand, most significant factors affecting the specific performance of the zonally-distributed droplet fin are mass flow rate of water, fin length and longitudinal spacing of the fins. The pressure drop across the zonally-distributed droplet fin is mainly affected by mass flow rate, fin length and longitudinal spacing of the fins. Temperature uniformity of the cooling fin is affected by mass flow rate, longitudinal spacing of the fins and also flow direction. The optimum design parameters for the zonally-distributed droplet fins are forward flow, mass flow rate 40 gs^{-1}, fin thickness 4 mm, fin length 12 mm, transverse spacing of the fins 9 mm, longitudinal spacing of the fins -3 mm and number of zones 3. For long cold plates, zonally-distributed cooling fins have superior performance compared to uniformly-distributed cooling fins. The fan power consumption for both cooling fins is similar to that for the straight channel at low flow rates but offer higher cooling performance.

In this study, experiments were conducted to validate the correlations for straight channel, uniformly-distributed droplet fin and zonally-distributed

droplet fin. Experimental data and correlations demonstrate good agreement qualitatively and quantitatively. The experimental results for all the cooling fins showed an increasing trend of average Nusselt number with the mass flow rate of cooling water. On the other hand, average friction factor and average variation of temperature of cooling fin decrease with the increasing of mass flow rate of cooling water. The zonally-distributed cooling fin is effective in reducing the temperature variation of a long heated area. Besides, the cooling performance of the droplet fin is higher than that of a straight channel for the same pumping power used.

CHAPTER 10

INTEGRATION ISSUES OF EVs BATTERY PACK

10.1 Introduction

In this chapter, the integration issue of the Li-ion cell into the EVs battery pack will be discussed from various points of view. This encompasses types of Li-ion battery, packaging of Li-ion battery, electrical, battery management system, assembly, thermal management, service and maintenance and testing. Besides, the converted EV using $LiFePO_4$ as an energy storage system will be used in a benchmarking study to provide a baseline for cell selection and integration of cells for the EVs battery pack.

10.2 Terminology of cell, module and battery pack

Battery pack in the EVs can be divided into three levels, the cell, module and pack. There are several issues associated with the integration of the Li-ion cells into the battery module and the battery pack of the EVs such as type of cell chemistries, electrical connection, battery management system, thermal management, packaging, cost, assembly, geometry of cells, services, and maintenance and safety as shown in Figure 10.1. These issues are critical for generating a comfortable and safe environment to bring out the best of each individual cell to give an optimum performance for a battery pack.
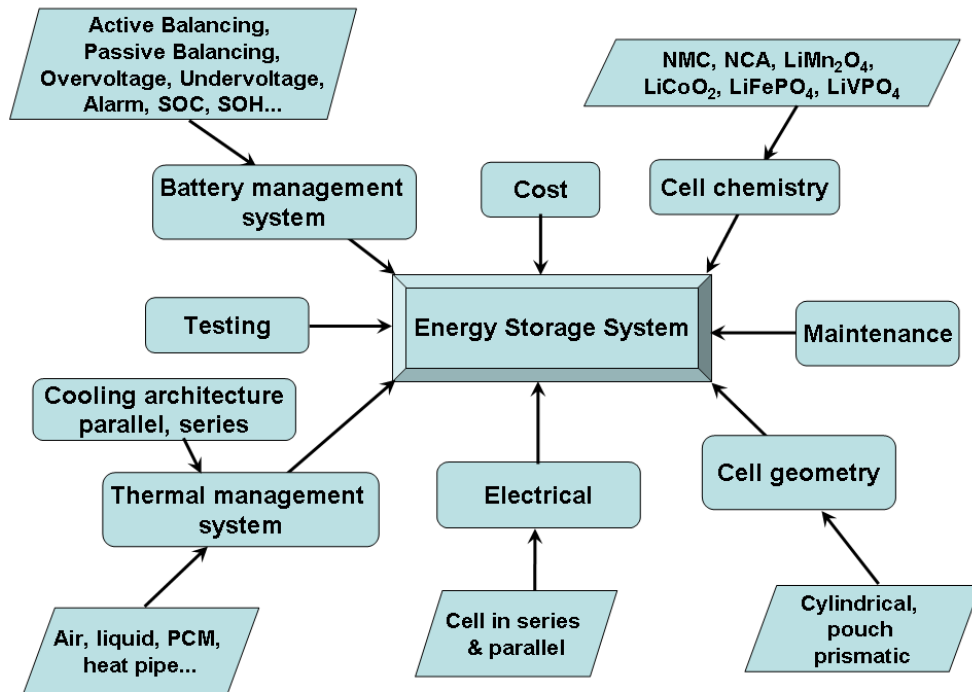
Figure 10.1 Integration issues of the Li-ion cell into EVs battery pack.

The cell consists of a single electrochemical unit with the lowest voltage of its chemistry (Pesaran et al., 2009). The unit cells are connected in series, parallel or mixed configurations to form a module to provide the necessary power for the traction motor and auxiliary systems. The number of cells can be connected in a module is normally limited by the monitoring capability of the module level battery management system. Each battery module has its own monitoring, electrical and thermal control and the components are closely packed. Next, the battery modules are connected in series, parallel or hybrid again to yield a battery pack. The battery pack is housed in a plastic or metal container with the battery pack management system and a thermal management system to interface with the traction and auxiliary power system of the EVs (Pesaran et al., 2009).

10.3 Few large cells versus many small cells

In this section, integration issues of various packaging of LFP cells will be explored, ranging from cylindrical, prismatic and pouch cell. Technical specifications of the cells used throughout this study are tabulated in Table 10.1. The benchmarking process is based on various packaging configurations of LFP cell into the converted EV using a Hyundai Trajet 2.0. Specifications of the converted EV are tabulated in Table 10.2.

Table 10.1 Details of LFP cells used in this study.

Parameters	Cell					
	18650	26650	38120	Prismatic	Pouch	Large Prismatic
Nominal Voltage, V	3.2	3.2	3.2	3.2	3.2	3.2
Nominal capacity, Ah	1.3	2.5	8.0	10.0	10.0	120.0
Cathode material	$LiFePO_4$	$LiFePO_4$	$LiFePO_4$	$LiFePO_4$	$LiFePO_4$	$LiFePO_4$
Anode material	Graphite	Graphite	Graphite	Graphite	Graphite	Graphite
Terminal connector	Spot welding	Spot welding	Screw	Screw	Screw	Screw
Diameter, m	0.018	0.026	0.038	-	-	-
Height, m	0.065	0.065	0.0146	0.140	0.261	0.287
Width, m	-	-	-	0.065	0.145	0.153
Thickness, m	-	-	-	0.018	0.0067	0.047
Weight, kg	0.030	0.082	0.355	0.285	0.261	4.2
Specific heat, $Jkg^{-1}K^{-1}$	900	900	998	1200	1200	1000
R, mΩ	0.20	0.20	0.30	0.30	0.40	0.30

Table 10.2 Specifications of converted EV.

Parameter	Value
Vehicle mass, kg	1828
Frontal area, m^2	3.238
Coefficient of drag, Cd	0.35
Rolling resistance,	0.011
Electric motor	47.8 kW, 314 Nm Max
Accessory electrical load	1000 W
Battery pack	19.5 kWh
Surrounding temperature, ^{o}C	30

There are two different types of topology for the battery pack with different type of cell packaging, which is known as the high voltage battery pack and low voltage battery pack. There are 120 cells connected in series for small cell (18650, 26650, 38120, prismatic and pouch cell) to yield a high voltage battery pack. On the other hand, 25 large prismatic cells are connected in series to form a low voltage battery pack and the power of the battery pack remains the same as the high voltage battery pack. For subjective criterion, a relative score of "-", "0" and "+" is used to represent the rating of the worst, fair and excellent. The discussion is evolved from various points of view, such as packing, assembly, electrical and control, thermal management, services and maintenances. New European driving cycle (NEDC) was used as a reference to assess the thermal performance of the battery pack.

10.3.1 Packing

Fabrication technology for small cell is more mature and reliable than large cell and the price is also cheaper due to mass production to fulfill the market requirement. On the other hand, fabrication of large cell is more difficult and is usually made to order as it is a product in a niche market. Therefore, the price also varies in a wide range. Table 10.3 displays the comparison of different cell packing for the battery pack. Several arguments have been prompted in determining the appropriate cell packaging used for the

battery pack. The paramount issue is space utilization. In reality the space available in the converted EV may not even be a regular shape or rectangular shape which is different for EVs that designed from scratch e.g. BMW i3, Tesla roadster, MiEV, etc. Large cell and small cell could make a significant difference when a battery needs to be retrofitted in a space carved out in an existing vehicle (Liionbms, 2014). Smaller cell can be packed in large quantity in the available space to improve the energy density, but this is not applicable for large cell. For example, the packing density of 18650 cell battery pack is 114 times higher than large prismatic cell, while the physical density of 18650 cell battery pack is only 1.5 times higher than large prismatic cell.

Table 10.3 Comparison of the battery pack formed by different type of cells.

Parameter	Type of cell					
	18650	26650	38120	Small Prismatic	Pouch	Big prismatic
Packing						
Number of cell	4800	2400	720	600	600	50
Weight, kg	192.0	196.8	255.6	171.0	172.5	210
Volume, m^3 (closed pack)	0.101	0.105	0.152	0.131	0.296	0.120
Packing density, cell/m^3	47524.75	22857.14	4736.842	4580.153	2027.027	416.667
Weight of interconnection, kg	1.217	0.621	12.11	10.24	10.75	1.164
Weight of cell holder, kg	81.6	40.8	12.24	10.2	42.22	1.0
Physical density of battery pack, kgm^{-3}	2720.96	2268.771	1841.776	1461.374	761.723	1768.033
Cell cost, USD	$\approx 3 - 11$	$\approx 7 - 18$	≈ 20	$\approx 20 - 40$	$\approx 20 - 40$	$\approx 150 - 400$
Assembly of single cell						
α, β orientation of cell (Boothroyd et al., 2011)	360°, 0°	360°, 0°	360°, 0°	360°, 360°	360°, 360°	360°, 360°
Cell handling + Insertion time, s (Boothroyd et al., 2011)	3.5	3.5	3.5	3.95	3.95	5.0
α, β orientation of interconnection (Boothroyd et al., 2011)	180°, 180°	180°, 180°	180°, 180°	180°, 180°	180°, 180°	180°, 180°
Interconnection handling + Insertion time per cell, s (Boothroyd et al., 2011)	15.72	15.72	15.72	7.72	15.72	7.72
α, β orientation of cell holder (Boothroyd et al., 2011)	360°, 360°	360°, 360°	360°, 360°	360°, 360°	360°, 360°	360°, 360°
Cell holder handling + Insertion time, s (Boothroyd et al., 2011)	7.4	7.4	7.4	7.4	9.4	7.4
Interconnection assembly time (two terminals), s (Boothroyd et al., 2011)	37	37	46.36	29.72	60.74	29.72

Assembly cost per cell (assumed 5 USD per hour)	0.0884	0.0884	0.101	0.0678	0.125	0.0692
Electrical and control						
Terminal contact resistance, mΩ	0.4	0.4	0.6	0.6	0.8	0.6
Complexity of wiring ranking	-	-	-	-	-	+
Cell monitoring	-	-	-	-	-	+
Reliability	+	+	+	+	+	-
Battery management system cost	-	-	-	-	-	+
Thermal management						
Heat Generated from contact resistance, kJ/cycle (Based on NEDC)	2.034	3.935	19.607	23.6747	34.090	284.097
Heat Generated from the battery pack, kJ/cycle (Based on NEDC)	219.906	215.670	193.04	215.440	218.991	214.304
Power consumption for cooling fan	1	0.967	1.380	1.837	0.604	6.763
Complexity of cooling system design	-	-	-	+	+	+
Services and Maintenance						
Identification of faulty cell	-	-	-	-	-	+
Ease of cell replacement and services	-	-	-	+	+	+
Uninterrupted operation if one unit cell fail	+	+	+	+	+	-

In general, cylindrical cell possess the highest packing density as compared to prismatic and pouch cell as shown in Table 10.3. Packing density of 18650 cell battery pack is about 47524.75 cell/m^3, followed by 26650 cell battery pack with packing density of 22857.14 cell/m^3 and large prismatic cell battery pack have the lowest packing density of 416.6667 cell/m^3. Although small prismatic cell and pouch cell have equal capacity, the packing density of small prismatic cell is 2 times higher than that of the pouch cell. This is due to the structure of the pouch cell with a large base surface area and thin thickness. The battery pack does not only comprise the batteries, but also the battery holders and interconnections are essential components of the battery pack. Interconnections are made of nickel strip or copper bus bar. The addition of interconnections and battery holder, the physical density of 18650 cell battery pack is 2720.96 kgm^{-3} and it is the highest in this study. On the other hand, the physical density of pouch cell is the lowest and it is about 3.5 times less than the 18650 cell battery pack. This is due to "soft" packaging of pouch cell as oppose to cylindrical and prismatic cell that used "hard" packaging and add to the weight of the battery pack. Typical example of a battery holder for various packaging of the cell is illustrated in Figure 10.2.

Figure 10.2 Various type of battery holder for cylindrical and pouch cell.

10.3.2 Assembly

Most of the EVs battery pack is manually assembled. Therefore, Boothroyd and Dewhurst DFA method for manual assembly can be used to estimate the assembly efficiency of the battery pack built by different types of cell packaging (Boothroyd et al., 2011). In manual assembly analysis, it is split into two distinct types of analysis which are known as manual handling and insertion analysis respectively (Boothroyd et al., 2011). α rotation refers to the alignment of the axis of the part corresponded to the axis of insertion. On the other hand, rotation of the part about its axis of rotation is called β rotation (Boothroyd et al., 2011). In this section, cell size, orientation of the cell, ease of handling and ease of insertion of the cell, interconnections and battery holder are examined to determine the handling and insertion time. The labor cost of the assembly is assumed to be 5 USD per hour. The total assembly cost of the battery pack could be calculated by multiplying the numbers of cell, battery holder and interconnections used. Prismatic cells with protruding male thread terminals exhibit a "Poka Yuke" feature that simplifies the assembly process of interconnections thus only spring washers and nuts are needed. 18650 and 26650 cells have bare surface and spot welding of nickel strip is used to electrically connection the cells. On the other hand, female threaded terminals are commonly used to assemble large cylindrical cell. However, for the cylindrical and pouch cell with the terminals at opposite ends, extra orientation of the cell is needed for the assembly process of interconnections.

Assembly cost of 1 unit of the prismatic cell and one unit of the pouch cell is USD 0.0692 and USD 0.125 respectively. Therefore, assembly of one unit prismatic cell battery pack is far more economical than assembly other

types of cell battery pack. Pouch cell with bare terminals required different assembly method. Holes need to be punched on the metal terminals to bridge the cell terminal to the bus bar using a screw and nut. Assembly cost for one unit of pouch cell using mechanical fastener required USD 0.125. Furthermore, pouch cell with soft packaging needs special attention during the assembly process. Compared to rigid casing of the cylindrical cell, careless handling of the soft packaging pouch cell will cause the development of local stresses. Therefore, extra structure is needed to protect the cell, reduce shock and vibration and exert compressive force on the cell to decrease delamination of the composite layer of active materials. Hence, any additional components and assembly process are involved in the pouch cell will incur extra manufacturing and assembly cost.

The assembly cost of the battery pack is directly proportional to the number of cells, interconnections, battery holders, BMSs and thermal management systems used in the battery pack. Assembly of one unit 18650 cell battery pack by excluding BMS will cost USD 424.32 and 85 hours of workmanship are required. On the other hand, assembly of 1 unit of large prismatic cell battery pack excluding BMS will cost only USD 3.46 and the process took less than 1 hour. As such, in the assembly point of view, large format cell will have significant advantages in the assembly process and the total production time can be shortened effectively to produce a more economical battery pack.

10.3.3 Electrical and control

Cells are connected in series to achieve the desired voltage and connected in parallel to increase the capacity of the battery pack. In reality, despite tight

control in cell fabrication process, variation in the capacity and resistance still exists. Hence, some cells will have a higher capacity and resistance while the others will have a lower capacity and resistance. Having more cells connected in parallel, to increase reliability of the battery pack and minimize the effects of low quality cells. Furthermore, the effect of the bad cell limiting the performance of that string, incapacitating the battery pack and causing the BMS shut down could be reduced (Andrea, 2010). For an example, two different types of battery pack (the 18650 cell and the large prismatic cell) with a 1% loss of the capacity over a month. Statistics show that, after 10 months, large prismatic cell battery pack will lose about 50% of its capacity while 18650 cell battery pack will lose only 20% of its capacity. The users of the large prismatic cell battery pack will certainly notice the degradation in the EV performance as compared to users of the 18650 cell battery pack.

An increase in the number of cells also means the number of the interconnections is also proportionally increased. Thus, this will increase the wiring complexity, copper loss, high probability of interconnection failure and cause difficulties in cell monitoring and faulty cell detection. Nevertheless, external contact resistance on the cell terminals should not be overlooked. An increase in the number of interconnection will also lead to more energy being wasted to overcome the external contact resistance between the terminals and the total usable energy of the battery pack is also reduced.

On the other hand, having fewer numbers of large cell will result in a lower BMS cost. For example, 18660, 26650, 38120, pouch cell and prismatic cell will have 120 cells connected in series and the BMS must monitor 384 V

while for large prismatic cell the BMS only need to monitor 80 V. Hence, less protection and monitoring circuit are required.

There are two techniques used for cell balancing namely dissipative (passive) balancing and non-dissipative (active) balancing. Passive balancing is also called bleeding cell balancer (Schalkwijk and Scrosati, 2002; Andrea, 2010). Bank of resistors are used to bleed the energy from good cells to match the voltage of the bad cells and thus heat is generated. This method is not energy efficient as most of the cells are good cells (Schalkwijk and Scrosati, 2002; Andrea, 2010). Active balancing is also called distribution cell balancers. A distribution cell balancer transfer energy from good cell to bad cell. This method can be realized by using capacitor or inductor (Schalkwijk and Scrosati, 2002; Andrea, 2010). The disadvantage of the capacitive balancing method is the highest efficiency is only 50% and the number of cells in series bank is limited to twelve (Battery management system, 2014). Moreover, substantial variation of cell voltage is needed and some of the Li-ion battery like LiFePO$_4$ system with a plateau of 3.25 V over SOC 10%-90% may present difficulties for capacitive active balancing. On the other hand, inductive cell balancers are faster and have higher efficiencies than capacitive cell balancers. Fly-back transformers are commonly used in this method. The transformer-based cell balancers are divided into bottom cell balancing and top cell balancing. In bottom cell balancing, a battery cell receives energy from the entire battery pack. In top balancing, the entire battery pack is receiving energy from a single cell. Comparison of different balancing method is shown in **Table 10.4** (Liionbms, 2014; Andrea 2010).

Table 10.4 Comparison of different balancing method.

Parameter	Dissipative	Non-dissipative
Method	Energy is removed	Energy is transferred
Thermal management	Needed	Not needed
Cost	Low	High
Power wasted in standby mode	No	Yes
Suitability for cell	Small capacity Slow charging Slow self discharge	Large capacity Fast charging High self discharge
Typical EV application Capacity 100Ah Delta leakage 4mA 100 cells in series 8 hours charge 4 hours balancing		
Balancing current, A	0.1	3
BMS cost per cell, $	1	10
On/off duty cycle during balancing, %	24	0.8
Conversion efficiency, %	n. a.	70
Standby heat power, W	n. a.	5
Conversion heat generated, W	n. a.	0.24
Total heat generated, W	0.8	2.74
Total cost, W	100	1000

10.3.4 Thermal management system

NEDC is used as a reference to assess the thermal performance of the battery packs. High current flow through the connectors will create additional losses due to the external contact resistances at the cell terminals. In 18650 cell battery pack, the current requirements are divided into many parallel banks and hence the contact resistance loss is reduced to minimum. Since the current flow in the large prismatic cell battery pack is high, the contact resistance loss is about 140 times higher than 18650 cell battery pack.

As the size of the cell grows bigger, rate of cooling from the cell is always a challenging task. Temperature gradient across the layered active material become large and accelerates the thermal aging of the cell. One of the possible solutions is using many small cells to distribute the heat generated. For example, in one cycle of NEDC, an average of 215 kJ of heat is generated. In

the 18650 cell battery pack the heat is shared equally among the 4800 cells. While in large prismatic cell, the heat is only shared with 50 cells and the thermal problem is more severe for large cell. Power consumption for cooling fan is calculated using Equation 10-1 (Pesaran 2002; Incropera et al., 2007) and the 18650 cell battery pack is used as a reference for comparison.

$$h_{forced} = 30\left(\frac{\dot{m}/\rho_{air}A}{5}\right)^{0.8} \tag{10-1}$$

In current study, axial cooling architecture is adopted to benchmark the cooling efficiency of battery packs. For a given mass flow rate of cooling air, prismatic cell has a higher cooling efficiency than other types of cell. Although the cooling efficiency of the larger prismatic cell is high, the large thermal resistance across the thickness of the cell prevents the heat generated from the cell being efficiently dissipated to the outer environment. The large base surface area of the pouch cell has a lower cooling efficiency, but the thickness of the pouch cell is only 6.7 mm which could help dissipate the heat generated faster and the internal temperature of the cell is more uniformly distributed. Therefore, this type of structure promotes better temperature uniformity and less prone to thermal aging.

Having a large number of small cells significantly increases the complexity and cost of a thermal management system, especially for cylindrical cell. The cylindrical geometry, the electrical live of the battery casing and the heat shrink wrapping of a cylindrical cell are not favorable for thermal management and prevent heat sink and cooling fins from being effectively attached to the surface of the cell to remove the heat generated.

Hence, from the thermal perspective, a cell with larger surface area to volume ratio is desired.

10.3.5 Services and maintenance

From services and maintenance point of view, having a large number of cells make the troubleshooting and maintenance of the battery pack tedious. For the 18650 and 26650 cell battery packs that use permanent spot welding to reduce the probability of loose contact, replacing a single faulty cell become unlikely. As such, they are more suitable for "use and throw" products. Hence, a small cell battery pack is arranged in such a way that cells in parallel are packed as a module and the module that contains a single faulty cell is replaced in its entirely. This type of battery pack does not encourage recycling or repair and is normally built with extra capacity. On the other hand, for the cell that using flexible terminal connection is preferable in the services and maintenance point of view and replacing a single cell is still possible. Besides, servicing and replacing faulty cell in the large prismatic cell battery pack is easier than in the small cell battery pack and the process can be completed within a second. However, degradation in the capacity for 1 or 2 cells in the large prismatic cell battery pack will cause an interruption in the operation of EVs.

Lastly, the distribution of EVs traction battery pack cost is illustrated in Figure 10.3 (Andrea, 2012). A large portion of the battery pack cost is due to the cells, followed by the assembly process and warranty. BMS cost is only less than 10% of the battery pack and also the labor cost for assembly of the battery pack. Besides, profit and warranty cost of the battery pack is about 10% and it is not a profitable business.
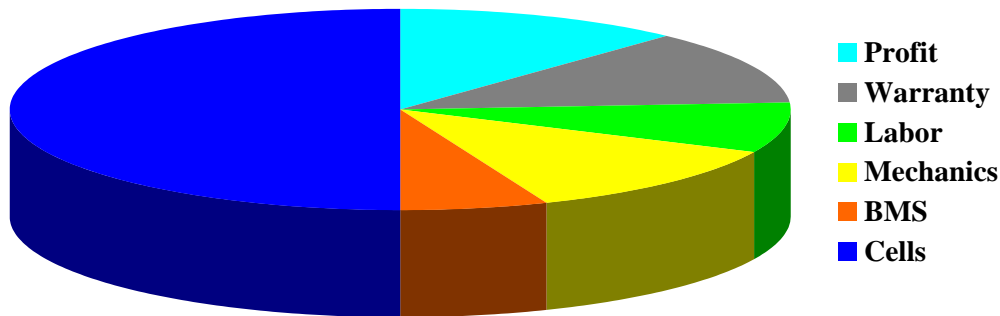
Figure 10.3 Traction battery pack cost.

10.4 Summary

Integration of a Li-ion cell into a battery pack is a critical factor which determines the performance, cost, reliability and safety of the EVs. Cost, packaging, electrical and control, assembly, thermal management and services and maintenance are the issues, which need to be addressed in the integration process. Having a large number of smaller cells allow the heat generated from the driving to be distributed evenly to all the cells and the battery pack is less affected by capacity fading. However, the large number of interconnections, long hours of the assembly process, and the increase in the chance of failure and difficulty in troubleshooting are the issues associated with a large number of small cells. On the other hand, while a smaller number of large cells will perform better in terms of assembly efficiency, ease of cell monitoring and servicing, they will perform poorly in terms of thermal management, thermal aging, low reliability, low flexibility in cell arrangement and capacity fading. A low voltage battery pack and a high voltage battery pack have its own advantages and disadvantages. A high voltage battery pack allows thin interconnections to be used, but a lot of high voltage switch devices and relays are needed to power on and off the high voltage circuit and additional cost is involved. On the other hand, a low voltage battery pack required thick interconnections to accommodate the high current flow from the large number

of cells in parallel banks. Besides, it also involves high current electronic devices such as high ampere current sensor and no control in the parallel bank which may lead to thermal runaway. Besides, extensive heat generated through the external contact resistance and high copper loss is another concern not to be overlooked for the low voltage battery pack. Active balancing and redistribution technique to reshuffle the energy used in the battery pack promotes energy efficient and more favorable from the thermal management point of view. However, the cost of the components involved is an obstacle to apply on the commercial EVs as compared with passive balancing. In order to enlarge the EVs market share, improving the internal structure of the cell to increase the rate of cooling, develop a high voltage cell to reduce the number of cells needed and developing larger capacity cells are the challenges nowadays.

CHAPTER 11

CONCLUSIONS AND FUTURE WORK

11.1 Conclusions

The main objectives of this work are to study the thermal issues related to batteries for electric vehicles (EVs) and to develop a few optimized thermal management systems for EV battery packs. The following are the main achievements and findings of this work:

1. The chemical, electrical and thermal behavior of Li-ion batteries during charging and discharging process were investigated by using a detailed finite element coupled electrochemical-thermal model. Good agreement between the numerical simulations and experimental results of the cell voltage and temperature were obtained under various operating conditions. There are three main heat generation sources in the cell which are reaction heat, ohmic heat and reversible heat. In the finite element electrochemical-thermal modeling a result, the reaction heat was found to be the major heat source during the constant current charging and discharging processes. The heat generation rate of the cell was positively correlated with the I_t-rates. Due to the intercalation reaction, the lithium ion concentration at the positive electrode is higher than that at the negative electrode during the charging process. On the other hand, while the lithium ion distribution is reversed during the discharging process and mainly determined by the de-intercalation of lithium ion in the negative electrode, the distribution of the lithium ion in the electrolyte is more uniform at low I_t-rates. This further indicates that charging cell at low I_t-rates can achieve a higher capacity

as compared to charging at high I_t-rate. In addition, it was found that imperfect contact between the connector and cell terminal will cause the development of large temperature gradients within the cell, further affecting the cell capacity. This is a significant factor should be taken into consideration in the design of cell, connectors and battery assembly. Thus, a rigid contact between the connector and cell terminal are needed to reduce the power losses and improve the non-uniformity of temperature within the battery pack.

2. Although coupled electrochemical-thermal finite element models can predict the aging and thermal behavior of the a Li-ion battery, coupled time variant spatial partial differential equations make them complex and their solution demands extensive computational resources. Hence, empirical models which represent the I-V characteristics of the battery were developed to investigate the electrical and thermal behavior of cylindrical LFP cells. The battery model gave good agreement with the experimental results. The skin temperature of the cell and the total heat generated from the cell increases with increasing I_t-rates and cell diameter. Heat exchange surface area per unit volume of the cell is a critical factor which determines the temperature developed within the cell. As the ratio of surface area to volume is reduced, the heat transfer ability goes down and the internal cell temperature escalates. The maximum temperature region inside the cell is located in the circular region of active material near the hollow core. Due to the large thermal resistance and insulation effect of the separator, the temperature difference within the cell in the radial direction is significant and it

increases with the diameter of the cell. This contributes to the slow rise of the skin temperature of large cells. Smaller cell sizes have better temperature uniformity within the cell. As the skin temperature of large cells rise slowly, monitoring the skin temperature of the cell is not sufficient as a safety precaution. The validated battery model was used to investigate the evolution of the battery pack temperature of a converted EV with different cooling air flow rate under UDDS, HWFET and US06 driving cycles. It was found that the heat generated from the battery module is the highest for the more aggressive US06 driving cycle and lowest for the UDDS driving cycle. In the less aggressive driving conditions for the UDDS and HWFET cycles, natural convection is sufficient to maintain the cell temperature at the optimum range of operating temperature. On the other hand, the more aggressive US06 cycle requires forced convection cooling. Hence, a well-designed thermal management system is needed for the EV battery pack especially under aggressive driving conditions to ensure safe and reliable operation of the battery pack. However, there are several limitations of the empirical battery model such as the internal resistance of the cell is not dependent on the temperature and rate of charging and discharging,

3. Although empirical battery model can give a good prediction of the electrical and thermal behavior of the Li-ion battery, there are some disadvantages associated with the empirical battery model. In empirical battery model, it is assumed that the internal resistance of the cell is constant throughout the charging and discharging cycle and does

not change with the I_t-rate. Besides, the temperature effect on the battery model behavior is neglected and the model parameters for discharging and charging are identical. Hence, Resistance Capacitance models were developed to investigate the electrical and thermal behavior of LFP pouch cell by taking the effect of temperature on the electrical characteristic into consideration. The equivalent circuit models gave good agreement with the experimental results of voltage and temperature over a wide range of temperature and SOC of the pouch cell. The LFP cell shows a more noticeable hysteresis effect as compared to Cobalt, Manganese and Nickel cathode systems. The hysteresis effect can be minimized by prolonging the resting duration before the OCV of the cell is measured. The heat generated from the cell is positively correlated with the I_t-rates. The validated battery model was used to investigate the thermal behavior of the EV battery pack under the UDDS and US06 tests. At the end of the US06 cycle, the average surface temperature of the cell could reach 52.3 ^{o}C. Hence, a well designed active thermal management system is desired for the EV battery pack to prolong the cycle life of the cell and ensure the safety and reliable operation of the battery pack.

4. At a high I_t-rate of charging and discharging, the conventional polymer insulation over the cell may create a substantial temperature rise inside the cell and this is not favored for thermal management and cycle life of the cell. It was found that a thin layer of Boron Nitride coating can be applied to the battery casing to improve the cooling of the cell. In addition, battery surface coated with Boron nitride also enables the

cold plate or cooling fins to be attached directly to the battery casing for effective cooling.

5. CFD simulations were utilized to analyze the flow field and thermal response of an air-cooled battery pack comprising 38120 cylindrical cells where the air flow was along the axial direction. Through the simulations, it was found that 30 gs^{-1} of cooling air was required to maintain the average cell temperature below 40 $^{\circ}$C and the variation of cell temperature within the battery pack was less than 3 $^{\circ}$C. Correlations of Nusselt number to Reynolds number were developed based on the steady state numerical simulations. In general, the correlations developed in this work show trends which are similar to most of the correlations in the open literature. The correlations developed were also validated with a series of experiments and showed good agreement both qualitatively and quantitatively. The correlations could be used to predict the thermal behavior of the cells in a battery pack using axial air cooling without having to go through detailed transient CFD simulations which will require extensive computational resources as well as time.

6. Cooling fins can be attached to the batteries to increase the heat transfer and maintain temperature uniformity within the battery module. Two types of cooling fins, namely plate fins and helical fins were investigated for use with air cooling. The batteries in the module were arranged in a trapezoidal configuration in order to improve the temperature uniformity downstream and upstream. The Taguchi method was used to optimize the design of the cooling fins. The most

important parameters affecting the heat transfer are mass flow rate of cooling air, number of fins and fin thickness. The pressure drop across the cooling fins was mainly affected by mass flow rate. The optimum design parameters for the plate-finned battery pack are mass flow rate 30 gs⁻¹, 9 fins per module, 0.2 mm fin thickness and made of aluminum. On the other hand, the optimum design parameters for the helical-finned battery pack are mass flow rate 30 gs⁻¹, 5 turns of the helical fin, 0.2 mm fin thickness and made of aluminum. However, the performance of the helical-finned pack is poorer than that of the plate-finned pack- the fan power consumption is higher and the cell temperature uniformity and cooling capacity are lower. The optimum conditions determined by the Taguchi method based on the simulation results were close to those obtained from wind tunnel tests. Parametric studies were carried out to develop the correlations for the Nusselt number, friction factor and variation of temperature across the cooling fins with the Reynolds number, fin pitch, hydraulic diameter, thickness of the fin, the diameter of the tube and the transverse distance of the cells.

7. Cooling with liquids can offer higher heat transfer coefficients and greater temperature uniformity among the cells compared to air cooling. Two different types of liquid cold plate designs were investigated, namely the uniformly-distributed droplet fins and the zonally-distributed droplet fins. The droplet fin has a sharp leading edge and a round trailing edge to streamline the incoming flow and create a turbulence wake at the trailing edge. It was found that

compared to conventional straight fin channels with a similar channel width and dimensions, the two above-mentioned designs enhanced the heat transfer performance multiple times and alleviate the non uniform temperature distribution observed at the downstream section of the conventional straight channel without the need for an increase in pumping power. The Taguchi method was used to optimize the design of the cooling fins. The most significant factors affecting the rate of heat transfer from the cooling fins are mass flow rate, fin length and longitudinal fin spacing. The pressure drop across the cooling fins is mainly affected by the mass flow rate, fin length and longitudinal fin spacing. The optimum design parameters for the uniformly-distributed droplet fin are mass flow rate 40 gs^{-1}, fin thickness 4 mm, fin length 12 mm, transverse fin spacing 9mm and longitudinal fin spacing -3 mm. On the other hand, the optimum design parameters for the zonally-distributed droplet fins are mass flow rate 40 gs^{-1}, fin thickness 4 mm, fin length 12 mm, transverse fin spacing 9 mm, longitudinal fin spacing -3 mm and number of zones 3. Zonally-distributed cooling fin have more superior performance in longer cooling path compared to the uniformly-distributed cooling fins. The fan power consumption for both cooling fins are similar to that for the straight channel at low flow rates but offer higher cooling performance. The optimum parameters determined by the Taguchi method based on numerical simulations are similar to those obtained from experiments. Parametric studies were carried out to develop the correlations of the Nusselt number, friction factor and temperature uniformity across the cold plate with the

Reynolds number, perimeter of the fin profile, height of the fin, transverse fin spacing and longitudinal fin spacing.

8. Using air as a heat transfer medium is the simplest approach, but it is not as effective as heat transfer using a liquid. The advantages of air cooling system are simple and compact design of the battery pack. The disadvantages are maximum flow rate of cooling air is limited to 100 m^3h^{-1}-250 m^3h^{-1}, low cooling performance and potential safety concern due to emission of toxic gaseous from the battery pack. This type of cooling system is suitable for the battery pack that uses a low I_t-rate of charging and that for a converted EV with limited space for the battery pack.

9. Liquid cooling is more complex compared to air cooling. In the liquid cooling system, the heat transfer between battery and liquid coolant is achieved by installing discrete tubings around the batteries or liquid-cooled cold plates to the battery surface or submerging the battery in a dielectric liquid. The thermal performance of a liquid cooling system is higher than that of an air-cooled system, and the temperature distribution among the cells is more uniform. The disadvantages of liquid cooling include the requirement of large space, increase of vehicle total weight, higher cost due to the needs of auxiliary components such as pumps, liquid-liquid heat exchanger and controller, and high thermal inertia due to high thermal mass. Liquid cooling is suitable for a battery pack using high rates of charging and discharging.

10. Integration of Li-ion cells into a battery pack is a critical factor which determines the performance, cost, reliability and safety of the EVs.

Cost, packaging, electrical and control, assembly, thermal management and services and maintenance are the issues which need to be addressed in the integration process. A large number of smaller cells allow the heat generated from the driving to be distributed evenly to all the cells and the battery pack is less affected by capacity fading. However, the high number of interconnections, long hours of the assembly process, an increase in the chance of failure and difficulty in troubleshooting are the issues associated with a large number of small cells. On the other hand, while a smaller number of large cells will perform better in terms of assembly efficiency, ease of cell monitoring and servicing, they will performed poorly in terms of thermal management, thermal aging, low reliability, low flexibility in cell arrangement and capacity fading. A large portion of the cost of the battery pack goes to the cells, assembly and warranty. The profit of the battery pack is only about 10%. However, the reliability of the battery pack is still the main challenge which needs to be overcome in order to enlarge the EV market share.

11.2 Recommendations for future work

Based on the experimental and numerical modeling results obtained, the discussion presented and conclusions drawn from this research work, some potential areas for further investigation are highlighted below:

11.2.1 Electrochemical-thermal modeling

The electrochemical model is only validated with the experimental results using constant current discharging and charging. Therefore, one possible avenue for future work is to apply a variable power to study the dynamic

behavior of the cell using different driving cycles. Instead of using the lumped thermal model to model the heat generation in the spiral-wound region, layer by layer heat generation and thermal resistance of each layer can be modeled to improve the accuracy of the model.

Another interesting area for improving the electrochemical-thermal model is to investigate the interface resistance caused by the Solid Electrolyte Interface (SEI). The SEI is formed randomly at the electrode-electrolyte interface. Decomposition of the SEI may affect ionic motion by pore plugging and can contribute to resistive electrical paths to parts of the cathode structure. Hence, SEI formation and decomposition are the other important factors which need to be considered in the electrochemical-thermal modeling as they can alter the electrochemical reaction in the cell (Chattopadhyay et al., 2012).

11.2.2 Empirical model

The internal resistance of the Li-ion battery in an electro-thermal model is assumed constant throughout the charging and discharging cycle and independent of SOC and temperature. Besides, the model is only validated at room temperature (25 ^{o}C). Another interesting area for future work is to characterize the electrical behavior of the cell at low temperature (5 ^{o}C) and high temperature (40 ^{o}C). The cell will have different capacities and electrical characteristics at different temperatures. In addition, internal resistance is a function of SOC and temperature can be integrated into the electro-thermal model to improve the accuracy of the model.

11.2.3 Equivalent circuit model

The parameter extraction for the equivalent circuit model for the current study is using one I_t-rate of pulse discharge current. It is assumed that the

impedance of the cell does not change when a higher current is used to extract the cell parameters. Therefore, in the future work, the effect of the magnitude of the parameter extracting current on the cell parameters can be investigated to develop a more accurate model. In addition, a battery pack can be tested to verify the predicted electrical and thermal response of the battery pack.

11.2.4 Boron nitride coating

Boron nitride coating can be applied to an actual cell to investigate the thermal response of the cell and benchmark it against the classic cell using conventional polymer insulation.

11.2.5 Liquid cooling

The cooling fins can be fabricated into liquid cold plates and insert into a battery pack to investigate the performance of the cooling fins. Besides, it is also important to investigate the transient response of the cold plate. This is because the operation of the battery pack is mostly in a dynamic state and the heat generation in the cell is also not in steady state, but gradually increased to a maximum at the end of charging or discharging.

11.2.6 Reliability analysis of the battery pack

Reliability of the battery pack is one of the challenges that need to be overcome in order to promote the use of EV. Hence, a Physics-of-Failure analysis of the battery pack can be carried out to explore the failures rates and reliability across the parametric space.

BIBLIOGRAPHY

1. Abdalla, A., Mayyas, A. T., and Hallaj, S. A. (2010). Themo-mechanical behaviors of the expanded graphite phase change material matrix used for thermal management of Li-ion battery packs. *Journal of Material Processing Technology*. **210**. 174-179.

2. Accuratus, (2013) http://www.accuratus.com/boron.html. Access August 2013.

3. Alaoui, C., and Salameh, Z. M. (2005). A novel thermal management for electric and hybrid vehicle. *IEEE transactions on Vehicular Technology*. **54 (2)**. 468-476.

4. Al-Hallaj, S., Prakash, J. and Selman, J. R. (2000). Characterization of commercial Li-ion batteries using electrochemical-calorimetric measurements. *Journal of Power Sources*. **87 (1-2)**. 186-194.

5. Al-Hallaj, S., and Selman, J. R. (2002). Thermal modeling of secondary lithium batteries for electric vehicle/hybrid electric vehicle applications. *Journal of Power Sources*. **110(2)**. 341-348.

6. Al-Hallaj, S., Kizileli, R., Lateefi, A., Sabbahi, R., Farid, M., and Selman, J. R. (2005). Passive Thermal Management Using Phase Change Material (PCM) for EV and HEV Li-ion Batteries. Proceedings of IEEE Conference on Vehicle Power and Propulsion, Chicago. 376-380.

7. Alrashdan, A., Mayyas, A. T., and Hallaj, S. A. (2010). Thermomechanical behaviours of the expanded graphite-phase change material matrix used for thermal management of Li-ion battery packs. *Journal of Materials Processing Technology*. **210(1)**. 174-179.

8. Andrea, D. (2010). Battery Management Systems for Large Lithium-ion Battery Pack, Artech House, Massachusetts.

9. Andrea, D. (2010) International conference on battery power. Dallas, Texas.

10. Andre, D., Meiler, M., Steiner, K., Wimmer, Ch., Soczka-Guth, T., and Sauer, D. U. (2011). Characterization of high-power lithium-ion batteries by electrochemical impedance spectroscopy. I. Experimental investigation. *Journal of Power Sources*. **196 (12)**. 5334-5341.

11. Andrea, D. (2012). Battery management systems. Clean Tech 2012, Colorado, USA.

12. Ansys, ANSYS CFX-Solver modeling guide, Canonsburg: ANSYS INC, Canonsburg. 2010.

13. Awarke, A., Jaeger, M., and Pischinger, S. (2012). Comparison of model predictions with temperature data sensed on-Board from the Li-ion polymer cells of an electric vehicle. *SAE International*. doi:10.4271/2011-01-2443.

14. Baehr, H. D. and Stephan, K. (2006). *Heat and mass transfer*. Springer-Verlag Berlin Heidelberg. Germany.

15. Bandhauer, T. M., Garimella, S., and Fuller, T. F. (2011). A critical review of thermal issues in Lithium-ion batteries. *Journal of the Electrochemical Society*. **158 (3)**. R1–R25.

16. Barker, J., Pynenburg, R., Koksbang, R., and Saidi, M. Y. (1996). An electrochemical investigation into the lithium insertion properties of $LixCoO_2$, *Electrochemica Acta*, **41**. 2481-2488.

17. Battery Management System. Retrieved February 2014. http://www.avdweb.nl/solar-bike/electronics/bms.html.

18. Battery university. (2011). Lithium-based batteries. In Battery University. Retrieved May 2012. http://batteryuniversity.com/learn/article/lithium_based_batteries

19. Battery and energy technologies. Retrieved January 2014. http://www.mpoweruk.com.

20. Battery Technology. Retrieved February 2014. http://endless-sphere.com/forums/viewtopic.php?f=14&t=38761&start=350.

21. Beale, S. (2012). Tube banks, Crossflow over. In thermopedia. Retrieved May 2012. http://www.thermopedia.com/content/1211/?tid=104&sn=1410.

22. Belavendram, N. (1995). Quality by design, first ed., Prentice Hall, London.

23. Bendell, A., Disney, J., Pridmore, and W. A. (1989). Taguchi methods: applications in world industry, first ed., Springer-Verlag, Berlin.

24. Bello, I., Chong, Y. M., Leung, K. M., Chan, C. Y., Ma, K. L., Zhang, W. J., Lee, S. T., and Layyous, A. (2005). Cubic boron nitride films for industrial applications. *Diamond Related Material*. **14**. 1784-1790.

25. Benger, R., Wenzl, H., Beck, H. P., Jiang, M., Ohms, D., and Schaedlich, G. (2008). Electrochemical and thermal modeling of lithium-ion cells for use in HEV or EV application. *Journal of World Electric Vehicle*. **3**.

26. Bernardi, D, Pawlikowski, E., and Newman, J. (1985). A general energy-balance for battery systems. *Journal of the Electrochemical Society*. **132 (1)**. 5-12.

27. Boothroyd, G., Dewhurst, P., and Knight, W. A. (2011). Product Design For Manufacture and Assembly, Third ed., CRC Press, New York.

28. Bosccche, P. V., Vergels, F., Mierlo, J. V., Matheys, J., and Autenboer W. V. (2006). SUBAT: An Assessment of Sustainable Battery Technology. *Journal of Power Sources*. **162(2)**. 913-919.

29. Buller, S., Thele, M., Doncker, R. W. D., and Karden, E., (2005). Impedance based simulation models of supercapacitors and Li-ion batteries for power electronic applications. *IEEE Transactions on Industry Applications*. **41**. 742-747.

30. Brodd, R. J. (2013) Batteries for sustainability, selected entries from the encyclopedia of sustainability science and technology, Springer.

31. Cai, L., and White, R. E. (2011). Mathematical modeling of a lithium ion battery with thermal effects in COMSOL Inc. Multiphysics (MP) software. *Journal of Power Sources*. **196 (14)**. 5985-5989.

32. Mikolajczak, C., Kahn, M., White, K., and Long, R. T. (2011). Lithium-ion batteries hazard and use assessment. Exponent Failure Analysis Associates, Inc.

33. Ceraolo, M., Lutzemberger. G., and Huria, T. (2011). Experimentally-determined models for high-power lithium batteries, Proceedings of the SAE 2011 world Congress & Exhibition. Doi:10.4271/2011-01-1365.

34. Chapman, C. L., and Lee, S. (1994). Thermal performance of an elliptical pin fin heat sink. Proceedings of 1994 IEEE/CPMT 10th. 24-31.

35. Chen Y., and Evans, J. W. (1994). Three-dimensional thermal modeling of Lithium-polymer batteries under galvanostatic discharge and dynamic power profile. *Journal of the Electrochemical Society*. **141 (11)**. 2947-2955.

36. Chen, S. C., Wan, C. C., and Wang, Y. Y. (2005). Thermal analysis of lithium-ion batteries. *Journal of Power Sources*. **140 (1)**. 111-124.

37. Chen, S. C., Wang, Y. Y., and Wan, C. C. (2006). Thermal analysis of spirally wound lithium batteries. *Journal of Electrochemical Society*. **153(4)**. A637-A648.

38. Chen, M., and Rincon-Mora, G. A. (2006). Accurate Electrical Battery Model Capable of Predicting Runtime and I-V Performance. *IEEE Transaction on Energy Conversion*. **21**. 504-511.

39. Chen, Q., Zeng, M., Zhang, J., and Wang, Q. (2010). Optimal design of bi-layer interconnector for SOFC based on CFD-Taguchi method. International Journal of Hydrogen Energy. **35**. 4292-4300.

338

40. Chiang, Y. H., Sean, W. Y., and Ke, J. C. (2011). Online estimation of internal resistance and open circuit voltage of lithium-ion batteries in electric vehicles. *Journal of Power Sources*. **196 (8)**. 3921-3932.

41. Demirbas, M. F. (2006). Thermal energy storage and phase change materials: An overview. *Energy Sources*, Part B. **1**. 85-95.

42. Dhameja, S. (2002). *Electric vehicle battery systems*. USA. Newnes.

43. Djouadi, M. A., Vasin, A., Nouveau, C., Angleraud, B., and Tessier, P. Y. (2004). Deposition of boron nitride films by PVD methods: transition from h-BN to c-BN. *Surface Coatings Technology*. **181-181**. 174-177.

44. Doyle, M., Fuller, T. F., and Newman, J. (1993). Modeling of galvanostatic charge and discharge of the lithium/polymer/insertion cell. *Journal of the Electrochemical Society*. **140 (6)**. 1526-1533.

45. Dubarry, M., and Liaw, B. Y. (2007). Development of a universal modeling tool for rechargeable lithium batteries. *Journal of Power Sources*. **174 (2)**. 856-860.

46. Doyle, M., and Newman, J. (1996). Comparison of modeling predictions with experimental data from plastic lithium ion cells. *Journal of the Electrochemical Society*. **143 (6)**. 1890-1903.

47. Fagas, G., Gammaitoni, L., Paul, D., and Berini, G. A. (2014). ICT-Energy-Concepts towards Zero: Power information and communication Technology. INTECH. Open access.

48. Fang, W., Kwon, O. J., and Wang, C. Y. (2010). Electrochemical thermal modeling of automotive Li-ion batteries and experimental validation using a three electrode cell. Int. *Journal of Energy Research*. **34**. 107-115.

49. Fleckenstein, M., Bohlen, O., Roscher, M. A., and Baker, B. (2011). Current density and state of charge inhomogeneities in Li-ion battery cells with $LiFePO_4$ as cathode material due to temperature gradients. *Journal of Power sources*. **196 (10)**. 4769-4778.

50. Forgez, C., Do, D. V., Friedrich, G., Morcrette, M. and Delacourt, C. (2010). Thermal modeling of a cylindrical LiFePO4/graphite lithium-ion battery. *Journal of Power Sources*. **195 (9)**. 2961-2968.

51. Fu, R., Choe, S. Y. B., Jackson, R. L., Flowers, G. T., Bozack, M. J., Zhong, L., and Kim, D. (2012). Vibration-Induced changes in the contact resistance of high power electrical connectors for hybrid vehicles. *IEEE Transactions on Components, packaging and Manufacturing Technology*. **2 (2)**.185-193.

52. Fuller, T. F., Doyle, M., and Newman, J. (1994). Simulation and optimization of the dual lithium ion insertion cell. *Journal of the Electrochemical Society*. **141**. **(1)**. 1-10.

53. Gallet, S. L., Chollon, G., Rebillat, F., Guette, A., Bourrat, X., Naslain, R., Couzi, M., and Bruneel, J. L. (2004). Microstructural and microtextural investigations of boron nitride deposited from BCl_3-NH_3-H_2 gas mixtures. *Journal of European Ceramic Society*. **24**. 33-44.

54. Ghosh, D., Maguire, P. D., and Zhu, D. X. (2009). Design and CFD simulation of a battery module for a hybrid electric vehicle battery pack. SAE 2009 World Congress and Exhibition. Detroit, MI. USA.

55. Ghosh, D., King, K., Schwemmin, B., and Zhu, D. X. (2010). Full hybrid electrical vehicle battery packs system design, CFD simulation and testing. SAE 2010 World Congress and Exhibition. Detroit, MI. USA.

56. Gu, W. B., and Wang, C. Y. (2000). Thermal and electrochemical coupled modeling of a lithium-ion cell. *Proceedings of the ECS*, 99.

57. Hall, G. T. and Marthinuss, J. E. Jr. (2004). *Air cooled compact heat exchanger design for electronics cooling*. Electronics cooling.

58. Han, S., Han, S., and Aki, H. (2014). A practical battery wear model for electric vehicle charging applications. *Applied Energy*. **113**. 1100-1108.

59. He, H., Xiong, R., and Fan, J. (2011). Evaluation of Lithium-ion Battery Equivalent Circuit Models for State of Charge Estimation by an Experimental Approach. *Energies*. **4**. 582-598.

60. Heckenberger, T. (2009). Li-ion Battery Cooling: More than just another cooling task. Stuttgart, Germany.

61. Hu, Y., Yurkovich, S., Guezennec, Y., and Yurkovich, B. J. (2009). A technique for dynamic battery model identification in automotive applications using linear parameter varying structures. *Control Engineering Practice*. **17 (10)**. 1190-1201.

62. Hu, X., Li, S., and Peng, H. (2012). A comparative study of equivalent circuit models for Li-ion batteries, *Journal of Power Source*. **198**. 359-367.

63. Huria, T., Ceraolo, M., Gazzarri, J., and Jackey, R. (2012). High fidelity electrical model with thermal dependence for characterization and simulation of high power lithium battery cells, Proceedings of the 2012 IEEE International Electric Vehicle Conference. Doi: 10.1109/IEVC.2012.6183271.

64. Huria, T., Ludovici, G., Lutzemberger, G. (2014). State of charge estimation of high power lithium iron phosphate cells. *Journal of Power Sources*. **249**. 92-102.

65. Huang, P. G., Bardina, J. E., and Coakley, T. J. (1997). Turbulence modeling validation testing and development, in: NASA Technical Memorandum 110446, California.

66. Huisseune, H., T;Joen, C., Brodeoux, P., Debaets, S., and Paepe, M. D. (2010). Thermal hydraulic study of a single row heat exchanger with helically finned tubes. *Journal of Heat Transfer*. **132**. 061801-1-8.

67. Husain, E., Narayanan, T. N., Tijerina, J. J. T., Vinod, S., Vajtai, R., and Ajayan, P.M. (2013). Marine corrosion protective coatings of hexagonal boron nitride thin films on stainless steel. ACS Applied Materials and Interfaces. **5**. 4129-4135.

68. IEC 62660-1: Electrically propelled road vehicles—Test specification for lithium-ion traction battery packs and systems—Part 1: High power applications, 2011. Available online: http://webstore.iec.ch/webstore/webstore.nsf/artnum/044728!opendocument (Retrieved March 2014).

69. IEC 62660-2: Secondary batteries for the propulsion of electric road vehicles—Part 2: Reliability and abuse testing for lithium-ion cells, 2011. Available online: http://webstore.iec.ch/webstore/webstore.nsf/artnum/044727!opendocument (Retrieved March 2014).

70. Increasing battery capacity and life with fluorine compounds. Retrieved January 2014. http://www.daikin.com/csr/feature2009/02_2.html.

71. Incropera, F. P and Dewitt, D. P. (2006*). Fundamental of Heat and Mass Transfer*. 5th edition. John Wiley & Sons.

72. International Energy Agency. (2010). Energy Technology Perspectives-Scenarios and Strategies to 2050. Retrieved April 2013. http://www.iea.org/techno/etp/etp10/English.pdf.

73. ISO 12405-1: Electrically propelled road vehicles—Test specification for lithium-ion traction battery packs and systems—Part 1: High power applications, 2011. Available online: http://www.iso.org/iso/iso_catalogue/catalogue_ics/catalogue_ics_browse.htm?ICS1=43&ICS2=120 (Retrieved March 2014).

74. ISO 12405-2: Electrically propelled road vehicles—Test specification for lithium-ion traction battery packs and systems—Part 2: High energy applications, 2011. Available online: http://www.iso.org/iso/iso_catalogue/catalogue_ics/catalogue_ics_browse.htm?ICS1=43&ICS2=120 (Retrieved March 2014).

75. Jarrett, A., and Kim, Y. I. (2011). Design optimization of electric vehicle battery cooling plates for thermal performance. *Journal of Power Sources*. **196**. 10359-10368.

76. Jarrett, A., and Kim, Y. I. (2014). Influence of operating conditions on the optimum design of electric vehicle battery cooling plates. *Journal of Power Sources*. **245**. 644-655.

77. Jensen, H., and Sorensen, G. (1996). Ion bombardment as a tool for duplex surface treatment in boron nitride film deposition. Surface Coatings Technology. **84**. 524-527.

78. Jeon, D. H., and Baek, S. M. (2011). Thermal modeling of cylindrical lithium ion battery during discharge cycle. *Energy Conversion and Management*. **52**. 2973-2981.

79. Jin, L. W., Lee, P. S., Kong, X. X., Fan, Y., and Chou, S. K. (2014). UIltra-thin minichannel LCP for EV battery thermal management. *Applied Energy*. **113**. 1786-1794.

80. JIS C 8711:2013: Secondary cells and batteries containing alkaline or other non- acid electrolytes- Secondary lithium cells and batteries for portable applications. Available online: http://www.webstore.jsa.or.jp/webstore/Com/FlowControl.jsp?lang=en&bunsyoId=JIS+C+8711%3A2013&dantaiCd=JIS&status=1&pageNo=0 (Retrieved March 2014)

81. Johnson, V., Pesaran, A. A., and Sack, T. (2000). Temperature Dependent Battery Models for High-Power Lithium-ion Batteries. Proceedings of 17th Electric Vehicle Symposium, Montreal, Canada.

82. Johnson, V. H. (2002). Battery Performance Models in ADVISOR. *Journal of Power Sources*. **110 (2)**. 321-329.

83. Jung, S., and Kang, D. (2014). Multi-dimensional modeling of large-scale lithium-ion batteries. *Journal of Power Source*. **248**. 498-509.

84. Karditsas, N. (2012). USABC Development of Advanced High Performance Batteries for EV Applications. Retrieved April 2013. http://www1.eere.energy.gov/vehiclesandfuels/pdfs/merit_review_2012/energy_storage/es138_karditsas_2012_p.pdf.

85. Kays, W. M. and London, A. L. (1964). *Compact heat exchangers*. 2nd ed., McGraw-Hill, New York.

86. Kelly, K. J., and Rajagopalan, A. (2001). Benchmarking of OEM hybrid electric vehicles at NREL. National Renewable Energy Laboratory. (NREL/TP-540-31086). Golden, CO.

87. Kim, I. H., Kim, K. S., Kim, S. H., and Lee, S. R. (1996). Synthesis of cubic boron nitride films using a helicon wave plasma and reduction of compressive stress, *Thin Solid Films*. **290-291**. 120-125.

88. Kim, G. H., Pesaran, A. A., and Spotnitz, R. (2007). A three-dimensional thermal abuse model for lithium-ion cells. *Journal of Power Sources*. **170**. 476-489.

89. Kim, G. H., Gonder, J., Lustbader, J., and Pesaran, A. A. (2008). Thermal Management of Batteries in Advanced Vehicles Using Phase Change Materials. Journal of World Electric Vehicle. **2(2)**. 46-59.

90. Kim, D. E., Kim, M. H., Cha, J. E, and Kim, S. O. (2008). Numerical investigation on thermal-hydraulic performance of new printed circuit heat exchanger model. *Nuclear Engineering and Design*. **238**. 3269-3276.

91. Kim, U. S. Shin, C. B., and Kim, C. S. (2009). Modeling for the scale up of a lithium ion polymer battery. *Journal of Power Sources*. **189 (1)**. 841-846.

92. Kizilel, R., Lateef, A., Sabbah, R., Farid, M. M., Selman, J. R., and Hallaj, S. A. (2008). Passive control of temperature excursion and uniformity in high energy Li-ion battery packs at high current and ambient temperature. *Journal of Power Sources*. **183(1)**. 370-375.

93. Koh, J. C. Y., and Fortini, A. (1973). Prediction of thermal conductivity elecltrical resistivity of porous metallic materials. *International Journal of Heat and Mass Transfer*. **16**. 2013-2022.

94. Konyashin, I., Loeffler, J., Bill, J., and Aldinger, F. (1997). A novel approach to deposition of cubic boron nitride coatings. Thin Solid Films. **308-309**. 101-106.

95. Kotcioglu, I., Cansiz, A., and Khalaji, M. N. (2013). Experimental investigation for optimization of design parameters in a rectangular duct with plate-fins heat exchanger by Taguchi method. *Applied Thermal Engineering*. **50**. 604-613.

96. Kroeze, R. C., and Krein, P. T. (2008). Electrical Battery Model for Use in Dynamic Electric Vehicle Simulations. IEEE Power Electronics Specialists Conference, Rhodes, Greece. 1336-1342.

97. Kumaresan, K., Sikha, G., and White, R. E. (2008). Thermal model for a Li-ion cell. *Journal of the Electrochemical Society*. **155**. A164-A171.

98. Kuper, Ch., Hoh, M., Houchin-Miller, G., and Fuhr, J. (2009). Thermal Management of hybrid Vehicle Battery Systems. Proceeding of EVS24 International Battery, Hybrid and Fuel Cell Electric Vehicle Symposium. Stavanger, Norway.

99. Larminie, J., and Dicks, A. (2003). *Fuel cell systems Explained*. Wiley 2003.

100. Lee, G. G., Allan, W. D. E., and Boulama, K. G. (2013). Flow and performance characteristics of an Allison 250 gas turbine S-shaped diffuser: effects of geometry variations. *International Journal of Heat and Fluid Flow*. **42**. 151-163.

101. Leon, O. A., Mey, G. D., Dick, E., and Vierendeels, J. (2004). Staggered heat sinks with aerodynamic cooling fins. *Microelectronics Reliability*. **44**. 1181-1187.

102. Li, J. S., Zhang, C. R., Li, B., Cao, F., and Wang, S. Q. (2011). Boron nitride coatings by chemical vapor deposition from borazine. *Surface coating Technology*. **205**. 3736-3741.

103. Lienhard, J. H. (2008). *A heat transfer textbook*. 3rd ed. Phlogiston press.

104. Lipp, A., Scwetz, K. A., and Hunold, K. (1989). Hexagonal Boron Nitride: Fabrication, Properties and Application. *Journal of European Ceramic Society*. **5**. 3-9.

105. Lithium ion cylindrical cell. Retrieved January 2014. http://www.headway-cn.com.

106. Lithium-ion battery management systems and large battery pack. Retrieved January 2014. http://liionbms.com/php/pouch_tips.php

107. Lithium ion rechargeable batteries. Technical hand book. Retrieved March 2014. http://www.sony.com.cn/products/ed/battery/download.pdf

108. Lithium iron phosphate based battery-Assessment of the aging parameters and development of cycle life model. *Applied Energy*. **113**. 1575-1585.

109. Liu, G., Zheng, H., Song, X., Ridgeway, P., Kim, S., Minor, A., Deng, Y., and Battaglia, V. (2009). Binder Interactions in the Electrodes of the Lithium-ion Batteries. Proceeding of TFUG Conference, San Jose, CA.

110. Mahamud, R., and Park, C. W. (2011). Reciprocating air flow for Li-ion battery thermal management to improve temperature uniformity. *Journal of Power Sources*. **196 (13)**. 5685-5696.

111. McKenzie, D. R., McFall, W. D., Reisch, S., James, B. W., Falconer, I. S., Boswell, R. W., Persing, H., Perry, A. J., and Durandet, A. (1996). Synthesis of cubic boron nitride thin films. *Surface Coatings Technology*. **78**. 255-262.

112. Menard, L., Fontes, G., and Astier, S. (2010). Dynamic energy model of a lithium-ion battery. *Mathematics and Computers in Simulation*. **81**. 327-339.

113. Menter, F. R., Kuntz, M., and Langtry, R. (2003). Ten years of Industrial Experience with the SST turbulence model. *Turbulence, Heat and Mass Transfer*. **4**.

114. Mikron, Table of emissivity of various surfaces. Retrieved August 2012. http://www.eng.lbl.gov/~dw/projects/DW4229_LHC_detector_analysis/calculations/emissivity2.pdf.

115. Moffat, R. J. (1988). Describing the uncertainties in experimental results. *Experimental Thermal and Fluid Science*. **1**. 3-17.

116. Moura, S. J. (2011). Techniques for battery health conscious power management via electrochemical modeling and optimal control. Phd Thesis. The University of Michigan.

117. Mudawar, I., Bharathan, D., Kelly, K., and Narumanchi, S. (2009). Two phase spray cooling of hybridf vehicle electronics. *IEEE Transactions on Components and Packaging Technologies*. **32 (2)**. 501-512.

118. Nagaura, T. (1990). A lithium ion battery. 4th International rechargeable battery seminar, Deerfield Beach, Florida.

119. Navidi, W. (2008). *Statistics for engineers and scientists*. New York: McGraw Hill.

120. Nyman, A., Zavalis, T. G., Elger, R., Behm, M., and Lindbergh, G. (2010) Analysis of the polarization in a Li-ion battery cell by numerical simulations. *Journal of the Electrochemical Society*. **157(11)**. A1236-A1246.

121. Ohshima, T., Nakayama, M., Fukuda, K., Araki, T. and Onda, K. (2006). Thermal behavior of small lithium-ion battery during rapid charge and discharge cycles. *Electrical Engineering in Japan*. **157(3)**. 1521-1528.

122. Ohzuk, T., and Brodd, R. J. (2007). An Overview of Positive-electrode Materials for Advanced Lithium-ion Batteries. *Journal of Power Sources*. **174(2)**. 449-456.

123. Omar, N., Daowd, M., Bossche, P. V., Hegazy, O., Smekens J., Coosemans, T., and Mierlo, J. V. (2012). Rechargeable Energy Storage Systems for Plug-in Hybrid Electric Vehicles Assessment of Electrical Characteristics. *Journal of Energies*. **5**. 2952-2988.

124. Omar, N., Daowd, M., Hegazy, O., Mulder, G., Timmermans, J., Coosemans, Th., Bossche, P. V., and Mierlo, J. V. (2012). Standardization work for BEV and HEV applications: Critical appraisal of recent traction battery documents. *Journal of Energies*. **5**. 138-156.

125. Omar, N., Monem, M. A., Firouz, Y., Salminen, J., Smekens, J., Hegazy, O., Gaulous, H., Mulder, G., Bossche, P. V. D., Coosemans, T., and Mierlo, J. V. (2014). Lithium iron phosphate based battery-Assessment of the aging parameters and development of cycle life model. *Applied Energy*. **113**. 1575-1585.

126. Onda, K., Ohshima, T., Nakayama, M., Fukuda, K. and Araki, T. (2006). Thermal behavior of small lithium-ion battery during rapid charge and discharge cycles. *Journal of Power Sources*. **158 (1)**. 535-542.

127. Ota, T., and Kon, N. (1977). Heat transfer in an axisymmetric separated and reattached flow over a longitudinal blunt circular cylinder. *Journal of Heat Transfer*. **99**. 155-157.

128. Pesaran, A. A., Vlahinos, A., and Burch, S. D. (1997). Thermal performance of EV and HEV battery modules and packs. Proceedings of the 14th International Electric Vehicle symposium, Orlando, Florida. USA.

129. Pesaran, A. A., Burch, S. D., and Keyser, M. (1999). An approach for designing thermal management systems for electric and hybrid vehicle battery packs. Proceedings of the 4th vehicle thermal management system, London, U.K.

130. Pesaran, A. A. (2001). Thermal performance of EV and HEV battery modules and packs. Proceedings of the advanced automotive battery conference. Golden, Colorado: National Renewable Energy Laboratory.

131. Pesaran, A. A. (2001). Battery Thermal Management in EVs and HEVs: Issues and Solutions. Proceeding of Advanced Automotive Battery Conference, Las Vegas, Nevada.

132. Pesaran, A. A., and Keyser, M. (2001). Thermal characteristics of selected EV and HEV batteries. Annual battery conference: advances and applications. Long beach, California.

133. Pesaran, A. A. (2002). Battery thermal models for hybrid vehicle simulations. *Journal of Power Sources*. **110(2)**. 377-382.

134. Pesaran, A. A., Bharathan, D., Kim, G., Vlahinos, A., and Duong, T. (2005). Improving battery design with electro-thermal modeling. 21st Electric vehicle symposium. Monte Carlo, Monaco.

135. Pesaran, A. A., Smith, K., and Markel, T. (2009). Impact of the 3Cs of Batteries on PHEV Value Proposition: Cost, Calendar Life and Cycle Life. Proceeding of Advanced Automotive Battery and EC Capacitor Conference, Long Beach, California.

136. Pesaran, A. A., Kim, G. H., and Keyser, M. (2009). Integration issues of cells into battery packs for plug-in and hybrid electric vehicles. EVS-24 International Battery, Hybrid and Fuel cell Electric Vehicle Symposium, Stavanger, Norway.

137. Rahmoun, A., Biechl, H., and Rosin, A. (2013). Evaluation of equivalent circuit diagrams and transfer functions for modeling of Lithium-ion batteries, *Journal of Electrical, Control and Communication Engineering*. **2 (1)**. 34-39.

138. Rao, L., and Newman, J. (1997). Heat generation rate and general energy balance for insertion battery systems. *Journal of the Electrochemical Society*. **144**. 2697-2704.

139. Rao, Z., and Wang, S. (2011). A Review of Power Battery Thermal Energy Management. *Renewable and Sustainable Energy Reviews*. **15(9)**. 4554-4571.

140. Rao, Z., Wang, S., and Zhang, G. (2011). Simulation and experiment of thermal energy management with phase change material for ageing $LiFePO_4$ power battery. *Journal of Energy Conversion and Management*. **52(12)**. 3408-3414.

141. Roscher, M. A., Bohlen, O., and Vetter, J. (2011). OCV hysteresis in Li-ion batteries including two-phase transition materials. *International Journal of Electrochemistry*. Doi:10.4061/2011/984320.

142. Ross, J. P. (1988). Taguchi techniques for quality engineering, 2nd ed., McGraw-Hill, New York.

143. Roth, E. P. and Doughty, D. H. (2004). Thermal abuse performance of high-power 18650 Li-ion cells. *Journal of Power Sources*. **128 (2)**. 308-318.

144. Rudolph, S. (1993) Composition and application of coatings based on boron nitride. *International Ceramic Review*. **42 (5)**. 303-305.

145. Sabbah, R., Kizilel, R., Selman, J. R., and Hallaj, S. A. (2008). Active (air-cooled) vs. passive (phase change material) thermal management of high power lithium-ion packs: Limitation of temperature rise and uniformity of temperature distribution. *Journal of Power Sources*. **182(2)**. 630-638.

146. Safari, M., and Delacourt, C. (2011). Modeling of a commercial graphite/$LiFePO_4$ cell. *Journal of the Electrochemical Society*. **158**. A562-A571.

147. Sahin, B., Yakut, K., Kotcioglu, I., and Celik, C. (2005). Optimum design parameters of a heat exchanger. *Applied Energy*. **82**. 90-106.

148. Saini, M., and Webb, R. L. (2003). Heat rejection limits of air cooled plane fin heat sinks for computer cooling. *IEEE Transactions on components and packaging technologies*. **26 (1)**. 71-79.

149. Sato, N. (2001). Thermal behavior analysis of lithium-ion batteries for electric and hybrid vehicles. *Journal of Power Sources*. **99 (1-2)**. 70-77.

150. Schalkwijk, W. A. V., and Scrosati, B. (2002). Advances in Lithium-ion batteries, Kluwer academic publishers, New York.

151. Schmidt, T. E. (1949). Heat transfer calculations for extended surfaces. *Refrigeration Engineering*. 351-357.

152. Shepherd C. M. (1965). Design of primary and secondary cells: II. An equation describing battery discharge. *Journal of the Electrochemical Society*. **112**. 657-664.

153. Shi, J., Wu, F., Chen, S., and Zhang, C. (2006). Thermal analysis of rapid charging nickel/metal hydride batteries. *Journal of Power Sources*. **157**. 592-599.

154. Shimadzu, Rechargeable Lithium-ion battery evaluation. Retrieved January 2014. www.ssi.shimadzu.com/industry/literature/C10G-E021.pdf.

155. Smith, E. M. (2005). *Advances in thermal design of heat exchangers*. John Wiley & Sons, Ltd. Chichester, West Sussex, England.

156. Smith, K., and Wang, C. Y. (2006). Solid state diffusion limitations on pulse operation of a lithium-ion cell for hybrid electric vehicles. *Journal of power sources*. **161 (1)**. 628-639.

157. Smith, K., and Wang, C. Y. (2006). Power and thermal characterization of a lithium-ion battery pack for hybrid electric vehicles. *Journal of Power Sources*. **160 (1)**. 662-673.

158. Smith, K. (2006). Electrochemical modeling, estimation and control. PhD thesis. The Pennsylvania State University.

159. Smith, K. A., Rahn, C. D., and Wang, C. Y. (2007). Control oriented 1D electrochemical model of lithium ion battery. Energy Conversion Management. **48**. 2565-2578.

160. Sparrow, E. M., and Samie, F. (1985). Heat transfer and pressure drop results for one-and two-row arrays of finned tubes. *International Journal of Heat and Mass Transfer*. **28 (12)**. 2247-2259.

161. Sparrow, E. M., and Geiger, G. T. (1985). Local and average heat transfer characteristics for a disk situated perpendicular to a uniform flow. *Journal of Heat Transfer*. **107**. 321-326.

162. Sparrow, E. M., Abraham, J. P., and Minkowycz, W. J. (2009). Flow separation in a diverging conical duct: effect of Reynolds number and divergence angle. *International Journal of Heat and Mass Transfer*. **52**. 3079-3083.

163. Srinivasan, V., and Wang, C. Y. (2003). Analysis of electrochemical and thermal behavior of Li-ion cells. *Journal of the Electrochemical Society*. **150 (1)**. A98-A106.

164. Srinivasan, V., and Newman, J. (2004). Discharge model for the lithium iron phosphate electrode. *Journal of the Electrochemical Society*. **151 (10)**. A1517-A1529.

165. Srinivasan, V. (2010). BATT November 2010 Quartely Report, Berkeley National Laboratory, Berkeley.

166. Sunden, B. (2012). Tubes, Crossflow over. In thermopedia. Retrieved May 2012. http://www.thermopedia.com/content/1216/

167. Swanepoel, G. (2001). Thermal Management System of Hybrid Electrical Vehicles using Heat Pipes. M. Sc. Thesis, Retrieved April 2014. http://www.mecheng.sun.ac.za/research/heatpipe/swanepoel_thesis.pdf.

168. Takano, K., Saito, Y. Kanari, K., Nozaki, K., Kato, K., Negishi, A. and Kato, T. (2002). Entropy change in lithium ion cells on charge and discharge. *Journal of Applied Electrochemistry*. **32**. 251-258.

169. Taheri, P., Hsieh, S., and Bahrami, M. (2011). Investigating electrical contact resistance losses in lithium-ion battery assemblies for hybrid and electric vehicles. *Journal of Power Sources*. **196 (15)**. 6525-6533.

170. Tang, X., Mao, X., Lin, J., and Koch, B. (2011). Li-ion battery parameter estimation for state of charge. Proceedings of the 2011 American Control Conference. 941-946.

171. Tango car. Retrieved February 2014. http://tangocars.blogspot.sg/2010/03/tango-with-32-kwhr-pack-of-headway.html

172. Teach you something about E-bike batteries. Retrieved February 2014. http://www.pedelecforum.de/forum/index.php?threads/teach-you-something-about-e-bike-batteries.18297/

173. The Boston Consulting Group. (2013). Batteries for Electric Cars: Challenges, Opportunities and the Outlook to 2020. Retrieved April 2013. http://www.bcg.com.

174. Thele, M., Bohlen, O., Sauer, D. U., and Karden E. (2008). Development of a voltage-behavior model for NiMH batteries using an impedance-based modeling concept. *Journal of Power Sources*. **175**. 635-643.

175. Thomas, K. E., and Newman, J. (2003). Thermal modeling of porous insertion electrodes. *Journal of the Electrochemical Society*. **150**. A176-A192.

176. Thorat, I. V. (2009). Understanding performance limiting mechanisms in Li-ion batteries for high rate applications. PhD thesis. Brigham Young University.

177. Thorat, I. V., Joshi, T., Zaghib, K., Harb, J. N., and Wheeler, D. R. (2011). Understanding rate-limiting mechanisms in $LiFePO_4$ cathodes for Li-ion batteries. *Journal of the Electrochemical Society*. **158**. A1185-A1193.

178. Tremblay O. (2007). A generic battery model for the dynamic simulation of hybrid electric vehicles. VPPC 2007, Proc. Vehicle Power and Propulsion conference. Arlington, TX. USA.

179. Tremblay O., and Dessaint L. (2009). Experimental validation of a battery dynamic model for EV applications. *Journal of World electric Vehicle*. **3**.

180. Tsai, C. H, Chang, C. L. and Chen, L. (2003). Applying grey relational analysis to the vendor evaluation model. *International Journal of the Computer, the Internet and Management*. **11 (3)**. 45-53.

181. Tsang, K. M., Sun, L., and Chan, W. L. (2010). Identification and modeling of Lithium ion battery. *Journal of Energy Conversion and Management*. **51**. 2857-2862.

182. Turgut, E., Cakmak, G., and Yildiz, C. (2012). Optimization of concentric heat exchanger with injector turbulators by Taguchi method. *Energy Conversion and Management*. **53**. 268-275.

183. Urbain, M., Rael, S., Davat, B., and Desprez, P. (2008). Energetical Modeling of Lithium-ion Battery Discharge and Relaxation. IEEE Power Electronics Specialists Conference, Rhodes, Greece. 1336-1342.

184. US DOE. (2013). One Million Electric Vehicles by 2015: February 2011 Status Report. Retrieved April 2013. http://energy.gov/sites/prod/files/edg/news/documents/1_Million_Electric _Vehicle_Report_Final.pdf.

185. Versteeg, H. K. and Malalasekera, W. (1999). *An introduction to computational fluid dynamics*. *The finite volume method*. Longman, London.

186. Viswanathan, V. V., Choi, D., Wang, D., Xu. W., Towne, S., Williford, R. E., Zhang, J. G., Liu, J., and Yang, Z. (2010). Effect of entropy change of lithium intercalation in cathodes and anodes on Li-ion battery thermal management. *Journal of Power Sources*. **195**. 3720-3729.

187. Wang, C. C., Chi, K. Y. and Chang, C. J. (2000). Heat transfer and friction characteristics of plate fin and tube heat exchangers, Part II: correlation. *International Journal of Heat and Mass Transfer*. **43**. 2693-2700.

188. Wang, C. S., Kasavajjula, U. S., and Arce, P. E. (2007). A discharge model for phase transformation electrodes: Formulation, experimental validation and analysis. *Journal of Physical Chemistry C*. **111**. 16656-16663.

189. Wang, J., Liu, P., Hicks-Garner, J., Sherman, E., Soukiazian, S., Verbrugge, M., Tataria, H., Musser, J., and Finamore, P. (2011). Cycle-life model for graphite-LiFePO$_4$ cells. *Journal of Power Sources*. **196**. 3942-3948.

190. Wenige, R., Niemann, M., Heider, U., Jungnitz, M., and Hilarius, V. (1997). Liquid Electrolyte Systems for Advanced Lithium Batteries. Proceeding of the Industrial Chemistry Symposium, Seoul, Korea.

191. Wiberg, R., and Lior, N. (2004). Heat transfer from a cylinder in axial turbulent flows. *International Journal of Heat and Mass Transfer*. **48**. 1505-1517.

192. Williford R, Viswanathan, V., and Zhang, J. G. (2009). Effects of entropy changes in anodes and cathodes on the thermal behavior of lithium ion batteries. *Journal of Power Sources*. **189 (1)**. 101-107.

193. Wu, H. H. (1996). *The introduction of Grey Analysis*. Gauli Publishing Co. Taipei.

194. Wu, M. S, Liu, K. H., Wang, Y. Y., and Wan, C. C. (2002). Heat dissipation design for lithium-ion batteries. *Journal of Power Sources*. **109 (1)**. 160-166.

195. Xie, G., Wang, Q. and Sunden, B. (2009). Parametric study and multiple correlations on air-side heat transfer and friction characteristics of fin and tube heat exchangers with large number of large diameter tube rows. *Applied Thermal Engineering*. **29**. 1-16.

196. Ye, F., Zhang, L., Liu, Y., Li, S., Su, M., Yin, X., and Cheng, L. (2012) Investigation on preparing boron nitride by nitriding pure boron at 1200-1550 $^\mathrm{o}$C. *Progress in Natural Science: Materials International*. **22**. 433-439.

197. Ye, Y., Saw, L. H., Shi, Y., Somasundaram, K., and Tay, A. A. O. (2014). Effect of thermal contact resistances on fast charging of large format lithium ion batteries. *Electrochemical Acta*. doi:10.1016/j.electacta.2014.04.134.

198. Yi J, Kim U. S., Shin C. B., Han, T., and Park, S. (2013). Three-dimensional thermal modeling of a lithium-ion battery considering the

combined effects of the electrical and thermal contact resistances between current collector tab and lead wire. *Journal of the Electrochemical Society*. **160**. A437-A443.

199. Zhang, S. S. (2007). An overview of the development of Li-ion batteries: From material, single cell to battery pack. *Advanced materials and methods for Lithium-ion batteries*. 1-22.

200. Zhang, X. (2011). Thermal analysis of a cylindrical lithium-ion battery. *Electrochemical Acta*. **56**. 1246-1255.

201. Zolot, M., Pesaran, A. A., and Mihalic, M. (2002). Thermal evaluation of Toyota Prius battery pack. The Future Car Congress.

202. Zukauskas, A. and Ulinskas, R. (1988). *Heat transfer in tube banks in crossflow*. Washingston, D. C. Hemisphere Publishing Corporation.

203. Zukauskas, A., Ulinskas, R. and Katinas, V. (1987). *Fluid dynamics and flow induced vibrations of tube banks.* Washingston, D. C. Hemisphere Publishing Corporation.